



TECHNISCHE  
UNIVERSITÄT  
WIEN

# Single-atom cavity quantum electrodynamics with whispering-gallery-modes: Single-photon nonlinearity and nonreciprocity

DISSERTATION

zur Erlangung des akademischen Grades

**Doktor der technischen Wissenschaften**

eingereicht von

**Michael Scheucher**

Matrikelnummer 0725612

Trauttmansdorffgasse 22/1/10, 1130 Wien

an der

Fakultät für Physik der Technischen Universität Wien

Betreuung: Prof. Dr. Arno Rauschenbeutel, E141 – Atominstitut

Diese Dissertation haben begutachtet:

---

(Prof. Dr. Barak Dayan)

---

(Prof. Dr. David Hunger)

---

(Prof. Dr. Arno  
Rauschenbeutel)

Wien, 14.06.2017

---

(Michael Scheucher)





TECHNISCHE  
UNIVERSITÄT  
WIEN

# Single-atom cavity quantum electrodynamics with whispering-gallery-modes: Single-photon nonlinearity and nonreciprocity

DISSERTATION

submitted in partial fulfillment of the requirements for the degree of

**Doktor der technischen Wissenschaften**

by

**Michael Scheucher**

Registration Number 0725612

Trauttmansdorffgasse 22/1/10, 1130 Wien

to the Faculty of Physics  
at the TU Wien

Advisor: Prof. Dr. Arno Rauschenbeutel, E141 – Atominstitut

The dissertation has been reviewed by:

---

(Prof. Dr. Barak Dayan)

---

(Prof. Dr. David Hunger)

---

(Prof. Dr. Arno  
Rauschenbeutel)

Wien, 14.06.2017

---

(Michael Scheucher)



# Kurzfassung

Für viele Anwendungen im Bereich der Quantentechnologie ist starke Kopplung zwischen Licht und Materie unverzichtbar. Sie ermöglicht zum Beispiel das Verbinden einzelner Knotenpunkte von großflächigen Quantennetzwerken und erlaubt es, eine deterministische Wechselwirkung zwischen einzelnen Photonen zu erzeugen. Starke Licht-Materie-Wechselwirkung wurde bereits in unterschiedlichen Systemen realisiert, unter anderem auch in optischen Resonatoren. Optische Bauelemente, die auf Resonatoren basieren, sind jedoch oft mit großen Verlusten verbunden, die für viele Anwendungen hinderlich sind. Um diese zu vermeiden, können sogenannte Flüstergalleriemoden-Resonatoren verwendet werden. Diese Resonatoren zeichnen sich nicht nur durch eine besonders hohe Güte und ein kleines Modenvolumen aus, sondern auch durch die hohe Effizienz beim Ein- und Auskoppeln von Licht. Außerdem treten aufgrund des starken transversalen Einschlusses des Lichts besondere Polarisationszustände auf, welche zu einer chiralen, d.h. richtungsabhängigen Wechselwirkung führen.

Im Rahmen dieser Arbeit wurden zwei neuartige optische Bauelemente demonstriert, welche auf dieser chiralen Wechselwirkung zwischen einzelnen Atomen und einem Flüstergalleriemoden-Resonator basieren. Das Erste ist ein nichtlinearer Phasenschieber für einzelne Photonen. Dabei nutzen wir die Nichtlinearität eines einzelnen Atoms aus, um den größtmöglichen nichtlinearen Phasenschub von  $180^\circ$  zwischen einzelnen Photonen und Photonenpaaren zu erzeugen. Zur Messung des Phasenschubs wurde die Dichtematrix des transmittierten Lichts mit Hilfe der Quantentomographie rekonstruiert. Darüber hinaus konnten wir zeigen, dass dieser Prozess Verschränkung zwischen den beiden, zuvor voneinander unabhängigen, Photonen erzeugt.

Das zweite optische Element ist ein Zirkulator mit vier Eingängen, der Licht von einem Eingang jeweils zum nächsten weiterleitet. Dieses nichtreziproke Verhalten basiert auf der chiralen Kopplung zwischen dem Resonator und einem einzelnen Atom. Die Funktionsweise des Zirkulators wird durch das Atom gesteuert und kann invertiert werden, indem das Atom in einem anderen Spinzustand präpariert wird. Dies ermöglicht es grundsätzlich, den Zirkulator in einer quantenmechanischen Überlagerung der beiden Richtungen zu betreiben. Außerdem wurden die nichtlinearen Eigenschaften der Zirkulators untersucht. Dabei konnten wir zeigen, dass unser System auch als photonenzahlabhängiger Router eingesetzt werden kann.

Die im Rahmen dieser Arbeit erzielten Ergebnisse stellen einen wichtigen Schritt hin zur Realisierung von neuartigen Komponenten zur faseroptischen quantenmechanischen Informationsverarbeitung dar.



# Abstract

The realization of strong light–matter interaction is crucial for many applications in quantum science and quantum technology. In particular, it allows one to link individual nodes of a large-scale quantum network or to mediate deterministic photon–photon interactions, which are required for many quantum protocols. Strong light–matter interaction has been successfully demonstrated in different systems, including optical resonators. However, for being applicable to photonic quantum information processing high photon losses of existing implementations hamper many applications. One way to avoid these losses is to employ whispering-gallery-mode resonators, which, despite their ultra-high quality and small volume, allow extremely efficiently coupling to waveguides. Furthermore, the strong transverse confinement of the light in these structures gives rise to extraordinary polarization properties which cause chiral, i.e. direction-dependent, coupling between light and matter.

In this thesis, I report on the realization of two novel photonic devices which are based on the chiral interaction between light circulating in a bottle microresonator and a single rubidium atom. The first device is a nonlinear phase shifter, that realizes a strong optical nonlinearity on the single photon level. This nonlinearity is based on the nonlinear response of a single atom, which is enhanced by the resonator. By performing quantum state tomography of the field passing the atom–resonator system, we demonstrate the maximal nonlinear phase shift of  $180^\circ$  between the case where single or pairs of photons pass the resonator. Furthermore, we verify that this process creates entanglement between two previously independent photons.

The second device is a four-port quantum circulator, which is formed by two fiber couplers and the resonator. The chiral coupling between the atom and the resonator then gives rise to non-reciprocal transmission properties. We also show that the operation direction of the circulator is controlled by the spin state of the atom and can be inverted. This, in principle allows one to prepare a superposition of the two circulator operation directions. Furthermore, we study the nonlinear performance of the demonstrated circulator. Here we observe that the system routes single photons to different ports as pairs of photons.

The results presented in this thesis are important steps toward realizing new, fully fiber-integrated components for quantum information processing.





# Contents

<b>1</b>	<b>Introduction</b>	<b>1</b>
<b>2</b>	<b>Non-transversal fields in evanescent waves</b>	<b>5</b>
2.1	Longitudinal fields and spin–momentum locking . . . . .	5
2.2	Total internal reflection and evanescent fields . . . . .	8
<b>3</b>	<b>The bottle microresonator</b>	<b>17</b>
3.1	Resonator properties . . . . .	18
3.2	General CQED parameters . . . . .	19
3.3	Optical whispering-gallery-modes . . . . .	20
3.4	Modes of bottle microresonators . . . . .	21
<b>4</b>	<b>Interaction between light and matter in WGMs</b>	<b>31</b>
4.1	Jaynes–Cummings Model . . . . .	32
4.2	Losses and driving: The master equation . . . . .	34
4.3	Strong coupling and fast cavity regime . . . . .	37
4.4	Coupling between a single atom and WGMs . . . . .	37
4.5	Chiral waveguides . . . . .	46
<b>5</b>	<b>Experimental apparatus</b>	<b>57</b>
5.1	General design consideration . . . . .	57
5.2	Experimental implementation of a BMR . . . . .	58
5.3	Basic experimental setup . . . . .	65
5.4	Experimental procedures . . . . .	70
<b>6</b>	<b>Nonlinear phase shift</b>	<b>85</b>
6.1	Working principle . . . . .	87
6.2	Experimental procedure . . . . .	92
6.3	Single-atom phase shift and polarization rotation . . . . .	94
6.4	Measuring single-photon nonlinearity . . . . .	95
6.5	Outlook: Implementing a photon–photon gate . . . . .	104
<b>7</b>	<b>Quantum circulator</b>	<b>107</b>
7.1	Characteristics of a nonreciprocal device . . . . .	108

7.2	Review of integrated nonreciprocal devices . . . . .	113
7.3	Working principle of the single atom-controlled circulator . . . . .	118
7.4	Theoretical description of the circulator . . . . .	120
7.5	Experimental procedure and modifications of the setup . . . . .	121
7.6	Experimental results . . . . .	125
7.7	Discussion and outlook . . . . .	132
<b>8</b>	<b>Summary and outlook</b>	<b>137</b>
	<b>List of acronyms</b>	<b>141</b>
	<b>Appendices</b>	<b>143</b>
A.1	Transition strengths for the $D_2$ -line of $^{85}\text{Rb}$ . . . . .	145
A.2	Numerical solution of the Master equation . . . . .	147
A.3	Chirally coupled atom–resonator–waveguide system . . . . .	148
A.4	Supplement to the circulator . . . . .	149
A.5	Second-order intensity correlation function . . . . .	151
A.6	Conditional single-atom phase shift . . . . .	152
A.7	Density matrix reconstruction . . . . .	153
A.8	Concurrence . . . . .	161
A.9	Legend for fiber network . . . . .	161
	<b>Bibliography</b>	<b>163</b>

# Introduction

The advent of quantum mechanics at the beginning of the 20<sup>th</sup> century fundamentally changed the way we look at the world today. Applying the physical principles of quantum mechanics revolutionized our understanding of physics and resulted in groundbreaking technologies, such as transistors, lasers and superconductors. Making use of these technologies enables us today to harness quantum phenomena, such as superposition and entanglement, for creating novel devices. Along this direction, the field of quantum science and technology emerged, which pursue four auspicious directions.

For example, a variety of quantum effects are employed in the field of quantum metrology [1] and quantum sensing [2]. By making use of the fragile nature of quantum superpositions and entanglement enables one to perform measurements with unprecedented sensitivity, even beyond the classical noise limit.

A second direction studies quantum simulators, which use well controlled artificial quantum systems to investigate the behavior and properties of less accessible systems [3]. Quantum simulators promise to simulate complex systems such as materials or chemical compounds, which due to their exponentially increasing computational complexity, cannot be simulated with classical computers.

Another very active field of research is quantum communication [4], where information is encoded in the form of quantum bits (qubits) which are stored, manipulated and distributed between nodes of a quantum network [5]. In particular, quantum cryptography, which allows secure transmission of information over long distances, has attracted considerable attention.

Probably the most advertized application of quantum physics is the realization of a quantum computer [6]. Instead of storing information using classical bits, which can either be 0 or 1, quantum computers use qubits to encode information. In contrast to a classical bit, a qubit can be prepared in a superposition of the states 0 and 1. In addition, the qubits can be entangled with each other. This enables quantum computers to manipulate large combinations of states all at once. As a consequence, they are able to perform particular computational tasks much more efficiently than their classical analogs.

In the past decades, a large number of physical systems are being explored to harness quantum

features for applications in quantum science and technology. Depending on the application, special requirements have to be fulfilled and different platforms might be favorable.

For many applications in quantum communication, such as quantum key distribution, optical photons are an obvious choice to act as flying qubits in order to transmit quantum information over long distance. Photons are well decoupled from their environment and are therefore relatively free of the decoherence that plagues other quantum systems. Moreover, photons were the first platform to demonstrate entanglement and played a key role in many fundamental studies of quantum mechanics [7].

In addition, photons are a natural choice for transmitting quantum information between the nodes of large scale quantum networks. In such networks, quantum information has to be generated, processed and stored locally in quantum nodes. These nodes are usually considered to be matter-based and are linked by photonic quantum channels. Their interplay requires efficient coupling between light and matter. The fact that the nodes are interconnected allows one to transport quantum states from site to site, and thereby enables the distribution of entanglement across the entire network.

In order to realize a quantum computer, the requirements for the qubits not only include good coherence properties, but they also have to be initialized, measured, and most importantly, a mechanism to implement a universal set of quantum logic gates has to be available [8]. A number of physical implementations of such gates are being explored, employing photons, along with ions, nuclear magnetic resonance, atoms, and superconducting qubits [6]. The manipulation and detection of single optical photons can be realized using well established techniques. However, it is hard to realize direct photon–photon interaction which is necessary for two-photon gates to entangle the qubits. One way to mediate this interaction is to strongly couple the photon to an auxiliary system, such as a single atom.

In order to employ photons in quantum information processing, it is essential to realize deterministic light–matter interaction. However, the interaction between single emitters and single photons is usually very small. One way to enhance their interaction is to employ collective effects of ensembles of emitters [9] or to use the field enhancement in resonators [10]. The interaction between quantized light in resonators and matter is studied in the framework of cavity quantum electrodynamics (CQED) [11]. If they are strongly coupled, a coherent energy exchange between the two can be observed. This regime was first demonstrated in the realm of superconducting microwave cavities and Rydberg atoms [12]. This research has led to numerous cutting-edge experiments, including fundamental tests of quantum mechanics. The achievements of this field were rewarded with a Nobel Prize in physics in 2012, which Serge Haroche received for his work on measuring and manipulating individual quantum systems [13].

For many applications, the physical properties of optical photons are favorable compared to microwave photons. Recent progress in experimental quantum optics enabled the realization of strong coupling between single emitters and single photons also in the visible spectral region [14–17]. Various types of optical resonators have been established, comprising Fabry–Pérot (FP) resonators based on high-reflective mirrors or fiber facets, photonic crystal cavities and whispering-gallery-mode (WGM) microresonators [18]. Among these, WGM resonators have attracted considerable interest for integrated photonic applications. WGMs confine light by means of total internal reflection in a dielectric, monolithic structure. The light then forms trav-

---

eling wave modes in which light circulates around the resonator's circumference. These WGMs can have extremely high quality and hence photons have a long lifetime in the resonator. Since WGM microresonators enable extremely efficient in and out-coupling of light, via frustrated total internal reflection between the resonator and a coupling waveguide, they are promising candidates for the implementation of new and efficient quantum and photonic applications [19]. Furthermore, they are inherently integrated and are compatible with standard chip-fabrication techniques [20], and thus promise to be easily scalable and integrable into existing technologies and future integrated optical circuits.

Due to the strong confinement in these new resonator types, light exhibits strong transversal field gradients on the order of the wavelength, thereby inducing strong longitudinal polarization components. This longitudinal polarization gives rise to a correlation between the propagation direction of the light and the local polarization, known as spin-momentum locking [21]. Recently it has been realized that this effect can be used to implement chiral, i.e. direction-dependent, light-matter interaction [22]. This new paradigm of light-matter interaction has far reaching consequences and enables a plethora of interesting new applications.

In this thesis, we investigate the implementation of fiber-integrated nanophotonic devices employing effects from the realm of CQED. In order to enable high efficient, i.e. low photon loss, operation of these devices, we employ a bottle microresonator (BMR) – a novel type of WGM resonators – as key element in our experiments. Due to its ultra high quality, small volume and efficient coupling to a nanofiber waveguide, the BMR is a powerful tool for nanophotonic applications. In our experiment, the light that circulates in the resonator is interfaced with single rubidium atoms, realizing strong light-matter interaction, which we then use to implement different photonic protocols.

The thesis is organized in the following manner: First the basic properties of strongly confined light fields will be discussed in Ch. 2. In particular, we will theoretically derive the emergence of spin-momentum locking of light in the case of total internal reflection at a planar interface.

Chapter 3 is devoted to the key element of our experiment, the BMR. After a general introduction to resonators, we will derive the electric field distribution of modes supported by our BMR and discuss their polarization properties.

In Ch. 4 a theoretical model for the description of light-matter in WGM resonators is developed. We start from the simple Jaynes-Cummings model, and consecutively extend the model such that it accurately describes the interaction between single multilevel atoms and WGMs. This provides the theoretical framework for the experiments discussed in this thesis. We then study two simplified situations, for which we can analytically solve our model. These solutions allow us to elaborate on the chiral interaction between light and matter. This is followed by a short description of chiral waveguides.

Chapter 5 is dedicated to the experimental setup which we employ to study the interaction between light and matter at the fundamental level of single photons and single atoms. After describing the hardware, we also introduce the most important experimental procedures that are necessary for operating the experiment.

In Ch. 6 we employ the BMR, which is chirally coupled to a single atom, to realize a nonlinear phase shifter. After analyzing the phase introduced by the presence of the atom, we investi-

gate the nonlinear behavior of the coupled atom–resonator system. By analyzing the transmitted light, we are able to reconstruct the two-photon state. We show that our system introduces a different phase shift for single photons or pairs of photons. In particular, we observe the maximal nonlinear phase shift of  $\pi$  at the level of single photons. Furthermore, we demonstrate that the interaction with our system causes entanglement between two initially independent photons.

In Ch. 7 we explicitly employ chiral light–matter interaction to realize a four-port optical circulator using our atom–resonator system. After characterizing its transmission properties, we also investigate its quantum attributes. First, we show that the operation direction of the circulator can be controlled by the internal state of the atom, which in principle allows one to create superposition states of the circulator operation. Secondly, we investigate the nonlinear response of the device.

Finally, in Ch. 8 we summarize the results and outline possible future steps for the experiment. In this context, we discuss an important future upgrade, which should enable us to trap single atoms in the vicinity of our resonator.

# Non-transversal fields in evanescent waves

## 2.1 Longitudinal fields and spin–momentum locking

In geometric and Gaussian optics it is very common to assume that the light beams are well collimated, and thus to apply the so-called paraxial approximation. From this one derives that the electromagnetic field oscillates solely in a plane perpendicular to the direction of propagation, forming a purely transverse wave. However, this approximation fails when beams are strongly focused or confined in transverse direction. These waves also exhibit longitudinal polarization components that oscillate in direction of propagation. Moreover, the longitudinal field components are in quadrature ( $90^\circ$  out of phase) with respect to the transverse component. As a consequence, the local electric field vector rotates around an axis that is perpendicular to its propagation direction forming a locally elliptically polarized field. Even though these effects are well known and applied in microwave engineering [23] and they have already been describe in 1959 for optical waves [24], they recently received a great deal of attention [25]. These phenomena, which are now often referred to as transverse spin angular momentum (SAM) of light, were intensively studied theoretically [26–31]. Furthermore, recent experimental advances made it possible to directly examine and probe the local properties of light [32–35]. One important consequence of transverse SAM is spin–momentum locking (SML), which links the local polarization to the propagation direction of the light [30]. Recently, this has been used for realizing directional channeling of light, which was demonstrated across various optical systems, including surface plasmon polaritons [36–39], tightly focused Gaussian beams [40], nanofiber waveguides [41,42], nanobeam waveguides [43] and photonic crystal waveguides [44,45]. However, the far-reaching consequences these local field properties have on the interaction of light and matter were often not taken into account [46].

In this chapter, we will give a short introduction on this transverse SAM of light and discuss its origin by introducing a intuitive explanation, that covers the essence of this phenomena. Then, we will discuss the emergence of transverse SAM in so-called evanescent fields, that occur when

light undergoes total internal reflection at a planar interface. This system is of particular interest, since it resembles the situation we encounter in our experiment very well. In the context of transverse SAM, we obtain the key result of this chapter, being the concept of SML.

### 2.1.1 From gradients to longitudinal fields

Any electromagnetic wave is fully described by Maxwell's equations. In particular, the electric field  $\mathbf{E}$  has to fulfill Gauß's law, which in a charge- and current-free dielectric media is given by

$$\operatorname{div} \mathbf{E} = 0 . \quad (2.1)$$

We now consider a monochromatic beam with frequency  $\omega$  propagating in positive  $y$ -direction whose electric field is given by  $\mathbf{E} = \mathcal{E} \exp i(\omega t - |\mathbf{k}|y) + c.c.$ , where  $\mathcal{E} = (\mathcal{E}_x, \mathcal{E}_y, \mathcal{E}_z)$  is the vector amplitude of the field and  $\mathbf{k}$  its wave vector. In addition, we assume that  $\mathcal{E}$  varies only slowly along the  $y$ -direction, thus

$$\partial \mathbf{E} / \partial y \approx -i|\mathbf{k}| \mathcal{E} \exp i(\omega t - |\mathbf{k}|y) + c.c. . \quad (2.2)$$

From Gauß's law we then obtain the longitudinal component

$$\mathcal{E}_y \approx -i \frac{\lambda}{2\pi} \left( \frac{\partial \mathcal{E}_x}{\partial x} + \frac{\partial \mathcal{E}_z}{\partial z} \right) . \quad (2.3)$$

Equation (2.3) shows that a strong longitudinal polarization component will occur as soon as the amplitude of the transverse field component varies on the length scale of  $|\mathbf{k}|^{-1} = \lambda/2\pi$ . The  $i$  in Eq. (2.3) imposes that the longitudinal field component is in quadrature to the transverse field components, i.e. has a phase retardation of  $\pi/2$ . Together with the transverse field components the light is thus elliptically polarized. When the longitudinal and the transverse field components have the same amplitude, i.e.  $|\mathcal{E}_y| = \sqrt{|\mathcal{E}_x|^2 + |\mathcal{E}_z|^2}$ , the local polarization is perfectly circularly polarized

There is a large variety of situations that feature strong gradients and thus show longitudinal polarization components. This includes tightly focused Gaussian beam but also two-wave interference and most importantly evanescent fields. In addition, it is also observed in near-fields of plasmonic systems or photonic crystal wave-guides.

### 2.1.2 Transverse spin angular momentum of light

Already at the beginning of the 20th century, Pointing suggested to assign angular momentum to circularly polarized light [47]. Today, we distinguish two kinds of optical angular momenta: Orbital angular momentum and spin angular momentum (SAM). The first is usually associated with patterned light beams, such as beams with Laguerre-Gaussian amplitude distribution [48], or displaced beams [49]. Light with circular or elliptical polarization possesses SAM, where the vector of the angular momentum is perpendicular to the plane in which the field rotates. In general, the SAM can be quantified by the local spin density, which is defined as [50]

$$\mathbf{S} = \operatorname{Im}[\epsilon_0 \mathbf{E}^* \times \mathbf{E} + \mu_0 \mathbf{H}^* \times \mathbf{H}] / 4\omega , \quad (2.4)$$



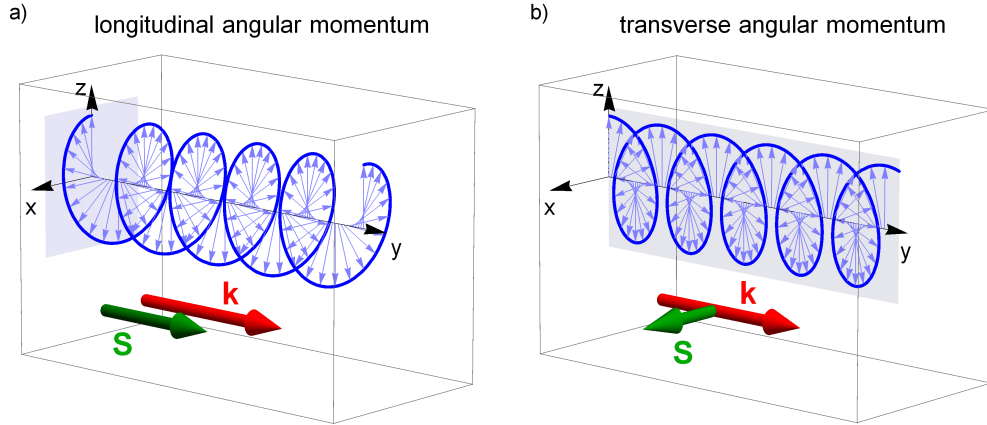


**Figure 2.1:** In order to illustrate the difference between transverse and longitudinal angular momentum of light we schematically show the electric field vectors (blue) for a given time along the wave’s propagation direction ( $y$ -direction) for the two cases. a) For the case of longitudinal spin angular momentum, the field rotates about an axis parallel to the direction of propagation. This situation occurs, e.g. for a circularly polarized plane wave. b) For the case of transverse spin angular momentum, the field rotates in a plane spanned by the propagation direction and a transverse vector. In both diagrams the gray plane indicates the plane in which the field rotates. The red arrow represents the wave vector  $\mathbf{k}$ , and thus the propagation direction, while the green arrow indicates the local spin of the electric field  $\mathbf{S}$ , which is either a) parallel or b) perpendicular to  $\mathbf{k}$ .

for light with frequency  $\omega$  and where  $\epsilon_0$  ( $\mu_0$ ) are the vacuum permittivity (permeability). In Eq. (2.4), we discriminate two contributions: The first part corresponds to the electric field induced spin density and the second to the magnetic field induced spin density. For a circularly polarized plane wave propagating in  $y$ -direction, the electric as well as the magnetic fields are purely transverse, and their field vectors rotate in a plane perpendicular to it. Thus, the spin density points along the propagation direction and one speaks of a longitudinal SAM, i.e.  $|S_t| = |S_y| > 0$  and  $|S_t| = |S_x + S_z| = 0$  (see Fig. 2.1a). From Eq. (2.4), we see that the transverse electric spin density vanishes as long as we have only transverse field components. However, for a wave that exhibits a longitudinal electric field component, which has a phase lack of, e.g.  $\pi/2$ , we obtain a non-vanishing transverse spin density vector, i.e.  $|S_t| > 0$  (see Fig. 2.1b). Thus, we can associate the elliptical polarization which stems from the additional longitudinal electric field component with a transverse SAM [21, 33, 50].

In the framework of this thesis, we are mainly interested in coupling light to emitters that have strong electric dipole transitions. Thus, the properties of the electric field are of major concern to us. In the following, we limit our discussion to the electric part of the spin density. Nonetheless, the generalization to its magnetic counterpart is straightforward.

### 2.1.3 Spin–momentum locking of light

The most important feature of the transverse SAM is its inherently linked to the propagation direction. If we reverse the propagation direction, the sense the field vector rotates changes, and thus the SAM flips. The inversion of propagation direction corresponds to changing the sign of the wave vector, i.e.  $\mathbf{k} \rightarrow -\mathbf{k}$ . From Eq. (2.3), we see that this also changes the sign of the longitudinal field component, and thus the rotation sense of the local polarization. For a wave propagating in positive  $y$ -direction ( $\mathbf{k} > 0$ ), that has equal amplitudes for its longitudinal and transverse field components, we obtain perfectly circularly polarized light,  $\mathcal{E}_{\sigma+} = |\mathcal{E}|(e_x + ie_y)/\sqrt{2}$ . In contrast, if we reverse the propagation direction ( $\mathbf{k} < 0$ ) we recover the orthogonal circular polarization,  $\mathcal{E}_{\sigma-} = |\mathcal{E}|(e_x - ie_y)/\sqrt{2}$ . This is a direct consequence of time reversal symmetry of Maxwell's equations. The reversal of time, i.e.  $t \mapsto -t$ , can be substituted by inverting the wave vector,  $\mathbf{k} \mapsto -\mathbf{k}$  and taking the complex conjugate of the electric field amplitude,  $\mathcal{E} \mapsto \mathcal{E}^*$ . For our case, this implies  $\mathcal{E}_{\sigma+} = (\mathcal{E}_{\sigma-})^*$ . In terms of the photon SAM, the waves propagating in  $\pm y$ -direction, i.e.  $k \lesseqgtr 0$ , will have opposite transverse spin  $S_t \lesseqgtr 0$ . Thus, this effect is often referred to as SML of light.

## 2.2 Total internal reflection and evanescent fields

For the particularly important case of evanescent fields at a planar interface, we can derive an analytical expression for the transverse and the longitudinal field components, which is done in the following.

The behavior of the transmitted and reflected waves at a planar interface largely depend on the polarization of the incident wave. In general, we can distinguish two different cases: transverse electric (TE) and transverse magnetic (TM) polarization. For the case of TE polarization, the electric field oscillates perpendicular to the plane of incidence, which is spanned by the incident wave vector and the normal to the surface of the interface (see Fig. 2.2). For TM polarization, the magnetic field oscillates perpendicular to the plane of incidence, and consequently the electric field oscillates in the plane of incidence. Thus, only TM waves allow electric field components which are parallel to the propagation direction. For that reason, we will focus our treatment to this particular input polarization.

### 2.2.1 Planar dielectric interface

Let us consider a plane wave of arbitrary polarization with frequency  $\omega$  that propagates in the  $xy$ -plane and encounters a boundary between two dielectric media with refractive indices  $n_1$  and  $n_2$  at  $x = 0$ , as depicted in Fig. 2.2. The electric field at a given time  $t$  in both media at position  $\mathbf{r} = (x, y, 0)$  is given by [51]

$$\mathbf{E}(\mathbf{r}, t) = \mathcal{E}(\mathbf{r}) \cdot e^{-i\omega t} = \begin{cases} (\mathcal{E}_{\text{in}} \cdot e^{i\mathbf{k}_{\text{in}} \cdot \mathbf{r}} + \mathcal{E}_{\text{ref}} \cdot e^{i\mathbf{k}_{\text{ref}} \cdot \mathbf{r}}) \cdot e^{-i\omega t} & \text{for } x \leq 0 \\ \mathcal{E}_{\text{trans}} \cdot e^{i(\mathbf{k}_{\text{trans}} \cdot \mathbf{r} - \omega t)} & \text{for } x > 0 \end{cases}, \quad (2.5)$$

where  $\mathcal{E}(\mathbf{r}) = (\mathcal{E}_x, \mathcal{E}_y, \mathcal{E}_z)$  is the time independent vector amplitude of the electric field. In the region  $x \leq 0$ , the wave is a superposition of an incident wave  $\mathcal{E}_{\text{in}} \cdot e^{i\mathbf{k}_{\text{in}} \cdot \mathbf{r}}$  and a reflected wave

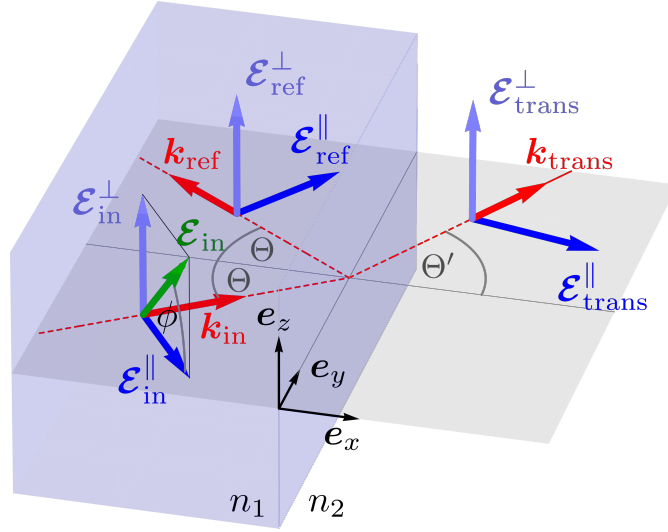


**Figure 2.2:** Electric field vectors  $\mathcal{E}$  for light incident on the interface between two dielectrics with refractive indices  $n_1$  and  $n_2$  at  $x = 0$ . The wave impinges on the interface under an angle  $\Theta$  and is refracted in the second dielectric under an angle  $\Theta'$ . We discriminate three different waves, the incident, the reflected and the transmitted, for which the corresponding electric field vectors are  $\mathcal{E}_i$ , where the index  $i \in \{\text{in, ref, trans}\}$ . Their propagation directions are indicated by the wave vectors  $\mathbf{k}_i$  (red arrows), which all lie in the plane of incidence (gray plane). We consider an incoming plane wave of arbitrary polarization which can be decomposed into components parallel to the plane of incidence  $\mathcal{E}_{\text{in}}^{\parallel} = \mathcal{E}_x \mathbf{e}_x + \mathcal{E}_y \mathbf{e}_y$  and perpendicular to the plane of incidence  $\mathcal{E}_{\text{in}}^{\perp} = \mathcal{E}_z \mathbf{e}_z$ . The amplitudes and phases of all polarization components can be calculated using Eqs. (2.7-2.9).

$\mathcal{E}_{\text{ref}} \cdot e^{i\mathbf{k}_{\text{ref}} \cdot \mathbf{r}}$ . In contrast, for  $x > 0$ , there only exists a single contribution, that is the transmitted wave  $\mathcal{E}_{\text{trans}} \cdot e^{i\mathbf{k}_{\text{trans}} \cdot \mathbf{r}}$ . The complex amplitude vectors of the electric field can be obtained directly by applying boundary conditions at the interface. For the electric field, we discriminate two polarization components:  $\mathcal{E}_i^{\parallel}$  which lies in the plane of incidence, and  $\mathcal{E}_i^{\perp}$  that is perpendicular to the plane of incidence, where the index  $i \in \{\text{in, trans, ref}\}$ . In this nomenclature,  $\mathcal{E}_i^{\parallel}$  and  $\mathcal{E}_i^{\perp}$  correspond to TM and TE polarization, respectively. An incoming field of arbitrary polarization with field amplitude  $\mathcal{E}_0$  can be decomposed into TE and TM polarization by

$$\mathcal{E}_{\text{in}}^{\parallel} = \mathcal{E}_0 \cos \phi \quad \text{and} \quad \mathcal{E}_{\text{in}}^{\perp} = \mathcal{E}_0 e^{i\zeta} \sin \phi, \quad (2.6)$$

where  $\phi$  determines their relative amplitude and  $\zeta$  their relative phase (see Fig. 2.2). Using Eq. (2.6), the complex electric field vector of the incoming wave can be expressed in Cartesian

coordinates as

$$\mathcal{E}_{\text{in}} = \begin{pmatrix} \mathcal{E}_{\text{in}}^{\parallel} \sin \Theta \\ -\mathcal{E}_{\text{in}}^{\parallel} \cos \Theta \\ \mathcal{E}_{\text{in}}^{\perp} \end{pmatrix}, \quad (2.7)$$

where  $\Theta$  is the angle of incidence. From Fresnel equations we obtain [51]

$$\mathcal{E}_{\text{ref}} = \begin{pmatrix} \mathcal{E}_{\text{in}}^{\parallel} \sin \Theta \frac{n_2 \cos \Theta - n_1 \cos \Theta'}{n_2 \cos \Theta + n_1 \cos \Theta'} \\ \mathcal{E}_{\text{in}}^{\parallel} \cos \Theta \frac{n_2 \cos \Theta - n_1 \cos \Theta'}{n_2 \cos \Theta + n_1 \cos \Theta'} \\ \mathcal{E}_{\text{in}}^{\perp} \frac{n_2 \cos \Theta' - n_1 \cos \Theta}{n_2 \cos \Theta' + n_1 \cos \Theta} \end{pmatrix}, \quad (2.8)$$

$$\mathcal{E}_{\text{trans}} = \begin{pmatrix} \mathcal{E}_{\text{in}}^{\parallel} \sin \Theta' \frac{2n_1 \cos \Theta}{n_2 \cos \Theta + n_1 \cos \Theta'} \\ -\mathcal{E}_{\text{in}}^{\parallel} \cos \Theta' \frac{2n_1 \cos \Theta}{n_2 \cos \Theta + n_1 \cos \Theta'} \\ \mathcal{E}_{\text{in}}^{\perp} \frac{2n_1 \cos \Theta'}{n_2 \cos \Theta + n_1 \cos \Theta} \end{pmatrix}. \quad (2.9)$$

Here, we assumed the magnetic permeability  $\mu_1 = \mu_2 \approx 1$ , which is valid for common dielectrics. The corresponding wave vectors are

$$\mathbf{k}_{\text{in}} = n_1 k_0 \begin{pmatrix} \cos \Theta \\ \sin \Theta \\ 0 \end{pmatrix}, \quad \mathbf{k}_{\text{ref}} = n_1 k_0 \begin{pmatrix} -\cos \Theta \\ \sin \Theta \\ 0 \end{pmatrix}, \quad \mathbf{k}_{\text{trans}} = n_2 k_0 \begin{pmatrix} \cos \Theta' \\ \sin \Theta' \\ 0 \end{pmatrix}. \quad (2.10)$$

In Eqs. (2.7-2.10), we have introduced the vacuum wave number  $k_0 = 2\pi/\lambda$  and the angle of refraction  $\Theta'$ . The latter can be obtained from Snell's law

$$n_2 \sin \Theta' = n_1 \sin \Theta. \quad (2.11)$$

This set of equations enables us to compute the field vector  $\mathbf{E}(\mathbf{r}, t)$  for any combination of dielectrics and incidence angles at any point in space and time. Note that the angle of incidence is defined such that positive (negative) angles, i.e.  $\Theta > 0$  ( $\Theta < 0$ ), correspond to waves incident from the  $y < 0$  ( $y > 0$ ) half space.

### 2.2.2 Total internal reflection

Equations (2.7-2.10) are formally valid for arbitrary angles of incidence  $\Theta$  and refractive indices of the two media. Thus, they also correctly describe the case of total internal reflection which occurs for  $\Theta > \Theta_c = \arcsin(n_2/n_1)$  and  $n_1 > n_2$ . In the following, we replace the subscript „trans“ with „ev“ whenever we encounter an evanescent instead of a transmitted field.

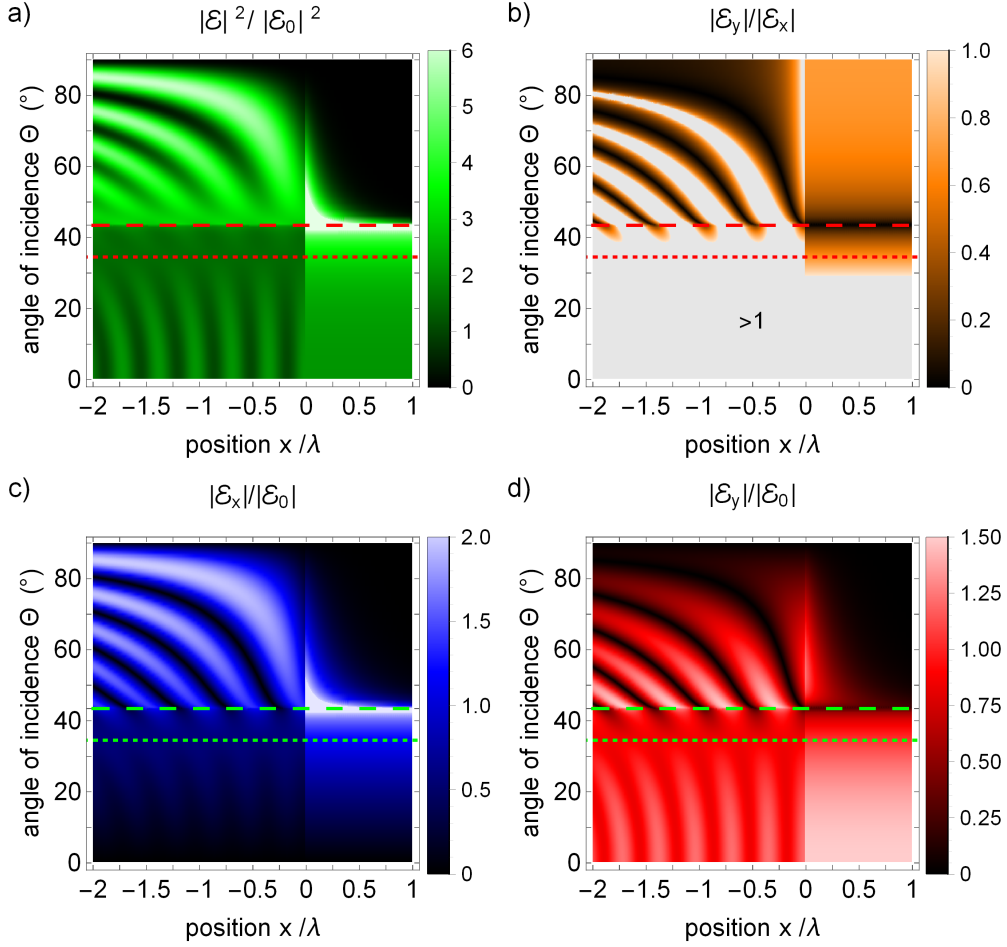


**Figure 2.3:** Electric field  $\mathcal{E}$  close to a planar dielectric interface between silica and vacuum ( $n_1 = 1.454$ ,  $n_2 = 1$  at  $x = 0$ ) for a plane wave with  $\phi = 0$ , i.e. TM polarization, as a function of the incident angles  $\Theta$  and the distance from the interface in  $x$ -direction. a)  $|\mathcal{E}|^2$  normalized to the input field  $|\mathcal{E}_0|^2$ . b) Ratio of the field components  $\mathcal{R} = |\mathcal{E}_y|/|\mathcal{E}_x|$ . Since we are mainly interested in the evanescent field ( $x > 0$  and  $\Theta > \Theta_c$ ), we discard values larger than one which can occur for  $x < 0$  and  $\Theta < \Theta_c$  in this plot (indicated in gray). c) & d) Absolute value of the electric field component perpendicular or parallel to the interface,  $\mathcal{E}_x$  or  $\mathcal{E}_y$ , respectively, normalized to the incident electric field amplitude  $\mathcal{E}_0$ . In all plots the dashed line corresponds to the critical angle  $\Theta_c = 43.5^\circ$  and the dotted line represents the Brewster's angle  $\Theta_B = 34.5^\circ$ .

Formally, if the angle of incident is larger than  $\Theta_c$ , then  $\sin \Theta'$  is real, and  $\cos \Theta'$  becomes imaginary. Using Snell's law we can rewrite the latter as

$$\cos \Theta' = i \sqrt{\left(\frac{n_1}{n_2}\right)^2 \sin^2 \Theta - 1} = i \xi. \quad (2.12)$$

Inserting this term into the wave vector of the field in the second medium  $\mathbf{k}_{\text{ev}} (= \mathbf{k}_{\text{trans}})$ , its  $x$ -component becomes imaginary. This gives rise to an exponentially decaying evanescent field in  $x$ -direction. The attenuation length can be directly calculated by inserting Eq. (2.12) into Eq. (2.5) and is given by

$$\delta = \frac{1}{n_2 k_0} \xi . \quad (2.13)$$

This decay length is proportional to the wavelength and decreases with increasing angle of incidence. The remaining real part of the wave vector, which defines the propagation direction in the evanescent field, is

$$k_{\text{ev}}^y = n_1 k_0 \sin \Theta . \quad (2.14)$$

In the evanescent field, the factor  $e^{i \mathbf{k}_{\text{trans}} \cdot \mathbf{r}}$  thus can be expressed as  $e^{-x/\delta} e^{i k_{\text{ev}}^y y}$ . The term  $\cos \Theta'$  also appears in the expression for field amplitudes of the reflected and evanescent (transmitted) wave,  $\mathcal{E}_{\text{ref}}$  and  $\mathcal{E}_{\text{ev}} (= \mathcal{E}_{\text{trans}})$ . This gives rise to a phase shifts of the respective waves. For an incoming beam of finite size, this phase shift causes an apparent longitudinal displacement of the reflected beam, known as Goose Hanchen shift [52]. In addition, a transverse displacement occurs for both reflected and transmitted beam, as first predicted by Fedorov [53].

As we are interested in longitudinal electric field components, which can only occur for TM incoming waves, the following discussion is limited to this case, i.e.  $\phi = 0$ . In Fig. 2.3 and Fig. 2.4, the two electric field components of a TM polarized incoming wave,  $\mathcal{E}_x$  and  $\mathcal{E}_y$ , their ratio  $\mathcal{R} = |\mathcal{E}_y/\mathcal{E}_x|$  and the absolute value squared of the total electric field  $|\mathcal{E}|^2 = |\mathcal{E}_x|^2 + |\mathcal{E}_y|^2$  are plotted as a function of the incident angles and the distance from the interface, for the case of an interface between silica and vacuum. The electric field in the dielectric ( $x < 0$ ) shows amplitude modulation due to interference of the incoming and reflected wave. This interference pattern undergoes a phase jump when crossing the Brewster's angle, i.e.  $\Theta_B = \arctan(n_1/n_2)$  and disappears for this angle, as the reflected wave vanishes. When increasing the angle of incidence, the wave vector  $k_x$  also increases. Thus, the period of the interference pattern increases as the incidence angle approaches  $\pi/2$ . For angles smaller than  $\Theta_c$  the field in the vacuum ( $x > 0$ ) is a propagating wave without amplitude modulation. For angles larger than  $\Theta_c$ , however, the transmitted field turns into an evanescent field that exponentially decays with  $x$ . Both the decay length and the amplitudes at the surface decrease with increasing  $\Theta$ . However, the latter stems from the fact that the mode volume is not defined for a plane wave and we normalize the amplitudes by  $\mathcal{E}_0$ .

When we compare the two field components of the evanescent field,  $\mathcal{E}_x^{\text{ev}}$  and  $\mathcal{E}_y^{\text{ev}}$ , we see that while the total field amplitude drops as we increase the angle of incidence, the two components, become almost of equal size. This becomes evident when looking at the ratio  $\mathcal{R}$  between the two field components which can be expressed in terms of the attenuation length  $\delta$  and the wave vector  $k_{\text{ev}}^y$  as

$$\mathcal{R}_{\text{ev}} = \left| \frac{\mathcal{E}_{\text{ev}}^y}{\mathcal{E}_{\text{ev}}^x} \right| = \left| k_{\text{ev}}^y \delta \right|^{-1} = \sqrt{1 - \left( \frac{n_2}{n_1 \sin \Theta} \right)^2} . \quad (2.15)$$

Interestingly,  $\mathcal{R}_{\text{ev}}$  does not depend on the lights wavelength and is only determined by the refractive indices of the two dielectrics involved and the angle of incidence. From Eq. 2.15, we see that for faster decaying fields the longitudinal field component becomes stronger. This is

in agreement with or previous result, where we stated that the longitudinal field component is proportional to the transverse field gradient (cf. Eq. (2.3) ). For the limiting case of grazing incidence, the ratio between the two field components approaches its maximum value

$$\mathcal{R}_{\text{ev}}|_{\Theta \rightarrow \pi/2} = \sqrt{1 - \left(\frac{n_2}{n_1}\right)^2}. \quad (2.16)$$

For the case of an interface between silica and vacuum  $\mathcal{R}_{\text{ev}} \leq 0.72$ .

### 2.2.3 Polarization properties and spin–momentum locking

In the following chapter, we want to study the interaction between light and matter. Therefore, we are interested in the overlap of the local field with the eigenpolarization of the emitters. For waves moving in positive and negative  $y$ -direction, we introduce the complex valued field overlap

$$\alpha_i = \frac{\mathcal{E}^+ \cdot \mathbf{e}_i^*}{|\mathcal{E}^+|} \quad \text{and} \quad \beta_i = \frac{\mathcal{E}^- \cdot \mathbf{e}_i^*}{|\mathcal{E}^-|}, \quad (2.17)$$

respectively, with  $i \in \{\sigma_+, \pi, \sigma_-\}$ . Here, we use the electric field vector  $\mathcal{E}^\pm$  for waves that effectively travel in  $\pm y$ -direction, i.e. incident from the  $y \leq 0$  half space or  $\Theta \geq 0$ . In addition, we defined  $\mathbf{e}_{\sigma_+} = (\mathbf{e}_x + i\mathbf{e}_y)/\sqrt{2}$ ,  $\mathbf{e}_{\sigma_-} = (\mathbf{e}_x - i\mathbf{e}_y)/\sqrt{2}$  and  $\mathbf{e}_\pi = \mathbf{e}_z$ , using the Cartesian unit vectors  $\mathbf{e}_x$ ,  $\mathbf{e}_y$  and  $\mathbf{e}_z$ . For the example of a TM plane wave impinging on a planar interface, the quantities  $|\alpha_{\sigma^\pm}|^2$  and  $|\beta_{\sigma^\pm}|^2$  are shown in Fig. 2.5 as a function of the incidence angle and the position along  $x$ .

For the evanescent field, the fact that  $\cos \Theta'$  is purely imaginary also imprints a fixed phase difference of  $\pi/2$  between the two field components (see Eq. 2.9). Thus, the evanescent field is elliptically polarized. The overlap with circular polarization is then given by

$$|\alpha_{\sigma^\pm}^{\text{ev}}| = |\beta_{\sigma^\mp}^{\text{ev}}| = \frac{1 \pm \mathcal{R}_{\text{ev}}}{\sqrt{2(1 + \mathcal{R}_{\text{ev}}^2)}}. \quad (2.18)$$

For the case of an interface between silica and vacuum and grazing incidence, we obtain  $|\alpha_{\sigma_+}^{\text{ev}}|^2 = |\beta_{\sigma_-}^{\text{ev}}|^2 = 0.97$  and  $|\alpha_{\sigma_-}^{\text{ev}}|^2 = |\beta_{\sigma_+}^{\text{ev}}|^2 = 0.03$ , i.e. the evanescent field is almost perfectly circularly polarized. Note that, the electric field inside the first dielectric ( $x < 0$ ) can locally exhibit perfect circular polarization.

As in the previous section, we can associated the elliptical polarization with a SAM of light. For TM polarization, the only nonzero component of the SAM is  $S_z$ , which in the case of total internal reflection is transverse to the effective propagation direction of the wave.  $S_z$  is shown in Fig. 2.5a as a function of the position  $x$  and the incidence angle  $\Theta$ . The key feature of the transverse SAM is that it flips sign when the propagation direction is reversed, which gives rise to SML. In Fig. 2.5a this becomes evident when comparing the spin density for propagation in  $+y$ -direction, i.e.  $\Theta > 0$ , with propagation in  $-y$ -direction, i.e.  $\Theta < 0$ . SML implies that

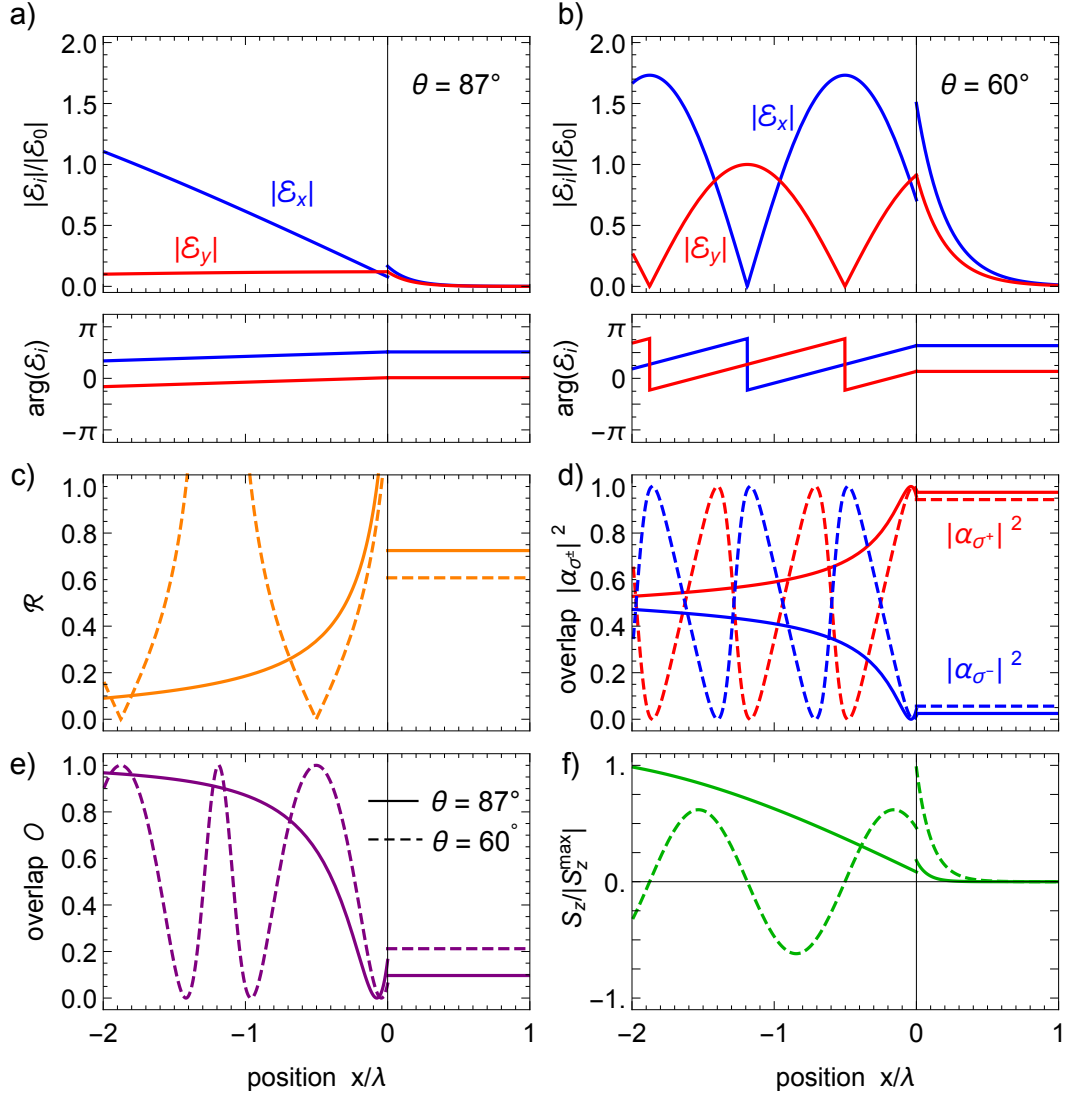


**Figure 2.4:** Polarization properties of a TM polarized wave incident from the negative  $y$  half space onto an interface between silica ( $n_1 = 1.454$ ) and vacuum ( $n_2 = 1$ ). Figures a) and b) show the amplitude and phase of the transverse  $\mathcal{E}_x$  (blue) and longitudinal  $\mathcal{E}_y$  (red) polarization component as a function of the distance from the interface, for two different angles of incidence. The first angle is close to gracing incidence,  $\Theta = 87^\circ$ , and the second is closer to the critical angle,  $\Theta = 60^\circ$ . c) The ratio between the two field components  $\mathcal{R} = |\mathcal{E}_y/\mathcal{E}_x|$ . d) The polarization overlap of the local field with  $\sigma^+$  (red) and  $\sigma^-$  (blue) polarized light. e) The overlap of two counter-propagating fields  $\mathcal{O}$ . f) The  $z$ -component of the spin density, which is normalized such that the maximal value of each curve shown equals to one. In c)-f), the solid line corresponds to  $\Theta = 87^\circ$  and dashed line to  $\Theta = 60^\circ$ .



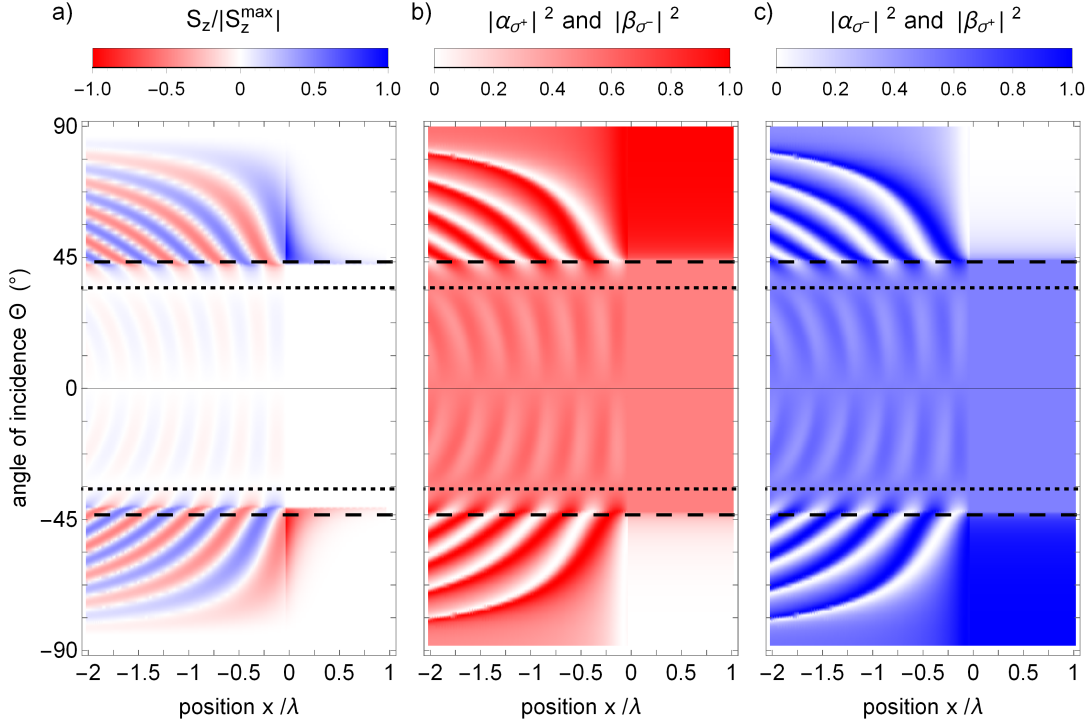


**Figure 2.5:** Illustration of the spin–momentum locking: a) Electric spin density  $S_z$  normalized such that its maximal values gives  $\pm 1$ . b) & c) Overlap of the local field with  $\sigma^+$ - and  $\sigma^-$ -polarized light,  $|\alpha_{\sigma^\pm}|^2$  and  $|\beta_{\sigma^\pm}|^2$ , as a function of the distance to the interface and the incidence angle for the same setting as in Fig. 2.3. Here, positive (negative) angles of incidence, correspond to waves incident from the  $y < 0$  ( $y > 0$ ) half space. The dashed and dotted line indicate the critical angle  $\Theta_c$  and the Brewster’s angle  $\Theta_B$ , respectively. The fact that the transverse spin also change its sign under inversion of propagation direction is a direct manifestation of SML. Note that in the second media ( $x > 0$ ) the overlaps are independent of  $x$ .

the field overlap with (+)-circular polarization is close to 1 for one propagation direction, i.e.  $|\alpha_{\sigma^+}|^2 \approx 1$  for one propagation direction, and close to 0 for the opposite propagation direction, i.e.  $|\beta_{\sigma^+}|^2 \approx 0$ , and vice versa for the overlap with (–)-circular polarization (see Fig. 2.5b and Fig. 2.4d). Furthermore, for our quantization axis along  $z$ ,  $\alpha_i$  and  $\beta_i$  fulfill the following relations  $|\alpha_{\sigma^+}|^2 = |\beta_{\sigma^-}|^2$ ,  $|\alpha_{\sigma^-}|^2 = |\beta_{\sigma^+}|^2$  and  $|\alpha_\pi|^2 = |\beta_\pi|^2$ . In addition, the three polarization states form a complete basis set and thus  $|\alpha_{\sigma^+}|^2 + |\alpha_{\sigma^-}|^2 + |\alpha_\pi|^2 = 1$ . For the case of TM polarization, this simplifies to  $|\alpha_{\sigma^+}|^2 = 1 - |\alpha_{\sigma^-}|^2$ .

Since the polarization depends on the propagation direction, the polarizations of two counter-propagating waves are no longer independent. We can quantify their polarization overlap by

introducing

$$\mathcal{O} = \frac{|\boldsymbol{\mathcal{E}}^+ \cdot (\boldsymbol{\mathcal{E}}^-)^*|^2}{|\boldsymbol{\mathcal{E}}^+|^2 |\boldsymbol{\mathcal{E}}^-|^2} = |\sum_i \alpha_i \beta_i^*|^2 . \quad (2.19)$$

If two counter-propagating waves have orthogonal local polarization, this value becomes zero, indicating maximum correlation between propagation direction and polarization. Thus,  $\mathcal{O} < 1$  is a clear indication for SML. However, if both waves have the same local polarization their overlap is 1, and they exhibit no SML. In Fig. 2.4, the overlap  $\mathcal{O}$  together with other quantities describing the polarization at the dielectric interface are plotted as a function of the distance to the interface for two exemplary incidence angles. In the evanescent field the overlap is given by

$$\mathcal{O}_{\text{ev}} = \left( \frac{1 - \mathcal{R}_{\text{ev}}^2}{1 + \mathcal{R}_{\text{ev}}^2} \right)^2 . \quad (2.20)$$

For an interface between silica and vacuum and gracing incidence, the overlap in the evanescent field is 0.1 , which indicates a high degree of SML.

In summary, we showed that strongly confined fields, such as evanescent fields, exhibit longitudinal field components which oscillate in quadrature to the transverse components. This gives rise to an elliptical local polarization and a transverse SAM of light. The sign of the transverse SAM, and thus the light's polarization, depends on the propagation direction of the wave, which is also known as SML. This phenomena lies at the heart of the experiments presented in the following chapters.

## The bottle microresonator

High quality optical resonators are being used across a wide range of fields, including quantum information processing, nonlinear optics, cavity optomechanics and telecommunications. [18] In particular, whispering-gallery-mode (WGM) resonators are attractive for many technical applications [19]. These resonators confine light along the surface of dielectric structures by continuous total internal reflection. This enables monolithic resonators of very high mechanical stability, with high quality factors and low mode volume. In addition, light can be coupled in and out of the resonator extremely efficiently via the near field, which is very beneficial for practical applications. WGM resonators are nowadays used for tunable filters [54], modulators [55] or microlasers [56]. In addition, one can harvest the resonator enhancement of nonlinear effects [57] to enable higher harmonic generation [58] or optical frequency combs [59], for example. Furthermore, narrowband photon pair sources [60] and all-optical switching [61] [62] has been realized. By measuring frequency shifts or broadening of their resonances, WGM resonators can be employed for high performance sensing of, e.g. forces, electric- and magnetic-fields or biomolecules [63]. WGMs resonators are also very successfully employed in fundamental studies including quantum chaos [64,65], parity-time symmetry breaking in optical systems [66,67], the quantum limit of optomechanics [68] and cavity quantum electrodynamics (CQED). In the latter, WGMs are coupled to single emitters, which recently has been employed for the realization of photon routers [69–71] and a single photon subtractor [72].

In this chapter, we will first discuss the most important properties of optical resonators. This is followed by a short introduction to WGMs in dielectric structures. The remainder of this chapter covers the specific properties of the bottle microresonator (BMR), a special type of WGM resonators, which is the key element of the experiments described in this thesis. We introduce an analytic model that enables us to compute the mode structure of BMRs. In particular, we focus on the polarization properties of WGMs which are of utmost importance when coupling light that circulates in the resonator to matter.

### 3.1 Resonator properties

A key attribute of optical resonators is to keep the light for a long time in its mode before it is dissipated. This property can be quantified using the finesse

$$\mathcal{F} = \frac{2\pi}{\mathcal{L}_{\text{tot}}}, \quad (3.1)$$

which gives a measure of how many round trips the light travels before it is lost from the resonator, where  $\mathcal{L}_{\text{tot}}$  is the incoherent round trip loss. For the classical textbook example of an optical resonator, the Fabry-Pérot (FP) resonator, the finesse can be obtained straightforwardly. In its basic implementation, a FP resonator consist of two mirrors with power reflectivity  $R$  close to one. On the one hand, light can exit the resonator by being transmitted through one of the mirrors, which then can be used to study the system's properties. On the other hand, there is also absorption and scattering in the mirror material which introduce incoherent losses. Assuming that the losses arise solely from the mirrors themselves, the round trip losses for a symmetric FP resonator are  $\mathcal{L}_{\text{tot}}^{\text{FP}} = 2(1 - R)$ , which is independent of the round trip length  $L$ . Thus, the finesse can be expressed as  $\mathcal{F}_{\text{FP}} = \pi/(1 - R)$ .

A different way to quantify the quality of a resonator is to use the so called quality factor<sup>1</sup>

$$Q = \omega\tau = \frac{\omega}{2\kappa} = \frac{\omega L \mathcal{F}}{2\pi c}, \quad (3.2)$$

which compares the life time  $\tau$  (or the energy decay rate  $2\kappa$ ) of the light stored in the resonator with its frequency  $\omega$ . The quality factor  $Q$  is a very commonly used figure of merit for describing oscillatory systems, not only in the optical domain. When expressed in terms of  $\mathcal{F}$ ,  $Q$  explicitly depends on the round trip length  $L$  of the resonator. For FP resonators, this means that  $Q$  is in principle unbound since the distance between the mirrors can be arbitrarily enlarged without introducing further losses. State of the art FP resonators achieve  $\mathcal{F} > 10^6$ , corresponding to  $Q > 10^7$  for near infrared light and a spacing between the mirrors  $L = 40 \mu\text{m}$  [75].

Compared to FP resonators, WGM resonators are conceptually different. These resonators are formed by monolithic dielectric structures that confine the light by means of total internal reflection. The losses are mainly caused by material absorption or surface roughness. Therefore, the losses accumulate over distance which causes  $\mathcal{L}_{\text{tot}}$  to depend on the round trip length  $L$ , and thus the geometry of the resonator. Using low absorption dielectrics, such as silica or calcium fluoride, and special fabrication processes allow one to realize ultra high  $Q$  in the range of  $10^8$ - $10^{11}$  [20, 73]. For BMRs the best achieved quality factor was  $3.6 \times 10^8$  [76].

Beside the quality factor  $Q$ , the spacial confinement of the light is the second key parameter a microresonator. In principle, the stronger the confinement the larger the enhancement of the lights intensity in the mode. The size of the mode is usually characterized by the mode volume  $V$ , which we define as the spacial integral of the normalized intensity distribution [77]

$$V = \frac{\int n^2(\mathbf{r})|\mathcal{E}(\mathbf{r})|^2 d\mathbf{r}}{|\mathcal{E}(\mathbf{r})|_{\text{max}}^2}, \quad (3.3)$$

<sup>1</sup>The discrepancy between the expression given here and those stated in e.g. Ref. [10, 73, 74] stems from different definitions of  $L$ , which in our case is the round trip length and in these references is defined as the mirror spacing.

where  $n(\mathbf{r})$  is the refractive index which depends on the position  $\mathbf{r}$ ,  $\mathcal{E}(\mathbf{r})$  the local electric field vector of the mode and  $|\mathcal{E}(\mathbf{r})|_{\max}^2$  its peak intensity. For various types of photonic crystal cavities mode volume below  $\lambda^3$  have been achieved. However, the attempt to realize ultra small mode volume in most cases comes at the expense of reduced quality factor  $Q$ . For example, photonic-crystal-slab defect nanocavities reached  $Q = 45000$  and  $V = 0.3 \cdot \lambda^3$  [78] and photonic crystal nanobeams achieved  $Q = 500$ ,  $V = 0.89 \cdot \lambda^3$  [79].

### 3.2 General CQED parameters

For the experimental realization of light–matter interaction it is favorable to increase the spatial and temporal confinement of light. As will become evident in the following, this requires the ratio  $Q/V$  to be maximized [18].

An atom whose transition falls within the linewidth of the resonator mode will experience an enhanced spontaneous decay rate into the mode. The enhancement is given by the Purcell factor or cooperativity parameter [80]

$$C = \frac{3}{4\pi^2} \left( \frac{\lambda}{n} \right)^3 \frac{Q}{V}, \quad (3.4)$$

which is proportional to  $Q/V$ . The modified atomic decay rate is then given by  $\gamma' = \gamma(1 + C)$ , where the free space decay rate is  $\gamma = \omega^3 \tilde{\mu}^2 / 6\pi\epsilon_0 \hbar c^3$  [81]. Here, we introduced the light's wavelength  $\lambda = 2\pi c / \omega$ , where  $\omega$  is the angular frequency and  $c$  is the speed of light. The transition dipole matrix element is defined as  $\tilde{\mu}^2 = |\langle J || e\hat{\mathbf{r}} || J' \rangle|^2 (2J + 1) / (2J' + 1)$  (cf. App. A.1). Since the enhancement originates from preferentially coupling to the mode of the resonator at rate  $\gamma C$ , the emission is directed into this mode which has great utility for channeling the emitted light. Furthermore, the probability for a photon to be spontaneously emitted into the cavity mode is  $C / (C + 1)$  [74].

In the framework of the Jaynes–Cummings model, coherent energy exchange between an atom and the resonator mode takes place at a rate given by the coupling strength  $g$ . It is determined by the electric field of a single photon at the position of the atom and the electric dipole matrix element  $\tilde{\mu}$  of the transition under investigation

$$g = \sqrt{\frac{\omega}{2\hbar\epsilon_0 V}} \tilde{\mu} \propto 1/\sqrt{V}. \quad (3.5)$$

From Eq. 3.5 it follows that smaller cavity volumes  $V$ , i.e. stronger confined modes, result in larger coupling strengths. However, in order to observe cyclic excitation, which is called Rabi oscillation, the coupling strength has to be larger than all loss channels. Stated more quantitatively,  $g \gg (\gamma, \kappa)$ , where  $\gamma$  and  $\kappa$  are the field decay rates of the atom and the resonator respectively. While  $\kappa$  is directly related with the quality factor  $Q$  (see Eq. 3.2),  $\gamma$  is defined by atomic properties.

It is instructive to explore strong coupling in terms of two dimensionless parameters [82]: The number of photons required to saturate a single atom

$$n_0 = \frac{\gamma^2}{g^2} \propto V, \quad (3.6)$$

and the critical atom number, i.e. the number of atoms required to significantly alter the intra-resonator field

$$N_0 = \frac{1}{C} = \frac{\gamma\kappa}{g^2} \propto \frac{V}{Q}. \quad (3.7)$$

In order to enter the strong coupling regime, both parameters have to be smaller than one, i.e.  $(n_0, N_0) < 1$ .

In a large class of applications the most important figure of merit can be expressed in terms of  $C$ . Thus, it is preferable to fabricate resonators with large  $Q/V$ . The highest values of  $Q/V$  to date have been reached with WGM microresonators and exceed  $10^6(\lambda/n)^3$  [83]. It should be noted, that for WGMs the  $Q/V$  value cannot be increased indefinitely by reducing  $V$ , since the reduction of mode volume ultimately comes at the expense of a reduced quality factor due to the emergence of tunneling loss [84, 85]. For the BMR used in our experiment we can estimate a mode volume of  $V \sim 900 \mu\text{m}^3$  which is approximately  $5800(\lambda/n)^3$  [86]. Together with a  $Q \sim 4 \times 10^7$  [87] we obtain a ratio  $Q/V \sim 7 \times 10^4(\lambda/n)^3$ , which is one order of magnitude lower than the best  $Q/V$  reported for BMRs [76].

### 3.3 Optical whispering-gallery-modes

In our experiment, we employ a so-called BMR resonator [76], a special type of WGM resonator. Other realizations of WGM microresonators include microspheres [88] or microtoroids [20]. In order to understand the working principle of a WGM resonator, it is instructive to use a simplified picture in which the trajectory of the light inside the resonator is represented by a ray as shown in Fig. 3.1c. Since the medium of the resonator is optically thicker than its surrounding, the light will be totally internally reflected when the angle of incidence  $\Theta$  is larger than the critical angle  $\Theta_c$  (c.f. Sec. 2.2.2). For a resonator with circular cross section, the initial angle fixes the angle of all subsequent reflections, and thus the light is guided around the resonator's circumference. The distance the light travels in the structure between two consecutive reflection is  $d = 2 R_0 \sin 2\Theta$ , where  $R_0$  is the radius of the resonator. For the limit of gracing incidence, i.e. when the incidence angle approaches  $\pi/2$ , the light is continuously totally internally reflected and forms so-called whispering-gallery waves, which were first described by Rayleigh for the case of acoustic waves in the gallery of St. Paul's Cathedral [89].

In order to form a whispering-gallery mode resonator, the resonance condition has to be fulfilled: The resonator field has to accumulate a phase delay of an integer multiple of  $2\pi$  after one round trip in order to interfere constructively. In other words, the optical path length in the structure has to be a multiple of the wavelength of the light. This condition fixes the resonance frequencies of the resonator. In contrast to FP resonators, where the light is reflected at normal incidence from a mirror and forms a standing wave mode, the eigenmodes of WGM resonators are running waves. Another essential feature of these resonators is the emergence of evanescent fields, which enable the coupling of light to and out of the resonator via frustrated total reflection and also allow one to couple single emitters to the resonator modes.

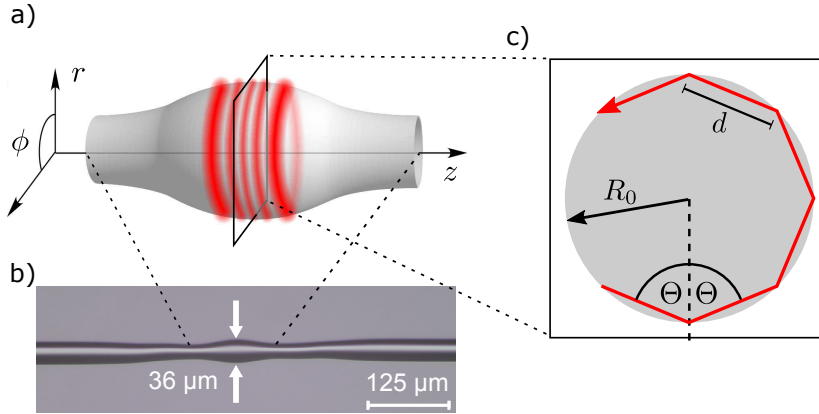


**Figure 3.1:** The bottle microresonator: a) Schematic of a bottle microresonator, including a mode structure with 5 axial rings, which corresponds to a mode with axial quantum number  $q = 4$ . b) Micrograph showing the micro tapered region of the resonator fiber. c) Total internal reflection inside the resonator illustrated in the ray path picture.

### 3.4 Modes of bottle microresonators

The previous chapter dealt with the simple case of total internal reflection at a planar interface. In our experiment, we employ a so-called BMR. The BMR is fabricated from an optical silica fiber, which is structured into the characteristic bottle shape (see Fig. 3.1) by a heat and pull process [90]. Total internal reflection provides the radial confinement, while the small axial curvature imposes a parabolic potential that prevents the light from escaping along the fiber direction. The resulting axial standing wave structure exhibits a significantly enhanced intensity at the so-called caustics, corresponding to the light's turning points. In the following, we introduce an analytic model which allows us to calculate the electric field distribution of BMRs.

#### 3.4.1 Analytic approximation of bottle microresonator modes

In order to obtain an idea of the mode structure and the polarization properties of BMR modes, we have to derive an accurate solution of the electromagnetic field for the resonator eigenmodes. Due to their spherical symmetry, there exists a direct analytic solution for microspheres [91]. For the prolate spheroidal bottle resonator, however, no exact derivation exists. Nevertheless, when making a few reasonable approximations we can obtain an accurate theoretical description of the WGM modes of a bottle microresonator. We follow the derivation which was introduced in Ref. [77] and is described in depth in Ref. [90, 92].

Due to the cylindrical symmetry of the bottle resonator, it is useful to change to cylindrical coordinates (radial  $r$ , azimuthal  $\phi$ , axial  $z$ ) as indicated in Fig. 3.1a. The electric field  $\mathcal{E}$  and magnetic field  $\mathcal{H}$  of bottle microresonator modes have to respect the Helmholtz equation

$$(\nabla^2 + |k|^2)\Psi = 0, \quad (3.8)$$

with  $\Psi = (\mathcal{E}, \mathcal{H})$  and  $|\mathbf{k}| = n \cdot k_0 = n \cdot \omega/c = n \cdot 2\pi/\lambda_0$  being the wave number of the mode with the vacuum wave number  $k_0$ , the angular frequency  $\omega$  and the vacuum wave length  $\lambda_0$ . Here,  $c$  is the speed of light and  $n$  the refractive index of the medium in which the light is propagating. Equation (3.8) directly follows from Maxwell's equations in the absence of charges and currents. We approximate the central shape of the resonator with a parabolic profile [90], which results in a quadratic dependence of the local radius  $R$  on  $z$ :

$$R(z) \approx R_0 \left( 1 - \frac{(\Delta k z)^2}{2} \right). \quad (3.9)$$

The resonator profile is characterized by the maximal radius  $R_0$  at the central part of the resonator and  $\Delta k$  which describes the curvature along the resonator axis. In the following, we assume that  $\Delta k$  is very small. As a consequence, the radius of the resonator  $R$  varies only slightly along  $z$  and we can neglect the radial component of the wave vector, i.e.  $k \approx \sqrt{k_\phi^2 + k_z^2}$ . In addition, we can obtain the axial dependence of the azimuthal wave vector  $k_\phi = k \cdot R_c/R(z)$ , where  $R_c$  is the radius at the caustic position. We can rewrite the wavefunction  $\Psi$  in cylindrical coordinates using the ansatz

$$\Psi = \mathcal{R}(r, R(z)) \cdot Z(z) \cdot \exp(im\phi). \quad (3.10)$$

The radial part  $\mathcal{R}$  still exhibits a weak dependence on  $z$  due to the small variation of the resonator radius along its axis. In Eq. (3.10), we already inserted the solution for the azimuthal part  $\Phi(\phi) = \exp(im\phi)$ , where  $m \in \mathbb{Z}$  is the angular momentum quantum number, which counts the number of wavelengths around the resonator circumference. It should be noted, that for waves propagating in opposite direction, the sign of the argument changes. Inserting this ansatz into Eq. (3.8), and omitting terms like  $\partial_z^2 \Phi$ , we obtain two separate differential equations [77]

$$\left( \partial_r^2 + \frac{1}{r} \partial_r + \left( \frac{mkR_c}{R(z)} \right)^2 - \frac{m^2}{r^2} \right) \mathcal{R} = 0, \quad (3.11)$$

$$\left( \partial_z^2 + k^2 - m^2 \frac{1 + \Delta k^2 z^2}{R_0^2} \right) Z = 0, \quad (3.12)$$

which can be solved independently for  $\mathcal{R}$  and  $Z$ .<sup>2</sup>

Since we assumed a parabolic radius profile, it should not be surprising that Eq. (3.12) is equivalent to the differential equation of a harmonic oscillator, for which the well known solutions are given by [77]

$$Z_{m,q}(z) = C_{m,q} H_q \left( \sqrt{\frac{\Delta E_m}{2}} z \right) \exp \left( -\frac{\Delta E_m}{4} z^2 \right). \quad (3.13)$$

Here,  $\Delta E_m = 2m\Delta k/R_0$  and  $H_q$  is the Hermite polynomial of order  $q$  with normalization constant  $C_{m,q} = (\Delta E_m / (\pi^{2^{2q+1}} (q!)^2))^{1/4}$ . The axial quantum number  $q$  gives the number of

---

<sup>2</sup>To obtain Eq. 3.12, and in the following an analytic expression for the radial wavefunction, we approximated the parabolic profile with  $R(z) = R_0/\sqrt{1 + (\Delta k z)^2}$ , which is well justified for our parameters,  $(\Delta k)^2 \ll 1$ .



intensity nodes in the axial intensity distribution. The implied resonance condition only allows quantized wave numbers of the form

$$k_{m,q} = \sqrt{\frac{m^2}{R_0^2} + (2q+1)\frac{m\Delta k}{R_0}}. \quad (3.14)$$

The radial wave equation Eq. (3.11) forms a Bessel differential equation. Therefore, the solutions for the axial field components are linear combinations of the Bessel functions  $J_m$  and Hankel functions  $Y_m$ . From their asymptotic behavior and the restriction to modes that are well localized at the resonator surface one can conclude that the solutions of the radial wave equation will have the form [90,92]:

$$\mathcal{R}_l(r, z) = \begin{cases} A_l \cdot J_m \left( \frac{2\pi n R_c}{\lambda_0 R(z)} \cdot r \right), & \text{for } r \leq R(z), \\ B_l \cdot Y_m \left( \frac{2\pi R_c}{\lambda_0 R(z)} \cdot r \right), & \text{for } r > R(z), \end{cases} \quad (3.15)$$

where the index  $l$  represents the respective vector component. To determine the constants  $A_l$  and  $B_l$ , we have to consider the boundary conditions of electromagnetic fields. Since the obtained solutions have to fulfill the resonance condition,  $\lambda_0$  and  $R_c$  cannot be chosen independently. This is incorporated by numerically solving the characteristic equation which is formed by the boundary condition of two field components [90]. From this, we can determine either  $R_c$  for a given  $\lambda_0$  or vice versa. The roots of the characteristic equation are labeled by the radial quantum number  $p$ , which gives the number of intensity nodes in radial direction. In addition, this result has to match Eq. 3.14 to give a coherent solution for both the axial and the radial wavefunction, which then gives WGM of the BMR.

Similar to the case of reflection at a planar interface, we obtain two classes of solutions: Modes having a electric field along  $z$ , i.e. parallel to the resonator surface, that are denominated as transverse electric (TE), and modes with a magnetic field parallel to the surface, named transverse magnetic (TM). Consequently, for TM modes (TE modes) only the field components  $\mathcal{H}_z$ ,  $\mathcal{E}_r$  and  $\mathcal{E}_\phi$  ( $\mathcal{E}_z$ ,  $\mathcal{H}_r$  and  $\mathcal{H}_\phi$ ) are nonzero.

In the following, we will discuss the resulting spectral behavior, the mode structure and the polarization properties of modes calculated using this approximate model, for the geometry used in the experiment.

### 3.4.2 Spectral properties

The structural parameters, such as the curvature  $\Delta k$  and the central radius  $R_0$ , define the spectral attributes of the bottle resonator. Supported modes are characterized by their radial, azimuthal and axial quantum numbers  $p$ ,  $m$  and  $q$ , respectively. The frequency difference between two adjacent modes is called free spectral range (FSR) range and can be approximated for axial and azimuthal modes by [77]

$$\Delta\nu_q \approx \frac{c\Delta k}{2\pi n} \quad \Delta\nu_m \approx \frac{c}{2\pi n R_0}. \quad (3.16)$$

For the bottle resonator geometry in our experiment,  $R_0 = 18 \mu\text{m}$ ,  $\Delta k = 0.012 \mu\text{m}^{-1}$  and  $n = 1.454$  (fused silica), this gives  $\Delta_q \approx 0.4 \text{ THz}$  and  $\Delta_m \approx 1.9 \text{ THz}$ .

### 3.4.3 Intensity distribution of BMR modes

From the analytic solution of the Helmholtz equation, we can calculate the field distribution for our bottle microresonator. In Fig. 3.2a the normalized intensity distribution at the surface is plotted for the three lowest order axial modes,  $q = \{0, 1, 2\}$  and the mode with  $q = 15$ . The fundamental axial mode  $q=0$  has a single intensity maximum, which is located at the center of the resonator  $z = 0$ . For higher order modes the intensity oscillates along  $z$  and the number of intensity nodes is given by  $q$ . The largest intensity of these modes is reached for the outermost maxima on each side, called the caustics. From the caustic on, the resonator field decays rapidly when moving further away from the resonator center in axial direction. While the fundamental mode extends over less than  $5 \mu\text{m}$  in axial direction, the extension increases for increasing  $q$ . For example, the mode with  $q = 15$  already extends over  $30 \mu\text{m}$ . In Fig. 3.2b the normalized intensity distribution for the first four resonances  $p = \{0, 1, 2, 3\}$  are shown as a function of the distance from the surface in radial direction for both eigenpolarizations, TM and TE. The radial quantum number  $p$  gives the number of intensity minima in radial direction. Outside the dielectric structure ( $r > 0$ ), the electric field decays exponentially, forming the evanescent field. For TM modes, the step at the surface is due to the discontinuity of the parallel electric field component at the boundary. Even though the intensity distribution inside the resonator changes drastically when varying  $p$ , the amplitude of the evanescent field is almost unaffected.

### 3.4.4 Polarization properties of BMR modes

We have seen in the previous chapter that for the process of total internal reflection of a plane wave at a planar interface, special polarization effects such as transverse spin angular momentum and spin–momentum locking (SML) of light can occur. Since BMRs also rely on total internal reflection, we anticipate similar effects.

Due to its cylindrical symmetry, BMRs support two degenerate counter-propagating modes, which we label CCW for the counter-clockwise and CW for the clockwise running wave mode. In cylindrical coordinates, they propagate in  $-\phi$ - or  $+\phi$ -direction, respectively (see Fig. 3.3). For our quantization axis along the resonator axis, i.e.  $e_z$ , the polarization states  $e_{\sigma^+} = (e_r + ie_\phi)/\sqrt{2}$ ,  $e_{\sigma^-} = (e_r - ie_\phi)/\sqrt{2}$  and  $e_\pi = e_z$  describe a full orthogonal basis.

For TE modes, within our approximation, only a single field component,  $\mathcal{E}_z$ , is present. However, for TM modes a transverse,  $\mathcal{E}_r$ , and the longitudinal,  $\mathcal{E}_\phi$ , electric field component occur. These are plotted as a function of the radial distance from the surface for  $p = \{0, 1\}$  in Fig. 3.4a-b. As expected, we obtain very similar polarization properties as for the plane wave in Sec. 2.2. Inside the resonator, we obtain an interference pattern giving  $p - 1$  peaks in radial directional. Along the interference pattern, the mode shows a variety of polarization states, ranging from perfectly circular to linear local polarization. In the evanescent field, the two components have nearly the same behavior, and their ratio  $\mathcal{R} = |\mathcal{E}_\phi/\mathcal{E}_r|$  only slowly decreases when increasing the distance to the surface, as depicted in Fig. 3.4c. The decrease can be explained by the fact

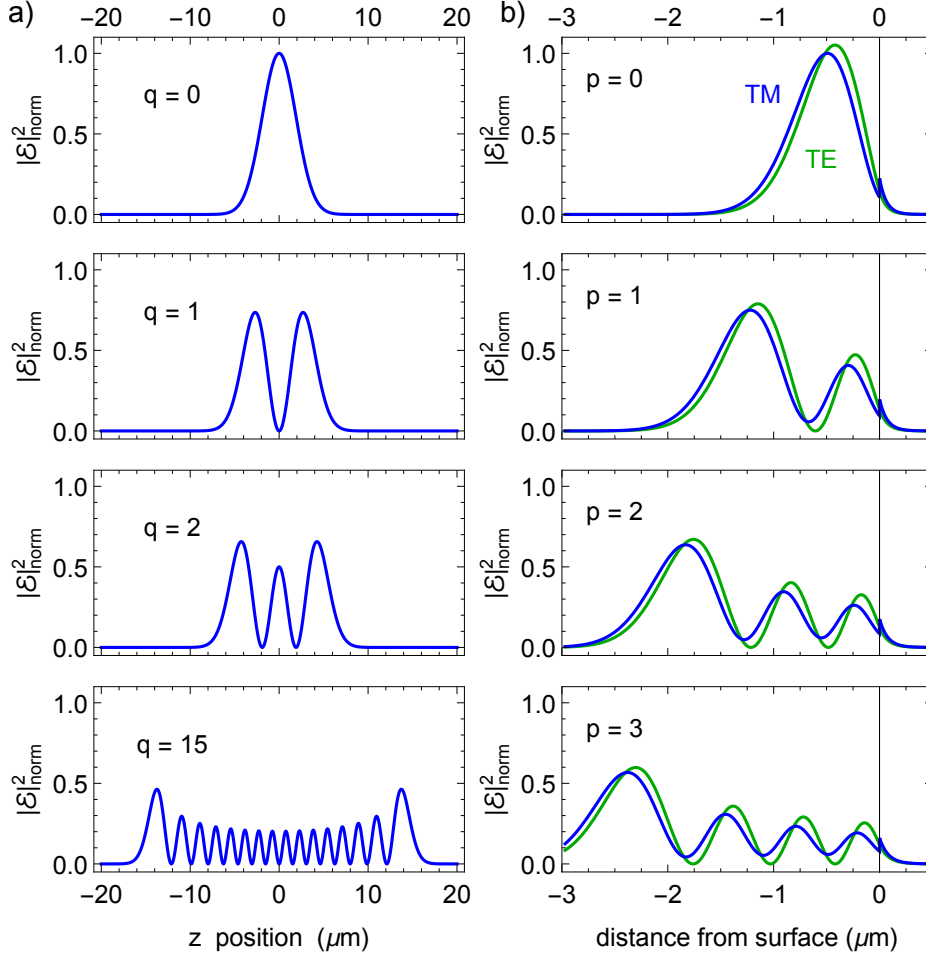


**Figure 3.2:** Distribution of  $|\mathcal{E}|^2$  for BMR modes along a) axial direction  $z$  and b) radial direction  $r$ , for the fundamental and several higher order modes. a) The axial intensity distribution  $|\mathcal{E}_{\text{norm}}^{\text{ax}}|^2 = |Z_{m,q}|^2$  is plotted for  $q = \{0, 1, 2, 15\}$  and a central radius  $R_0 = 18.48 \mu\text{m}$ . b) The radial intensity distribution is plotted for TM (blue) and TE (green) modes. All are normalized to give the same circulating power, i.e.  $|\mathcal{E}_{\text{norm}}^{\text{rad}}|^2 = |\mathcal{E}_{\text{TM}}|^2 / 2\pi \int_0^\infty n(r)^2 |\mathcal{E}_{\text{TM}}|^2 r dr \max(|\mathcal{E}_{\text{TM}}|_{p=0}^2)$ , where  $|\mathcal{E}_{\text{TM}}|^2 = |\mathcal{E}_r|^2 + |\mathcal{E}_\phi|^2$ . The modes shown have radial quantum numbers  $p = \{0, 1, 2, 3\}$  and corresponding caustic radii  $R_c = \{18.48, 19.23, 19.84, 20.38\}^{\text{TM}}, \{18.42, 19.15, 19.76, 20.30\}^{\text{TE}} \mu\text{m}$ . All resonances shown in a) and b) are calculated for the resonator curvature  $\Delta k = 0.012 \mu\text{m}^{-1}$ , the refractive index of Silica  $n = 1.454$ , the azimuthal quantum number  $m = 206$  and the resonance wavelength  $\lambda_0 = 780 \text{ nm}$ .

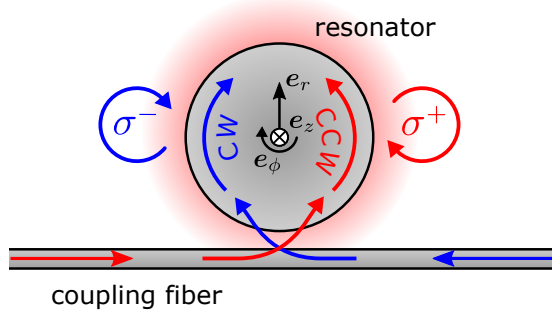


**Figure 3.3:** Schematic of a bottle resonator coupled to a tapered optical nanofiber. When sending light from the right side onto the resonator, light which couples into the resonator will, exclusively couple into the CW propagating running wave mode, which in the evanescent field is almost perfectly  $\sigma^-$ -polarized. If the probing direction is reversed, i.e. sending light from left onto the resonator, only the CCW mode is driven, for which we obtain an almost perfectly  $\sigma^+$ -polarized evanescent field.

that a WGM has not a single wave vector, but a wave vector distribution. As we have seen for the planar interface, wave vectors corresponding to smaller angles of incidence yield a slower decay of the evanescent field than larger angles, and at the same time the longitudinal component is weaker for these angles. Thus, for larger distances from the surface, wave vectors with smaller incidence angle dominate, and consequently  $\mathcal{R}$  decreases. For a resonator made out of silica the ratio close to the surface is  $\mathcal{R} = 0.7$ , which is in good agreement with the prediction for a beam undergoing total internal reflection under gracing incidence, see Eq. (2.16). In addition, the field components have a fixed phase delay of  $\pi/2$ , giving elliptically polarized light in the evanescent field. More quantitatively, the polarization overlap of the CCW propagating mode with perfectly  $\sigma^+$ -polarized light is  $|\alpha_{\sigma^+}| = 0.97$  and with  $\sigma^-$ -polarized light is  $|\alpha_{\sigma^-}| = 0.03$  (see Fig. 3.4d). For light in the CW mode the evanescent field has almost perfect  $\sigma^-$  polarization,  $|\beta_{\sigma^-}| = 0.97$  and  $|\beta_{\sigma^+}| = 0.03$ . Here, we have adapted the definition from Eq. (2.17) such that  $\alpha_i$  and  $\beta_i$  correspond to the CCW and CW propagating running wave modes of the resonator, respectively. Again, we can associate a spin angular momentum (SAM) with this elliptical polarization. The only non-vanishing electric spin component is  $S_z$ , which is orthogonal to the propagation direction of the running wave modes, which is given by  $e_\phi$ .  $S_z$  is plotted in Fig. 3.4f as a function of the distance to the surface. In analogy to the case of a planar interface, the sign of the longitudinal field component, and thus the sign of the local spin density, depends on the propagation direction of the light in the resonator, i.e. the resonator field and in particular the evanescent field exhibits SML.

Due to their large degree of SML, two counter-propagating TM modes are almost orthogonally polarized. Thus, even when we excite two counter-propagating modes, they do not form a standing wave, but a polarization gradient field [93, 94]. Thus, the local polarization is always linear and the direction of polarization rotates a full turn every wavelength. We can compute the local overlap of two counter-propagating modes for our resonator geometry using Eq. 2.19, which is shown in Fig. 3.4. For the evanescent field close to the surface we obtain  $\mathcal{O} = 0.1$ . When

superimposing two counter-propagating modes of equal amplitude, they will interfere and the contrast of the intensity modulation is given by  $I_{\max} - I_{\min} = \sqrt{\mathcal{O}}$ .

For the approximate derivation of the resonator modes the assumption that the electromagnetic fields do not vary significantly along the resonator axis was required. In order to show that this is a valid approximation for the prolate spheroidal BMR, we numerically calculate the full vectorial field distribution for our resonator geometry. For this purpose, we employ the finite element solver software COMSOL. In Fig. 3.5, the electric field along the resonator surface in axial direction is depicted for the two lowest order axial TM-modes,  $q = 0$  and  $q = 1$ . In contrast to the analytic approximation, a small field component in axial direction emerges,  $\mathcal{E}_z \neq 0$ . In addition, we plot the ratio between the desired transverse and the longitudinal electric field component and the overlap of the local electric field with perfect circular polarization. From these plots it becomes evident, that even when taking into account the finite curvature the special polarization properties remain unchanged along the resonator axis.

In summary, in the whole region of non-vanishing electric field, the polarization properties of the evanescent field can in very good approximation be considered constant ( $|\alpha_{\sigma+}|^2 = |\beta_{\sigma-}|^2 = 0.97$ ,  $|\alpha_{\sigma-}|^2 = |\beta_{\sigma+}|^2 = 0.03$  and  $\mathcal{O} = 0.1$ ). This results in a very high degree of SML in the evanescent field of TM polarized resonator modes. In the following chapter, we will discuss in detail how we can incorporate the polarization properties into the mode we use to describe the light-matter interaction and how these affect the nature of the interaction.

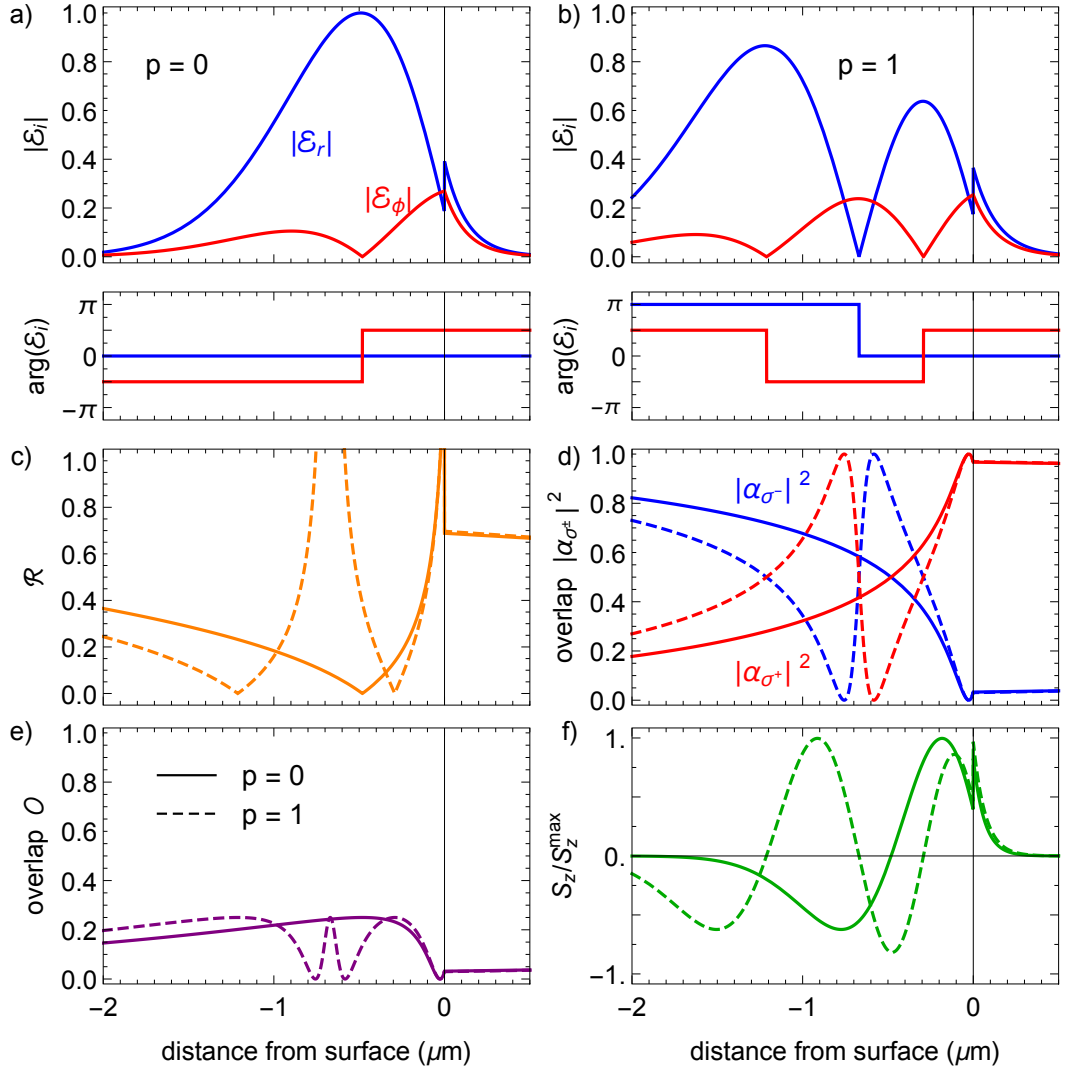


**Figure 3.4:** Polarization properties of the electric field for the two lowest radial TM modes of the bottle microresonator,  $p = 0$  and  $p = 1$ . a) & b) The amplitude and phase of the transverse  $\mathcal{E}_r$  (blue) and longitudinal  $\mathcal{E}_\phi$  (red) electric field components as a function of the distance from the resonator surface. The electric fields are normalized to the maximum value of  $|\mathcal{E}_{\text{TM}}|_{p=0}$ . c) The ratio between the two field components  $\mathcal{R} = |\mathcal{E}_\phi / \mathcal{E}_r|$ . d) The polarization overlap of the local field of a counter clockwise running wave mode with  $\sigma^+$  (red) and  $\sigma^-$  (blue) polarized light. e) The polarization overlap  $\mathcal{O}$  of two counter-propagating modes. f) z-component of the spin density  $S_z$ . In panel c)-f) the solid lines correspond to  $p = 0$  and dashed lines to  $p = 1$ , respectively.

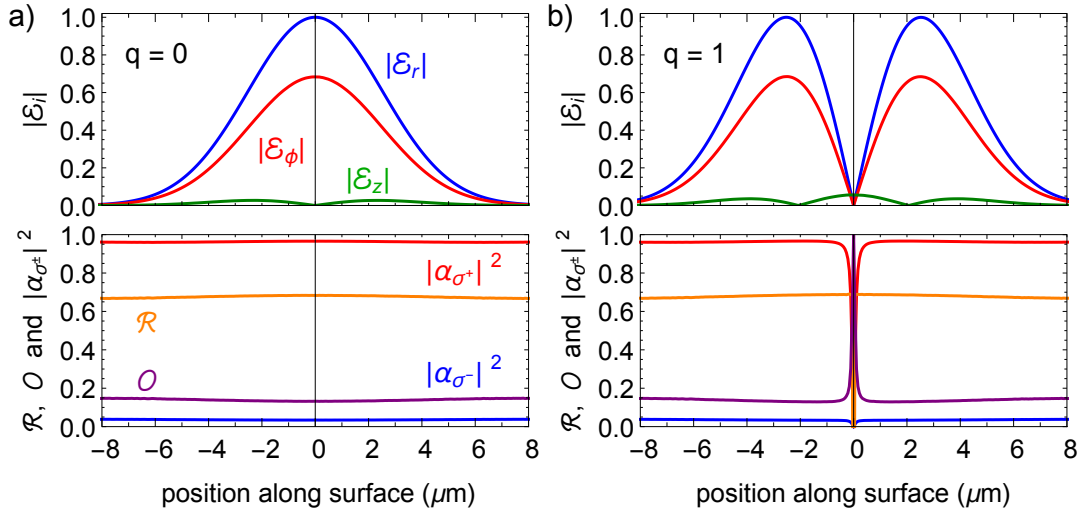


**Figure 3.5:** Polarization properties of the electric field for the two lowest axial modes of the bottle microresonator, a)  $q = 0$  and b)  $q = 1$ , obtained from numerical simulations. The top panels show the amplitude of all polarization components  $\mathcal{E}_r$  (blue),  $\mathcal{E}_\phi$  (red) and  $\mathcal{E}_z$  (green) along the resonator surface. The electric field components are normalized to the maximum value of  $|\mathcal{E}_r|$ . The lower panels depict the ratio  $\mathcal{R} = |\mathcal{E}_\phi/\mathcal{E}_r|$ , the polarization overlap of the local field of a counter clockwise running wave mode with  $\sigma^+$  (red) and  $\sigma^-$  (blue) polarization and the overlap of two counter-propagating modes  $\mathcal{O}$ .





# Interaction between light and matter in WGMs

The description of the interaction of light and matter in high finesse cavities is generally referred to as cavity quantum electrodynamics (CQED) [11]. This field of research was founded by the theoretical predictions made by Jaynes and Cummings in 1963 [95]. First experimental realizations relied on superconducting microwave cavities and thermal atomic beams [96]. This system was successfully used for a variety of ground breaking experiments, including the implementation of a single-atom maser [96], the observation of the first vacuum Rabi oscillations [97], nondestructive photon detection [98], fundamental studies of entanglement [99] and the generation of non-classical states of light, such as Schrödinger cat states [100] or photon Fock states [101]. Since then, the development of low-loss, dielectric reflection coatings enabled the fabrication of high finesse cavities also in the optical regime [75]. The most common type of resonators are of Fabry-Pérot (FP) type which confine the light between two highly reflective mirrors. Furthermore, important technological advances made it possible to trap and cool single atoms such that they can be precisely positioned in the resonator field, enabling a stable coupling in FP resonators [102]. This enabled one to investigate the interaction between light and matter in numerous outstanding experiments in the optical domain at the level of individual atoms [10]. Some major achievements of this thriving research field are the realization of nondestructive photon detection [103], deterministic single photon sources [104, 105], single photon routing [106] and basic building blocks of future quantum networks and tools for quantum information processing [107–109]. Since then, FP resonators have been further optimized, for increasing the light–matter coupling by, e.g., reducing the mode volume through implementing fiber-based cavities [74].

In the mean time, advances in micro- and nanofabrication made completely different resonator designs possible. On the one hand, the field of photonic crystal cavities emerged which combined moderate quality factors with extremely small mode volumes [110]. On the other hand, whispering-gallery-mode (WGM) resonators were devised [20, 76]. These resonators comprise ultra high quality factors with small mode volumes having the additional advantage of almost

lossless in- and outcoupling of light via frustrated total internal reflection [111]. This is an essential requirement when proceeding from proof-of-principle demonstrations to applicable devices that rely on low photon loss. In addition, most WGM resonator setups are inherently fiber integrated and are compatible with on-chip integration [20]. This makes large scale fabrication and integration feasible, which is hard to achieve with bulk systems, such as FP resonators. WGM resonators have been successfully employed for realizing strong light–matter coupling [17, 46] which enabled the demonstration of photon routers [69–71, 112].

However, the strong confinement in, e.g., photonic crystals and WGM resonators, is accompanied by strong transverse field gradients on the sub-micrometer scale. It was shown in Ch. 3 that these strong gradients give rise to special polarization effects, such as longitudinal field components and spin–momentum locking (SML) of light. These effects have been ignored for quite some time when considering the interaction between light and matter. Only recently, the necessity of including the full vectorial description of the light field when coupling it to matter in WGM resonators was pointed out in Ref. [46]. Most importantly, these polarization components gives rise to a chiral, i.e. direction-dependent, light–matter interaction, and paves the way for many interesting new applications in the realm of chiral quantum optics [22].

In this chapter, we will first introduce the basic idea of light–matter interaction using the simple model of a single two level atom coupled to a single mode of the quantized field, introduced by Jaynes and Cummings. In the following, we will extend this model by introducing further degrees of freedom and coupling the system of interest to the environment. This will lead to a model that fully describes the interaction between a single multilevel atom and a WGM resonator. Furthermore, we will discuss two instructive examples for a simplified situation which very accurately describes the situation we encounter in our experiment. Finally, we will interpret these results in the context of chiral waveguides.

## 4.1 Jaynes–Cummings Model

The coherent exchange of energy between a single atom and a single optical mode lies at the heart of quantum optics. In free space, the large number of surrounding modes usually leads to irreversible loss of energy due to spontaneous emission. By introducing a cavity, the density of modes can be modified such that the interaction of the atom with the resonator modes dominates over the interaction with all other modes. Then the emission process becomes reversible and an emission and re-absorption process can be observed. This is often referred to as vacuum Rabi oscillations.

A fully quantum mechanical formalism to theoretically describe this behavior was first introduced by Jaynes and Cummings in 1963 [95]. They considered the interaction between a single two level atom, which resides either in its ground state  $|g\rangle$  or excited state  $|e\rangle$ , and a single quantized mode of the electromagnetic field. The field is described by its bosonic creation operator  $\hat{a}^\dagger$  and annihilation operator  $\hat{a}$ . When the creation operator is applied  $n$  times to the vacuum state, we obtain the  $n$ -photon Fock state  $|n\rangle = (\hat{a}^\dagger)^n / \sqrt{n!} |0\rangle$ . The coherent evolution of the system is governed by the Hamiltonian, which consists of three parts. The first part describes

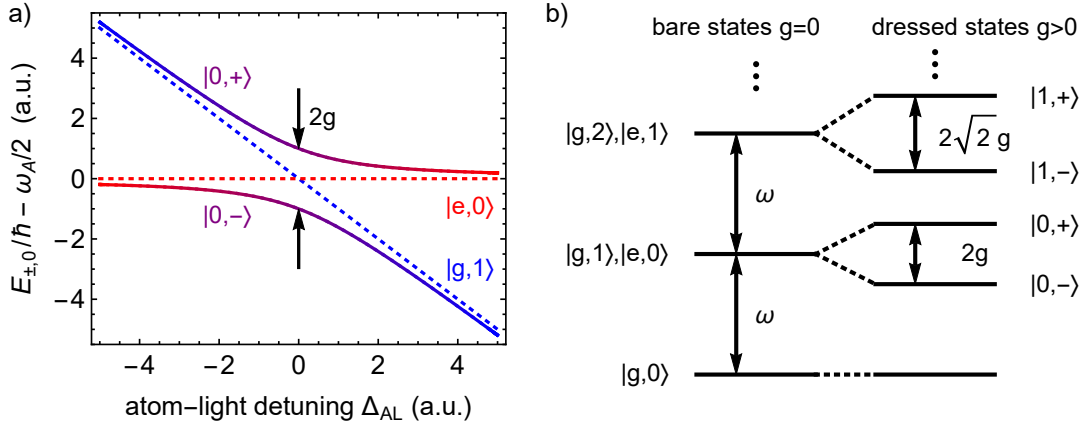


**Figure 4.1:** a) Eigenfrequencies of the lowest ( $n = 0$ ) dressed states as a function of the atom-light detuning  $\Delta_{AL} = \omega_A - \omega_L$ . The dashed lines correspond to the bare states and solid lines to the dressed states, where the color gradient corresponds to the relative amplitudes of the bare states. For large detuning the dressed states approach the bare states. At zero detuning  $\omega_L = \omega_A = \omega$  the eigenfrequencies undergo an avoided crossing with a splitting of  $2g$ . b) Eigenfrequencies of the bare and dressed states for zero detuning,  $\omega = \omega_A = \omega_L$ , for different numbers of excitations. For the dressed states the eigenfrequencies form an anharmonic ladder, often referred to as *Jaynes–Cummings ladder*.

the quantized single mode light field, which for zero ground state energy can be written as

$$\hat{H}_L = \hbar\omega_L\hat{a}^\dagger\hat{a}, \quad (4.1)$$

where  $\omega_L$  is the light's frequency. The second term specifies the free atom

$$\hat{H}_A = \frac{1}{2}\hbar\omega_A\hat{\sigma}_z. \quad (4.2)$$

Here, we have introduced the transition frequency between the ground and excited state  $\omega_A$  and the atomic inversion operator  $\hat{\sigma}_z = |e\rangle\langle e| - |g\rangle\langle g|$ . The interaction between the atom and the field can be written in the dipole and rotating wave approximation as

$$\hat{H}_I = \hbar g(\hat{a}^\dagger\hat{\sigma}_- + \hat{a}\hat{\sigma}_+), \quad (4.3)$$

where we have introduced the atomic raising and lowering operators,  $\hat{\sigma}_+ = |e\rangle\langle g|$  and  $\hat{\sigma}_- = |g\rangle\langle e|$  respectively. In addition, we have defined the coupling strength  $g$ , which is proportional to the field strength per photon at the position of the atom (cf. Eq. (3.5)). The total Hamiltonian,  $\hat{H} = \hat{H}_L + \hat{H}_A + \hat{H}_I$ , only couples the states  $|e, n\rangle \leftrightarrow |g, n+1\rangle$ , which are often referred to as *bare states*. It is straight forward to diagonalize the Hamiltonian, yielding the following eigenenergies

$$E_{\pm,n} = \frac{\hbar}{2}\left((2n+1)\omega_A \pm \Omega_n\right), \quad (4.4)$$

where we have introduced the quantum Rabi frequency  $\Omega_n = \sqrt{4g^2(n+1) + \Delta_{AL}^2}$ , with the detuning between the atomic transition and the light field  $\Delta_{AL} = \omega_A - \omega_L$ . The eigenstates associated with the energy eigenvalues are the so-called *dressed states*

$$|n, +\rangle = \cos(\phi_n/2) |g\rangle |n+1\rangle + \sin(\phi_n/2) |e\rangle |n\rangle \quad (4.5)$$

$$|n, -\rangle = -\sin(\phi_n/2) |g\rangle |n+1\rangle + \cos(\phi_n/2) |e\rangle |n\rangle, \quad (4.6)$$

where  $\phi_n$  is defined through  $\tan \phi_n = 2g\sqrt{n+1}/\Delta_{AL}$ . In Fig. 4.1a, the lowest lying dressed states  $|0, \pm\rangle$  are plotted as a function of the atom–light detuning. If the light field is tuned to the atomic resonance  $\omega_L = \omega_A$ , such that  $\Delta_{AL} = 0$ , the eigenenergies undergo an avoided crossing with an on-resonance energy splitting of  $\hbar g \sqrt{n+1}$ . For the lowest excitation, i.e.  $n = 0$ , the energy splitting between the dressed states is  $2g$ , often referred to as vacuum-Rabi splitting. On resonance, the eigenenergies reduce to a simple form and yield the anharmonic Jaynes–Cummings ladder shown in Fig. 4.1b.

This easy model already describes many interesting phenomena arising from the quantum nature of the light–matter interaction, such as Rabi oscillations including their collapse and revival [113]. Moreover, it can be straight forwardly extended to describe multilevel atoms and multiple modes [114].

In the following, the simple Jaynes–Cummings model will be extended to also take weak coupling to the environment, which ultimately leads to losses, into account.

## 4.2 Losses and driving: The master equation

Experimentally, it is extremely challenging to isolate a quantum system from the environment. In addition, if one manages to perfectly decouple the system of interest from its surroundings, it is impossible to interrogate it and its properties will remain as uncharted territory. In order to probe the quantum system, one has to allow a controlled coupling to the environment. As a consequence, we are inevitably confronted with a so-called open quantum system. Unfortunately, it is not possible to take into account all additional degrees of freedom introduced by the environment. In order to tackle this problem, several approaches have been developed to approximate the system [114, 115]. This includes the Langevin equation [116], quantum trajectory techniques [117, 118] and the master equation approach [119].

Here, we will consider the master equation approach as introduced e.g. in Ref. [120]. The basic idea is to treat the dissipation of the system of interest  $S$  as the coupling to a much larger reservoir  $R$ . The state of the composite system  $S \otimes R$  is represented by the compound density matrix  $\hat{\rho}_{SR}$  and evolves according the von-Neumann equation  $\dot{\rho}_{SR}(t) = -\frac{i}{\hbar} [\hat{H}_{SR}, \hat{\rho}_{SR}(t)]$ , which is equivalent to Schrödinger’s equation for the density matrix calculus. The aim is to derive an effective equation for the evolution of the reduced density operator  $\hat{\rho}_S(t) = \text{Tr}_R[\hat{\rho}_{SR}(t)]$  of the system. In order to accomplish this, we have to make two approximations. First we assume that the coupling between the system and the reservoir is weak such that the state of the large reservoir is not altered by the system, which is known as Born approximation. In addition, we assume that the reservoir has a short memory, meaning that correlations in the reservoir decay fast, which is known as Markov approximation. Using these assumptions, we can derive the

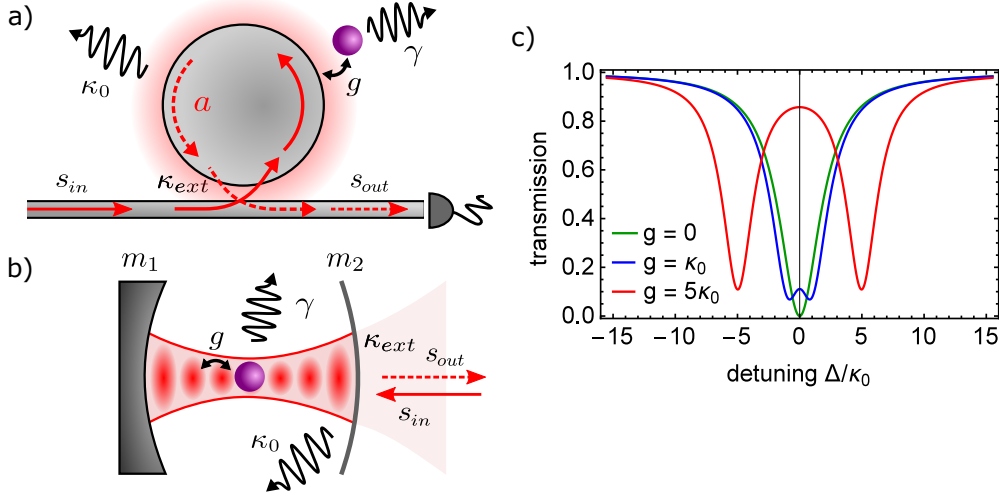


**Figure 4.2:** Compound atom–resonator system for a) a WGM resonator interfaced by a coupling fiber and b) a single-sided ( $R_{m_1} = 1$  and  $R_{m_2} < 1$ ) FP resonator that is coupled to a free space mode. The atom is coupled to the resonator mode with strength  $g$  and has an atomic decay rate  $\gamma$  into free space. The resonator mode, which is subject to intrinsic losses at rate  $\kappa_0$ , is coupled to the input–output mode with  $\kappa_{\text{ext}}$ . c) Transmission spectra through the nanofiber for different coupling atom–resonator strengths  $g/\kappa_0 = \{0, 1, 5\}$ ,  $\Delta_{AL} = \Delta_{CL} = \Delta$  and  $\gamma = \kappa_{\text{ext}} = \kappa_0$ .

master equation, which in Lindblad form can be written as

$$\frac{d\hat{\rho}_S}{dt} = -\frac{i}{\hbar}[\hat{H}_S, \hat{\rho}_S] + \sum_k \mathcal{D}[\hat{c}_k]. \quad (4.7)$$

Here,  $\hat{c}_k$  are system operators which are subject to losses due to their coupling to the reservoir and

$$\mathcal{D}[\hat{c}_k] = \Gamma_k(2\hat{c}_k\hat{\rho}_S\hat{c}_k^\dagger - \hat{c}_k^\dagger\hat{c}_k\hat{\rho}_S - \hat{\rho}_S\hat{c}_k^\dagger\hat{c}_k). \quad (4.8)$$

Their respective coupling rates to the reservoir, i.e. the field or atomic decay rates, are given by  $\Gamma_k$ . The master equation can be written in an abbreviated form as  $\dot{\rho}_S = \mathcal{L}\hat{\rho}_S$ , using the Liouvillian super operator  $\mathcal{L}$ . A commonly used method to numerically solve the master equation is outlined in App. A.2.

Using the master equation the Jaynes–Cummings model can be extended to a more realistic system: Let us assume that we place a single two-level atom inside a single mode resonator. Due to the coupling to the free space modes the atomic excitation decays at the amplitude decay rate  $\gamma = \omega^3\mu^2/6\pi\epsilon_0\hbar c^3$  [81]. Moreover, the resonator itself is not perfectly isolated, and thus photons can leave the resonator. The light can be scattered into the environment from which we cannot recover the photons. These are denoted as intrinsic resonator losses, which occur with the field decay rate  $\kappa_0$ . In order to account for controlled in and out coupling of the resonator,

we introduce an open optical mode that couples to the resonator. For a FP resonator this is typically a free space mode incident on one of the cavity mirrors (see Fig. 4.2b), while for WGM resonators this mode corresponds to the guided mode of a nearby waveguide, such as a tapered fiber coupler (see Fig. 4.2a). The coupling rate between the desired input mode and the resonator mode is denoted as  $\kappa_{\text{ext}}$ . The total resonator field decay is thus given by  $\kappa_0 + \kappa_{\text{ext}}$ . Since we consider now an open system we are able to interrogate and probe it. This can be done by an external driving field, which can either directly excite the atom or the cavity. For now, we consider the latter case. Thus, we have to add a driving term to the Hamiltonian. After transforming the total Hamiltonian into a frame that rotates with the frequency  $\omega_p$  of the pump field, we then obtain an extended Jaynes–Cummings Hamiltonian

$$\hat{H}/\hbar = \underbrace{\Delta_{RP} \hat{a}^\dagger \hat{a}}_{\hat{H}_L} + \underbrace{\Delta_{AP} \hat{\sigma}_+ \hat{\sigma}_-}_{\hat{H}_A} + \underbrace{g(\hat{a}^\dagger \hat{\sigma}_- + \hat{a} \hat{\sigma}_+)}_{\hat{H}_I} + \underbrace{i\epsilon(\hat{a} - \hat{a}^\dagger)}_{\hat{H}_{\text{drive}}} . \quad (4.9)$$

Here, we have replaced the frequency of the atomic transition and the resonator frequency by the detuning with respect to the frequency of the driving field,  $\Delta_{AP} = \omega_A - \omega_P$  and  $\Delta_{RP} = \omega_R - \omega_P$  respectively. The last term,  $\hat{H}_{\text{drive}}$ , represents the coupling to the driving field and  $\epsilon = \sqrt{2\kappa_{\text{ext}}} \langle s_{\text{in}} \rangle$ , where  $\langle s_{\text{in}} \rangle$  is the amplitude of the incident field. In addition, we assumed that the driving field is in a coherent state.<sup>1</sup> For this simple case the master equation for the atom–resonator system is then given by

$$\frac{d\hat{\rho}}{dt} = -\frac{i}{\hbar} [\hat{H}, \hat{\rho}] + (\kappa_0 + \kappa_{\text{ext}})(2\hat{a}\hat{\rho}\hat{a}^\dagger - \hat{a}^\dagger\hat{a}\hat{\rho} - \hat{\rho}\hat{a}^\dagger\hat{a}) + \gamma(2\hat{\sigma}_-\hat{\rho}\hat{\sigma}_+ - \hat{\sigma}_+\hat{\sigma}_-\hat{\rho} - \hat{\rho}\hat{\sigma}_+\hat{\sigma}_-) . \quad (4.10)$$

Equation (4.10) allows us to calculate the temporal evolution of the coupled system in the presence of dissipation. In many cases, we are interested in the system properties after the transient state. In the weak driving limit, i.e.  $\langle n \rangle \ll 1$ , we can assume that we have at most a single excitation in our system and restrict the state space to  $\{|g, 0\rangle, |g, 1\rangle, |e, 0\rangle\}$  which enables us to obtain an analytic steady-state solution for the density matrix  $\hat{\rho}^{ss}$ . Using this, we can obtain the expectation value of a system operator  $\hat{c}$  via  $\langle \hat{c} \rangle = \text{Tr}[\hat{\rho}^{ss} \hat{c}]$ . The steady state expectation value of the cavity mode amplitude and the atomic coherence are

$$\langle \hat{a} \rangle = \frac{-i\epsilon(\gamma + i\Delta_{AP})}{g^2 + (\gamma + i\Delta_{AP})(\kappa_0 + \kappa_{\text{ext}} + i\Delta_{RP})} , \quad (4.11)$$

$$\langle \hat{\sigma}_- \rangle = \frac{-\epsilon g}{g^2 + (\gamma + i\Delta_{AP})(\kappa_0 + \kappa_{\text{ext}} + i\Delta_{RP})} . \quad (4.12)$$

In the weak driving limit the intra-resonator photon number and the excited state population can be obtained via  $n_{\text{res}} = |\langle \hat{a} \rangle|^2$  and  $\rho_{ee} = |\langle \hat{\sigma}_- \rangle|^2$ , respectively. In order to gain information from the system we can analyze the light in the output mode. The field amplitude  $\hat{s}_{\text{out}}$  of the output mode is a superposition of the input field  $\hat{s}_{\text{in}}$  and the field that couples from the resonator mode back into the output mode [121]

$$\hat{s}_{\text{out}} = \hat{s}_{\text{in}} - i\sqrt{2\kappa_{\text{ext}}} \hat{a} . \quad (4.13)$$

<sup>1</sup>Note that this driving term is valid for WGM, ring resonators and single-sided FP resonators. For symmetric FP resonators this term would change to  $\epsilon_{\text{FP}} = \sqrt{\kappa_{\text{ext}}} \langle s_{\text{in}} \rangle$ .

The amplitude transmission coefficient through the waveguide can be calculated using

$$\begin{aligned}
 t = \frac{\langle \hat{s}_{\text{out}} \rangle}{\langle \hat{s}_{\text{in}} \rangle} &= 1 - i\sqrt{2\kappa_{\text{ext}}} \frac{\langle \hat{a} \rangle}{\langle \hat{s}_{\text{in}} \rangle} = \\
 &= \frac{g^2 + (\gamma + i\Delta_{AP})(\kappa_0 - \kappa_{\text{ext}} + i\Delta_{RP})}{g^2 + (\gamma + i\Delta_{AP})(\kappa_0 + \kappa_{\text{ext}} + i\Delta_{RP})} \xrightarrow{\kappa_0=0} \frac{C-1}{C+1}, \quad (4.14)
 \end{aligned}$$

where in the final expression we used the single atom cooperativity  $C = g^2/\gamma(\kappa_0 + \kappa_{\text{ext}})$  and evaluated the expression on resonance, i.e.  $\Delta_{AP} = \Delta_{RP} = 0$  and for the case  $\kappa_0 = 0$ . The power transmission is then defined as  $T = |t|^2$ . The transmission spectra for  $\Delta_{AP} = \Delta_{RP} = \Delta$  are depicted in Fig. 4.2c for different coupling strengths  $g$ , to show the emergence of the characteristic Rabi splitting.

### 4.3 Strong coupling and fast cavity regime

Due to the interaction with the environment, the dynamics of the coupled system also depend on the loss rates of the individual system. In order to observe the coherent interaction, which is described by the simple Jaynes–Cummings model, the rate at which it takes place has to be larger than all loss rates. This parameter regime is commonly known as *strong coupling* and can be summarized as

$$g \gg (\kappa_0, \kappa_{\text{ext}}), \quad (4.15)$$

which also implies  $C \gg 1$ . In this regime, already a single resonant atom suffices to significantly alter the resonator field and thereby the transmission,  $N_0 < 1$ . At the same time, a single photon is enough to saturate the atom,  $n_0 < 1$ . When looking at the transmission spectrum the avoided crossing of the coupled eigenmodes becomes evident as a Rabi splitting, which is considered as a clear signature of the strong coupling regime (see Fig. 4.2c). Reaching the regime of strong light–matter coupling has long been considered as the Holy Grail of quantum optics. However, for most applications it is desirable to deterministically couple photons to matter, making use of the strong light–matter interaction. After the interaction however, the photon should be extracted again from the resonator with high probability. This requires one to operate the experiments in the so-called *fast cavity* or *Purcell* regime [10]. In this regime, the coupling between the waveguide and the cavity is the dominant rate, while all actual losses are still smaller than the coherent interaction

$$\kappa_{\text{ext}} > g > \kappa_0, \gamma \quad \text{and} \quad C > 1. \quad (4.16)$$

Most of the experiments presented in this thesis are performed in this regime.

### 4.4 Coupling between a single atom and WGMs

The simple model, which was introduced in the previous section, treats the electric field of the resonator modes as a scalar quantity and does not take into account its polarization. This can be an appropriate description for FP resonators, for which the light forms a single standing wave mode between the two mirrors. In contrast, WGM resonators support two degenerate counter-propagating running wave modes, which have diverse polarization characteristics (cf. Ch. 3).

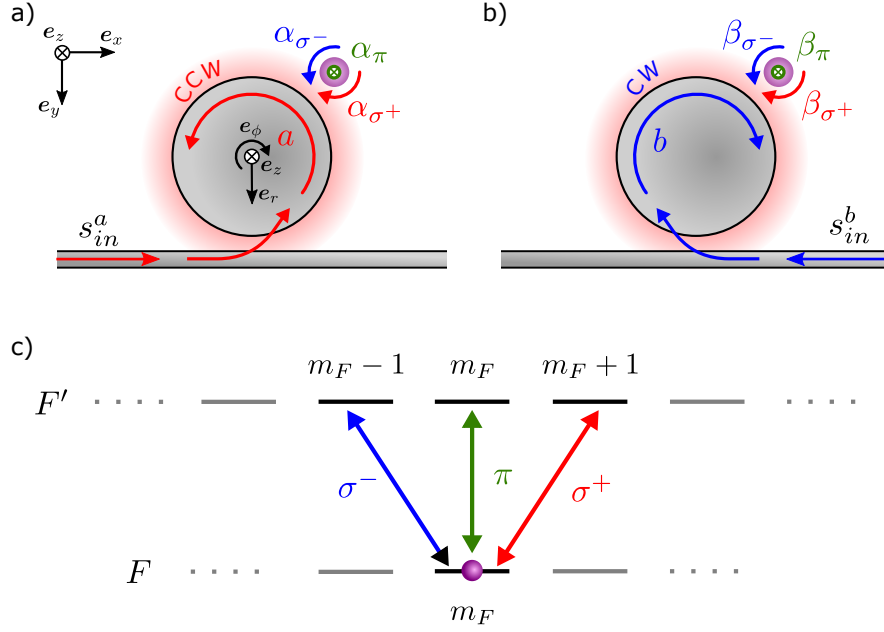


**Figure 4.3:** Schematic of light–atom coupling in WGM resonators. a) When launching light in the positive  $x$ -direction through the coupling fiber we excite the counter-clockwise (CCW) propagating running wave mode  $a$ . At the position of the atom the polarization is described by the three overlaps  $\alpha_i = \mathcal{E}^a \cdot e_i^* / |\mathcal{E}^a|$  between the local field vector  $\mathcal{E}^a$  and the atomic eigenpolarizations,  $e_i \in \{e_{\sigma^+}, e_\pi, e_{\sigma^-}\}$ . b) When launching light in the negative  $x$ -direction through the coupling fiber we excite the clockwise (CW) propagating running wave mode  $b$ . At the position of the atom the polarization is described by the three overlaps  $\beta_i = \mathcal{E}^b \cdot e_i^* / |\mathcal{E}^b|$  between the local field vector  $\mathcal{E}^b$  and the atomic eigenpolarizations. c) If the light in the resonator is resonant with the  $F \rightarrow F'$  the different polarization components  $\{\sigma^-, \pi, \sigma^+\}$  drive transitions between  $m_{F'} = m_F + \Delta_{m_F}$ , with  $\Delta_{m_F} = \{-1, 0, +1\}$ .

Until recently, this polarization structure was not taken into account for describing the interaction between light and matter. However, it was shown in Ref. [86] that this can qualitatively change the coupling, giving rise to chiral light–matter interaction [22]. In this section we extend the master equation approach to fully and accurately describe the situation we encounter in our experiment. This model includes a vectorial treatment of the resonator fields, thus correctly describing the running wave modes supported by the WGM resonator. Consequently, we also have to take into account the complex level structure of the alkali atoms. Based on this general model, we apply a few approximations, that will allow us to derive an instructive analytic solution, that is adequate for many cases and allows one to gain a deeper understanding of chiral light–matter interaction.



#### 4.4.1 Accurate description of light–matter interaction in WGMs

The accurate description of the light–matter interaction in WGM resonators requires a quantum mechanical treatment, which takes into account the full vectorial nature of the resonator field. For the purpose of giving a general description, it is useful to decompose the polarization of the resonator modes into the eigenpolarization of the atom along its quantization axis. In the following, we consider two degenerate counter-propagating modes,  $a$  and  $b$ , which can be pumped by sending light through the coupling fiber from opposite directions (see Fig. 4.3a-b). For the atom, we have to take into account the complete magnetic sub-structure of the atomic levels (see App. A.1 for the level structure of  $^{85}\text{Rb}$ ). Due to its internal structure, atoms are non-polarization maintaining scatterers and the coupling strength between the atom and the light depends on the light’s polarization and the atomic state. As a consequence, the two counter-propagating modes can couple to different transitions of the atom with different coupling strengths.

We consider the case where the resonator interacts with the  $F \rightarrow F'$  transition of a single atom, where  $F$  and  $F'$  are the hyperfine ground and excited states respectively. For sake of readability, we do not include the possibility that the atom has several ground or excited hyperfine states, although, our model can readily be extended to this case. The resonator-guided light can drive different atomic transitions, where  $\pi$ -polarized light will drive transitions with  $\Delta m_F = 0$  and  $\sigma^\pm$ -polarized light drives transitions with  $\Delta m_F = \pm 1$  (see Fig. 4.3c). Here,  $m_F$  and  $m_{F'}$  are the Zeeman sublevels of the ground and excited state, respectively. In a reference frame rotating at the probe light frequency  $\omega_P$ , the uncoupled part of the Hamiltonian is given by the sum of

$$\begin{aligned} \hat{H}_A/\hbar = & \sum_{m_F=-F}^F \mu_B g_F m_F B |F, m_F\rangle \langle F, m_F| \\ & + \sum_{m_{F'}=-F'}^{F'} (\mu_B g_{F'} m_{F'} B + \Delta_{AP}) |F', m_{F'}\rangle \langle F', m_{F'}| , \end{aligned} \quad (4.17)$$

and

$$\hat{H}_R/\hbar = \Delta_{RP}(\hat{a}^\dagger \hat{a} + \hat{b}^\dagger \hat{b}) . \quad (4.18)$$

Here, we introduced  $|F, m_F\rangle$  and  $|F', m_{F'}\rangle$  as the atomic ground and excited states, respectively, and  $\Delta_{AP}$  ( $\Delta_{RP}$ ) is the detuning between the atomic transition (resonator) and the pump field. We also assume the presence of a magnetic field  $B$  that defines the quantization axis and results in an energy shift for each Zeeman level of  $\Delta E_Z/\hbar = \mu_B g_F m_F B$ , where  $\mu_B$  is the Bohr magneton and  $g_F$  is the Landé  $g$ -factor of the corresponding energy level.  $\hat{a}$  and  $\hat{b}$  ( $\hat{a}^\dagger$  and  $\hat{b}^\dagger$ ) are the photon annihilation (creation) operators of the corresponding mode. The Hamiltonian that describes the light–matter interaction is given by

$$\hat{H}_I/\hbar = g_a \hat{a} \hat{d}_a^\dagger + g_a^* \hat{a}^\dagger \hat{d}_a + g_b \hat{b} \hat{d}_b^\dagger + g_b^* \hat{b}^\dagger \hat{d}_b . \quad (4.19)$$

Here,  $g_a$  and  $g_b$  describe the interaction strengths of the atom with the two resonator modes. More specifically,  $g_i = \psi_i(\mathbf{r}) \sqrt{\omega/2\hbar\epsilon_0 V} \tilde{\mu}$  (cf. Eq. 3.5), using the mode volume  $V$  of the resonator mode with resonance frequency  $\omega$ ,  $\psi_i(\mathbf{r})$  is the mode function of the respective resonator field at the position of the atom  $\mathbf{r}$  which is normalized to be 1 at the field maximum,

and  $\tilde{\mu} = \sqrt{(2J+1)/(2J'+1)} \cdot \langle J || e\hat{r} || J' \rangle$  is the reduced atomic transition dipole matrix element [122] with the dipole operator  $e\hat{r}$  and the total angular momenta  $J$  and  $J'$  of the ground and excited states, respectively. The total atomic lowering operators for the interaction with the two resonator modes can be separated into the atomic eigenpolarizations and are then given by

$$\begin{aligned}\hat{d}_a &= \alpha_{\sigma^+} \hat{d}_{+1} + \alpha_{\pi} \hat{d}_0 + \alpha_{\sigma^-} \hat{d}_{-1}, \\ \hat{d}_b &= \beta_{\sigma^+} \hat{d}_{+1} + \beta_{\pi} \hat{d}_0 + \beta_{\sigma^-} \hat{d}_{-1},\end{aligned}\quad (4.20)$$

respectively. In this expression, the complex coefficients  $\alpha_i$  and  $\beta_i$  reflect the polarization overlap between the atomic eigenpolarizations and the field of the resonator modes  $a$  and  $b$  (see Fig. 4.3), which are defined in Eq. (2.17). The operators  $\hat{d}_{\Delta m_F}$  are the atomic lowering operators that include all possible transitions with  $\Delta m_F \in \{+1, 0, -1\}$  and are given by [123]<sup>2</sup>

$$\hat{d}_{\Delta m_F} = \sqrt{\frac{2J'+1}{2J+1}} \sum_{m_F=-F}^F \mu_{m_F}^{m_F+\Delta m_F} |F, m_F\rangle \langle F', m_F + \Delta m_F|. \quad (4.21)$$

The strengths of the respective transition can be expressed in terms of 3-j and 6-j symbols by [122]

$$\mu_{m_F}^{m_{F'}} = \sqrt{(2F'+1)(2F+1)(2J+1)} \begin{pmatrix} F' & 1 & F \\ m_{F'} & q & -m_F \end{pmatrix} \begin{Bmatrix} J & J' & 1 \\ F' & F & I \end{Bmatrix}. \quad (4.22)$$

Here,  $q = (0, \pm 1)$  for transition involving  $(\pi, \sigma^\pm)$  polarized light and the last two terms are the Wigner 3-j and 6-j symbols, respectively. If we choose the atom to be located close to the symmetry plane ( $z = 0$ ) and align its quantization axis with the symmetry axis of the resonator ( $z$ -axis), the polarizations of transverse magnetic (TM) and transverse electric (TE) modes coincide with the atomic eigenpolarizations  $e_{\sigma^\pm}$  and  $e_\pi$ . In this basis, the atomic operators simplify to  $\hat{d}_a = \hat{d}_b = \hat{d}_0$  for TE modes and to  $\hat{d}_a = \alpha_{\sigma^+} \hat{d}_{+1} + \alpha_{\sigma^-} \hat{d}_{-1}$  and  $\hat{d}_b = \beta_{\sigma^+} \hat{d}_{+1} + \beta_{\sigma^-} \hat{d}_{-1}$  for TM modes, where  $\alpha_{\sigma^+} (\beta_{\sigma^-}) \gg \alpha_{\sigma^-} (\beta_{\sigma^+})$  and  $|\alpha_{\sigma^\pm}| = |\beta_{\sigma^\mp}|$ .

For completeness, we also introduce a coupling rate  $h$  between the resonator modes, due to scattering by e.g. surface roughnesses or impurities. The full Hamiltonian of the coupled atom-cavity system finally reads

$$\hat{H}/\hbar = (\hat{H}_A + \hat{H}_R + \hat{H}_I)/\hbar + h\hat{a}^\dagger \hat{b} + h^* \hat{b}^\dagger \hat{a} + i\epsilon_a(\hat{a} - \hat{a}^\dagger) + i\epsilon_b(\hat{b} - \hat{b}^\dagger). \quad (4.23)$$

Here, the last two terms describe the pumping of the resonator modes  $a$  and  $b$  by external light fields via the coupling fiber. For the case where the incident wave can be treated as a classical coherent field,  $\epsilon_a = \sqrt{2\kappa} \langle s_{in}^a \rangle$  and  $\epsilon_b = \sqrt{2\kappa} \langle s_{in}^b \rangle$ , where  $\langle s_{in}^a \rangle$  and  $\langle s_{in}^b \rangle$  is the mean amplitude of the field propagating in positive or negative  $x$ -direction through the waveguide [124]. The full time evolution including the steady state can again be calculated using the master equation

<sup>2</sup>Note that we added the term  $\sqrt{(2J'+1)/(2J+1)}$  in accordance with Ref. [81]. For the  $D_2$ -line of <sup>85</sup>Rb this factor is  $\sqrt{2}$ . Together with the transition strength for the cycling transitions  $\mu_{m_F=\pm 3}^{m_{F'}=\pm 4} = 1/\sqrt{2}$ , we obtain  $\hat{d}_{\pm 1} = 1$ . Consequently,  $g_i$  corresponds to the coupling strength for driving the cycling transition (cf. App. A.1).

approach introduced in 4.2, but now we have to take into account all the decay channels including each atomic excited state and both counter-propagating modes

$$\frac{d\hat{\rho}}{dt} = -\frac{i}{\hbar}[\hat{H}, \hat{\rho}] + (\kappa_{ext} + \kappa_0)(\mathcal{D}[\hat{a}] + \mathcal{D}[\hat{b}]) + 2\gamma \sum_{m_F, m_{F'}} \mathcal{D}[\hat{d}_{m_F}^{m_{F'}}]. \quad (4.24)$$

If several ground or excited hyperfine states have to be considered, the sums in Eq. (4.17) and Eq. (4.24) have to be extended to all possible states.

From solving the full master equation we can extract the expectation values of the resonator field amplitudes  $\langle \hat{a} \rangle$  and  $\langle \hat{b} \rangle$ . When we probe the system only from one side such that we drive mode  $a$  we can calculate the fiber transmission amplitude from the input–output relation

$$\hat{s}_{out}^a = \hat{s}_{in}^a - i\sqrt{2\kappa_{ext}} \hat{a}, \quad (4.25)$$

according to Eq. (4.14)

$$t = 1 - i\sqrt{2\kappa_{ext}} \frac{\langle \hat{a} \rangle}{\langle \hat{s}_{in}^a \rangle}. \quad (4.26)$$

Due to direct mode–mode coupling and scattering of light between the two counter-propagating modes by the atom, mode  $b$  can also become populated. The light in mode  $b$  can couple back into the coupling fiber, leading to a finite reflection signal, that can be calculated using

$$\hat{s}_{out}^b = -i\sqrt{2\kappa_{ext}} \hat{b}, \quad (4.27)$$

via

$$r = -i\sqrt{2\kappa_{ext}} \frac{\langle \hat{b} \rangle}{\langle \hat{s}_{in}^a \rangle}. \quad (4.28)$$

When probing from the opposite direction, i.e. pumping mode  $b$ , the mode operators  $\hat{a}$  and  $\hat{b}$  have to be interchanged.

In order to get an idea of what the consequences of the full vectorial description of the resonator mode and the multi-level structure of the atom are, we will now discuss two simple but instructive examples.

#### 4.4.2 Simple analytic solutions

We only consider the case of TM modes, for which the evanescent field is elliptically polarized. Thus, the only non-vanishing overlaps are  $\alpha_{\sigma+}$  and  $\alpha_{\sigma-}$  for the CCW propagating mode  $a$ , and  $\beta_{\sigma+}$  and  $\beta_{\sigma-}$  for the CW propagating mode  $b$ . Due to the cylindrical symmetry of the resonator, both running wave modes,  $a$  and  $b$ , have the same field amplitude at the position of the atom, and thus  $g_a = g_b = g$  (cf. Eq. (4.19)). Moreover, time reversal symmetry of Maxwell's equations implies that  $|\alpha_{\sigma+}| = |\beta_{\sigma-}|$ ,  $|\alpha_{\sigma-}| = |\beta_{\sigma+}|$  and  $|\alpha_{\sigma-}|^2 = 1 - |\alpha_{\sigma+}|^2$ . Therefore, the polarization properties of the resonator modes can be condensed into a single parameter, which we choose to be  $|\alpha_{\sigma+}|^2$ .

Until now, we have not made a single approximation and this model gives the exact description of the interaction of a single scatterer with WGM resonator modes. Let us now consider the case where the atom is prepared in a well defined ground state  $|F, m_F\rangle$ . For TM-modes, the light in the resonator modes can now only drive the  $\Delta m_F = \pm 1$  transitions, thus, forming a V-level system, as depicted in Fig. 4.3c. The respective interaction strength of the two competing transitions now depend on two parameters. The first is the polarization overlap of the local field with  $\sigma^+$  or  $\sigma^-$ . The second is the dipole matrix elements, for the two transitions  $|F, m_F\rangle \rightarrow |F', m_F \pm 1\rangle$  (cf. App. A.1).

In the following, we will discuss two examples, where we take into account the vectorial nature of the resonator field, but limit the number of atomic levels involved in the interaction. First, we consider the symmetric case, where the atom has a  $\sigma^+$  and a  $\sigma^-$  transition that couples to the resonator light. Secondly, we study the case where the atom exclusively couples to  $\sigma^+$ -polarized light. For both cases we will be able to derive an analytic solution for the steady state of the cavity modes  $\langle a \rangle$  and  $\langle b \rangle$ .

### Coupling between polarization-independent scatterer and WGMs

Let us now consider the case where the atom is prepared in the  $|F=0, m_F=0\rangle$  ground state. The light in the resonator modes now drives the  $\Delta m_F = \pm 1$  transitions between the ground state and the  $|F'=1, m_F = \pm 1\rangle$  excited states, forming a V-like level structure, as depicted in Fig. 4.4a. For these two transitions, the dipole matrix elements are of equal size,  $\mu_0^{+1} = \mu_0^{-1}$ , yielding  $\hat{d}_{+1} = \hat{d}_{-1}$ . Therefore, the total interaction strength between the light field and the atom does not depend on the light's polarization. Thus, the atom couples to the light of TM modes independent of their polarization composition. However, depending on its polarization the light couples to one or both transitions. These simplifications already enable us to derive an analytic steady state solution for the expectation value of the two cavity modes, in the absence of mode–mode coupling and if only mode  $a$  is pumped

$$\langle \hat{a} \rangle = \frac{-i\sqrt{2\kappa_{\text{ext}}}\tilde{\gamma}(g^2 + \tilde{\gamma}\tilde{\kappa})s_{\text{in}}^a}{\tilde{\gamma}^2\tilde{\kappa}^2 + g^2\tilde{\gamma}\tilde{\kappa} + g^4(2|\alpha_{\sigma^+}|^2 - 1)^2}, \quad (4.29)$$

$$\langle \hat{b} \rangle = \frac{i2\sqrt{2\kappa_{\text{ext}}}g^2\tilde{\gamma}\alpha_{\sigma^+}\beta_{\sigma^+}s_{\text{in}}^a}{\tilde{\gamma}^2\tilde{\kappa}^2 + g^2\tilde{\gamma}\tilde{\kappa} + g^4(2|\alpha_{\sigma^+}|^2 - 1)^2}. \quad (4.30)$$

Here, the atom and resonator detunings have been absorbed into the new variables,  $\tilde{\gamma} = \gamma + i\Delta_{AP}$  and  $\tilde{\kappa} = \kappa_{\text{ext}} + \kappa_0 + i\Delta_{RP}$ . Equations (4.29) and (4.30) not only contain the usual system parameters but also depend on the polarization overlap of the atomic dipole with the local fields via  $\alpha_{\sigma^+}$  and  $\beta_{\sigma^+}$ , which in turn can be written as a single parameter.

In Fig. 4.4b, transmission and reflection spectra, calculated using Eqs. (4.26-4.28) together with Eqs. (4.29-4.30), are shown for different polarization overlap. If the resonator field is perfectly circularly polarized, i.e.  $|\alpha_{\sigma^+}|^2 = 1$  or  $|\alpha_{\sigma^+}|^2 = 0$ , it drives a closed cycling transition between the ground state and one of the two excited states. Since there is no polarization overlap between the two counter-propagating modes no, light will be scattered from mode  $a$  into mode  $b$  via the atom. This realizes the ideal situation where each resonator mode is independently coupled to

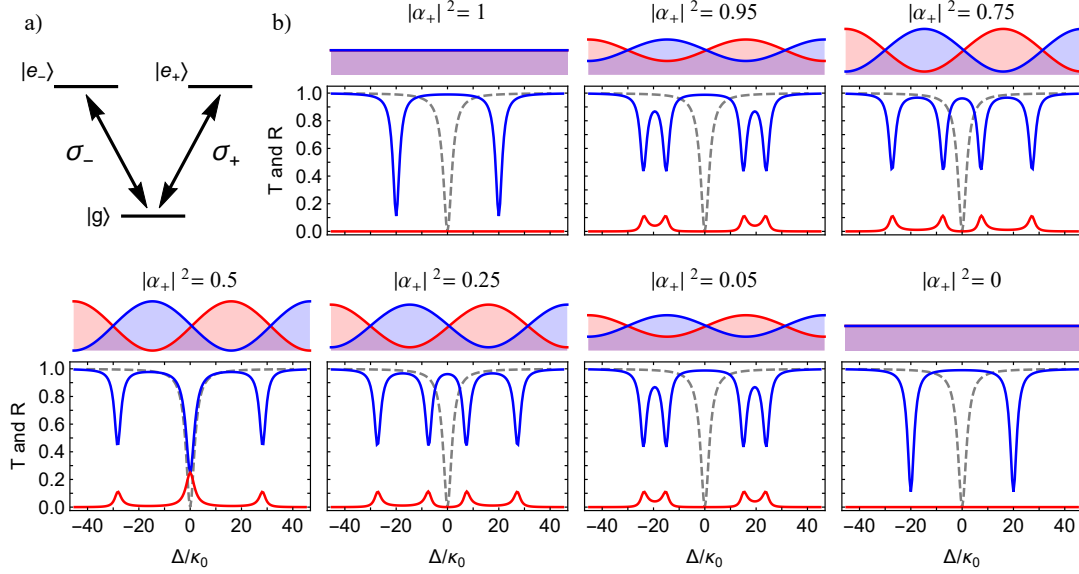


**Figure 4.4:** a) V-like atomic level structure of a  $|F=0\rangle \rightarrow |F'=1\rangle$  transition, with a quantization axis that is aligned with the resonator. The atom is coupled to TM polarized light, which can drive  $\sigma^+$  and  $\sigma^-$  transitions. For this level structure, the coupling between the atom and  $\sigma^+$ - or  $\sigma^-$ -polarized light is equal. b) Transmission (blue) and reflection (red) through the waveguide coupled to the atom–resonator system, for different overlaps  $|\alpha_{\sigma^+}|^2$ . Due to SML of the resonator field, the change from  $|\alpha_{\sigma^+}|^2 > 1/2$  to  $|\alpha_{\sigma^+}|^2 < 1/2$  can be interpreted as a change of the probing direction. For comparison, the empty resonator spectrum is plotted as a dashed line. The small inset on top of each spectrum represents the intensity modulation of two standing wave modes for the respective setting. All shown spectra were calculated using Eq. (4.29) and the following parameters:  $(g, \gamma, \kappa_{\text{ext}}, h) = (20, 1, 1, 0)/\kappa_0$ .

an effective two-level atom. In this case, Eq. (4.29) and Eq. (4.30) reduce to the expression we obtained for the extended Jaynes–Cummings model (cf. Eq. (4.11)). The transmission spectra shows two resonances separated by  $2g$ , and the reflection is zero for all detunings. If the polarization deviates from perfect circular polarization, i.e.  $|\alpha_{\sigma^+}|^2 \neq (0, 1)$  the situation drastically changes. Instead of a two-resonance spectrum, we observe two additional resonances emerging. In order to understand the physical origin of this behavior, it is instructive to change basis and consider the standing wave modes defined by the operators  $\hat{A} = (\hat{a} + \hat{b})/\sqrt{2}$  and  $\hat{B} = (\hat{a} - \hat{b})/\sqrt{2}$ . When there is a finite polarization overlap between the two running wave modes, their superposition  $\hat{A} + \hat{B}$  will show intensity modulations along the circumference. This modulation is schematically shown as inset above each spectrum in Fig. 4.4b. Without loss of generality, we place the atom at a maximum of one standing wave mode, and thus at a minimum of the other mode. Since the coupling strength of the atom to the resonator now depends on the local field strength, it differs for the two standing wave modes, yielding two different vacuum-Rabi splittings. If the overlap between the two running wave modes is increased, the intensity modulation

becomes further pronounced and the two central dips will move close together while the two outer dips slightly move apart. For  $|\alpha_{\sigma^+}|^2 = 1/2$ , both modes,  $a$  and  $b$ , have the same linear polarization, i.e. are in an equal superposition of  $\sigma^+$ - and  $\sigma^-$ -polarized light. As a consequence, we obtain two fully modulated standing waves, of which only one couples to the atom. In this case, the two central resonances will merge at zero detuning, while the outer dips show an enlarged splitting of  $2\sqrt{2}g$ . This is caused by the intensity modulation which reduces the effective mode volume of the standing wave modes. However, for this setting, only half of the light that couples from the fiber to the resonator actually interacts with the atom. As direct consequence, the on-resonance transmission is bound to 0.25. In addition, the atom will scatter light between the modes, which populates the un-pumped mode  $b$  and results in a finite reflection. When we flip the sign of the spin of the local polarization, i.e.  $|\alpha_{\sigma^+}|^2 > 0.5$  the system responds symmetrically, meaning that we obtain the same spectra (cf. the first and the last panel in Fig. 4.4b). Due to SML, this situation corresponds to sending light from the opposite direction through the waveguide and thus directly pumping the mode  $b$ .

While this system is conceptually interesting to understand the interaction between light and matter in WGM resonators, atoms are in general not in such a highly symmetric V-system. In our experiment in particular, we typically prepare the atom in a closed cycling transition for which the coupling to the two modes is not symmetric.

### Coupling between polarization-dependent scatterer and WGMs

Let us now consider the case where the atom is prepared in the outermost  $m_F$ -state, such that  $\sigma^+$ -polarized light drives a closed cycling transition between  $|F, m_F\rangle$  and  $|F', m_F + 1\rangle$ . The transition strength of the  $|F, m_F\rangle \rightarrow |F', m_F - 1\rangle$  transition, which is driven by  $\sigma^-$ -polarized light, is significantly smaller. The ratio between the two competing transition strengths can be calculated using the 3-j symbol (see App. A.1). For the  $|F=3\rangle \rightarrow |F'=4\rangle$  transition of the  $D_2$ -line of  $^{85}\text{Rb}$ , which is the transition we are currently using in the experiment, this ratio is 28.

As a consequence, for many experimental settings the coupling to the state  $|F=4, m_{F'}=2\rangle$  can be neglected and the level scheme reduces to a simple two-level system, which exclusively couples to  $\sigma^+$ -polarized light, as shown in Fig. 4.5a. For this case, analytic solutions for the steady state of the resonator modes can be obtained

$$\langle \hat{a} \rangle = \frac{-i\sqrt{2\kappa_{\text{ext}}} \left( (1 - |\alpha_{\sigma^+}|^2)g^2 + \tilde{\gamma}\tilde{\kappa} \right) s_{\text{in}}^a}{\tilde{\kappa} (g^2 + \tilde{\gamma}\tilde{\kappa})}, \quad (4.31)$$

$$\langle \hat{b} \rangle = \frac{i\sqrt{2\kappa_{\text{ext}}} g^2 \alpha_{\sigma^+} \beta_{\sigma^+} s_{\text{in}}^a}{\tilde{\kappa} (g^2 + \tilde{\gamma}\tilde{\kappa})}. \quad (4.32)$$

By inserting these formulas into Eqs. (4.26)-(4.28), we can again calculate the transmission and reflection through the waveguide, which is plotted in Fig. 4.5b.

If the local polarization of the pumped mode perfectly coincides with  $\sigma^+$ , i.e.  $|\alpha_{\sigma^+}|^2 = 1$ , the light in mode  $a$  drives the atomic transition, while light in mode  $b$  does not interact with the atom. The spectral response is the same as that we obtained from the previous model and shows a two-resonance spectrum, where the resonances are split by  $2g$ . When the overlap of the

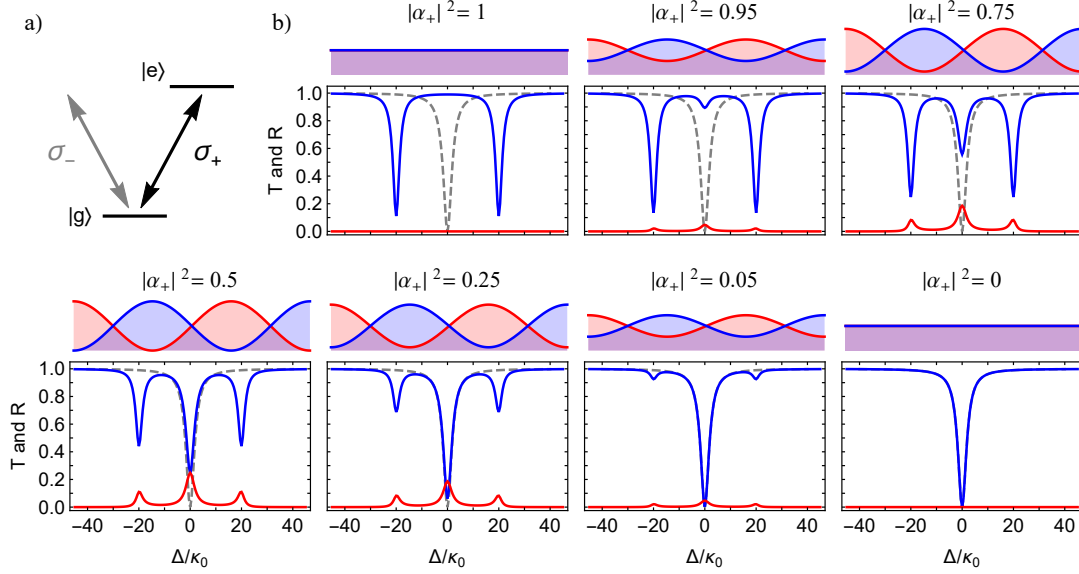


**Figure 4.5:** a) Same as Fig. 4.4 but for an effective two level atom, where only  $\sigma^+$ -polarized light couples to the atom. b) Transmission (blue) and reflection (red) through the waveguide coupled to the atom–resonator system, for different overlaps  $|\alpha_{\sigma^+}|^2$ . For comparison, the empty resonator spectrum is plotted as a dashed line. The small inset on top of each spectra represents the intensity modulation of two standing wave modes for the respective settings. All shown spectra were calculated using Eq. (4.31) and the same parameters as for Fig. 4.4.

mode with  $\sigma^-$ -polarized light is small, i.e.  $|\alpha_{\sigma^+}|^2 < 1$ , this part of the light does not interact with the atom, causing a small transmission dip emerging on resonance. At the same time, the depth of the resonances at  $\pm g$  decrease. The on-resonant transmission again reaches 0.25 for  $|\alpha_{\sigma^+}|^2 = 1/2$ . For  $|\alpha_{\sigma^+}|^2 = 0$ , the light does not couple to the atom any more and the spectrum resembles that of an empty resonator. In contrast to the previous model, the position of the resonance dips at  $\Delta = 0, \pm g$  is independent of  $|\alpha_{\sigma^+}|^2$  and only their depths change.

When we change the probing direction through the coupling fiber, we drive the other of the two counter-propagating WGMs. Due to SML in TM modes, two counter-propagating modes have different orthogonal circular polarization. In combination with a scatterer that only couples to one of these polarizations, this realizes a highly asymmetric transmission through the waveguide (cf. the first and the last panel in Fig. 4.5b). This effect has been employed to create nonreciprocal devices, such as optical diodes [125], and is also the key ingredient for the optical circulator which will be discussed in Ch. 7.

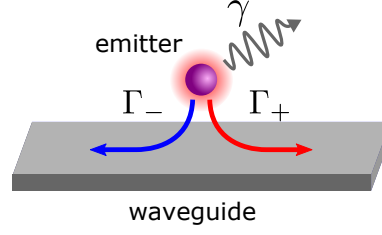


**Figure 4.6:** Schematic of a single emitter coupled to a single mode waveguide. The emitter decays into free space at rate  $\gamma$  and couples to the respective forward or backward propagating waveguide mode with  $\Gamma_+$  and  $\Gamma_-$ .

## 4.5 Chiral waveguides

In the last section, we saw that coupling a single atom to a WGM can give rise to a direction-dependent, i.e. chiral, interaction between light and matter. As a consequence, the transmission properties of the light sent through the coupling fiber depends on the probing direction. This can be understood in the context of chiral quantum optics using the simple model of a chiral waveguide that is coupled to a single emitter. In the following, we will introduce this model and briefly discuss the consequences of the chiral light–matter interaction. Furthermore, we show how the atom–resonator system can be described in this picture.

### 4.5.1 Emitter directly coupled to a waveguide

Let us consider a simple system which consists of a waveguide supporting a pair of counter-propagating modes and a single emitter placed in its vicinity (see Fig. 4.6). When the emitter is excited, it can lose its energy either into free space at a rate  $\gamma$  or into the forward (+) or backward (−) propagating waveguide mode, at rate  $\Gamma_{\pm}$ , respectively. The emission rates into the waveguide modes are governed by  $\Gamma_{\pm} \propto |\boldsymbol{\mu}^* \cdot \boldsymbol{\mathcal{E}}_{\pm}|^2$ , where  $\boldsymbol{\mathcal{E}}_{\pm}$  is the vector amplitude of the respective mode and  $\boldsymbol{\mu}$  is the complex dipole matrix element of the emitter. We have learned, that in the presence of transverse spin angular momentum, the local field vectors of the two counter-propagating modes can differ, i.e.  $\boldsymbol{\mathcal{E}}_+ \neq \boldsymbol{\mathcal{E}}_-$ . Thus, the corresponding emission rates are in general not symmetric,  $\Gamma_+ \neq \Gamma_-$ . For the general case, we can define the two directional coupling parameters

$$\beta_+ = \frac{\Gamma_+}{\Gamma_+ + \Gamma_- + \gamma}, \quad \beta_- = \frac{\Gamma_-}{\Gamma_+ + \Gamma_- + \gamma}, \quad (4.33)$$

which give the ratio of the emission probability into the ( $\pm$ ) waveguide mode  $\Gamma_{\pm}$  to the total emission rate, including the decay into free space  $\gamma$ . The two parameters can be combined to give the total coupling efficiency of the emitter into the waveguide,  $\beta = \beta_+ + \beta_-$ . Using the directional coupling parameters, the transmission and reflection amplitudes of light propagating in the forward (+) or backward (−) directions inside the waveguide, for the case where the light and the emitter are resonant, can be obtained from

$$t_{\pm} = 1 - 2\beta_{\pm}, \quad (4.34)$$



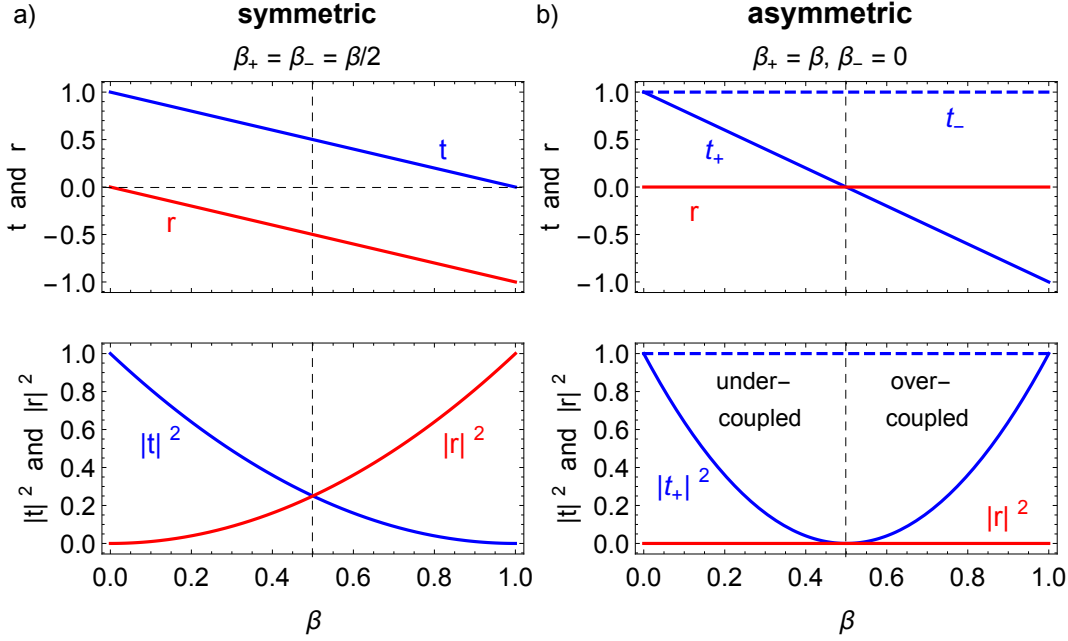


**Figure 4.7:** Transmitted and reflected amplitude (top) and power (bottom), normalized to the respective input, as a function of  $\beta$  for symmetric a) and fully asymmetric b) coupling to the waveguide. For the asymmetric graphs, the dashed line corresponds to the transmission for the backward probing.

$$r_{\pm} = -2\sqrt{\beta_{+}\beta_{-}}. \quad (4.35)$$

Using this simplified model, we can discuss most of the key features of chiral light–matter interaction. In Fig. 4.7 the transmission (reflection) amplitude and the power transmission (reflection) are plotted as a function of  $\beta$  for two special cases: symmetric coupling, i.e.  $\beta_{+} = \beta_{-}$ , and fully asymmetric coupling, i.e.  $\beta_{+} > 0$  and  $\beta_{-} = 0$ .

### Symmetric coupling

As long as  $\beta \ll 1$ , the emitter preferentially couples to non-guided modes. In this regime the scatterer mainly acts as a loss channel for the guided light (see Fig. 4.8a). As  $\beta$  increases, the transmission drops while an increasing fraction of the light is reflected. For  $\beta = 0.5$ , both transmission and reflection reach 0.25 of the incident power, while half the light will be dissipated into free space. When  $\beta > 0.5$ , the light couples very efficiently to the scatterer and is efficiently coupled back into the opposite direction of the waveguide. The transmission steadily decreases and the reflection increases until, for  $\beta = 1$ , the emitter becomes a perfect mirror, where all the light will be reflected, i.e.  $|r_{\pm}|^2 = 1$  and  $|t_{\pm}|^2 = 0$ , as indicated in Fig. 4.8e. Most importantly, the transmission and reflection is independent of the probing direction for all  $\beta$ .

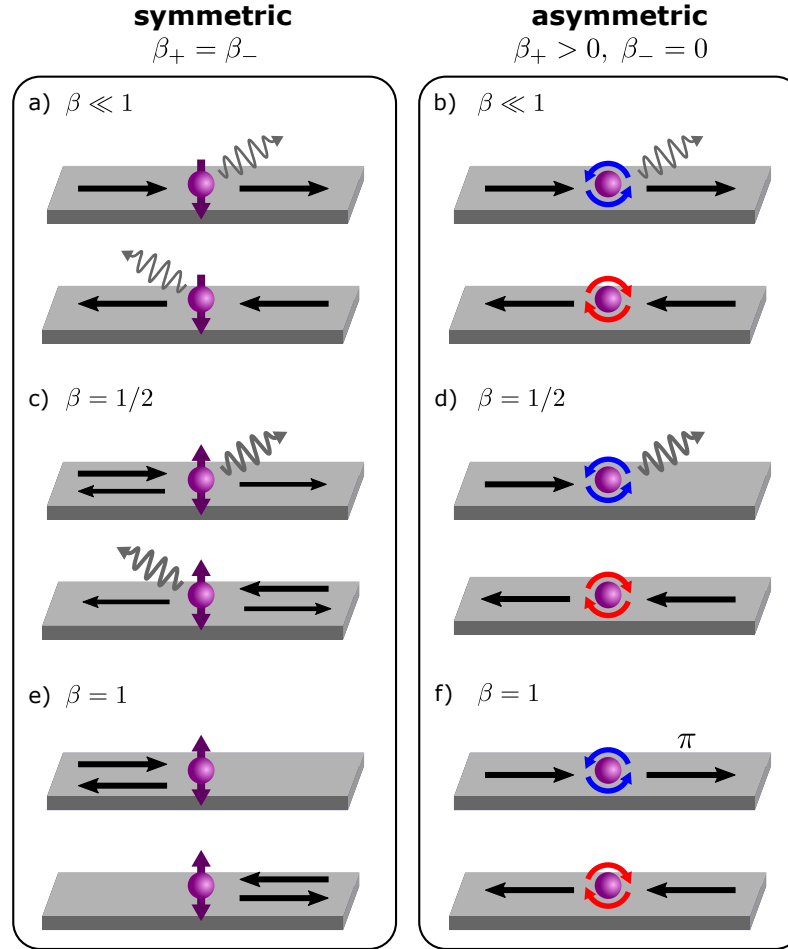


**Figure 4.8:** Resonant photon-emitter interaction for symmetric  $\beta_+ = \beta_-$  a,c,e) and fully asymmetric  $\beta_+ \gg \beta_-$  b,d,f) waveguide-emitter coupling.  $\beta \ll 1$ : a) For symmetric coupling, the light in the waveguide is only marginally influenced by the weak coupling to the scatterer. This introduces an additional loss channel to the waveguide, which is independent of the propagation direction. b) If  $\beta_+ > 0, \beta_- = 0$ , only one direction is affected by the presence of the scatterer, giving a small direction-dependent loss.  $\beta = 0.5$ : c) The symmetric waveguide reflects and transmits 25% of the incident light while 50% is scattered into free space. d) For the asymmetric case, all the light is dissipated by the scatterer when it is probed in forward direction. In backward direction, light is fully transmitted. This can be employed to realize an optical diode.  $\beta = 1$ : e) The scatterer acts as a perfect mirror, reflecting all light incident from one side. f) In both directions, the waveguide is perfectly transparent, but the scatterer imprints a phase of  $\pi$  onto the forward transmitted light. The purple, red and blue arrows indicate the local polarizations of the waveguide modes. For the asymmetric case, the local polarization depends on the propagation direction and the scatterer only couples to the polarization indicated by blue arrows.

### Fully asymmetric coupling

For the fully asymmetric case, i.e.  $\beta_- = 0$ , we obtain fully direction-dependent scattering properties of the emitter, meaning that it only interacts with light propagating in one direction. Consequently, the forward propagating light will be modified, i.e.  $t_+ \neq 1$ , while the backward propagating light is not altered and  $t_- = 1$ . In addition, the scatterer never reflects the incoming signal, i.e.  $r_{\pm} = 0$ . As we increase  $\beta$ , the forward transmission will decrease. For  $\beta = 0.5$ , the coupling rate to free space is equal to the coupling rates into the guided mode,  $\Gamma_+ = \gamma$ , and the forward transmission becomes zero. Since the light cannot be reflected, all the light is scattered out of the waveguide by the scatterer, which thus acts as a perfect absorber (see Fig. 4.8d). For  $\beta > 0.5$ , the transmission rises again with increasing  $\beta$  until the transmission reaches 1 for  $\beta = 1$ . However, for  $\beta > 0.5$ , the interaction with the scatterer imprints an additional phase of  $\pi$  onto the transmitted light compared to the uncoupled case.

We can summarize the previous results for the forward transmitted light by defining three coupling regimes between the waveguide and the emitter:

**Under-coupling:** As long as  $\beta_+ < 0.5$ , the coupling rate to the forward mode is smaller than the coupling rate to all modes, which include the decay into free space modes and the backward propagating mode,  $\Gamma_+ < \Gamma_- + \gamma$ . In this regime, the transmitted light is dominated by the light which did not couple to the scatterer. As  $\beta$  approaches 0.5, the forward transmission continuously decreases because a fraction of the light that interacted with the emitter destructively interferes with the forward propagating light in the waveguide.

**Critical coupling:** When  $\beta_+ = 0.5$ , the field from the emitter and the field propagating in the waveguide's forward direction have the same amplitude but opposite sign. Thus, they perfectly cancel and the transmission becomes zero. For the symmetric case, critical coupling can only be reached for the limit  $\beta = 1$ .

**Over-coupling:** This regime can only be reached for asymmetric coupling between the waveguide and the emitter. When  $\beta_+$  surpasses 0.5, the light is very efficiently coupled from the waveguide to the scatterer and back into the waveguide. Thus, the amplitude of light that interacted with the scatterer exceeds that of the light that stayed in the waveguide, yielding a finite transmission. However, the interaction with the scatterer introduced an additional phase of  $\pi$  compared to the transmitted light in the under-coupled case.

### 4.5.2 Resonator enhanced chiral waveguide

Realizing deterministic coupling between light guided in a waveguide and a single emitter, i.e.  $\beta > 0.5$ , is experimentally challenging. In our experiment, we make use of the enhanced interaction in optical resonators. Therefore, the light in the waveguide is first coupled into a resonator and the resonator field is interfaced with the emitter.

The interaction between the waveguide and WGMs resonator, with or without an atom coupled to it, can be described in the above framework of chiral waveguides. In contrast to the directly coupled emitter considered above, the resonator has two counter-propagating eigenmodes (CW,

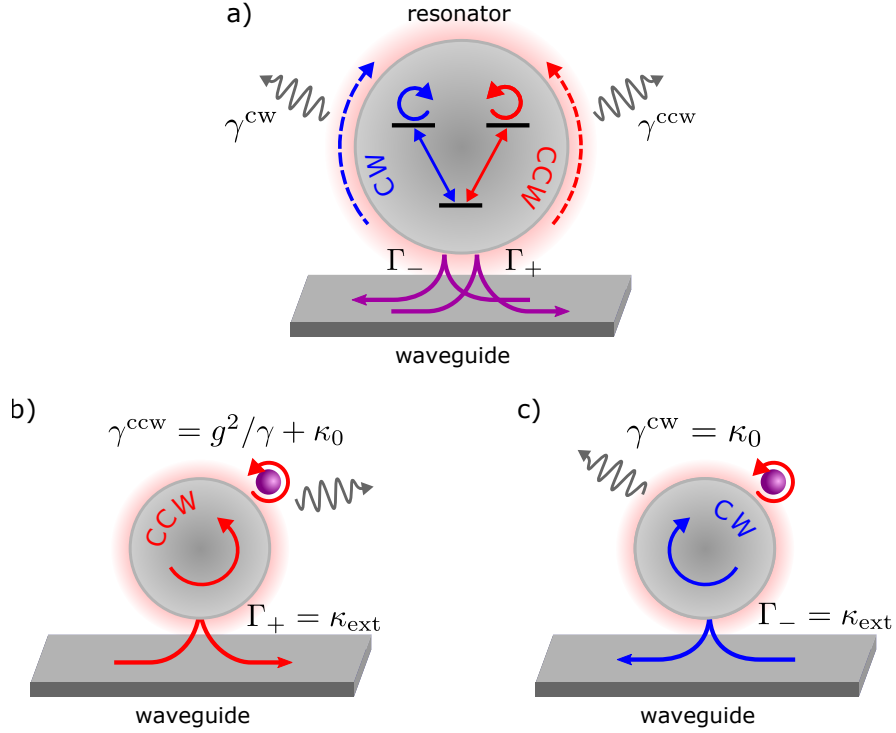


**Figure 4.9:** a) The coupling between the resonator and the waveguide can be understood as the coupling between the waveguide modes and a  $V$ -like atom. The two excited states correspond to light populating the clockwise (CW) or counter-clockwise (CCW) mode of the resonator. The coupling between waveguide modes and the resonator modes is described by the coupling rates  $\Gamma_{\pm}^{cw,ccw}$ . The resonator mode is subject to intrinsic losses which are described by  $\gamma^{cw,ccw}$ . For the case of an empty resonator, the CCW (CW) mode exclusively couples to the waveguide mode that propagates in positive (negative) direction, i.e.  $\Gamma_+^{ccw} = \Gamma_-^{cw} = \kappa_{ext}$  and  $\Gamma_+^{cw} = \Gamma_-^{ccw} = 0$ . In this case,  $\gamma^{cw,ccw}$  can be identified as the empty resonator loss rate  $\kappa_0$ . b) The presence of an atom that only couples to the CCW mode changes the total resonator losses to  $\gamma^{ccw} = g^2/\gamma + \kappa_0$  for light that propagates in the positive direction. c) Since the atom does not couple to the CW mode, the resonator losses and thus the transmission of the light propagating in negative direction is not altered by the atom.

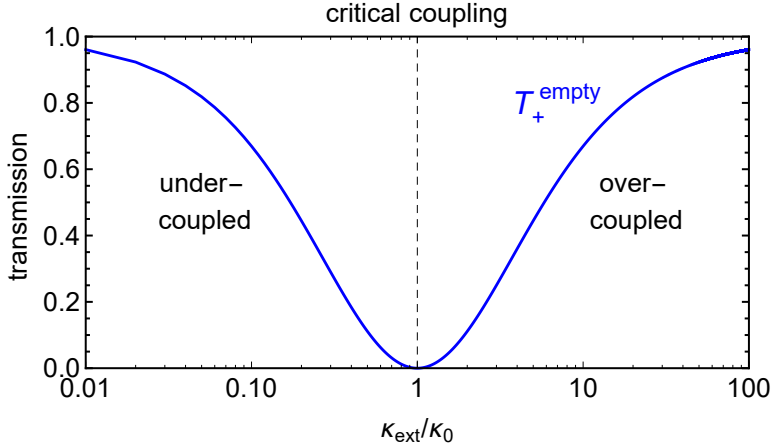


**Figure 4.10:** On-resonant transmission through the coupling fiber  $T_+ = |t_+|^2$  as a function of the coupling rate between the empty resonator and the coupling fiber,  $\kappa_{\text{ext}}$ .

CCW) that couple to the two waveguide modes that propagate in  $(+, -)$  direction (cf. Fig. 4.9a). Thus, we have to introduce a set of  $\beta_j^i$ , where  $i \in \{\text{CCW}, \text{CW}\}$  and  $j \in \{+, -\}$ , to fully characterize the coupling between the waveguide and the resonator. For example  $\beta_+^{\text{ccw}}$  relates the coupling rate between the forward  $(+)$  propagating waveguide mode and the CCW resonator mode to the total emission rate of this resonator mode. The resulting transmission amplitude in forward  $(+)$  and backward  $(-)$  probing direction are now given by<sup>3</sup>

$$t_{\pm} = 1 - 2\beta_{\pm} = 1 - 2(\beta_{\pm}^{\text{ccw}} + \beta_{\pm}^{\text{cw}}). \quad (4.36)$$

The reflection amplitude does not depend on the probing direction and can be calculated using

$$r_{\pm} = -\sqrt{\beta_+^{\text{ccw}} \beta_-^{\text{ccw}}} - \sqrt{\beta_+^{\text{cw}} \beta_-^{\text{cw}}}. \quad (4.37)$$

### Empty resonator

In order to understand the origin of these  $\beta$ -factors, let us first consider the case where no scatterer is coupled to the resonator modes ( $g = 0$ ). The resonator can be interpreted as a V-type emitter, where the excited states correspond to having a photon in the CCW or CW mode, as illustrated in Fig. 4.9. For the empty resonator, each of the two transitions only couples to one of the two propagation directions of the waveguide mode. If the resonator has been excited from one propagation direction, it can only decay into the waveguide mode that propagates in the same direction. Thus for the empty resonator, each probing direction is perfectly asymmetric. The corresponding  $\beta$ -factors are

$$\beta_+^{\text{ccw}}|_{g=0} = \beta_-^{\text{cw}}|_{g=0} = \frac{\kappa_{\text{ext}}}{\kappa_0 + \kappa_{\text{ext}}}, \quad (4.38)$$

<sup>3</sup>Note that  $\beta_{\pm}$  are defined for the coupling between the  $(\pm)$  waveguide mode and the resonator, which consists of two independent modes. Thus, it makes no sense to define a total coupling rate  $\beta = \beta_+ + \beta_-$  as was done for the chiral waveguide.

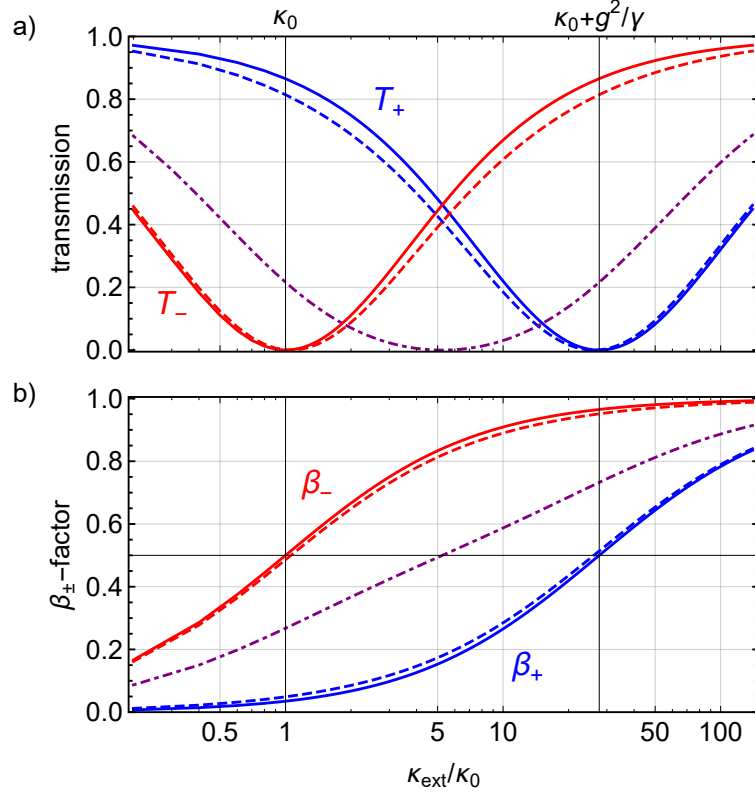


**Figure 4.11:** a) On-resonant forward,  $T_+ = |t_+|^2$ , and backward,  $T_- = |t_-|^2$ , transmission through the coupling fiber in the presence of an atom as a function of the coupling rate between the resonator and the coupling fiber, in units of the intrinsic resonator loss rate  $\kappa_0$ , for different resonator field configurations. For perfect chiral coupling, i.e.  $|\alpha_{\sigma+}|^2 = 1$ , the resonator is critically coupled,  $T_{\pm} = 0$ , at  $\kappa_{\text{ext}} = \kappa_0 + g^2/\gamma$  and  $\kappa_{\text{ext}} = \kappa_0$ , respectively (solid lines). For  $|\alpha_{\sigma+}|^2 = 0.5$ , the transmission is independent of the probing direction, i.e.  $T_+ = T_-$  (dash-dotted line). b) Total  $\beta$ -factor for forward and backward probing, i.e.  $\beta_{\pm} = \beta_{\pm}^{\text{ccw}} + \beta_{\pm}^{\text{cw}}$ , as a function of the coupling rate between the resonator and the coupling fiber  $\kappa_{\text{ext}}$ , for different polarization overlaps  $|\alpha_{\sigma+}|^2$ . Critically coupling requires  $\beta_{\pm} = 0.5$ , which can be easily verified by comparing a) and b). In both graphs, the solid lines correspond to  $|\alpha_{\sigma+}|^2 = 1$ , the dashed lines to  $|\alpha_{\sigma+}|^2 = 0.97$  and the dash-dotted lines to  $|\alpha_{\sigma+}|^2 = 0.5$  and the following parameters were used:  $(g, \gamma, \kappa_0) = 2\pi \times (20, 3, 5)$  MHz. For  $|\alpha_{\sigma+}|^2 < 0.5$ , the transmission and  $\beta$ -factors become the curves obtained for the opposite probing direction, i.e.  $T_-(|\alpha_{\sigma+}|^2) = T_+(1 - |\alpha_{\sigma+}|^2)$  and  $\beta_-(|\alpha_{\sigma+}|^2) = \beta_+(1 - |\alpha_{\sigma+}|^2)$ .

$$\beta_-^{\text{ccw}}|_{g=0} = \beta_+^{\text{cw}}|_{g=0} = 0. \quad (4.39)$$

with the direction independent transmission amplitude

$$t_{\pm}|_{g=0} = \frac{\kappa_0 - \kappa_{\text{ext}}}{\kappa_0 + \kappa_{\text{ext}}} = \frac{\gamma^{\text{ccw,cw}} - \Gamma_{\pm}}{\gamma^{\text{ccw,cw}} + \Gamma_{\pm}}. \quad (4.40)$$

In the last step of Eq. (4.40), we have identified the competing intrinsic resonator loss rate of the empty resonator mode,  $\gamma^{\text{ccw,cw}} = \kappa_0$ , and the waveguide–resonator coupling rate,  $\Gamma_{\pm} = \kappa_{\text{ext}}$ . From this equation it also becomes evident that we are able to over-couple the empty resonator if  $\kappa_{\text{ext}} > \kappa_0$ . However, the transmission past the empty resonator is independent of the probing direction. Since the two modes of the resonator do not couple, the reflection amplitude is always zero,  $r_{\pm}|_{g=0} = 0$ .

The power transmission,  $T = |t|^2$ , as a function of  $\kappa_{\text{ext}}$  is shown in Fig. 4.10. Similar to the case of the chiral waveguide, we can assign three different coupling regimes: The under-coupled regime, for which the internal resonator losses are larger than the resonator–waveguide coupling. If  $\kappa_{\text{ext}} = \kappa_0$ , the transmission drops to zero, which is called critical coupling. And, finally, when the coupling the waveguide becomes the dominate rate, i.e.  $\kappa_{\text{ext}} > \kappa_0$ , we speak of an over-coupled resonator (cf. Sec. 4.5).

### Coupled atom-resonator system for perfect chirality

Let us now consider the case where an atom is coupled to the resonator field. We assume a two-level atom that has only a  $\sigma^+$ -polarized transition (cf. Sec. 4.4.2). Furthermore, we assume that the resonator modes exhibit perfect circular polarization, i.e.  $|\alpha_{\sigma^+}|^2 = |\alpha_{\beta^-}|^2 = 1$ . Thus, the atom exclusively couples to the CCW mode. As a consequence, we obtain two different loss rates for the two counter-propagating resonator modes

$$\gamma^{\text{cw}} = \kappa_0 \quad \text{and} \quad \gamma^{\text{ccw}} = \frac{g^2}{\gamma} + \kappa_0, \quad (4.41)$$

while the waveguide coupling rate for the two probing directions is unaltered,  $\Gamma_{\pm} = \kappa_{\text{ext}}$ . For this case, the  $\beta$ -factors are

$$\beta_+^{\text{ccw}}|_{|\alpha|^2=1} = \frac{\kappa_{\text{ext}}}{g^2/\gamma + \kappa_0 + \kappa_{\text{ext}}} \quad (4.42)$$

$$\beta_-^{\text{cw}}|_{|\alpha|^2=1} = \frac{\kappa_{\text{ext}}}{\kappa_0 + \kappa_{\text{ext}}}, \quad (4.43)$$

$$\beta_+^{\text{cw}}|_{|\alpha|^2=1} = \beta_-^{\text{ccw}}|_{|\alpha|^2=1} = 0. \quad (4.44)$$

The on-resonant transmission amplitudes in forward and backward direction are

$$t_-|_{|\alpha|^2=1} = \frac{\gamma^{\text{cw}} - \Gamma_-}{\gamma^{\text{cw}} + \Gamma_-} = \frac{\kappa_0 - \kappa_{\text{ext}}}{\kappa_0 + \kappa_{\text{ext}}} \quad (4.45)$$

$$t_+|_{|\alpha|^2=1} = \frac{\gamma^{\text{ccw}} - \Gamma_+}{\gamma^{\text{ccw}} + \Gamma_+} = \frac{\kappa_0 + g^2/\gamma - \kappa_{\text{ext}}}{\kappa_0 + g^2/\gamma + \kappa_{\text{ext}}}. \quad (4.46)$$

For the backward probing direction we recover the empty resonator. In forward direction, the presence of the atom introduces additional resonator losses. Those are given by the atom's steady

state excited state population per intra-resonator photon, i.e.  $\rho_{ee}/n_{\text{res}} = g^2/\gamma^2$  (cf. Sec. 4.2), multiplied by its decay rate  $\gamma$ . The additional resonator losses shift the critical coupling point to higher  $\kappa_{\text{ext}}$ , more specifically to  $\kappa_{\text{ext}} = \kappa_0 + g^2/\gamma$ . Thus, the interaction with the atom, can place a formally critically or over-coupled resonator into a different coupling regime. As the atom only interacts with one of the two counter-propagating resonator modes, this yields a direction-dependent, i.e. chiral, transmission. In contrast to the toy model of a chiral waveguide, where a direction-dependent waveguide–emitter coupling is realized, in WGMs the direction-dependent transmission stems from the modified resonator losses. Note that  $\beta_{\pm}$  were defined via the transmission and reflection amplitudes of the waveguide. Thus, these quantities do not directly provide information of the directional coupling of the atom into the waveguide. For the case of perfect chiral coupling, the fraction of the atomic emission into the resonator mode compared to the free-space emission is

$$\frac{g^2}{g^2 + \gamma(\kappa_0 + \kappa_{\text{ext}})} = \frac{C}{C + 1}, \quad (4.47)$$

where we used the cooperativity  $C = g^2/\gamma(\kappa_0 + \kappa_{\text{ext}})$ . Furthermore, in the fast cavity regime the fraction of photons emitted into the CCW resonator mode and then coupled out into the forward propagating waveguide mode is [10]

$$\frac{\kappa_{\text{ext}}}{\kappa_0 + \kappa_{\text{ext}}} \frac{g^2}{g^2 + \gamma(\kappa_0 + \kappa_{\text{ext}})} = \frac{\kappa_{\text{ext}}}{\kappa_0 + \kappa_{\text{ext}}} \frac{C}{C + 1}. \quad (4.48)$$

Since the atomic dipole has no overlap with the CW mode, no photons are coupled into the backward propagating waveguide mode.

### Coupled atom–resonator system for imperfect chirality

In our experimental system, we do not encounter perfect chiral coupling. This stems from imperfect circular polarization of the resonator modes, i.e.  $|\alpha_{\sigma+}|^2 \neq 1$ . As a consequence, the emitter couples the two counter-propagating modes. For this general case, the corresponding  $\beta$ -factors can be obtained from inserting Eqs. (4.31-4.32) into Eqs. (4.26-4.28) and comparing them with Eqs. (4.36-4.37), and are given by

$$\beta_{+}^{\text{ccw}} = \frac{\kappa_{\text{ext}}}{\kappa_0 + \kappa_{\text{ext}}} \frac{C|\beta_{\sigma+}|^2 + 1 + \chi(|\beta_{\sigma+}|^2)}{2(C + 1)}, \quad (4.49)$$

$$\beta_{-}^{\text{cw}} = \frac{\kappa_{\text{ext}}}{\kappa_0 + \kappa_{\text{ext}}} \frac{C|\alpha_{\sigma+}|^2 + 1 + \chi(|\alpha_{\sigma+}|^2)}{2(C + 1)}, \quad (4.50)$$

$$\beta_{+}^{\text{cw}} = \frac{\kappa_{\text{ext}}}{\kappa_0 + \kappa_{\text{ext}}} \frac{C|\beta_{\sigma+}|^2 + 1 - \chi(|\beta_{\sigma+}|^2)}{2(C + 1)}, \quad (4.51)$$

$$\beta_{-}^{\text{ccw}} = \frac{\kappa_{\text{ext}}}{\kappa_0 + \kappa_{\text{ext}}} \frac{C|\alpha_{\sigma+}|^2 + 1 - \chi(|\alpha_{\sigma+}|^2)}{2(C + 1)}, \quad (4.52)$$

where we have used  $\chi(x) = \sqrt{C^2(2x^2 - x) + 2Cx^2 + 1}$  and  $|\beta_{\sigma+}|^2 = 1 - |\alpha_{\sigma+}|^2$  for clarity. For the total  $\beta_{\pm}$  in forward and backward propagation direction we obtain a more compact



expression

$$\beta_+ = \beta_+^{\text{cw}} + \beta_+^{\text{ccw}} = \frac{\kappa_{\text{ext}}}{\kappa_0 + \kappa_{\text{ext}}} \frac{C|\beta_{\sigma^+}|^2 + 1}{C + 1}, \quad (4.53)$$

$$\beta_- = \beta_-^{\text{cw}} + \beta_-^{\text{ccw}} = \frac{\kappa_{\text{ext}}}{\kappa_0 + \kappa_{\text{ext}}} \frac{C|\alpha_{\sigma^+}|^2 + 1}{C + 1}. \quad (4.54)$$

The corresponding modified resonator loss rates and resonator–waveguide coupling rates can be found in App. A.3.

The on-resonance transmission in forward (+) and backward (–) direction as a function of  $\kappa_{\text{ext}}$  is shown for different polarization overlaps in Fig. 4.11a. The imperfect polarization overlap reduces the effective coupling between the atom and the resonator, thus shifting the critical coupling point for the forward transmission toward smaller coupling. Contrarily, for backward probing direction, the local polarization has a finite overlap with the atomic dipole which results in a residual coupling between the atom and the resonator field. This modifies the transmission and the critical coupling point is shifted toward higher  $\kappa_{\text{ext}}$ . When using the overlap that we have obtained for our bottle microresonator,  $|\alpha_{\sigma^+}|^2 = 0.97$  and  $|\alpha_{\sigma^-}|^2 = 0.03$ , we see that the obtained transmissions are only slightly different from the perfect chiral case. In addition, in Fig. 4.11b we plot  $\beta_{\pm}$  as a function of  $\kappa_{\text{ext}}$ , for our system parameters  $(g, \gamma, \kappa_0) = 2\pi \times (20, 3, 5)$  MHz. The difference between  $\beta_-$  and  $\beta_+$  is maximal for moderate over-coupling of  $\kappa_{\text{ext}}/\kappa_0 \approx 5.3$ , which can easily be achieved in our experiment, and we obtain 0.82 and 0.18 for  $\beta_-$  and  $\beta_+$ , respectively.

In this chapter, we have presented a model to quantum mechanically treat the interaction between light and matter, using the master equation approach to account for the coupling of the system to the environment. This model was then extended to accurately describe the situation we encounter in our experiment, where a single atom couples to the modes of a WGM resonator. In addition, we derived a simplified analytic solution, which still describes our experiments very precisely. We also showed that the direction-dependence of the atom–light interaction can be understood in the context of chiral waveguides, where our system can be interpreted as an emitter that is chirally coupled to a single mode of a waveguide.



# Experimental apparatus

In this chapter our experimental apparatus will be described. Most of the design and construction was carried out before I joined the experiment. The discussion in this chapter gives the reader an overview in order to follow the experimental procedures and understand the basic functionalities of the setup. For further explanations and deeper insights, I refer to the previous theses conducted on this very experiment [86, 87, 92, 126–128].

This chapter is organized in the following manner. First, we briefly introduce general design considerations which are essential for realizing strong light–matter interaction using single atoms and a bottle microresonator (BMR). Then, the most relevant details for fabricating and employing a BMR in a cavity quantum electrodynamics (CQED) experiment are summarized. This is followed by a short introduction to the experimental setup and the most important experimental procedures.

## 5.1 General design consideration

The experiment is designed to investigate light–matter interaction at its fundamental limit of single photons and single quantum emitters. The key element is the BMR, which confines the light in an extremely small mode volume  $V$  and has an extremely high  $Q$ -factor, such that a single emitter in its vicinity is strongly coupled to single photons circulating inside the resonator. As a quantum emitter single rubidium atoms were chosen. These are hydrogen-like atoms which are well studied and can be controlled and manipulated very precisely using optical and magnetic methods. In order to avoid perturbations from background gas the experimental system is placed inside an ultra high vacuum (UHV) chamber. To increase the interaction time between the atom and the light, we employ laser cooled atoms. The cooling is done by means of a magneto-optical trap (MOT), followed by an optical molasses cooling stage. To avoid pollution of the resonator by atoms from the background gas required for the MOT, a two-chamber design was chosen, where the MOT is located in one and the BMR in the other chamber. To transfer the atoms from the MOT to the resonator an atomic fountain is used, which is adjusted such that the turning

point of the center-of-mass of the atomic cloud is at the position of the resonator. During the time where the cloud is in the vicinity of the resonator, several atoms come close enough to strongly couple to the resonator field. However, these atom transits last only for approximately 1-3  $\mu\text{s}$ , and happen non-deterministically. In order to perform measurements while the atoms are strongly coupled, their presence has to be detected in real-time. The short interaction times also prevent us from directly scanning the properties, such as the frequency of the interrogation light field to obtain a spectrum of the atom-resonator system in a single experimental run. Thus, we have to employ two laser fields, one for detecting the atoms and one for probing the coupled system, whose properties have to be prepared in advance. Due to the short interaction times, we have to alternate between the laser beams on the time scale of a few tens of nanoseconds. In our experiment, this is achieved using electro-optical modulator (EOM)-controlled Mach-Zehnder (MZ) modulators as fast switches and a field programmable gate array (FPGA)-based real-time detection.

Due to the high quality of our resonator, the modes we are working with have linewidths that are comparable with that of the atomic transition. Since the resonance is subject to drifts, a frequency lock is necessary to keep the mode resonant with the atom. For that purpose, we send a locking laser beam first through an EOM that modulates two frequency sidebands onto the light, and then through the coupling fiber. The transmitted signal is monitored using a fast, high gain avalanche photo diode (APD). A software-based Pound-Drever-Hall (PDH) locking scheme is then employed to obtain an error signal for locking the resonator frequency. In order to keep the noise level of the frequency lock low, this lock requires relatively high optical powers ( $\sim 100$  nW). However, for the investigation of light-matter interaction we have to work on the level of single photons, and therefore require even lower optical powers ( $\sim 10$  pW corresponding to a photon flux of  $\sim$  MHz), which are then recorded using single photon counting modules (SPCMs). To protect the detectors from the light which is used for frequency locking, a microelectromechanical (MEM)-switch directs the light transmitted through the coupling fiber between the SPCMs and the APD and the resonator frequency lock is put on hold during the actual measurement. Since we only need small amounts of light at almost the same frequency, all optical beams for the interrogation of the atom-resonator system (not including the MOT-system) originate from a single diode laser.

## 5.2 Experimental implementation of a BMR

In the following, we will review some important properties of BMRs which render them highly advantageous for CQED experiments.

### 5.2.1 Fabrication of high- $Q$ BMRs

There are various ways of fabricating whispering-gallery-mode (WGM) microresonators. The essential ingredients for producing high- $Q$  resonators are to use a low-absorption dielectric, and to make its surface as smooth as possible, in order to avoid scattering losses. The highest achieved values of  $Q$  are realized using macroscopic crystalline WGM resonators, made of e.g.

CaF<sub>2</sub>. Using such resonators with a large diameter of 0.5 mm,  $Q \sim 10^{11}$  were achieved [73]. However, for CQED applications the requirement of sufficiently small mode volume, more precisely a large ratio  $Q/V$ , demands micron-sized resonators. The first WGM microresonators were silica microspheres. Those are usually produced by melting a glass rod with a flame or a laser. The molten glass then forms a droplet due to surface tension. Using this procedure, resonators soon reached  $Q \sim 10^9$ - $10^{10}$  for resonator diameters between 100-800  $\mu\text{m}$  [129, 130]. With the objective to further decrease the mode volume and to make the fabrication compatible with chip-based semiconductor processing methods, micro-toroid resonators were devised. Those were developed from microdisc resonators, which are commonly fabricated using a combination of lithography and dry etching. Due to etch-related blemishes their Q-factor usually does not exceed  $Q \sim 10^5$  [131]. For microtoroidal resonators, the microdiscs are further processed in additional reflow steps. By heating the disc, the surface tension smooths the surface and collapses the silica disc to a toroidal shape. This process enables the realization of resonators that reach  $Q \sim 10^8$  [20, 132]. Moreover, new fabrication processes including chemical etching enabled  $Q \sim 10^9$  in wedge-resonators on a silicon chip, which do not require a reflow process [133].

Compared to the multistep fabrication of micro toroids, the process of making a high  $Q$  BMR is relatively straightforward. The bottle resonator for the CQED experiment is fabricated with a fiber pulling rig using a heat-and-pull process [62]. The initial resonator fiber (PWF 200 T, Ceramoptik) has a diameter of 500  $\mu\text{m}$  with a 200  $\mu\text{m}$  core and is tapered down to 36  $\mu\text{m}$  over a length of 6 mm. For microstructuring, the taper is heated locally using a focused CO<sub>2</sub>-laser and pulled again to obtain two microtapers. This step causes the characteristic bottle shape shown in Fig. 3.1b. The characteristic curvature of the bottle resonator used in the experiment is  $0.014 \mu\text{m}^{-1}$  for a central diameter of 36  $\mu\text{m}$ . Since the resonator surface is inherently smoothed by surface-tension during the heat-and-pull process, no additional reflow step is required. With this production technique modes with  $Q \sim 4 \times 10^8$  have been demonstrated [76]. For the resonator mounted in our experiment we observe modes with  $Q$  as high as  $4 \times 10^7$ , corresponding to an intrinsic field decay rate of  $\kappa_0 \approx 2\pi \times 5 \text{ MHz}$ .

### 5.2.2 Evanescent coupling of WGMs with tapered optical fibers

The fact that a resonator structure sustains high- $Q$  modes, implies that these modes are extremely well decoupled from their environment. But if we want to make use of the strong field enhancement we also have to be able to interface the mode and couple light into and out of the resonator in an efficient manner. For WGM resonators, free space coupling turned out to be very inefficient [134]. Several approaches to increase the coupling efficiency using nanoparticles have been introduced [135]. In order to feed and probe the resonator field with high efficiency, light is usually coupled in and out of the resonator by frustrated total internal reflection. This is achieved by overlapping the evanescent field of the resonator with the evanescent field of a coupling device. Depending on their application, experiments commonly use dielectric prisms [136], side-polished fibers [137] or tapered optical fibers or waveguides [138]. When using tapered optical fibers for this purpose, the coupling can be performed with close to 100% efficiency [138], thereby exceeding the coupling efficiencies of all other types of optical microresonators, where the coupling through the cavity mirrors inevitably is accompanied by losses.

The coupling efficiency between resonator modes and coupler modes is determined by the spatial overlap of the fields, by the resonance condition of the resonator and by the wave vector distribution of the mode in the resonator and the coupler. The latter corresponds to a phase-matching condition which has to be fulfilled to enable constructive interference between the fields of the coupler and the resonator at the coupling junction [139].

In our experiment, two coupling fibers are mounted inside the vacuum chamber. Both fibers are produced from a standard optical single-mode glass fiber (F-SF, Newport) and are tapered down to a minimal diameter of 500 nm. In order to fulfill the phase-matching condition, the minimum-diameter section of the fibers is not exactly at the position of the resonator, but rather shifted such that the resonator is coupled to a region of intermediate diameter. The transmission of both ultra-thin fibers including the taper-transitions in the setup has been measured to be larger than 95% [86].

Due to the evanescent coupling, the rate at which the light couples into and out of the resonator can be adjusted by changing the mode overlap. Mounting the coupling fibers on nano-positioning stages allows us to freely adjust the coupling rate  $\kappa_{\text{ext}}$ . This is not possible for most Fabry-Pérot (FP) resonators, where  $\kappa_{\text{ext}}$  is a parameter which is fixed by design and fabrication. Depending on the mode which is used a stable coupling from the under-coupled far into the over-coupled regime can be achieved. This will be used extensively for the measurements reported in chapter 6 and 7. In particular, the capability of the setup to interface the resonator with two fibers synchronously will be essential for the experiments performed in Ch. 7.

### 5.2.3 Mode–mode coupling

Due to the rotational symmetry of WGM resonators, light can propagate clockwise (CW) or counter-clockwise (CCW). Therefore, WGM microresonators support pairs of degenerated modes, which counter-propagate inside the resonator. Whether the CW or CCW rotating mode is excited from a waveguide depends on the direction of propagation of the light inside the waveguide. In an ideal WGM resonator, the two modes are uncoupled and do not interact with each other. However, Rayleigh scattering at imperfections of the surface or in the bulk material can inverse the propagation direction of light in one mode and redirect it to the other [140]. The mode–mode coupling is usually characterized by the rate  $h$ . The coupling between the two running waves lifts the degeneracy of the standing wave eigenmodes and yields a splitting of their resonance frequency by  $\pm h$ . When the mode–mode coupling dominates the resonator loss rates,  $h > (\kappa_0, \kappa_{\text{ext}})$ , it can be observed as a splitting in the resonator spectrum. In addition, the scattering into the counter-propagating mode will give rise to a reflection signal, i.e light propagating in the opposite direction through the coupling fiber with respect to the probing direction. While the transmission through the coupling fiber which is coupled to the empty resonator has to be symmetric with respect to the probing direction, there can be an asymmetry in the reflection due to interference between scattered light from several scatterers [141, 142].

While mode–mode coupling is strongly pronounced and significantly reduces the resonator performance for microspheres or toroids, it seems negligible for most modes formed in the BMR, in particular transverse magnetic (TM)-modes. This can be explained by the fact that the prolate shape gives rise to a small polarization overlap of counter-propagating modes compared to res-

onator types with larger curvature. For the modes which we use for the following experiments, the mode–mode coupling rates are listed in Tab. 5.1.

#### 5.2.4 Frequency tuning

In order to realize strong coupling between the atoms and the light it is essential to align the frequency of both the probing light and the resonator with the atomic transition frequency. For the laser light this can straight forwardly be achieved by locking the laser on the desired atomic transition (cf. Sec. 5.4.2). To stabilize the frequency of the resonator to the same frequency one has to be able to tune its resonance frequency in a controlled manner. For FP resonators, this frequency tuning can be achieved by changing the distance between the two mirrors, which usually is done by mounting one mirror on a piezo element. However, for WGM resonators it is less straight forward. The first attempts to tune the frequency were done by heating the resonator. The thermal modification of the refractive index of the resonator’s material gives rise to a shift of the resonance frequency. As heat source electric heaters [143] or external lasers [144] can be used. Another possibility is to exert strain on the resonator using a piezo element which is either connected to two bars which are attached to the resonator structure [145] or, as possible for bottle microresonators, to directly use the two end of the resonator fiber [146, 147]. The latter approach is also used in our experiment. The strain will affect the resonator’s refractive index  $n$  and diameter  $D$  and thus causes a fractional change in the resonator’s eigenfrequency

$$\frac{\Delta\nu}{\nu_0} = \frac{-\Delta n}{n} - \frac{\Delta D}{D} . \quad (5.1)$$

This enables us to tune the resonance frequency of the bottle resonator over a range of several hundred GHz [146]. In our experiment the linewidth of the resonator and the atomic linewidth are comparable. Thus, in order to allow continuous operation, an active frequency stabilization is required. As explained in Sec. 5.4.2, this is achieved using a Pound–Drever–Hall (PDH) resonator frequency stabilization, which acts on the tuning piezo elements.

#### 5.2.5 Characterization of the modes used in the CQED experiment

In order to obtain a spectrum that spans several free spectral ranges (FSRs) of the resonator installed in our experiment, we employ an external cavity diode laser (Velocity, New Focus), which allows us to scan its output wavelength mode-hop-free over a range of up to 16 nm centered around 845 nm. In order to measure the spectrum of the resonator, coupling fiber  $A$  (cf. Fig. 5.5) is aligned approximately at the center of the mode structure of the bottle resonator and the laser frequency is scanned over 10 nm and the transmission signal through the fiber is detected with an APD. The signal from this scan is shown in Fig. 5.1a and the obtained FSR is in good agreement with the expected numbers obtained from Eq. (3.16) using a radius  $R \sim 18 \mu\text{m}$ . Determining the radial, azimuthal and axial quantum numbers  $p$ ,  $m$  and  $q$  of a certain mode is challenging, since these parameters cannot be obtained exclusively from the spectrum. In particular, it is practically impossible to directly determine the radial quantum number  $p$  of a mode experimentally since the characteristic radial intensity distribution is formed inside the

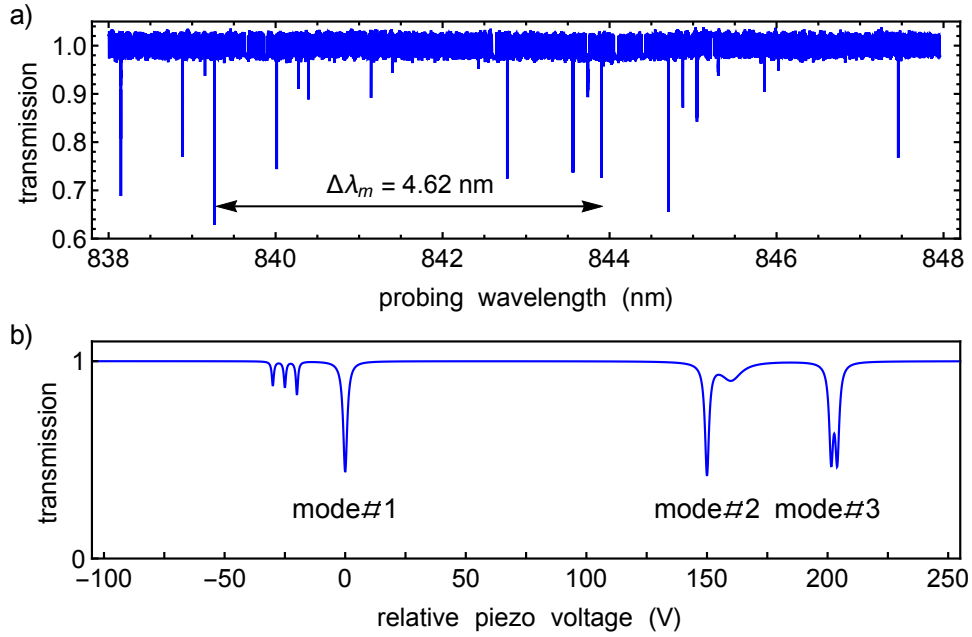


**Figure 5.1:** a) Spectrum of the bottle resonator used in the CQED experiment. To obtain this spectrum a tunable laser was scanned over 10 nm while the fiber transmission was recorded. A repeating mode pattern can be identified, with a separation of  $\Delta\lambda_m=4.62 \text{ nm}$  or  $\Delta\nu_m= 1.96 \text{ THz}$ , which is in good agreement with Eq. (3.16). b) In a typical experiment, the laser frequency is kept fixed at the atomic resonance and the resonance frequency of the resonator is tuned to the desired frequency by pulling at the end of its fiber with a piezo. When scanning the piezo offset voltage over a wide range, when the polarization is aligned with the TM eigenpolarization, three prominent modes appear, as schematically shown here. These three modes have a fixed distance of approximately  $\sim 150 \text{ V}$  and  $\sim 50 \text{ V}$  respectively.

resonator. However, all experiments are performed with the bottle modes that first become visible in the fiber spectrum when approaching the resonator with the coupling fiber. Since modes with smaller  $p$  have smaller mode volume it is reasonable that these modes have the lowest radial order, i.e.  $p \approx 0$ . Using this assumption, the azimuthal quantum number  $m$  can be estimated by taking into account the resonator diameter and the resonance wavelength, which yields  $m \approx 200$ . In principle, the axial mode structure can be observed from outside the resonator via the light that is scattered into free space, especially when using erbium doped resonators [76]. However, the resonator used in the experiment is made out of pure silica, to avoid any unnecessary reduction of the  $Q$ -factor. Furthermore, only limited optical access is provided, which makes it impossible to observe a clear mode structure from scattered light. Another possibility to determine  $q$  is to scan the axial mode profile using the coupling fiber as a probe. The axial mode number  $q$  can then be inferred from the axial modulation of the resonator–fiber coupling rate. However, in our



mode	$\kappa_0/2\pi$ (MHz)	$h/2\pi$ (MHz)	$\bar{g}/2\pi$ (MHz)	$\bar{\sigma}_g/2\pi$ (MHz)	q
#1	4.5	<1	19.8	9.7	1<q<4
#2	6	<1	16.6	6.1	1<q<5
#3	5	6.8	28.7	11.6	q<3

**Table 5.1:** Summary of the characteristic parameters obtained for the three most frequently used resonator modes.

experiment this approach is difficult since the axial extension of the bottle modes exceeds the vertical scan range of the piezo actuator in the nano-positioning stages. For this reason, one has to make use of the slip-stick mode of the positioning stages which, however, results in unpredictable jumps of the fiber position. Furthermore, the translation stages of the coupling fibers are not perfectly aligned with the resonator fiber. This makes continuous scans very difficult to perform and the result of such a scan is not very reliable. Thus, only an estimate of  $q$  can be obtained from such scans, which is included in Tab. 5.1.

While for the long transmission scan shown in Fig. 5.1a a tunable laser was used, for usual experiments we have to work at a fixed frequency corresponding to the transition frequency of the atom. For this purpose a offset voltage is applied to the piezo pulling at the end of the resonator fiber. When scanning the piezo between 0 and 1 kV we obtain a mode spectrum which is schematically shown in Fig. 5.1b. The voltage offsets might vary slightly for different temperature settings. From this spectrum, we choose one of the three modes depicted in Fig. 5.1b for our experiments. These modes distinguish themselves from other modes by a very narrow linewidth and the fact that they can be over-coupled very well. Historically, the modes are numbered #1-3. For all three modes we managed to strongly couple single atoms to the resonator field. From a fit to the spectra which are shown in Fig. 5.2, we can obtain an estimation of the coupling strength between the resonator and the atom. These values, together with other resonator parameters are summarized in the Tab. 5.1. It should be noted, that the obtained coupling strengths depend on the experimental settings and the data analysis (cf. Sec. 5.4.7). Thus, the coupling strengths and their distribution might vary for different experiments even though the same modes are used.

We can compare the coupling strength  $g$  obtained from fitting the Rabi spectra with the expectation from the field distribution we have derived in Sec. 3.4. Figure 5.3 shows  $g$  as a function of the distance from the resonator surface calculated for TM polarized modes coupled to the cycling transition of the D2-line of a  $^{85}\text{Rb}$  atom. As expected, the coupling strength is highest for the fundamental mode reaching  $g_{q=0}^s = 2\pi \times 56$  MHz at the surface, while the axial mode with  $q = 3$  reaches up to  $g_{q=3}^s = 2\pi \times 44$  MHz at the surface. The coupling strength decays with an attenuation length of  $\delta_{q=0}^g = 131$  nm and  $\delta_{q=3}^g = 130.4$  nm, respectively, which we obtain by fitting the curve to  $g(r) = g_i^s \exp(r/\delta_i^g)$ . Figure 5.3 also shows the distribution of the distance of the atoms from the resonator surface inferred from the fitted coupling strength distribution for mode #2. Assuming that mode #2 has an axial quantum number  $q \leq 3$  the mean distance of the atoms which contribute to the spectra is between 125-160 nm from the surface.

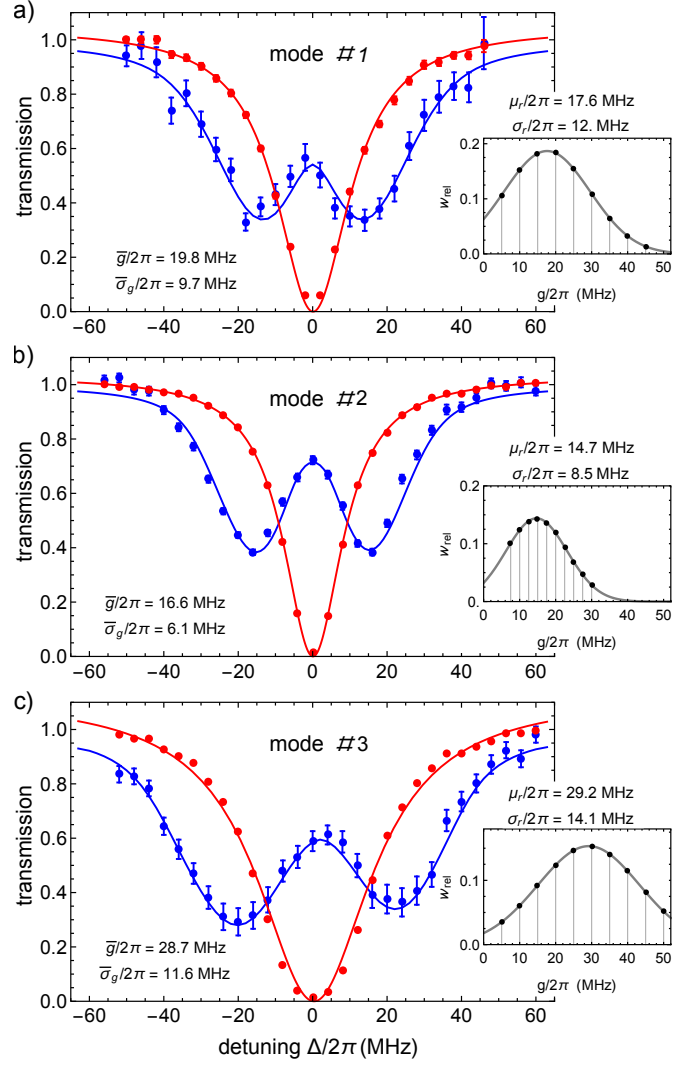


**Figure 5.2:** Measured Rabi spectra for a) mode #1, b) mode #2 and c) mode #3 . The dots are experimental data with (blue) and without atom (red) and the error bars indicate the  $1\sigma$  statistical error. The solid lines correspond to a theoretical fit using the full quantum mechanical model (cf. Sec. 4.4.1), having only the distribution of the coupling strength as free parameters. The average transmission spectrum is computed from a discrete set of coupling strengths, where the relative weight  $w_{\text{rel}}$  of each simulated spectrum is determined by a normal distribution, with mean  $\mu_r$  and standard deviation  $\sigma_r$ . From the truncated distribution we obtain the mean coupling strength  $\bar{g}$  and the standard deviation  $\bar{\sigma}_g$ . These values can be obtained with the common definition for the mean value and the standard deviation for a discrete data set and are summarized in Tab. 5.1.

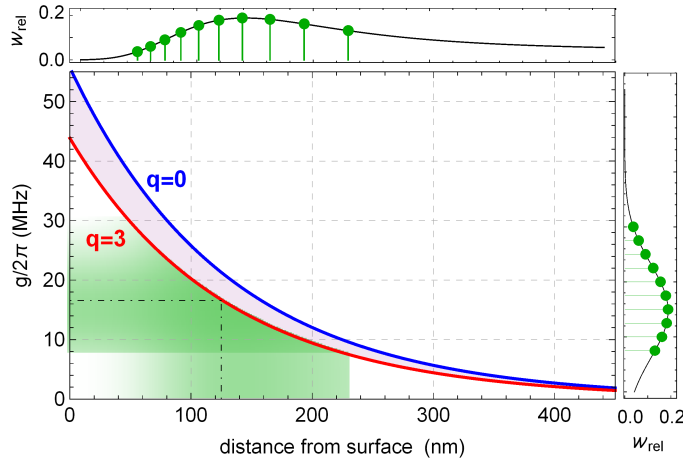


**Figure 5.3:** Distribution of coupling strengths  $g$  of a  $^{85}\text{Rb}$  atom in the evanescent field of a BMR calculated as a function of the distance from the resonator surface. The coupling strength is calculated for TM modes with axial quantum number  $q = 0$  (blue) and  $q = 3$  (red) and for the case where we probe the cycling transition  $|F = 3, m_F = 3\rangle \rightarrow |F' = 4, m_{F'} = 4\rangle$  of the  $D_2$ -line. The green area indicates the  $g$ -distribution we have obtained from fitting the Rabi spectra of mode #2 (cf. inset in Fig. 5.2b), which is translated into a position distribution. For clarity the distribution of both  $g$  and the position are indicated at the right and the top, respectively. The dash-dotted line shows the mean coupling strength  $\bar{g} = 2\pi \times 16.6$  MHz and the corresponding distance to the surface which is  $\sim 125$  nm for  $q = 3$ .

## 5.3 Basic experimental setup

In the following, the key elements of the experimental setup will be described. This includes the vacuum chamber, the laser system and the fiber network.

### 5.3.1 Vacuum chamber and fiber mounting

The goal of our experimental setup is to study the interaction between laser-cooled rubidium atoms and the evanescent field of the BMR. In order to be able to cool the rubidium atoms, the resonator and the atom source are placed in an UHV chamber. For cooling and delivering atoms, a MOT in combination with an atomic fountain is employed (see Sec. 5.4.1). The MOT is operated in a different chamber as the resonator, because for fast loading of the MOT an enhanced background pressure of rubidium vapor is required. This would inevitably lead to a contamination of the resonator surface, hence introduce additional losses and degrade its quality factor. Thus, a two-chamber design, as depicted in Fig. 5.4a, was chosen. The lower chamber, the so-called MOT-chamber, contains the rubidium dispensers and is surrounded by the MOT setup. The upper chamber, the so-called science-chamber, contains the resonator and coupling

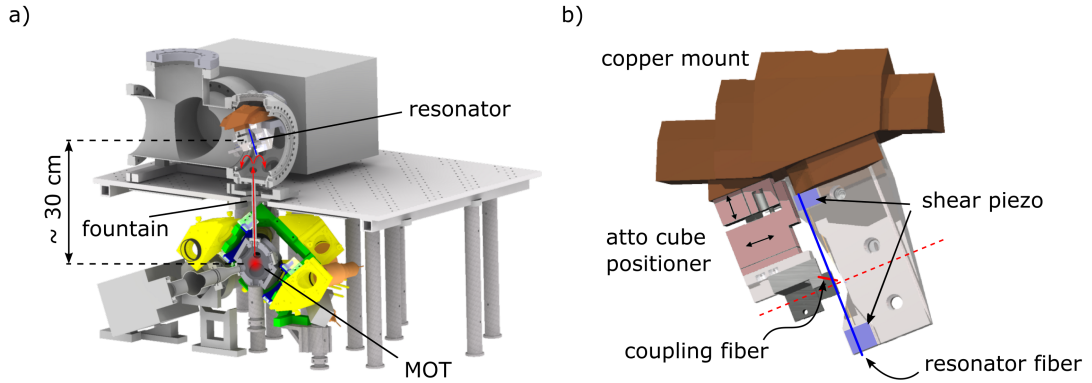


**Figure 5.4:** a) Cross-section through the vacuum chamber setup. The atoms are trapped and cooled in the lower vacuum chamber. Then, they are launched toward the upper chamber, passing through the differential pumping tube. In the upper chamber the resonator and the coupling fibers are mounted. b) The fiber mounting stage is fixed on a massive copper block which is connected to the vacuum chamber by four viton rings. The mount of the resonator fiber (blue line) is rigidly connected to the copper block, and comprises two shear piezos which enable frequency tuning of the resonator. The two coupling fibers, which are indicated by the solid and dashed red lines, are both mounted on a 2D attocube piezo positioner. Using those, the coupling fiber can be moved along the resonator axis and toward the resonator. In this sketch only one coupling fiber mount is shown to improve visibility. The second coupling fiber is indicated by the dashed red line. Figures adapted from [87, 126].

fibers, including all the hardware required for their positioning. The two vacuum chambers are connected via a narrow tube, which keeps up the required pressure gradient and serves as a feed-through for the laser-cooled atom cloud enabling the delivery to the resonator. While the upper chamber is kept at  $\sim 5 \times 10^{-10}$  mbar, the MOT-chamber operates at a higher background pressure of  $\sim 10^{-8}$  mbar.

The BMR is glued onto shear piezo stacks which enable strain-tuning of the resonance frequency and we mounted inside the science-chamber. The resonator can be interfaced by two coupling fibers whose four fiber ends leave the chamber via teflon-sealed swagelok adapters (Vacom GmbH) and are connected to the fiber network (cf. Sec. 5.3.3). The section of each coupling fiber that includes the tapered region is mounted on a two-axis translation stages (ANPx101 and ANPz101, Attocube) at right angle to each other. These stages employ a so-called slip-stick method, which combines a large travel range for rough alignment and high resolution for fine tuning of the fiber position. This enables us to precisely adjust the distance between each coupling fiber and the resonator as well as their position along the resonator axis. The coupling between resonator and coupling fiber depends on the overlap of the evanescent field of the resonator mode with the evanescent field of the fiber-guided mode. Since both decay exponentially on the sub-micrometer scale, this coupling is extremely sensitive to relative position changes of

the resonator or the coupling fiber. Thus, a lot of effort has been put into isolating the fibers and their mounts from mechanical vibrations. This is done by mounting the fiber holders and translation stages on a 2 kg gold-plated copper block (see Fig. 5.4b) which rests on four viton rings, thus avoiding rigid contact between the chamber and the fiber mounts. In addition, the massive copper block serves as a vibration dump. Furthermore, the mounting of the whole vacuum chamber, especially the upper part, has been designed to provide optimal damping of vibrations.

### 5.3.2 Laser system

The CQED experiment employs several lasers which are set up on the so-called laser table while the vacuum chamber is set up on the so-called science table. This section will briefly discuss the basic elements and functionalities of the laser setup. A detailed discussion of the laser setup can be found in Ref. [86, 127].

#### MOT-lasers

In order to produce enough optical power for the MOT, a diode-tapered-amplifier laser system (MOPA, Sacher Lasertechnik GmbH) is employed. For cooling the atoms, this laser has to be red-detuned to the cooling transition. Therefore, its frequency is locked to the cross-over peak of the transitions  $|F=3\rangle \rightarrow |F'=3\rangle$  and  $|F=3\rangle \rightarrow |F'=4\rangle$  using frequency modulation spectroscopy. The cooling light is split into two paths and each path is sent through a double-pass acousto-optic modulator (AOM) setup [148]. This enables us to perform frequency sweeps or scans which are necessary for the atomic fountain and the polarization gradient cooling. The AOMs are driven by a RF-signal generated by direct digital synthesizer (AODS 20160 STD, Crystal Technology), which is frequency doubled and amplified (ZHL-1-2W+, Minicircuit), allowing any predefined frequency pattern. Then the respective beams are coupled into polarization maintaining (PM) fibers and connected to two fiber-clusters (Schäfter+Kirchhoff GmbH) which equally distribute the light into six beams of  $\sim 25$  mW output power. The outputs of the fiber cluster are then directly connected to the MOT cage which prepares the six pairwise counter-propagating collimated beams of orthogonal circular polarization. In order to achieve a stable MOT, a repump laser is required to recycle the atoms which have been transferred off-resonantly into the  $|F=2\rangle$  dark state to the cooling cycle. Therefore, a grating-stabilized diode laser (DL100, Toptica) is used, which is stabilized to the  $|F=2\rangle \rightarrow |F'=3\rangle$  transition via a side-of-fringe lock (see Fig. 5.6b). Usually, several mW are sufficient to efficiently repump the atoms.

#### Stabilization and interrogation laser

For all tasks concerning the control and interrogation of the resonator, we need light that is close to resonance with respect to the atomic transition. These tasks include frequency and resonator–fiber distance stabilization, as well as, detecting and probing the atoms. Since these task only

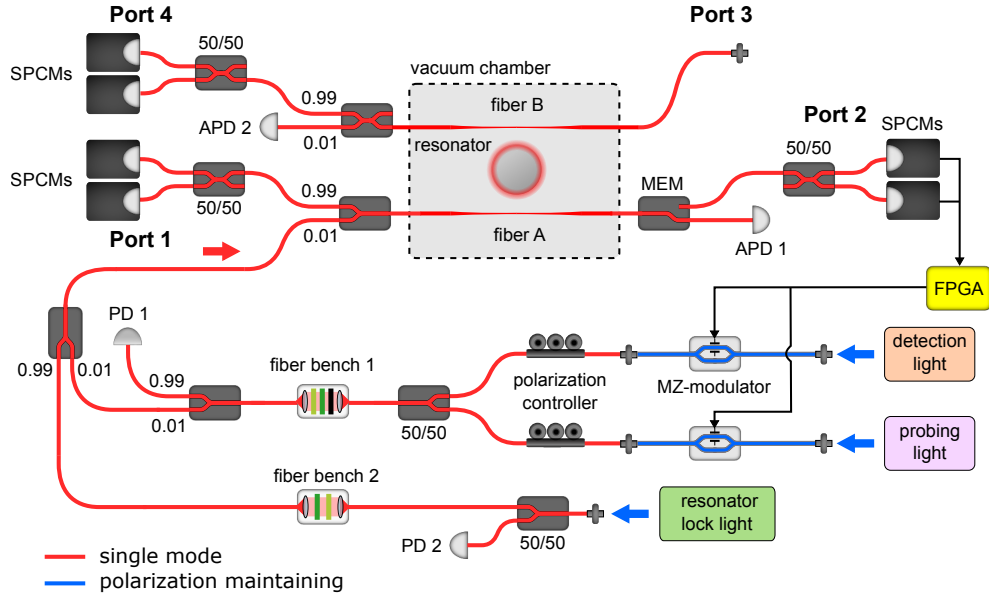


**Figure 5.5:** Fiber network for light preparation, distribution and detection in the CQED experiment. For a detailed explanation see main text. For the experiments described in chapter 6 and 7 the fiber network had to be adapted to fulfill the special requirements. For an description of the symbols used see legend in App. A.9. Figure adapted from Ref. [86].

require very low light powers, a single external cavity diode laser (DL Pro, Toptica Photonics AG) is employed. This laser is locked to the  $|F=3\rangle \rightarrow |F'=4\rangle$  hyperfine transition  $^{85}\text{Rb}$  (see Fig. 5.6b). The beam is divided into four paths. Each path is equipped with an AOM in double-pass configuration, which enables frequency tuning of  $\pm 100$  MHz with respect to the locking frequency, as well as, power regulation and stabilization. One part of the light is used for stabilizing the resonator frequency (see Sec. 5.2.4). For this locking scheme the light has to be modulated. Thus, the beam is also sent through an EOM. The other two beams are used for detecting and probing the atom-resonator system.

All beams are then coupled into PM fibers and transferred to the science table, where they are fed into the fiber network.

### 5.3.3 Basic fiber network

Once the different beams for controlling and probing the resonator are prepared they are transferred from the laser table onto the science table via PM fibers. Here, the different fields are injected into different ports of an optical fiber network. This fiber network is used to distribute and attenuate the different beams, which are then sent onto the resonator. In addition, it provides polarization control and highly efficient collection of the photons coming from the resonator. The basic setting is depicted in Fig. 5.5. However, for the experiments presented in the following chapters, the fiber network was modified compared to this basic configuration in order to

satisfy the specific requirements. All fibers of the fiber network are chosen to be single-mode non-polarization maintaining fibers. To ensure good polarization stability we employ an air-conditioning which keeps the temperature on the table stable (better than  $\pm 1^\circ$ ). In addition, the fibers are fixed to the optical table using tape.

The core of the fiber network is formed by two tapered optical fibers which are used to interface the resonator. In the following they will be referred to as fiber *A* and *B*, and their respective ends are numbered as port 1 to 4 (see Fig. 5.5). Both fibers are mounted inside the vacuum chamber and spliced to the fiber network. Since fiber *A* is used for most standard procedures, such as frequency stabilization and atom detection, the fiber network for this fiber is much more elaborate than for fiber *B*. In the following, the different parts of the fiber network are discussed in more detail.

### Stabilization beam

Before sending the modulated stabilization beam onto the resonator, the light first passes a fiber-based 50/50-beam splitter (BS) where half of the light is directed onto a photodiode (PD2). This generates an error signal for an intensity stabilization. The remaining light passes through a fiber bench, which comprises wave plates in order to align the light's polarization with the resonator eigenpolarization. Then, the light is combined with the detection arm on a 99/1-BS. Since we do not want to send too much power through the tapered fiber, the beam is further attenuated by an additional 99/1-BS. The remaining light, which is typically several hundred nW, is sent into the chamber via port 1 and exits via port 2. Then, a MEM fiber-optic switch (MEMS OSW12, Thorlabs) directs the light onto an avalanche photodiode (APD1). The photodiode signal is subsequently used for generating the PDH frequency-lock signal and for the stabilization of the distance between the fiber and the resonator.

### Detection beam

The light used for detecting atoms in the resonator mode also arrives on the science table via a PM fiber and passes through a fiber-integrated MZ intensity-modulator (NIR-MX800-LN-10, Photline). The MZ modulators allow sub-nanosecond switching of the light fields. The detection light then passes through a polarization controller before being sent onto a 50/50-BS, where it is combined with the probing light. Then, the light is transmitted through a fiber bench where first the polarization is cleaned with a thin-film polarizer and its polarization is adjusted using wave plates. Before the detection light is combined with the resonator stabilization beam, some light is extracted and sent onto PD1 for intensity stabilization. This signal is also used for the calibration of the working point of the MZ-modulator. Since we want to interrogate the atom-resonator system on the single-photon level we further attenuate the beam to several pW by using two 99/1 fiber BS. The remaining light is then sent into the chamber where it interacts with the resonator. After passing the chamber, the light is directed by the MEM-switch onto SPCMs (SPCM-AQRH-13-FC, Perkin Elmer) which record the transmitted photons. The flexibility of the fiber network allows us to quickly adapt the setup to detect atoms also from the opposite

direction, i.e. from port 2 instead of port 1. Therefore, we only have to connect the fiber of the detection beam to port 2 and monitor the photon counts detected by the SPCMs in port 1.

### **Probing beam**

During the short interaction window, there is no time to switch the properties of the detection laser beam, such as power, frequency or polarization. Therefore, it is necessary to prepare an additional probing light field in advance that can then be used for interrogating the atom–resonator system. After the detection of an atom in the resonator mode, the detection field is switched off and the probing field on. The frequency and amplitude of the probing light are prepared on the laser table. Then it is transferred to the science table via a PM fiber. There, it is coupled into the fiber network and processed in a similar way as the detection light. For intensity stabilization the signal from the internal photo diode (PD) of the probe’s MZ modulator is employed. After the probe has interacted with the atom–resonator system, the transmitted light is recorded by the same SPCMs in port 2 that are used for the detection procedure. While in the standard configuration the probe is co-propagating with the detection, the fiber network makes it possible to straightforwardly change the probing direction to all other ports. For some applications, it is not necessary to change the light’s properties between the probing and detection setting. In this cases, the switching between the two fields is simply disabled and the system is probed by the detection light.

The standard configuration of probe and detection light, as described above, is used for measuring vacuum Rabi splittings, as shown in Fig. 5.2.

## **5.4 Experimental procedures**

In the following, the key experimental procedures to operate the experiment will be described. This includes the laser-cooling and transfer of the atoms to the resonator, the frequency and distance stabilization of the resonator and an overview of the real-time detection scheme.

### **5.4.1 Atom preparation and delivery**

For our experiments, individual atoms have to be delivered reliably into the evanescent field of the resonator. Before bringing the atoms close to the resonator, their motional degrees of freedom have to be cooled. This is done by means of a MOT, followed by a polarization gradient cooling step. During this process a cloud of approximately  $5 \times 10^7$  atoms is trapped from the background vapor in the MOT-chamber. This commonly used technique uses six slightly red-detuned ( $\delta = 12$  MHz), pairwise counter-propagating laser beams of orthogonal circular polarization in combination with a magnetic field produced by two coils in anti-Helmholtz configuration (see Fig. 5.6). After the MOT-phase, the atoms are launched toward the resonator using an atomic fountain. This is done by switching off the magnetic field and red- and blue-detuning the lower and upper beam triplets by  $\Delta\omega$  with respect to each other. The detuning is achieved by applying a linear ramp with a slope of 1 MHz/ms. In this way a moving molasses is created, which accelerates the center-of-mass of the atom cloud in z-direction. The initial



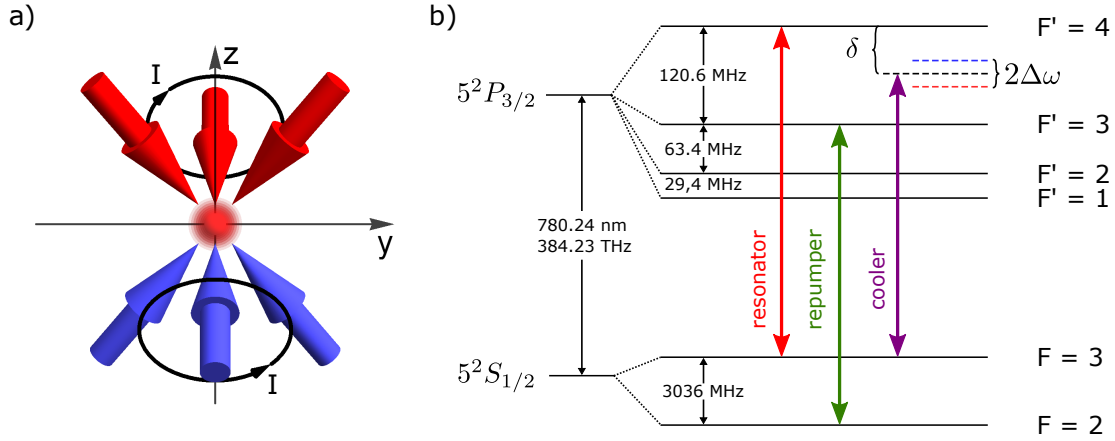


**Figure 5.6:** a) MOT-configuration: The beams are aligned in a 1-1-1 configuration, in which all beams have an angle of  $54.7^\circ$  to the (vertical)  $z$ -axis. This enables the atomic cloud to be launched toward the resonator, i.e. in  $z$ -direction, without having the beams transiting the science chamber. The polarization of the beams is chosen such that counter-propagating beams are always of opposite circular polarization. The coils in anti-Helmholtz configuration that generate the quadrupole field are indicated as black circles. The color code of the arrows indicates the respective detuning for the moving molasses phase. b) Hyperfine structure of the  $^{85}\text{Rb}$  D<sub>2</sub>-line: The red arrow indicates the frequency of the resonator, which is resonant to the  $|F=3\rangle \rightarrow |F'=4\rangle$  transition. The purple arrow shows the frequency of the cooling lasers of the MOT, which are red-detuned from the  $|F=3\rangle \rightarrow |F'=4\rangle$  transition by  $\delta = 12$  MHz. In order to launch the atomic fountain, the upper and lower beams are red- and blue-detuned respectively by  $\Delta\omega$ , as indicated in a). For the polarization gradient cooling the two beams are further red-detuned of  $\delta = 50$  MHz. The green arrow shows the repump transition, which is used for recycling the atoms that decayed to the  $F=2$  ground state during the cooling process.

velocity  $v_0$  of the cloud only depends on the detuning  $\Delta\omega$  and the wave vector  $k$  via [87, 126]

$$v_0 = \sqrt{3} \frac{\Delta\omega}{k}. \quad (5.2)$$

This corresponds to the velocity of the atoms for which the experienced Doppler shift balances the detuning. The additional factor  $\sqrt{3}$  stems from the angle between the beams and the propagation direction of the atoms, and reduces the effective wavelength of the molasses laser beams. By adjusting the detuning of the respective MOT beams, the turning point of the cloud can be set exactly to the position of the resonator. The detuning that is usually applied in the experiment is  $\Delta\omega = \pm 2\pi \cdot 1.77$  MHz with respect to the initial MOT-laser frequency. The cloud takes  $\sim 240$  ms to travel the distance of 30.5 cm between the center of the MOT and the resonator, which is located in the upper chamber. Before the atoms leave the MOT-beam cross section, an additional polarization gradient cooling (PGC) step is performed. Therefore, the light's frequency is further shifted for all beams simultaneously to the red by  $\delta \approx 50$  MHz. The additional

3 ms of PGC reduce the temperature of the atoms to  $6 \mu\text{K}$ . This temperature was estimated from a time-of-flight experiment, as described in Ref. [62, 86].

### 5.4.2 Resonator frequency stabilization

In our experiment, the active stabilization of the mode's resonance frequency is achieved using a PDH locking scheme [149]. PDH locks offer several advantages, namely, they effectively decouple power fluctuations from frequency fluctuations, have a large recapture range, and are not limited by the resonator linewidth. In order to generate an error signal for locking, light that is resonant to the desired transition frequency passes through an EOM, driven by a local oscillator at 42.8 MHz. The EOM performs a frequency modulation of the laser field, thereby generating two frequency side bands. The light is then sent onto the resonator. The transmitted light is then recorded by a high-gain APD and the obtained signal is mixed with the local oscillator. After low-pass filtering we obtain the error signal is then analyzed by a LabView-based PID locking routine which acts on the piezo that tunes the resonator. The bandwidth of the control loop is mainly limited by the computational speed of the computer used [87]. During the experimental phase in which atoms arrive at the resonator, the frequency lock is put on hold and the stabilization light switched off.

### 5.4.3 Fiber-resonator coupling stabilization

For typical measurements the experiment is continuously acquiring data for several hours. During that time, the relative position between the resonator and the coupling fiber, and thus the evanescent coupling between the resonator mode and the fiber-guided mode, can change. There are ways to actively stabilize the coupling between the resonator and the coupling fiber, by means of the PDH technique [150]. Due to the stability of our present setup an active distance stabilization is, however, not necessary. When operating the experiment continuously for several hours, we only counteract on slow drifts by interrupting the sequence every 300-500 sequence run, which corresponds to 10-15 minutes, to perform an automatic distance calibration. For the standard distance calibration, the coupling fiber is first withdrawn by a predefined distance. While approaching the resonator again, the transmission signal is recorded by the APD. For the critical coupling point the transmission should be zero. By fitting the recorded signal the control program determines the point of minimal transmission, which should correspond to the critical coupling point, and then places the coupling fiber at the determined position. This procedure can also be extended for the case of two fibers coupled to the resonator [86].

### 5.4.4 Determining the resonator-fiber coupling

In the experiments presented in the following, we extensively make use of the fact that we can change the coupling between the resonator and the respective coupling fibers by changing the gap between them. For the evaluation of the experiments it is important to know both the intrinsic loss rate  $\kappa_0$  and the coupling rate between the resonator and the respective coupling fiber. These parameters can in principle be obtained by measuring a spectrum of the empty

$I$ (A)	$\Delta_B$ (MHz)	$B_z$ (G)
0	2.2	1.6
55	6.6	4.8

**Table 5.2:** The level shift introduced by the external magnetic fields, when 0 or 55 A are supplied to the bias coil [122].

resonator, as shown in Fig. 5.2. However, since these measurements are conducted at the level of single photons and performed in a pulsed sequence they are very time consuming. Therefore, we pursue the following protocol outside the sequence to obtain the coupling parameters. We send the stabilization laser onto the resonator and monitor the fiber transmission using the APD. At the same time, the resonance frequency of the resonator mode is modulated by applying an sinusoidal voltage ramp to the tuning piezo. This yields the empty resonator transmission spectrum, which is exemplarily shown in Fig. 5.7a. In order to obtain a frequency calibration of this measurement, we modulate the laser frequency using an EOM. This results in sidebands at well known frequencies, which are used as a frequency ruler. The measured APD signal is then deconvoluted with the piezo ramp and then fitted using a Lorentzian. The total resonator loss rate  $\kappa_{\text{tot}}$  correspond to the half width at half maximum (HWHM) of the fitted curve. In order to determine the intrinsic resonator losses we interfaced the resonator with a single fiber coupler such that it is critically coupled, i.e.  $\kappa_A = \kappa_0$ , where  $\kappa_A$  is the coupling rate between fiber  $A$  and the resonator mode. The intrinsic resonator losses can be obtained via  $\kappa_{\text{tot}} = 2\kappa_0$  as shown in Fig. 5.7b. Once  $\kappa_0$  is known, the resonator–fiber coupling rate can also be determined away from the critical coupling position using  $\kappa_A = \kappa_{\text{tot}} - \kappa_0$ , as shown in Fig. 5.7c. When the resonator is interfaced by two fibers, denoted  $A$  and  $B$ , the second fiber introduces an additional loss rate  $\kappa_B$  to the resonator. When fiber  $A$  is critically coupled, i.e.  $\kappa_A = \kappa_0 + \kappa_B$ , we can deduce the coupling rate to the second fiber using  $\kappa_{\text{tot}} = 2(\kappa_0 + \kappa_B)$ , as shown in Fig. 5.7d.

### 5.4.5 Bias field

The science chamber is surrounded by several sources of magnetic background fields, such as ion getter pumps or earth’s magnetic field. In order to guarantee a well-defined quantization axis for the atoms, we apply a small bias field along the resonator axis. Since magnetic bias coils were not considered when devising the setup, a single coil is placed on top of the science chamber, as shown in Fig. 5.8. The coil consists of six windings and induces an in-homogenous magnetic field. However, since the coil is aligned with the resonator axis, the field can be assumed to be constant over the extend of the resonator. From the position of the coil and for maximal current of 55 A which can be supplied by our current source (HPS-11560, Voltcraft), the calculated magnetic field along the resonator axis at the position of the resonator amounts to  $B_z \approx 5$  G (see Fig. 5.8). From the fits to the Rabi spectra and lifetime measurements of the atoms in the resonator modes, the magnetic field experienced by the atom can be measured [86]. The measured frequency shifts  $\Delta_B$  and deduced magnetic fields  $B_z$  are summarized in Tab. 5.2. We obtain a background magnetic field  $B_z^{\text{offset}} \approx 1.6$  G and an additional bias field  $B_z^{\text{bias}} \approx 3.2$  G

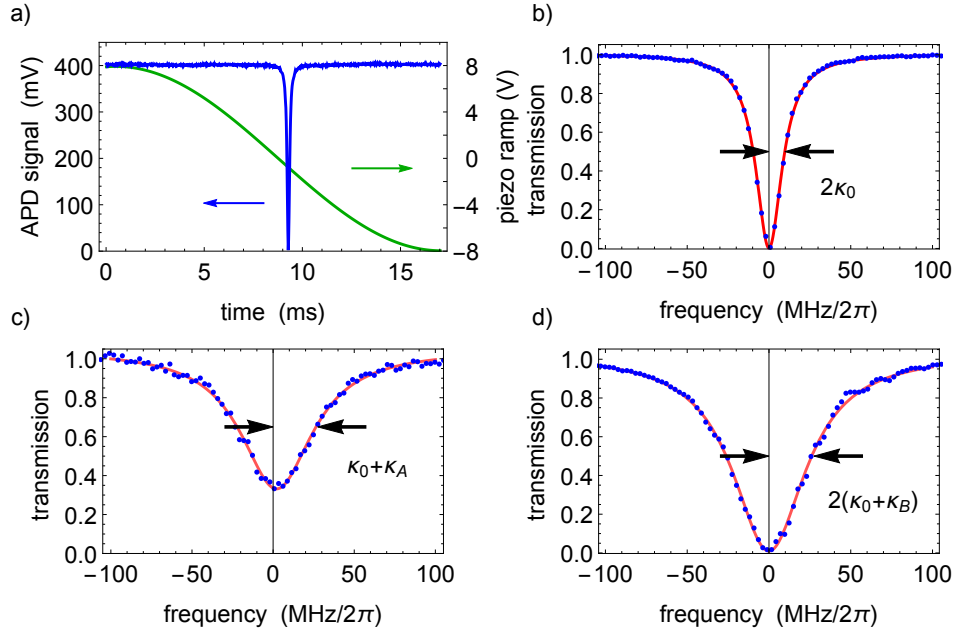


**Figure 5.7:** a) Measured APD signal (blue) when sinusoidally scanning the piezo voltage, which tunes the resonator. Exemplary spectra obtained for mode #2 when it is interfaced by a single coupling fiber which is b) critically coupled or c) over-coupled. In addition, the spectrum of the mode when it is interfaced by two fibers, is shown in d). In b-d) the blue dots are the measured APD signal and the red lines are the Lorentzian fits.

along the resonator axis. These results are in good agreement with the calculated values. The present current source has a rise time of 50 ms for reaching the maximal current of 55 A.

#### 5.4.6 Sequence

The experimental sequence is controlled by a computer program triggering and controlling most of the tasks described before. A single sequence run lasts  $\sim 1.7$  s and is schematically shown in Fig. 5.9. Each cycle starts with loading the MOT. For that time period, the cooling and repump lasers and the magnetic fields for the MOT are switched on. At the same time, the calibration of the MZ modulators is performed. This is necessary since even slight changes of the temperature cause the relative phase of the two arms to drift, changing the working point of the MZ modulators. During the MOT loading phase, the MEM directs the stabilization light onto the APD and the frequency of the resonator is locked to the atomic resonance. After approximately 1.3 s the magnetic fields of the MOT are switched off and the atomic fountain is launched. This is followed by a short PGC phase. When the atoms have left the cooling beam cross section, the cooling and repump lasers are turned off using AOMs and mechanical shutters to avoid any stray light during the actual measurements. The cloud takes  $\sim 240$  ms to travel to the resonator,

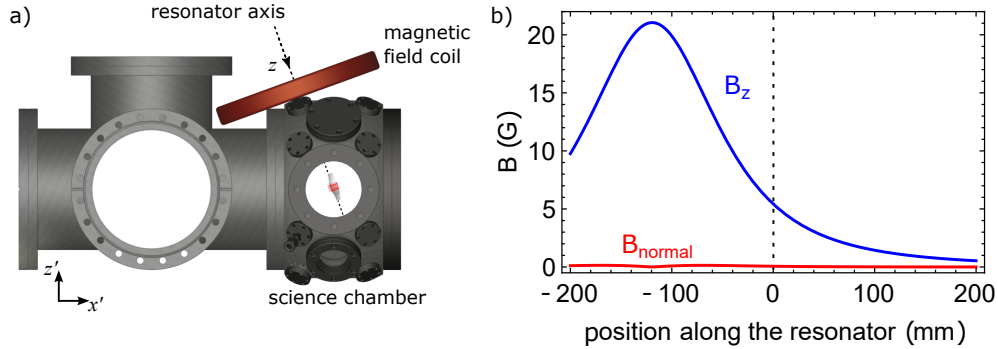


**Figure 5.8:** a) The coil used to generate the magnetic bias field is placed on top of the science chamber and is aligned with the resonator axis. b) The magnetic field components parallel  $B_z$  and normal  $B_{\text{normal}}$  to the resonator axis, as a function of the position along the resonator axis. The position of the resonator is supposed to be indicated with a dashed line. At this position the magnetic field created by the coils is  $B_z \approx 5$  G for a maximal current of  $I = 55$  A. Figure adapted from Ref. [86].

which is located in the upper chamber. During this time, the coil used to create the magnetic bias field along the resonator axis is switched on. Shortly before the cloud reaches the resonator the frequency stabilization of the resonator is put on hold and the corresponding laser beam is switched off. Now, the detection light field is switched on and the MEM directs the light passing the resonator onto the SPCMs which are now gated on and the FPGAs start recording photons. Once the atom-trigger FPGA detects an atom, it triggers the probing routine which is described in detail in Sec. 5.4.7. The cloud remains close to the resonator for approximately 100 ms during which atoms arrive at the resonator (see Fig. 5.13d). This time window is referred to as detection window. After the end of the detection window the sequence is started again by loading the MOT.

### 5.4.7 Real-time atom detection

During the detection window, several atoms get close enough to the surface to enter the evanescent field of the resonator mode. However, it is not possible to predict when a single atom strongly couples to the mode. Thus, an active detection scheme has to be applied, capable of detecting and reacting on the presence of an atom in real time. Since the atom transits are limited to a few microseconds this imposes a strict time constraint for detecting the presence of the atom and to subsequently probe the coupled system.

For the purpose of detecting strongly coupled atoms, we make use of the fact that their presence significantly alters the properties of the resonator field [151], and thus of the light transmitted through the coupling fiber. For the two experiments discussed in the following, two different techniques have been employed. Both rely on the same principle: In the absence of an atom almost no light reaches the detection port. This significantly changes when the atom arrives in the resonator mode. The arrival of the atom causes a burst of photons which can be used to her-

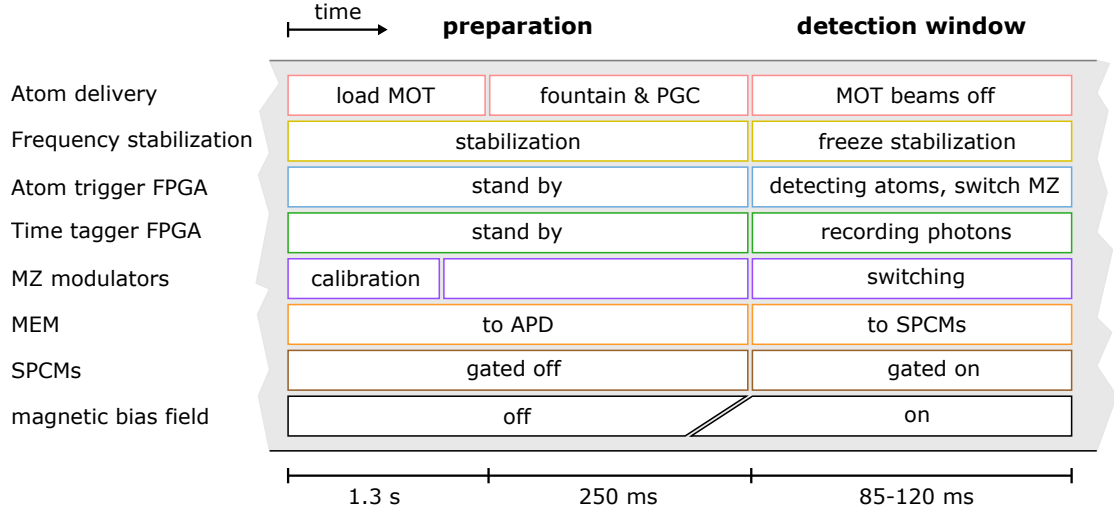


**Figure 5.9:** Time line of the experimental sequence. A sequence run can be divided into two parts, the preparation phase and the actual experiment, which will be performed during the detection window. During the preparation phase, the atoms are cooled and delivered to the resonator and all necessary calibration and stabilization routines are performed. In the detection window, the cloud of atoms surrounds the resonator and the FPGAs detect single atoms and record photons. Once an atom is detected, the MZ modulator switch on and off different probing beams, in order to perform the actual experiment. After approximately 100 ms the cloud has left the surrounding of the resonator and a new sequence starts with the preparation phase.

and their presence. However, to accurately distinguish the transmission increase caused by atom transits from fluctuations of the transmitted power, it is crucial to realize close-to-zero transmission to the detection port. In our experiment this can be realized by employing two different methods, which will be briefly discussed in the following.

### Atom detection for critically coupled fiber

The standard method achieves a dark detection port by critically coupling the fiber to the empty resonator, see Fig. 5.11a. This means that the coupling rate between the coupling fiber and the resonator  $\kappa_A$  is equal to the total loss rate of the resonator, including internal losses  $\kappa_0$ . When the resonator is interfaced by two second fibers,  $\kappa_B$  has to be added to the intrinsic resonator losses, i.e.  $\kappa_A = \kappa_0 + \kappa_B$ . In addition, the polarization of the detection light has to be aligned with the eigenpolarization of the resonator mode. Depending on how well the input polarization is adjusted, the remaining transmission through the fiber becomes less the 1-2 %. When an atom strongly couples to the resonator field the transmission increases to  $\sim 70$  % (cf. Eq. (4.14)). This increasing photon rate at the detection port is used for detecting the presence of an atom. This scheme is applicable for experiments which only use a single input polarization, which has to be aligned to the resonator eigenpolarization. Nevertheless, it can be straightforwardly used with

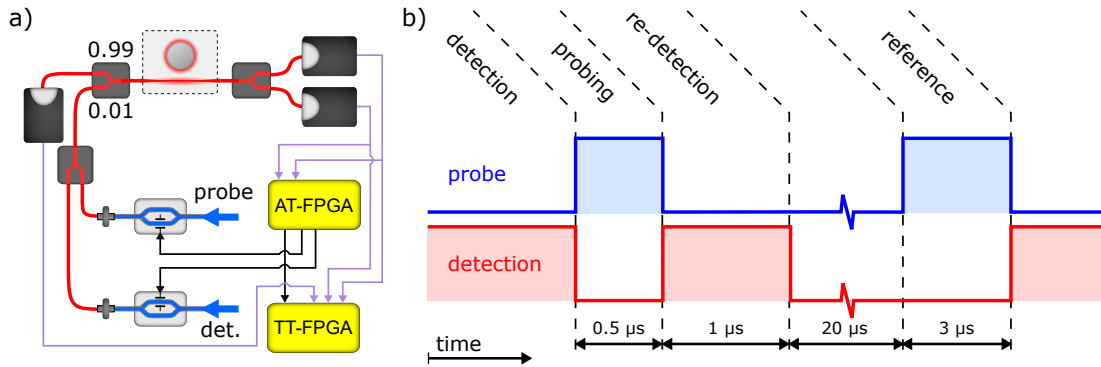


**Figure 5.10:** a) Schematic of the wiring of the atom-trigger (AT) and time-tagger (TT) FPGAs, which are used for detecting atoms and recording the arrival times of the photons. b) Standard sequence that is executed after the detection of an atom. First, during the probing window the detection and probe lasers are switched off and on, respectively. This is followed by a re-detection phase for which the detection (probe) light is switched on (off) again. After a wait time, which is much larger than the time the atom couples to the resonator field, a second probe pulse is sent onto the now empty resonator.

two fibers coupled to the resonator, as long as fiber *A* remains critically coupled. This technique is employed for the experiments described in chapter 7.

### Atom detection based on polarization rotation

For the second technique we make use of the polarization change introduced by the atom, when sending not only the resonator eigenpolarization but also the orthogonal polarization through the coupling fiber. The light with resonator eigenpolarization interacts in the usual way with the resonator and atom. Due to the large birefringence of the resonator, the orthogonal polarization is unaffected by the resonator and the atom, and is always fully transmitted. For realizing a dark detection port for the empty resonator, we send the transmitted light onto a polarizing beam splitter (PBS) and adjust its polarization such that we obtain zero power to one port of the PBS. The presence of the atom will change the losses and phase of the polarization component that couples to the resonator, and thus the polarization of the transmitted light. When the light now impinges on the PBS the previously dark port will have an increased count rate. This can be used for heralding the presence of an atom, even when the fiber is not critically coupled.

In Fig. 5.12 exemplary transmission bursts in the detection port caused by atom transits are shown. When averaging over many such events, we can estimate the mean atom life time to  $1-2 \mu\text{s}$ .

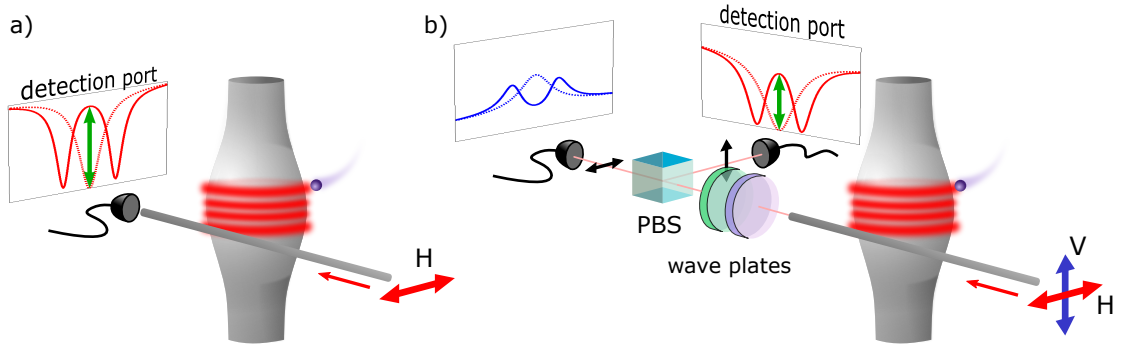


**Figure 5.11:** a) Standard detection scheme based on critical coupling. Light polarized along the resonator eigenpolarization, i.e.  $H$ -polarized, is sent through the coupling fiber and the transmission is monitored at the fiber end. As long as there is no atom present in the resonator mode, the critically coupled empty resonator reduces the transmitted power to almost zero. The presence of an atom causes an increased on-resonance transmission, which can be used for triggering on the presence of the atom. b) Detection scheme based on polarization rotation. A superposition of  $H$ - and  $V$ -polarized light is sent onto the resonator. Using the wave plates in the output, the on-resonance transmission can be minimized in the detection port. The presence of the atom will modify the loss and phase of the  $H$ -component, and thus change the polarization of the output field. This yields an increased count rate in the detection port. In both, b) and c), the small inset shows transmission spectra without (dashed) and with (solid) atom. The green arrows indicate the large transmission change used for heralding the presence of an atom.

### Atom-trigger FPGA

During the detection window, the transmission is continuously monitored by two SPCMs in the detection port. The SPCMs produce a TTL pulse whenever they detect a photon, with quantum efficiency of  $\sim 60\%$ . The signal is then sent on an FPGA (XEM3010, Opal Kelly). This so-called atom-trigger-FPGA, continuously records all photons detected by the SPCMs in the detection port. If the number of counts within a time window  $\Delta t_{\text{trig}}$  exceeds a certain threshold  $N_{\text{trig}}$  it triggers an atom coupling event. The FPGA records the time stamp of the coupling event relative to the beginning of the detection window and sends a trigger pulse to a second FPGA, responsible for recording all photon arrival times. In addition, the FPGA has several TTL outputs which can be used for switching the MZ modulators to turn off or on the detection and probing light fields. The internal delays caused by the triggering process of the FPGA are approximately 40 ns. The additional electronic and optical delays and the rise time of the MZ modulator give rise to a total delay of  $\Delta t_{\text{delay}} \approx 180$  ns between the time the  $N_{\text{trig}}$ -th photon, that triggers the coupling event, and the time the probing light, which is subsequently switched on, is detected. This can be seen in Fig. 5.13a and b. Typical values used for the atom trigger process using a detection beam with mean photon flux of 10-15 photons/ $\mu\text{s}$  are  $\Delta t_{\text{trig}} = 1.2 \mu\text{s}$  and  $N_{\text{trig}} = 7$ . For a detailed discussion of the atom-detection and its technical implementation see Ref. [127].



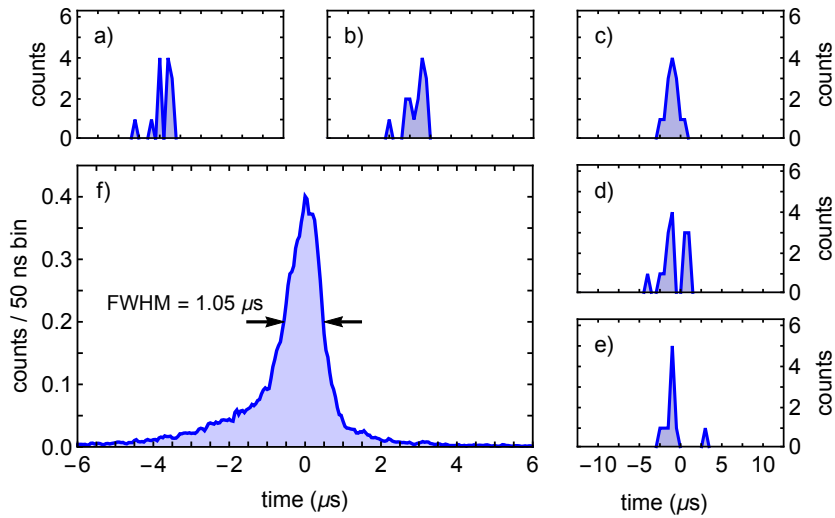


**Figure 5.12:** a)-e) Typical transmission traces of single atom transits, for a critically coupled empty resonator. f) Mean transmission averaged over 1700 atom transits, such as depicted in a)-e). The mean photon arrival time was shifted to be at  $t = 0$  for each atom transit. For this setting a mean atom life time of  $1.05 \mu\text{s}$  can be deduced.

### Time-tagger FPGA

In addition to the atom-trigger FPGA, a second FPGA (XEM3005, Opal Kelly) is employed to record the arrival time of each photon click from all SPCMs used in the experiment. The so-called time-tagger FPGA reaches sub-nanosecond resolution by making use of internal hardware delays on the chip. Each FPGA can handle maximally 5 SPCMs at once. To keep the amount of data transferred to the computer manageable, the window in which the photons are recorded is limited to  $25 \mu\text{s}$  before and after the time-tagger FPGA gets triggered by the atom-trigger FPGA. For each atom trigger event the absolute timing of each arriving photon is recorded and then referenced to the signal from the atom-trigger FPGA, in order to obtain a relative time within the detection window. These time tags of a detected photon together with the corresponding number of the detector are saved with  $1/8 \text{ ns}$  resolution. The time-tagging unit is extremely powerful, since it not only allows us to compute the temporal evolution of the photon flux at several output ports from the stored data, but it also allows time-correlated photon counting, i.e to compute correlations between different detectors. This enables us to obtain second-order intensity correlation functions, which are essential to investigate nonlinear effects.

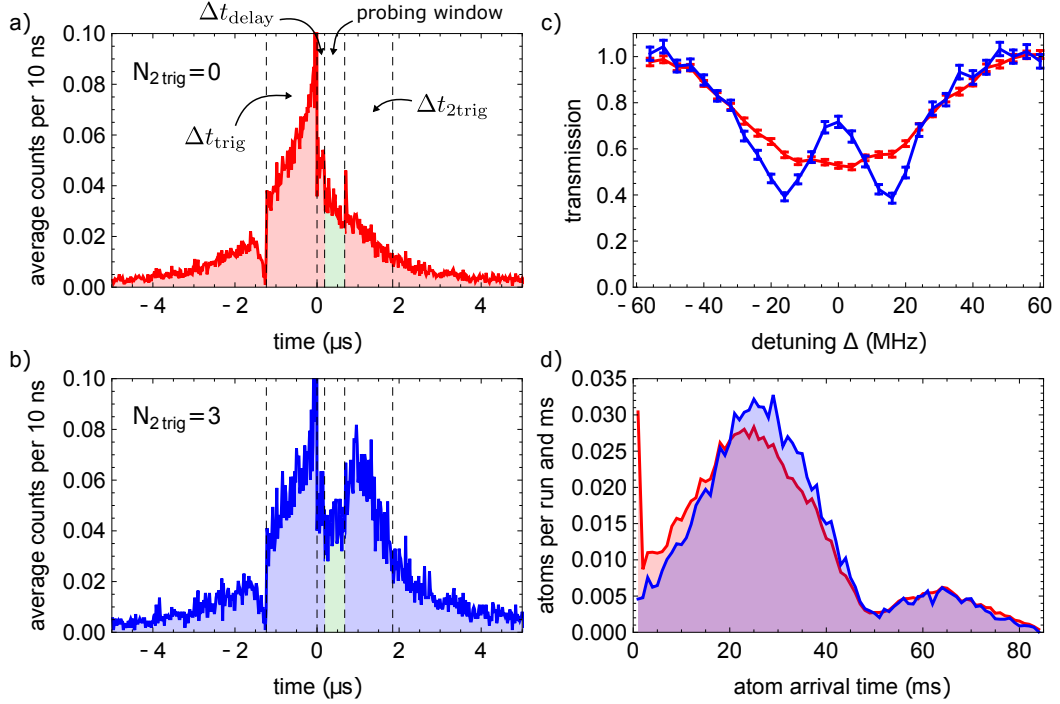


**Figure 5.13:** Averaged fiber transmission for a typical detection sequence and two different second trigger values, a)  $N_{2\text{trig}} = 0$  and b)  $N_{2\text{trig}} = 3$ . The prominent features of this plot can be identified as artifacts of the detection and probing process. The significantly enhanced transmission at  $t=0$  marks the time when the  $N_{\text{trig}}$ -th photon within  $1.2 \mu\text{s}$  was detected. Thus, there has to be a detected photon for each event. The sharp dip to almost zero transmission at  $t = -1.2 \mu\text{s}$  appears because, if a photon had been detected at this time, the FPGA would have triggered one time-bin earlier. Since we only select events for which a certain number of photons were detected within the first detection window, the overall transmission is significantly increased. Immediately after  $t=0$  the transmission drops to its unbiased value. After  $\sim 0.2 \mu\text{s}$  the detection light is switched off and the probe light turned on. This corresponds to the total delay between the detection of an atom coupling event and the probing light arriving at the detector. The time window in which the probe light is switched on for  $500 \text{ ns}$  is marked in green. After the probing window, the probe light is switched off and the detection light on again. When choosing  $N_{2\text{trig}} > 0$  a second peak follows at  $0.7 \mu\text{s}$  caused by the biasing of the re-detection. Applying a second trigger criterion of  $N_{2\text{trig}} = 3$  within the re-detection interval produces an almost constant transmission during the probing window. However, the re-detection leads to a reduction of the valid atom coupling events by a factor of 3 (see Tab. 5.3). The small spikes that appear whenever the detection or the probing light is switch on or off corresponds to the ring up or down of the resonator. c) Measured Rabi spectrum for different second trigger values,  $N_{2\text{trig}} = 0$  (red) and  $N_{2\text{trig}} = 3$  (blue). d) The histogram of the atom detection time within the  $85 \text{ ms}$  detection window normalized by the total number of trigger events. It shows two peaks, each corresponding to a certain velocity class of atoms that couple to the resonator on their way up or down.

### Re-detection

The coupling between the atom and the resonator mode varies during the atom transit. Therefore, the transmission after the atom detection is not constant but follows approximately an exponential decay. This is partially caused by the fact that we continuously loose atoms which either leave the evanescent field or crash against the resonator surface. For the latter case the interaction with the surface would lead to a large shift of the atomic transition and the atoms are lost for our purposes. In order to make sure that we only take atoms coupling events into account, for which the atom remained strongly coupled during the complete duration of the probing window, we perform a second detection. For that purpose the detection beam will be switched on again within a time window of  $\Delta t_{2\text{trig}} \approx 1\mu\text{s}$  (see Fig. 5.10b). Only those events which still show an increased transmission, i.e. reach a threshold number of detected photons  $N_{2\text{trig}}$  within this time window, will be post-selected for further data analysis. For events which do not fulfill the second trigger criterion it is very likely that the atom was lost during the actual measurement. Applying a second trigger criterion, i.e.  $N_{2\text{trig}} > 0$ , also reduces the number of trigger events caused by photon or transmission noise  $n_{\text{false}}$ , which we refer to as false trigger events. In Fig. 5.13a and Fig. 5.13b the transmission as a function of time is plotted for two values of  $N_{2\text{trig}}$ . For  $N_{2\text{trig}} = 3$  the transmission remains constant over the whole probing window. We thus only select atoms which are stably coupled to the resonator field. Furthermore, in Fig. 5.13c measured Rabi spectra that are evaluated for different  $N_{2\text{trig}}$  are compared. While the splitting can be clearly observed for  $N_{2\text{trig}} = 3$ , for  $N_{2\text{trig}} = 0$  the splitting is completely washed out [87]. When comparing the number of trigger events that fulfill the second detection criterion with runs where the atomic fountain was not launched, i.e. no atoms will arrive at the resonator, we can estimate the probability of false trigger events to be less than 0.01% after applying the second trigger event (cf. Tab. 5.3).

### 5.4.8 Optical pumping and atomic state preparation

Since the evanescent field of TM modes is almost perfectly circularly polarized, the atom gains angular momentum when it absorbs a resonator photon, i.e. the light drives  $\Delta m_F = \pm 1$  transitions. Thus, already the interaction with the detection light can modify the atomic state. In particular, this allows us to control and prepare the atom before the interrogation in e.g. the outermost  $m_F$ -state of the Zeeman manifold. The preparation process is a combination of two effects. On the one hand, our detection scheme is more sensitive to atoms already in the outermost  $m_F$ -state which has a larger transition strength than other  $m_F$  states. On the other hand, the atoms are actively pumped into this state by the detection process. As a consequence, the atoms that are detected with light that is coupled into the CCW(CW) mode should be in the  $m_F = +3(-3)$  state after the detection. This enables us to prepare the two orthogonal spin-states  $|F=3, m_F = \pm 3\rangle$ , by just detecting the atoms from different directions through the coupling fiber. Once the atom is detected, it is possible to transfer its population to the opposite side of the atomic level scheme by exciting the counter-propagating TM mode, as indicated in Fig. 5.14a [86]. To experimentally observe optical pumping, we detect the atom first using a field in the CCW mode and then switch on a counter-propagating probe beam which couples to the CW mode. We apply a second trigger criterion for the probe beam, thereby post-selecting only events where after  $2.5\mu\text{s}$

$N_{2\text{trig}}$	$n_{\text{events}}^{N_{2\text{trig}}}$	$n_{\text{events}}^{N_{2\text{trig}}}/n_{\text{events}}^0$	$n_{\text{false}}$	$P_{\text{false}}$	$T(\Delta = 0)$
0	54739	100%	66	0.024	$0.528 \pm 0.012$
1	29747	54%	14	0.009	$0.685 \pm 0.019$
2	22011	40%	3	0.003	$0.688 \pm 0.022$
3	17189	31%	0	$> 10^{-4}$	$0.717 \pm 0.024$

**Table 5.3:** Effect of the re-detection on a transmission measurement. The total number of trigger events without applying a second trigger criterion is  $n_{\text{events}}^0$ . When increasing the threshold for the re-detection, i.e. detecting  $N_{2\text{trig}}$  photons within the re-detection window, the number of events decreases to  $n_{\text{events}}^{N_{2\text{trig}}}$ . The number of false trigger events, which we obtain from runs in which the cloud is not launched (every 20-th sequence run), is  $n_{\text{false}}$ . The probability of having a false trigger event is then given by  $P_{\text{false}} = 20 \cdot n_{\text{false}}/n_{\text{events}}^{N_{2\text{trig}}}$ . The on-resonance transmission  $T(\Delta = 0)$  increases when increasing  $N_{2\text{trig}}$ . This is possible due to selecting atoms which are stronger coupled to the mode. For larger  $N_{2\text{trig}}$ , the  $\pm 1\sigma$  statistical error of the transmission increases. This can be caused by the decreasing number of events taken into account and the decay of the transmission within the probing window caused by losing the atoms.

the transmission in backward direction has more than  $N_2^{\text{trig}} = 6$  counts in a time window of  $\Delta t_{2\text{trig}} = 1 \mu\text{s}$ . In Fig. 5.28 c, the average normalized transmission of the probe beam through the coupling fiber is shown for a mean photon flux of 30 photons/ $\mu\text{s}$ , which corresponds to an intra-resonator photon number  $n_{\text{res}} = 0.4$ . We observe a linear increase of the transmission which saturates around 70% to a stable value after  $\sim 2 \mu\text{s}$ . This behavior can easily be explained with optical pumping: Initially, the atom is prepared in the  $|F = 3, m_F = +3\rangle$  ground state by the detection process. Subsequently, we probe with nearly perfectly  $\sigma^-$ -polarized light, that drives the  $|F = 3, m_F = 3\rangle \rightarrow |F' = 4, m_{F'} = 2\rangle$  transition which is only weakly coupled to the resonator (see Fig. 5.14a). Thus, we observe a transmission resembling that of an empty cavity (see left inset of Fig. 5.14b). However, when the probe light is applied long enough the atom eventually scatters a photon and is then transferred under the emission of a  $\sigma^+$ -polarized photon to the  $m_F = 1$  ground state. With each photon scattering,  $m_F$  decreases and the coupling strength to the  $\sigma^-$ -polarized mode increases (cf. App. A.1) and reaches its maximum when the atom arrives in the outermost  $m_F$ -state, for which the probe light drives a closed cycling transition (see right inset in Fig. 5.14b). In principle, when neglecting decays into free space, after three scattering events the atom ends up in the  $|F = 3, m_F = -3\rangle$  ground state.

For the experiment, a more relevant quantity is the number of photons that have to impinge onto the coupled atom–resonator system in order to change the atomic population. We can model this situation numerically, using the full quantum mechanical model introduced in Sec. 4.4.1, by comparing the time of the process with the mean number of photons in the weak coherent driving field. For the simulation, we take into account the Zeeman manifold of the ground and excited states and consider both counter-propagating modes with their correct polarizations. From this, we estimate that 12 photons have to impinge onto the resonator to reduce the population of the initial ground state ( $m_F = +3$ ) to  $1/e$ . Moreover, 20 photons are required to transfer  $1/e$  of

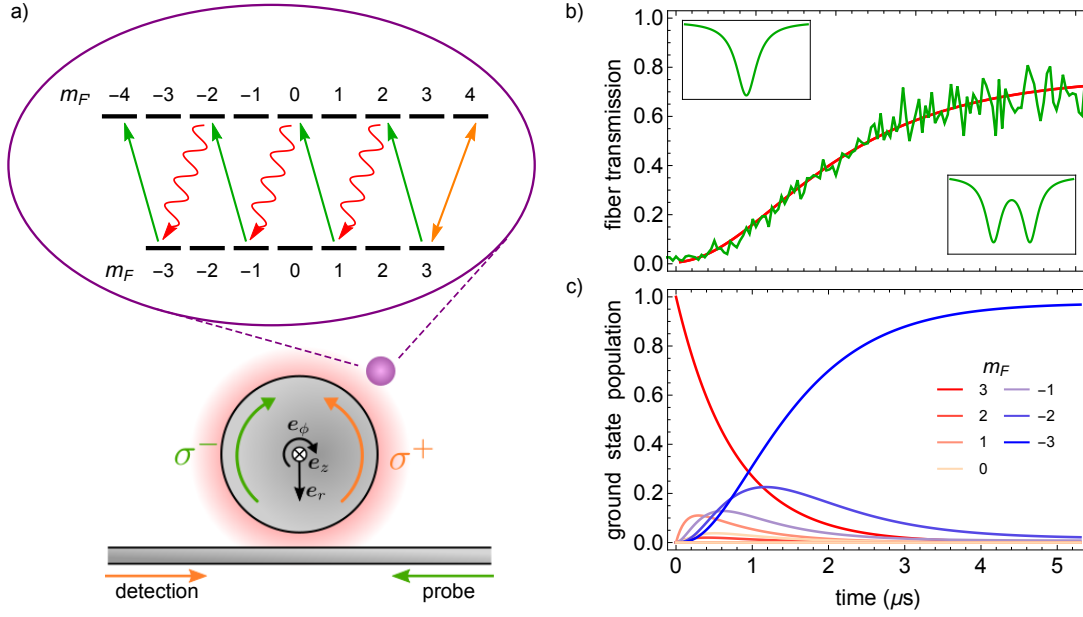


**Figure 5.14:** a) Illustration of the optical pumping process: Level scheme of the  $|F=3\rangle \rightarrow |F=4\rangle$  transition. After the detection light (orange), which is  $\sigma^+$ -polarized, has prepared the atom in the  $|F=3, m_F=3\rangle$  ground state, counter-propagating probe light (green), which is  $\sigma^-$ -polarized, pumps the atom toward the  $m_{F'} = -3$  ground state. The red arrows indicate the decay process. b) Average fiber transmission during the pumping process for an atom coupled to mode #2, which is critically coupled in the absence of the atom. After  $2.5 \mu\text{s}$  the second trigger criterion is evaluated for the probe light. The insets illustrate the transmission spectra for the initial situation, where the atom is only weakly coupled, and for the situation after pumping, where the atom is strongly coupled. The red lines show the theoretical predictions for our experimental parameters,  $(g, \gamma, \kappa_0, \kappa_{\text{ext}}, s_{\text{in}}^b) = 2\pi \times (16.6, 3, 5, 5, 0.4)$  MHz and a magnetic bias field of  $B = 5$  G. c) Evolution of the population of the individual Zeeman ground states, calculated for the same parameters used in b). Figure adapted from Ref. [86].

the population to the opposite state ( $m_F = -3$ ). The efficiency of the pumping process strongly depends on the detuning of the respective atomic level with the resonator mode. Thus, by applying magnetic fields or inducing light shifts, the  $|m_F=3\rangle \rightarrow |m_{F'}=2\rangle$  transition can be detuned with respect to the  $|m_F=3\rangle \rightarrow |m_{F'}=4\rangle$  transition, and thus the pumping can be strongly suppressed. Already applying a small magnetic field of 5 G increases the number of photons necessary to transfer the population out of the initial Zeeman state to 18. From this simulation, we also obtain the resulting transmission, which is shown in Fig. 5.14b.



## Nonlinear phase shift

Photons that travel through free space do not interact with each other and are well decoupled from their environment. This, in combination with the large bandwidth of optical photons, makes optical signals, which are guided in optical glass fibers, the preferred method for communicating information over long distances, enabling unprecedented communication speed [152], for example. Furthermore, in the context of quantum information processing, the decoupling from the environment, and thus their robustness against decoherence renders photons a promising candidate for encoding quantum bits (qubits). Compared to other systems, such as trapped ions or solid state qubits, the high mobility makes photons also a versatile resource for quantum cryptography and quantum communication [4]. Since individual photons can easily be manipulated, e.g., using wave plates or interferometers, single-qubit operations are straightforward to incorporate. However, the weak interaction between photons turns out to be a drawback for realizing photon–photon entangling operations which are essential for many applications. A possible approach to implement effective photon–photon interaction is the use of Kerr nonlinearities. Such nonlinearities might be introduced by linear optics and projective measurements, as proposed by Knill, Laflamme and Milburn [153]. There, the nonlinearity arises through the post-selection on certain photon detection events. As an example, this approach has recently been used to implement quantum algorithms in systems of up to four photons [154]. However, these protocols are inherently probabilistic and require significant resource overheads [153]. This makes it difficult to scale the process to a larger number of photons or operations.

A deterministic approach, which promises scalability, is to directly employ Kerr-nonlinear media. In a Kerr medium, the light modifies the material’s index of refraction, such that the light propagation becomes power-dependent. These media are typically characterized by a refractive index  $n_{\text{Kerr}}$  that has a nonlinear component [155]

$$n_{\text{Kerr}} = n_0 + n_2 I . \quad (6.1)$$

Here,  $n_0$  is the ordinary refractive index,  $I = n_0 \epsilon_0 c |E|^2 / 2$  is the optical intensity of a probe beam and  $n_2 = \frac{3}{2n_0^2 \epsilon_0 c} \chi^{(3)}$  is the coefficient that characterizes the strength of the optical Kerr

nonlinearity, where  $c$  is the speed of light,  $\epsilon_0$  the permittivity of free space and  $\chi^{(3)}$  the third-order nonlinear optical susceptibility. A monochromatic beam, with vacuum wavelength  $\lambda$ , traversing a Kerr medium of length  $L$  will then experience a nonlinear phase shift

$$\phi_{\text{NL}} = \frac{2\pi}{\lambda} \chi^{(3)} |E|^2 L. \quad (6.2)$$

Conventional materials such as fused silica or silicon have rather small  $\chi^{(3)}$ , which are on the order of  $\sim 10^{-24}$ - $10^{-18}$   $\text{m}^2/\text{V}^2$  [155]. However, quantum logic protocols operate in the single-photon regime. At this level, these materials yield negligible phase shifts for typical settings [156]. This makes Kerr media-based optical quantum computing extremely challenging, if not impossible.

Advances in quantum optics have opened up new possibilities for realizing Kerr nonlinearities which show significant response at the single-photon level. For example, the saturation of atomic absorption can be employed. In the simplest case, an atom can be considered as a two-level system, having a single ground state  $|g\rangle$  and an excited state  $|e\rangle$ . It only absorbs light when it is in  $|g\rangle$ , whereas it emits or amplifies light when it is in  $|e\rangle$ . Such a two-level system can only absorb a single photon within the lifetime of its excited state. Thus, its response changes after the first absorption. In order to exploit the nonlinear response of an atom, deterministic interaction between the light field and the atom is required. To enhance the atom–light interaction different methods can be pursued. For example, it is possible to map the photon onto the collective state of an atomic ensemble using a second control field. For a weak probe field, the control field induces a spectral transparency window in the otherwise opaque medium through electromagnetically induced transparency (EIT) [157]. An additional switching laser that is coupled to another metastable state can then be used to destroy the quantum interference associated with EIT causing a strong nonlinear response [158].

An alternative approach exploits the strong atom–atom interactions for atoms in a state with a high principal quantum number, a so-called Rydberg state, onto which the photon is mapped using Rydberg EIT [159]. The nonlinearity in this case arises from the so-called Rydberg excitation blockade, which is a consequence of the strong interaction between two Rydberg atoms that tunes the two-photon transition out of resonance. This prevents the simultaneous excitation of two atoms that are separated by less than the blockade radius [160]. Thereby, it destroys the transparency for other incoming photons and leads to absorption for multiple photons.

Another technique is to enhance the nonlinearity by means of an optical resonator, thus allowing high nonlinear response with weak electromagnetic fields. The enhancement of the nonlinear interaction depends on the quality factor  $Q$  and mode volume  $V$  of the resonator. Of particular interest is the case where the nonlinearity is mediated by a single atom which is coupled to the resonator field. For strong coupling this gives rise to the nonlinear energy level structure of the Jaynes–Cummings model (cf. Sec. 4.1). In this regime, a single photon already saturates the atom, thus it modifies the response of the atom–resonator system at the level of single photons, yielding large nonlinearities [161, 162].

Using the aforementioned techniques a large variety of ground breaking experiments have been performed employing strong nonlinear effects for realizing single-photon switches [70, 163] and transistors [164–166], two-photon gateways [167], nondestructive photon detection [103],



and photon routers [69,71]. In addition, several implementations of nonlinear phase shifters have been demonstrated. For nonlinear phase-shifters, the seminal paper by Turchette et al. [168] achieved a nonlinear phase shift of  $0.1\pi$  in transmission of a high finesse Fabry-Pérot (FP) cavity containing a single atom. For the reflected signal from a single-sided photonic crystal cavity containing a weakly coupled quantum dot, a phase shift of  $0.015\pi$  was obtained [169]. Photons transmitted through an atomic ensemble showing Rydberg blockade combined with EIT achieved a nonlinear phase shift of  $0.32\pi$  [170]. Here, we report a nonlinear phase shift of  $\pi$  between the cases of individual photons and pairs of photons passing a whispering-gallery-mode (WGM) resonator which is coupled to a single atom. This amounts to the largest possible nonlinear phase shift for the smallest amount of light. In addition, we demonstrate that this effective photon-photon interaction causes entanglement of two initially independent photons.

At this point we should note, that after our results were published, two experiments were performed, showing large nonlinear response. The first stored a photon in an atomic ensemble which creates a phase shift of  $\pi$  for a second light pulse by means of Rydberg blockade combined with EIT [171]. The second experiment demonstrated a conditional phase shift of  $\pi/3$  between a signal photon stored in an atomic ensemble and a control photon traversing a cavity containing the memory [172].

This chapter is organized in the following manner. First, we introduce the working principle of our single-photon nonlinearity and the experimental procedure to observe it. Then, we investigate the phase shift introduced by the presence of a strongly coupled single atom. Most importantly, we study the nonlinear phase shift on the single-photon level and fully characterize the transmitted two-photon output state by means of quantum state tomography. Finally, we give a short outlook of how to realize a deterministic photon-photon gate using our system. Parts of this chapter were published in Ref. [173].

## 6.1 Working principle

In our experiment, we harvest the nonlinearity of a single atom by enhancing its interaction with the light field by means of an optical resonator. The first demonstrations of a single-photon nonlinearity in the realm of cavity quantum electrodynamics (CQED) were performed in transmission through a double-sided FP cavity. Since the on-resonant transmission through a FP, which is coupled to atoms, is very low, these experiments were conducted far detuned from resonance, resulting in rather small nonlinear phase shifts [168]. In order to avoid this limitation, we follow the proposal of Hoffman et al. [161], who suggested to use the reflection from a single-sided FP resonator that is operated in the over-coupled regime. Here, we employ a whispering-gallery-mode WGM resonator which is interfaced by a tapered fiber coupler. Making use of the chiral light-matter interaction, the fiber transmission is the physical equivalent of the reflection from a single-sided FP.

The nonlinearity is induced by a single  $^{85}\text{Rb}$  atom that is evanescently coupled to our WGM resonator. The system is sketched in Fig. 6.1. For the experiment we select a transverse magnetic (TM) polarized resonator mode. Light which is guided in the coupling fiber that couples to this mode has a polarization which, in the following, we will refer to as horizontally ( $H$ -) polarized.

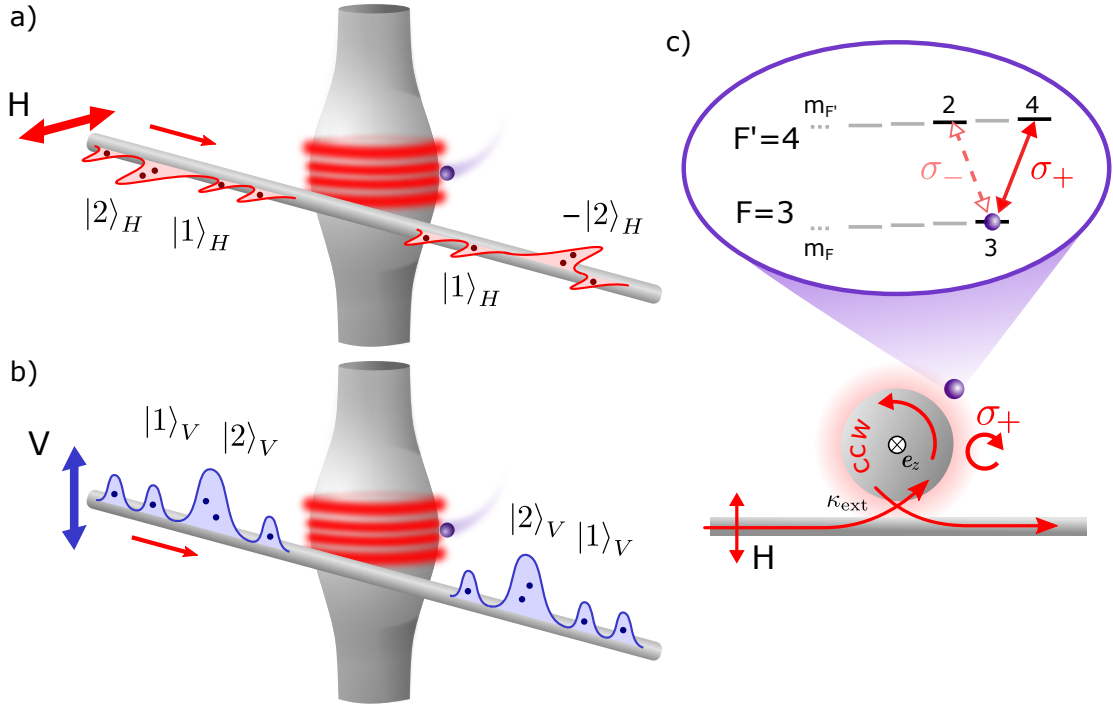


**Figure 6.1:** a) When the light is horizontally ( $H$ -) polarized, the presence of an atom in the resonator mode prevents single  $H$ -polarized photons from entering, and as a consequence, no phase shift occurs. However, in the case where two photons arrive at the same time, the response of the system changes due to the nonlinearity of the atom–resonator system and an additional phase shift of  $\pi$  is imprinted onto the light. b) In contrast, when the incident light is vertically ( $V$ -) polarized, it does not couple to the resonator mode. Thus, no phase shift occurs and the light simply passes the resonator unaffected. This polarization component serves as a phase reference. c) Schematic of the fiber–resonator and resonator–atom coupling including a scheme of the atomic levels involved. The interaction of the atom with the circularly polarized resonator light field, i.e.  $\sigma^+$ -polarized for the CCW propagating mode, drives the cycling transition  $|F=3, m_F=3\rangle \rightarrow |F=4, m_{F'}=4\rangle$ . In this case, the atom cannot emit photons into the counter-propagating,  $\sigma^-$ -polarized CW resonator mode. Thus, we obtain the favorable situation where the atom only interacts with a single resonator mode, similar to the case of a strongly birefringent, single-sided FP resonator.

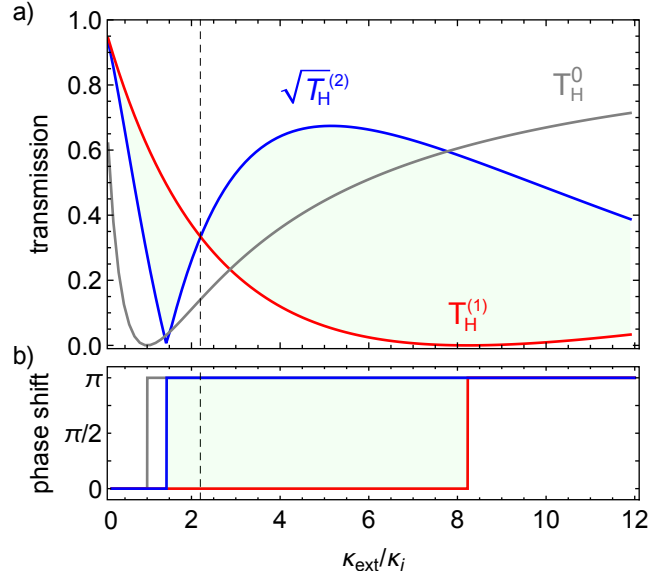


**Figure 6.2:** Comparison of single- and two-photon component of the output field as a function of the resonator–fiber coupling rate  $\kappa_{\text{ext}}$  in units of the intrinsic resonator loss rate  $\kappa_i$ . a) The single-photon transmission of  $H$ -polarized photons,  $T_H^{(1)}$ , compared to the square root of the two-photon transmission,  $(T_H^{(2)})^{1/2}$ . For comparison, the transmission for the empty resonator,  $T_H^0$ , is also shown. b) The phase of a single photon,  $\phi_1$ , two-photon component,  $\phi_2$ , in the output field. All curves are calculated on resonance for our experimental parameters  $(g, \gamma, \kappa_i) = 2\pi \times (13.5, 3, 8.4)$  MHz. The green shaded area indicates the parameter regime in which a) nonlinear transmission or b) nonlinear phase shifts occur. The dashed line indicates the point for which the spectra in Fig. 6.3 are plotted.

Light with orthogonal polarization, which will be referred to as vertically ( $V$ -) polarized light, does not couple to the resonator since, due to the strong birefringence of the resonator, no transverse electric (TE) modes exist close to the resonance frequency of the atom. Thus,  $V$ -polarized light is fully transmitted. On resonance, when  $H$ -polarized light passes the resonator it will partially couple into the resonator and then couple back into the fiber, thereby acquiring a phase shift of  $\pi$  due to the interaction with the resonator mode. The transmission through the coupling fiber of this polarization component is then given by

$$t_H = \frac{\kappa_L - \kappa_{\text{ext}}}{\kappa_L + \kappa_{\text{ext}}}. \quad (6.3)$$

Here,  $\kappa_{\text{ext}}$  is the fiber–resonator coupling strength,  $\kappa_L$  the resonator loss rate. For the case of an empty resonator, the losses stem from the intrinsic resonator losses,  $\kappa_L^0 = \kappa_i$ , where the superscript indicates the absence of the atom. In the following, we consider the case where the empty resonator operates in the over-coupled regime, i.e.,  $\kappa_{\text{ext}} > \kappa_L^0$ . In this regime, the amplitude of the light that couples from the resonator back into the fiber is larger than that of

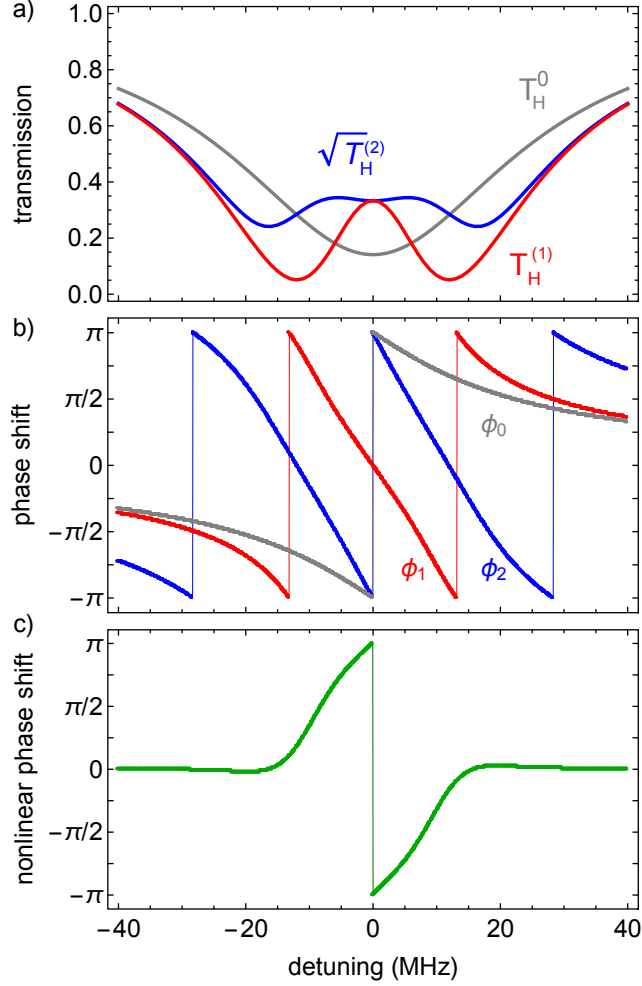


**Figure 6.3:** Comparison of single- and two-photon component of the output state as a function of the probe light detuning, for the setting where  $T_H^{(1)} = (T_H^{(2)})^{1/2}$  on-resonance, i.e.  $\kappa_{\text{ext}} = 2.8\kappa_i$ . a) The single-photon transmission of  $H$ -polarized photons,  $T_H$ , compared to the square root of the two-photon transmission,  $(T_H^{(2)})^{1/2}$ . For comparison, the transmission for the empty resonator,  $T_H^0$ , is shown. b) The phase of a single photon,  $\phi_1$ , and two-photon component,  $\phi_2$ , in the output field. c) Nonlinear phase shift which is calculated from  $\phi_{\text{NL}} = \phi_2 - 2\phi_1$ . All curves are calculated for our experimental parameters  $(g, \gamma, \kappa_i, \kappa_{\text{ext}}) = 2\pi \times (13.5, 3, 8.4, 23.5)$  MHz.

the light transmitted without interacting with the resonator. Consequently, the phase of the total light field in the nanofiber after the interaction with the resonator equals  $\pi$ , i.e.  $t_H^0 < 0$ .

The situation is different if an atom is coupled to the resonator. In this case, the presence of the atom, which interacts with strength  $g$  with the light in the resonator, significantly suppresses the intra-resonator field by changing the effective resonator loss rate to  $\kappa_L^{(1)} = \Gamma + \kappa_i$ , where the superscript indicates the presence of the atom and single photons impinging onto the resonator. The additional term  $\Gamma = \frac{g^2}{\gamma}$  is the atom-induced loss rate, which is given by the product of the excited state population per intra-resonator photon in the weak driving limit  $g^2/\gamma^2$ , multiplied by the atom decay rate  $\gamma$  (cf. Sec. 4.5.2). For sufficiently strong coupling strength  $\kappa_L^{(1)} > \kappa_{\text{ext}}$ , and the atom puts the system in the under-coupled regime. In this case, photons that arrive one by one do not acquire a phase shift, i.e.  $t_H^{(1)} > 0$ . Thus, the presence of the atom can be used to shift the phase of single photons, if  $\kappa_L^0 < \kappa_{\text{ext}} < \kappa_L^{(1)}$ .

However, as the atom is strongly coupled to the resonator, it acts as a saturable absorber on the single-photon level. As a consequence, the atom-induced losses per photon are significantly smaller when two  $H$ -polarized photons are incident on the resonator at the same time, i.e.  $\kappa_L^{(2)} \ll \kappa_L^{(1)}$ . For adequate values of  $\kappa_{\text{ext}}$ , i.e.  $\kappa_L^{(2)} < \kappa_{\text{ext}} < \kappa_L^{(1)}$ , the system is again in the over-coupled regime and the two-photon wavefunction acquires a phase of  $\pi$ , i.e.  $t_H^{(2)} < 0$ , as shown in Fig. 6.1a. When neglecting optical losses, the interaction with the coupled atom–resonator system modifies  $H$ -polarized photons according to

$$\begin{aligned} |1\rangle_H &= \hat{a}_H^\dagger |0\rangle \longmapsto \hat{a}_H^\dagger |0\rangle, \\ \sqrt{2} |2\rangle_H &= \hat{a}_H^\dagger \hat{a}_H^\dagger |0\rangle \longmapsto -\hat{a}_H^\dagger \hat{a}_H^\dagger |0\rangle. \end{aligned} \quad (6.4)$$

In Eq. (6.4), we have introduced the creation operator for a photon in the output mode of the coupling fiber at a given time,  $\hat{a}_H^\dagger$ . Since the phase acquired by pairs of photons is not twice the phase shift acquired by single photons, this corresponds to a nonlinear phase shift, which in this ideal situation is  $\pi$ .

In order to incorporate photon loss which is introduced by the atom–resonator system, we define transmission coefficients for single photons and pairs of photons in the output mode as

$$t_H^{(1)} = \frac{\langle \hat{s}_{\text{out}}^\dagger \rangle}{\langle \hat{s}_{\text{in}}^\dagger \rangle} \quad \text{and} \quad t_H^{(2)} = \frac{\langle \hat{s}_{\text{out}}^\dagger \hat{s}_{\text{out}}^\dagger \rangle}{\langle \hat{s}_{\text{in}}^\dagger \hat{s}_{\text{in}}^\dagger \rangle}, \quad (6.5)$$

where we introduced the creation operator of the  $H$ -polarized input field  $\hat{s}_{\text{in}}^\dagger$  and of the output field  $\hat{s}_{\text{out}}^\dagger$  operators. The latter can be obtained from the input–output relation  $\hat{s}_{\text{out}} = \hat{s}_{\text{in}} - \sqrt{2\kappa_{\text{ext}}}\hat{a}_{\text{res}}$ , using the resonator field operator  $\hat{a}_{\text{res}}$ . From Eq. (6.5), we can compute  $T_H = |t_H^{(1)}|^2$  and  $T_{HH} = |t_H^{(2)}|^2$ , which give the ratio between the expectation value for obtaining one or two photons at the output for light that interacted with the atom–resonator system or not. The respective phases of the one- and two-photon component are given by

$$\phi_1 = \arg(\hat{s}_{\text{out}}^\dagger) \quad \text{and} \quad \phi_2 = \arg(\hat{s}_{\text{out}}^\dagger \hat{s}_{\text{out}}^\dagger). \quad (6.6)$$

For a linear system, the state of photon pairs should be the product of the two single-photon states, thus  $T_H^{(2)} = T_H^{(1)} \cdot T_H^{(1)}$  and  $\phi_2 = 2\phi_1$ . In order to get an idea of how the experimental

parameters influence this process we numerically calculate these transmission values. For this purpose, we only consider a two-level atom coupled to a single resonator mode for which we do not take into account its imperfect circular polarization in order to reduce computational complexity. To correctly account for two-photon effects, we include the first two excitations of the resonator mode and use a weak coherent field as input. Figure 6.2a shows  $T_H^{(1)}$  and  $(T_H^{(2)})^{1/2}$ , as a function of the resonator–fiber coupling rate in the presence and absence of an atom. The corresponding phases for the empty resonator, single-photon and two-photon component,  $\phi_0$ ,  $\phi_1$  and  $\phi_2$ , are plotted in Fig. 6.2b. The phase flips occur at the respective critical coupling points. Thus, in order to obtain a nonlinear phase shift, we have to set the resonator–fiber coupling to this intermediate region. In Fig. 6.3 the spectral response of the system in this intermediate region is plotted in addition with the resulting nonlinear phase shift,  $\phi_{\text{NL}} = \phi_2 - 2\phi_1$ . From these plots it becomes evident that it is essential to work on resonance to obtain the maximal nonlinear phase shift.

In order to measure the phase shift experimentally, we launched  $H$ - and  $V$ -polarized light through the coupling fiber. As already mentioned, the  $V$  component does not couple to the TM resonator mode and is thus not affected by the resonator (see Fig. 6.1d). Thus, when sending, both  $H$ - and  $V$ -polarized light through the coupling fiber, the  $V$ -component can act as phase reference for the  $H$ -component. Choosing  $+45^\circ$  (i.e.,  $H+V$ ) as input polarization, the quantum states for the case of two photons before and after the interaction with a lossless atom–resonator system are given by

$$\begin{aligned} |\psi_{\text{input}}\rangle &= \frac{1}{2\sqrt{2}} \left( \hat{a}_H^\dagger \hat{a}_H^\dagger + 2\hat{a}_H^\dagger \hat{a}_V^\dagger + \hat{a}_V^\dagger \hat{a}_V^\dagger \right) |0\rangle = \frac{1}{\sqrt{2}} \hat{a}_D^\dagger \hat{a}_D^\dagger |0\rangle \\ &= \frac{1}{2} \left( \hat{a}_V^\dagger \hat{a}_D^\dagger + \hat{a}_H^\dagger \hat{a}_{\bar{D}}^\dagger \right) |0\rangle, \end{aligned} \quad (6.7)$$

$$\begin{aligned} |\psi_{\text{output}}\rangle &= \frac{1}{2\sqrt{2}} \left( -\hat{a}_H^\dagger \hat{a}_H^\dagger + 2\hat{a}_H^\dagger \hat{a}_V^\dagger + \hat{a}_V^\dagger \hat{a}_V^\dagger \right) |0\rangle \\ &= \frac{1}{2} \left( \hat{a}_V^\dagger \hat{a}_D^\dagger - \hat{a}_H^\dagger \hat{a}_{\bar{D}}^\dagger \right) |0\rangle, \end{aligned} \quad (6.8)$$

respectively. Here we introduced the creation operators for vertical, plus ( $D$ ), and minus ( $\bar{D}$ )  $45^\circ$ -polarized photons  $a_V^\dagger$ ,  $a_D^\dagger = (a_H^\dagger + a_V^\dagger)/\sqrt{2}$  and  $a_{\bar{D}}^\dagger = (a_H^\dagger - a_V^\dagger)/\sqrt{2}$ , respectively. Due to the nonlinear interaction, an additional phase occurs for the  $a_H^\dagger a_H^\dagger |0\rangle$  term which, in the case of a  $\pi$  phase shift, results in the minus sign. As a consequence, the output state  $|\psi_{\text{output}}\rangle$  is no longer separable. Thus, two previously independent photons are entangled, which becomes evident when comparing the last expressions in Eq. (6.7) and Eq. (6.8).

## 6.2 Experimental procedure

In the following, we want to experimentally study the phase shift induced by our system in two situations. First, we investigate the phase shift between the case of an empty resonator and the case where a strongly coupled atom is present in the resonator mode. Second, we will look at

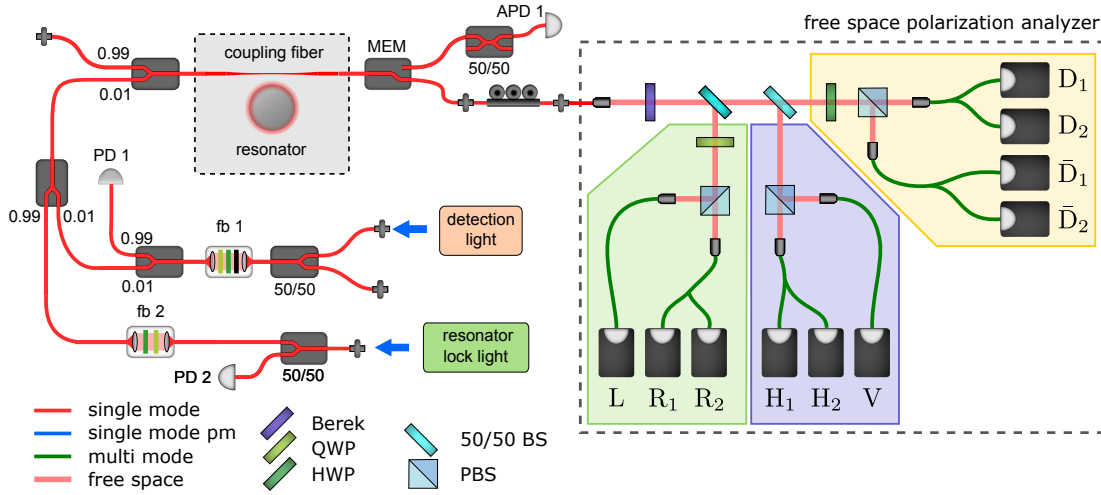


**Figure 6.4:** The setup for measuring the nonlinear phase shift consists of the fiber network and a free space polarization analyzer. For an explanation of the symbols used see legend in App. A.9.

the nonlinear phase shift between the case where one or two photons simultaneously interact with the atom–resonator system. For this purpose, we use the TM polarized mode #3 which has an internal loss rate  $\kappa_0 = 2\pi \times 5$  MHz and a mode–mode coupling  $h = 2\pi \times 6.8$  MHz (cf. Sec. 5.2.5), which for simplicity we treat in our theoretical model as a total intrinsic loss rate  $\kappa_i = \sqrt{\kappa_0^2 + h^2} = 2\pi \times 8.4$  MHz. This mode was chosen, because it enables stable coupling to the fiber for  $\kappa_{\text{ext}} \gg \kappa_i$ . We tune the bottle microresonator (BMR) and the incident light into resonance with the  $|F=3\rangle \rightarrow |F'=4\rangle$  transition of the  $D_2$ -line of  $^{85}\text{Rb}$ . Furthermore, we make use of the chiral light–matter interaction, which occurs for TM modes that are coupled to atoms in the cycling transition (cf. Sec. 4.4), to realize the situation where the atom only interacts with a single resonator mode, as depicted in Fig. 6.1c. We probe the coupled atom–resonator system by continuously sending a weak coherent laser beam onto the resonator with a power corresponding to a flux of 14 photons/ $\mu\text{s}$ . This corresponds to an intra-resonator photon number of  $n_{\text{res}} = 0.13$ , for a critically coupled, empty resonator. The polarization properties of the transmitted light are then investigated using a polarization analyzer setup, as shown in Fig. 6.4. This free space setup analyzes the light’s polarization in three orthogonal bases which are separated from the output beam using nonpolarizing beam splitters (BSs). Each basis is equipped with wave plates or a Berek compensator and a polarizing beam splitter (PBS) cube to perform a projective measurement. The bases are adjusted such that the first PBS projects onto the resonator eigenbasis, given by  $(H-V)$ , the second PBS projects onto  $\pm 45^\circ$  polarization basis,  $(D-\bar{D})$ , and the third PBS on the right and left circular polarization basis,  $(R-L)$ . While  $H-V$  is fixed by the resonator mode, the other two are assigned arbitrarily since we cannot identify the relative phase between the two components. After passing through the PBS the beams are coupled into multi-mode fibers and sent onto single photon counting modules (SPCMs). For the reconstruction of the two-photon polarization state we have to analyze the cases where two photons simultaneously exit the coupling fiber. For this, we measure correlations of photon

detection events between combinations of basis states. In order to measure the correlations between the same basis states, some ports are equipped with multi-mode fiber beam splitters. Due to the limited number of SPCMs available, only a single SPCM is used in the  $V$  and  $L$  basis. In total, we employ ten SPCMs, as shown in Fig. 6.4. The arrival times of all photons are then recorded by the time-tagger FPGA (cf. Sec. 5.4.7) and are then used to calculate the transmission to the respective ports and to compute photon correlation functions.

### 6.2.1 Atom detection for an over-coupled resonator

For the experiments discussed in this chapter, the empty resonator is not critically coupled, but has to be over-coupled. Thus, we require a new scheme to detect atoms in the resonator field, which is introduced in the following (see also Sec. 5.4.7 or Ref. [128]). We adjust the ratio of the amplitudes of the two polarization components,  $H$  and  $V$ , of the incident light field such that they have the same amplitude after the interaction with the empty resonator. Without atom, the resonator imprints a phase shift close to  $\pi$  on the  $H$ -component of the incident light and rotates the output polarization to  $\bar{D}$ , thereby minimizing the power at the  $D$ -detectors. When an atom couples to the resonator, this phase shift disappears and the transmission of the  $H$ -component changes. This results in a change of the polarization of the transmitted light which causes a measurable signal on the  $D$ -detectors. This realizes a situation similar to our standard detection scheme and allows us to detect atoms in the over-coupled regime. After the atom detection, we collect our measurement data in the subsequent 500 ns time interval, followed by a 1  $\mu$ s re-detection, which ensures that the atom is still coupled to the resonator at the end of the measurement window. For the atom detection we employed a first trigger criterion of  $N_{\text{trig}} = 7$  within 1.2  $\mu$ s and a second trigger criterion  $N_{\text{trig}2} = 2$  for the re-detection.

## 6.3 Single-atom phase shift and polarization rotation

Before investigating nonlinear effects, we analyze the polarization change of the transmitted light between the empty resonator case and the case where an atom is coupled. This polarization change stems from the phase shift of the probing field conditioned on the presence of the atom. Such a phase shift is key for realizing nondestructive photon detection [103] or the realization of atom–photon entanglement [174, 175]. In order to find the optimum working point we measure the atom-induced phase shift, as a function of the fiber–resonator coupling strength  $\kappa_{\text{ext}}$ . To determine the phase shift it is sufficient to measure the power detected in the ports of the  $H$ - $V$  and  $D$ - $\bar{D}$  basis, for the case with atom,  $P_H$ ,  $P_V$ ,  $P_D$  and  $P_{\bar{D}}$ , and without an atom present,  $P_H^0$ ,  $P_V^0$ ,  $P_D^0$  and  $P_{\bar{D}}^0$ . The transmitted powers are normalized to the total signal obtained in the respective basis when the resonator is far detuned from the probe frequency, and are shown in Fig. 6.5. In the case where no atom is present, the transmitted field is purely  $\bar{D}$ -polarized. The atom now shifts the phase between the  $H$ - and  $V$ -component and causes the polarization to rotate. In the ideal case, when the transmitted amplitudes do not change due to the atom, the interaction only causes the sign of the  $H$ -component to flip, and we expect the output field to be  $D$ -polarized. From a polarization analysis, we determine the overlap of the output light field with  $D$ -polarization, as well as, the survival probability of the incident photons. The results



are shown in Fig. 6.6a. We observe a monotonous increase of the photon survival probability with the coupling rate  $\kappa_{\text{ext}}$  while the overlap with  $D$ -polarization reaches a maximum of 0.82 for  $\kappa_{\text{ext}} = 2 \kappa_i$ . This demonstrates the significant effect a single atom has on the transmitted light.

In order to model this behavior theoretically, we assume a normal distribution of the atom–resonator coupling strength  $g$ , which originates from the motion of the atom through the resonator mode. We then fit this distribution, with the mean coupling strength  $\bar{g}$ , the standard deviation  $\sigma_g$ , and the detuning between the atom and the probe light as the only free parameters. From this fit, which very well reproduces our measurements, we obtain  $\bar{g} = 2\pi \times (13.5 \pm 1.5)$  MHz,  $\sigma_g = 2\pi \times 4$  MHz and  $\Delta_{AP} = 2\pi \times 2.2$  MHz.

Assuming that the  $V$ -polarized light is unaffected by the resonator, the relative phase shift  $\Delta\phi$  introduced by the atom can be obtained by comparing the phase shift introduced by the empty resonator  $\phi_0$  with the phase shift when the atom is present  $\phi_1$  and can be directly inferred from the measurements in Fig. 6.5 via [176]:

$$\Delta\phi = \phi_1 - \phi_0 \quad \text{using} \quad \cos(\phi_i) = \frac{P_D^i - P_D^i}{2\sqrt{P_H^i P_V^i}} \quad (6.9)$$

Here, the superscript of  $P$  indicates whether the transmitted power is measured with or without the atom present. In Fig. 6.6b,  $\Delta\phi$  is plotted as a function of the resonator–fiber coupling strength. For  $\kappa_{\text{ext}} = 1.9\kappa_i$  we obtain a maximal phase shift of  $\phi_{\text{lin}} = 0.85\pi$ . This conditional phase shift is comparable to the results in [174, 177] and much larger than those recently reported for solid-state systems [178]. The fact that we do not reach the maximal value of  $\pi$  can be related to the non-zero detuning and the distribution in coupling strengths. For the optimal setting the largest atom-induced phase shift is accompanied by a small probability of recovering the photon  $(P_H^0 + P_H^i)/2 = 0.2$ . For higher recovery probability one would have to increase  $\kappa_{\text{ext}}$  for which finite detunings however would significantly reduce the phase shift (cf. lines in Fig. 6.6b).

## 6.4 Measuring single-photon nonlinearity

In order to measure the nonlinear response of our atom–resonator system, we have to determine the phase shift between the single and pairs of photon exiting the coupling fiber. This is achieved by means of quantum state tomography. From that, we will be able to examine the nonlinear behavior of our system and the nonclassicality of the obtained output state.

### 6.4.1 Correlation measurements and tomography

We now choose the working point  $\kappa_{\text{ext}}^{\text{nl}} = 2.8 \kappa_i = 2\pi \times 23.5$  MHz, for which we expect a photon number-independent loss and, as a consequence, an effective dispersive nonlinearity. In order to experimentally determine the nonlinear phase shift imprinted on the weak coherent input field, we analyze the transmitted light in three complementary polarization bases by recording correlation counts between the different detectors. Figure 6.7 shows the measured correlations recorded for all detector combinations. In total, we obtain a set of 19 non-trivial combinations

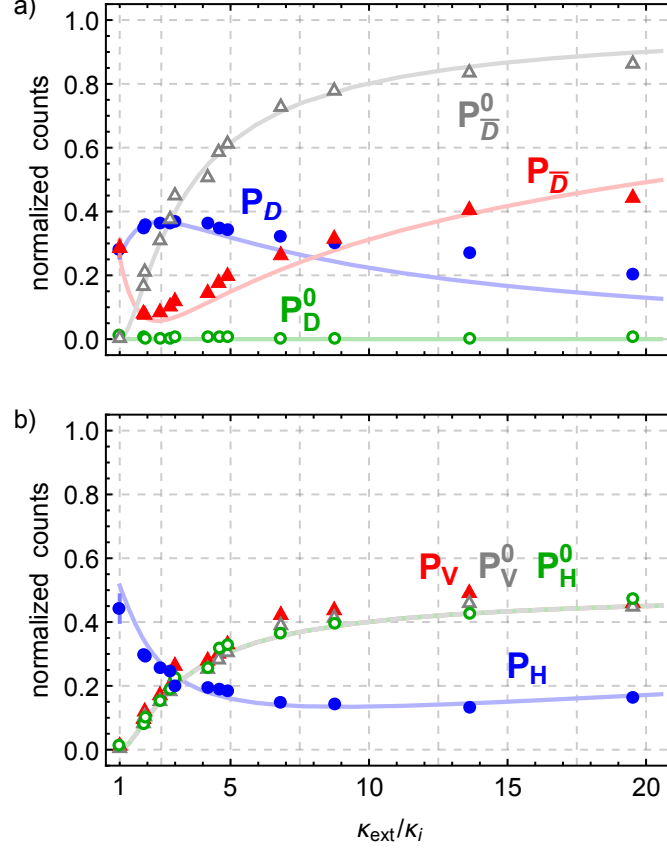


**Figure 6.5:** a) (b) Measured power  $P_D$  and  $P_{\bar{D}}$  ( $P_H$  and  $P_V$ ) at the respective port of the polarization analyzer, normalized to the total incident power at each basis when the resonator is far off-resonant, as a function of the resonator–fiber coupling strength  $\kappa_{\text{ext}}$  (in units of  $\kappa_i = 2\pi \times 8.4$  MHz). In order to determine  $\kappa_{\text{ext}}$  for each fiber setting, we employ the procedure described in Sec. 5.4.4. Solid lines are a theoretical fit of the data, which yields a variation of the atom–resonator coupling strength ( $\bar{g} = 2\pi \times 13.5$  MHz,  $\sigma_g = 2\pi \times 4$  MHz) and an atom–light detuning of  $\Delta_{AP} = 2\pi \times 2.2$  MHz. Without atom, the input polarization is adjusted such that all light is sent onto the  $\bar{D}$ -port, and  $P_{\bar{D}}^0 \approx 1$ . Thus, the  $V$ -component has the same amplitude as the  $H$ -component after passing the resonator, i.e.  $P_H^0 = P_V^0$ . As a consequence, for measurements close to critical coupling,  $\kappa_{\text{ext}} \approx \kappa_i$ , the  $V$ -component of the incoming light is small. The presence of the atom increases the power measured in the  $D$ -port. This signal is used for heralding the atom coupling event. Since the  $V$ -component does not couple to the resonator, it is unaffected by the presence of the atom, i.e.  $P_V = P_V^0$  independent of  $\kappa_{\text{ext}}$ .

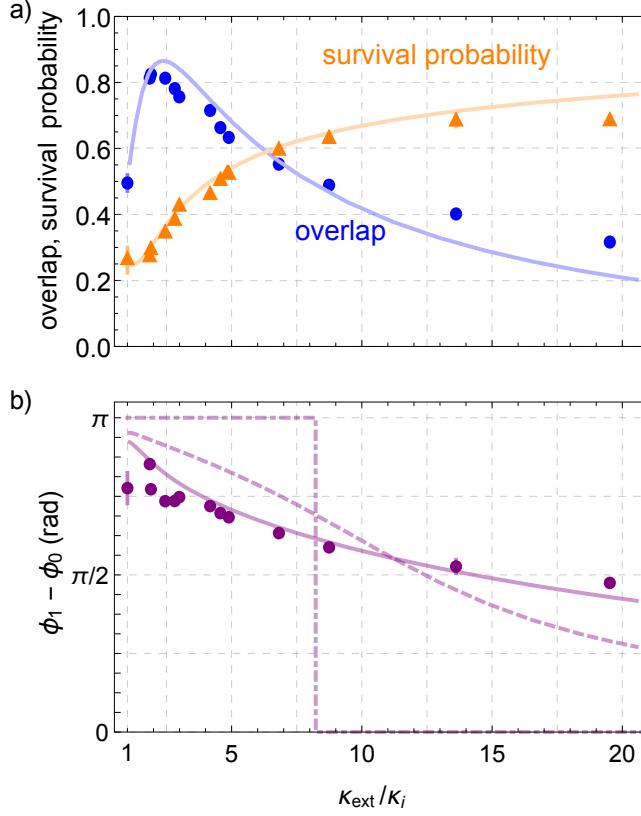


**Figure 6.6:** a) Overlap of the polarization of the transmitted light with  $D$ -polarization and survival probability of the incident photons as a function of the resonator–fiber coupling strength  $\kappa_{\text{ext}}$  (in units of  $\kappa_i$ ). The input polarization was set such that, without an atom coupled to the resonator, the transmitted light was fully  $D$ -polarized. The maximum overlap with  $D$ -polarization is observed at  $\kappa_{\text{ext}} = 2\kappa_i$ . The solid line is the theoretical prediction using the parameters obtained from fitting the power transmission (cf. Fig. 6.5). b) Phase shift caused by the presence of the atom,  $\phi_1 - \phi_0$ , as a function of the resonator–fiber coupling strength  $\kappa_{\text{ext}}$ . Error bars correspond to the  $1\sigma$  statistical error. The solid line correspond to theoretical predictions using the fitted parameters which include a detuning of  $\Delta_{AP} = 2\pi \times 2.2$  MHz and a distribution of atom–resonator coupling strengths. The dashed lines show the phase shift obtained for a single coupling strength  $g = 2\pi \times 20$  MHz with detuning. For comparison, the dotted line corresponds to the phase shift obtained on resonance and for a single coupling strength  $g = 2\pi \times 20$  MHz. In this case, the phase shift vanishes for  $\kappa_{\text{ext}} > g^2/\gamma + \kappa_i \approx 8.2\kappa_i$ .

detector	H <sub>1</sub>	H <sub>2</sub>	V	D <sub>1</sub>	D <sub>2</sub>
transmission	0.107	0.104	0.202	0.213	0.208

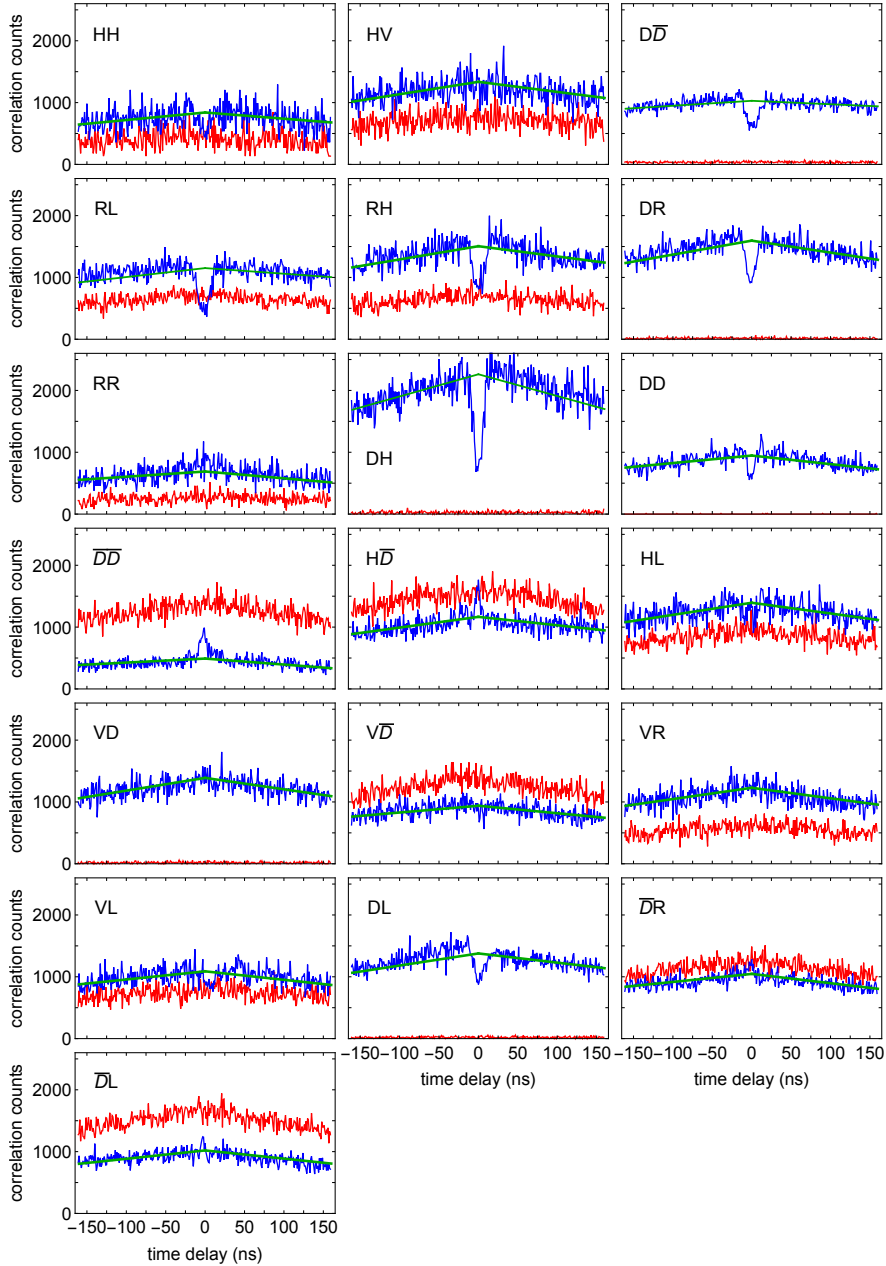
  

detector	$\bar{D}_1$	$\bar{D}_2$	R <sub>1</sub>	R <sub>2</sub>	L
transmission	0.264	0.186	0.160	0.157	0.339

**Table 6.1:** Transmission probability of a photon to the detector, which measures the photon eigenpolarization (e.g. of an  $H$ -polarized photon to the detector H<sub>1</sub>) in our polarization analyzer setup, shown in Fig. 6.4.

of correlations. The correlation settings  $VV$  and  $LL$  were not accessible because only one SPCM was available for the  $V$  and the  $L$  basis. The correlation functions linearly decrease for large time delays between the photons which is a consequence of the finite time window of 500 ns used for recording the correlation functions. We clearly observe photon bunching and anti-bunching for certain combinations at zero time delay that vanishes when the time delay between the photons increases beyond the effective atomic lifetime  $\tau_{sp} = 1/2\gamma' = 8$  ns, where  $\gamma' = g^2/(\kappa_{\text{ext}} + \kappa_i) + \gamma$  is the Purcell-enhanced emission rate [179]. The (anti-) bunching indicates that two simultaneously arriving photons have a different polarization than individual photons. In the following, we want to determine the nonlinear phase shift by comparing the phase acquired by two photon output states with one or two  $H$ -polarized photons. This information is contained in the density matrix of the two-photon polarization state. In order to reconstruct this density matrix from the measured correlations, we have to correct the measured data for the detector efficiency and the optical losses along the respective path. This is given by the product of the transmission probabilities given in Tab. 6.1 for each detector combination. For correlations of two photons in the same polarization state, an additional correction factor of 2 occurs. This is necessary since we evaluate only cross-correlations and not auto-correlations for reconstructing the photon density matrix, which are not available due to the detector dead time. In Tab. 6.2 the corrected coincidence counts together with the normalized correlation functions for zero time delay,  $C^{(2)}(0)$ , are listed. Depending on the chosen detector combination, they show significant bunching or anti-bunching, with values ranging from 0.35 to 1.73. However, no bunching or anti-bunching features are apparent in the absence of the atom, as shown in Fig. 6.7. This verifies that the atom is the physical origin of the nonlinearity. These normalized correlation counts will in the following be used for reconstructing the density matrix of the two-photon output state.

In our experiment, the photons under investigation are guided in the same fiber mode, and are thus indistinguishable by our measurement. Thus we have no means of labeling the photons. As a consequence, not all 16 entries of the  $4 \times 4$  density matrix can be determined. Instead, we



**Figure 6.7:** Measured correlation functions between different detector combinations as a function of the delay between detection events for a bin size of 3 ns. Data are corrected for optical losses to the respective detectors. The respective combination of bases is indicated in the upper left corner of each plot. The green lines are fits to the long time-delay behavior of the data. The case where an atom couples to the resonator is shown by blue data. For comparison, the empty resonator case is shown in red. In the absence of the atom, all correlations involving the  $D$ -detectors are almost zero, since this port is supposed to be dark for atom detection.

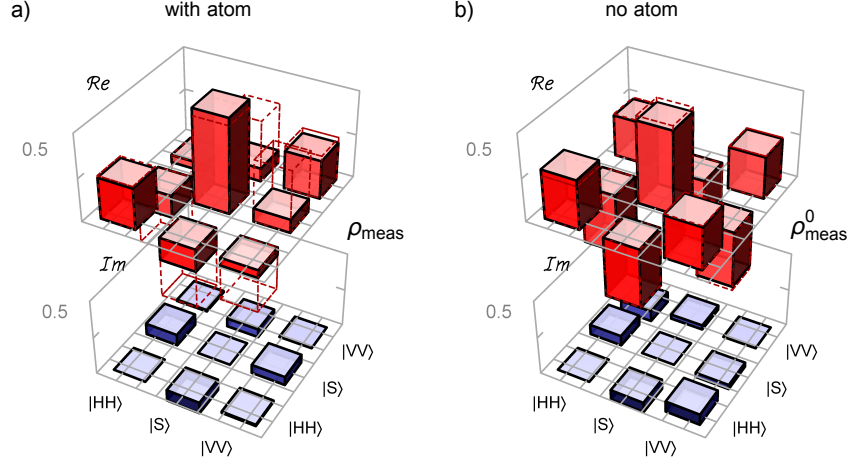


**Figure 6.8:** The reconstructed density matrix  $\hat{\rho}_{\text{meas}}$ , a) for the case when an atom is coupled and b) when no atom is present. The real and imaginary parts are displayed in red and blue, respectively. The dashed lines indicate the density matrix for the ideal state  $\hat{\rho}_{\text{output}}$ .

can identify the accessible density matrix [180, 181]

$$\hat{\rho}_{\text{acc}} = \begin{pmatrix} \begin{pmatrix} \rho_{HH,HH} & \rho_{HH,S} & \rho_{HH,VV} \\ \rho_{S,HH} & \rho_{S,S} & \rho_{S,VV} \\ \rho_{VV,HH} & \rho_{VV,S} & \rho_{VV,VV} \end{pmatrix} & 0 \\ 0 & (\rho_{A,A}) \end{pmatrix}, \quad (6.10)$$

which consists of a  $3 \times 3$  symmetric and  $1 \times 1$  antisymmetric subspace. In Eq. (6.10) we used the basis states  $|HH\rangle$  and  $|VV\rangle$ , as well as the symmetric and the antisymmetric basis states  $|S\rangle = (|HV\rangle + |VH\rangle)/\sqrt{2}$  and  $|A\rangle = (|HV\rangle - |VH\rangle)/\sqrt{2}$ , respectively. The lack of coherence between the symmetric and antisymmetric subspaces reflects the lack of information about the labeling of the photons. Since photons are bosons, their overall wavefunction has to be symmetric. As long as there is no distinguishing degree of freedom, photons can only populate the symmetric  $3 \times 3$  subspace. However, the existence of an additional degree of freedom, which is correlated with the polarization and is ignored by our measurement, can be inferred from population in the antisymmetric subspace. In our experiment, the photons originate from a coherent laser beam. Thus, we can assume that the photons arrive within a time much shorter than the coherence time of our laser ( $\sim 1 \mu\text{s}$ ) and are thus indistinguishable in all degrees of freedom. As a consequence, the two-photon state of simultaneously arriving photons should be limited to the symmetric subspace of a two-qubit Hilbert space, i.e.  $\rho_{A,A} = 0$ . In App. A.7 we verify that the reconstruction of the full  $4 \times 4$  accessible density matrix gives the same results as the reconstruction of the restricted  $3 \times 3$  subspace.

For the reconstruction of the density matrix of the two-photon output state, we use the 19 corrected correlation functions. The reconstruction is performed by numerically finding the den-

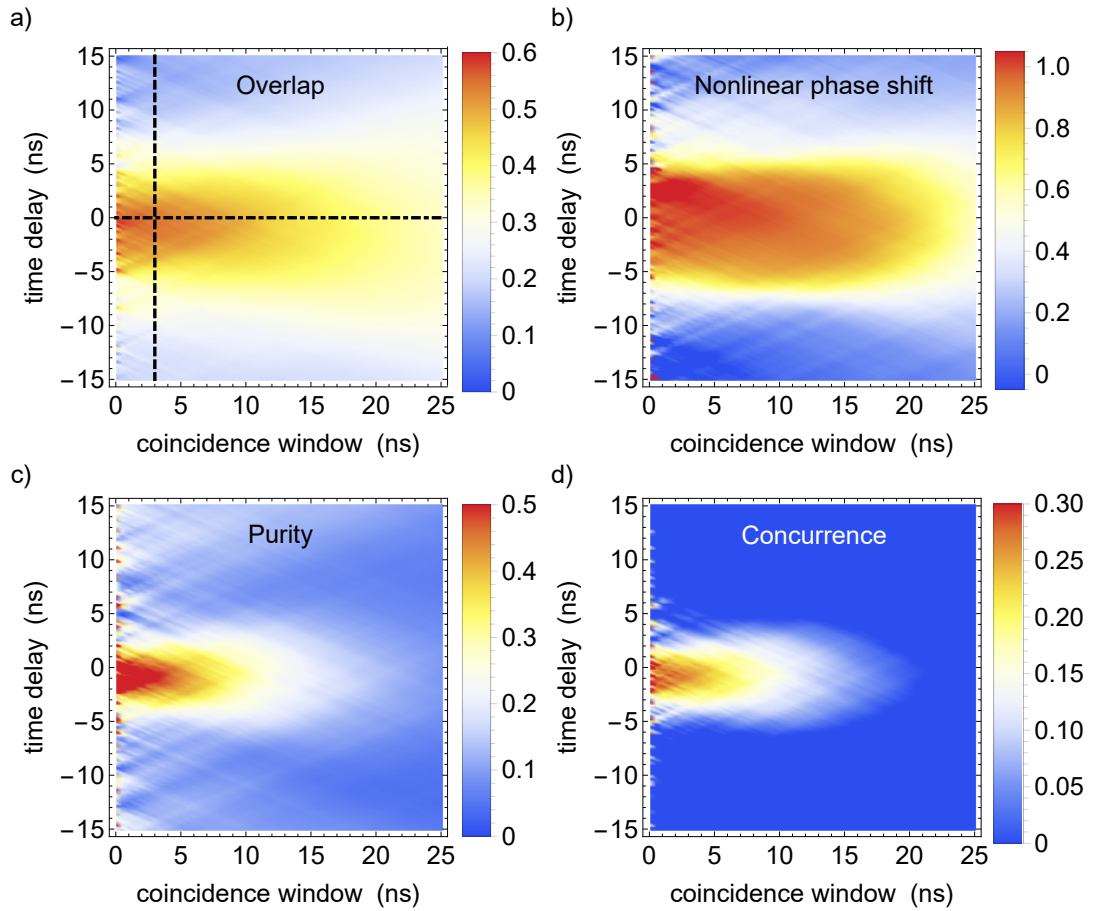
	HH	HV	D $\bar{D}$	RL	RH	DR	RR	DH	DD	$\bar{D}\bar{D}$
$C_{\text{nl}}$	1429	4163	1921	1435	2535	2854	2471	2361	1870	2552
$C_0$	2519	4007	3086	3299	4515	4785	2067	6784	2841	1473
$C^{(2)}(0)$	0.57	1.04	0.62	0.44	0.56	0.60	1.20	0.35	0.66	1.73

	$\bar{D}H$	HL	VD	$V\bar{D}$	VR	VL	DL	$\bar{D}R$	$\bar{D}L$
$C_{\text{nl}}$	4918	4100	4159	2533	3578	2718	2732	3574	3165
$C_0$	3497	4205	4167	2815	3686	3265	4132	3140	3058
$C^{(2)}(0)$	1.41	0.98	1.00	0.90	0.97	0.83	0.66	1.14	1.03

**Table 6.2:** Corrected correlation counts  $C_{\text{nl}}$  for zero time delay and a time window of 3 ns, compared to the expected correlation counts  $C_0$  for independently arriving photons, which we obtain by extrapolating the behavior at large time delays to zero delay (see green lines in Fig. 6.7). From these values we calculated the normalized correlation function  $C^{(2)}(0) = C_{\text{nl}}/C_0$ .

sity matrix of the two-photon state that best describes our measured data using a maximum likelihood estimation [182]. The reconstruction procedure is discussed in detail in App. A.7. Figure 6.8 shows the reconstructed density matrix  $\hat{\rho}_{\text{measured}}$  for zero mean detection time difference and a width of 3 ns for the coincidence window. The reconstructed density matrix is in good qualitative agreement with the density matrix that is expected for the output state  $\hat{\rho}_{\text{output}} = |\psi_{\text{output}}\rangle\langle\psi_{\text{output}}|$  under ideal conditions. For comparison, we also show the density matrix reconstructed from correlations obtained for the case without an atom coupled to the resonator,  $\hat{\rho}_{\text{measured}}^0$ . Figure 6.9a shows the overlap of the measured two-photon state with the ideal state,  $\langle\psi_{\text{output}}|\hat{\rho}_{\text{measured}}|\psi_{\text{output}}\rangle$  as a function of the time delay between the photon detections and the length of the coincidence window. For clarity, we also plot cuts for varying mean delay along 3 ns window length, and zero mean delay as a function of the window length in Fig. 6.10. In order to obtain a measure of decoherence in our system, i.e. to what extent the output state is in a mixed state, we compute the purity  $\text{Tr}[\hat{\rho}^2]$  of the final state, which is shown in Fig. 6.10 and Fig. 6.9c. The maximal purity of  $\hat{\rho}_{\text{measured}}$  is  $0.48 \pm 0.02$  indicating a significant reduction of coherence, which also accords well with the fact that the diagonal elements of the measured density matrix agree well with the theory while the off-diagonal elements are much reduced. The loss of coherence originates predominantly from averaging over shot-to-shot fluctuations of the atomic position which results in a fluctuating atom–resonator coupling strength and a concomitant variation of the output state. Another source of decoherence originates from cases where three photons simultaneously interact with the resonator, which we cannot distinguish from two-photon states. For our experimental setting, the average photon number of the incident light within the 3 ns coincidence window is 0.04, from which, together with the known losses and detection efficiencies, we estimate that approximately 4.1% of the detected correlations originate from three-photon events.



**Figure 6.9:** a) Overlap of the experimentally prepared state  $\hat{\rho}_{\text{measured}}$  with the ideal state  $\hat{\rho}_{\text{output}}$ . b) Nonlinear phase shift, c) purity and d) concurrence of the two-photon state as a function of the coincidence window size and the mean photon–photon delay. Data are calculated from the corresponding density matrices, which are obtained from a maximum likelihood estimation. The dashed lines in a) indicate the data plotted in Fig. 6.10



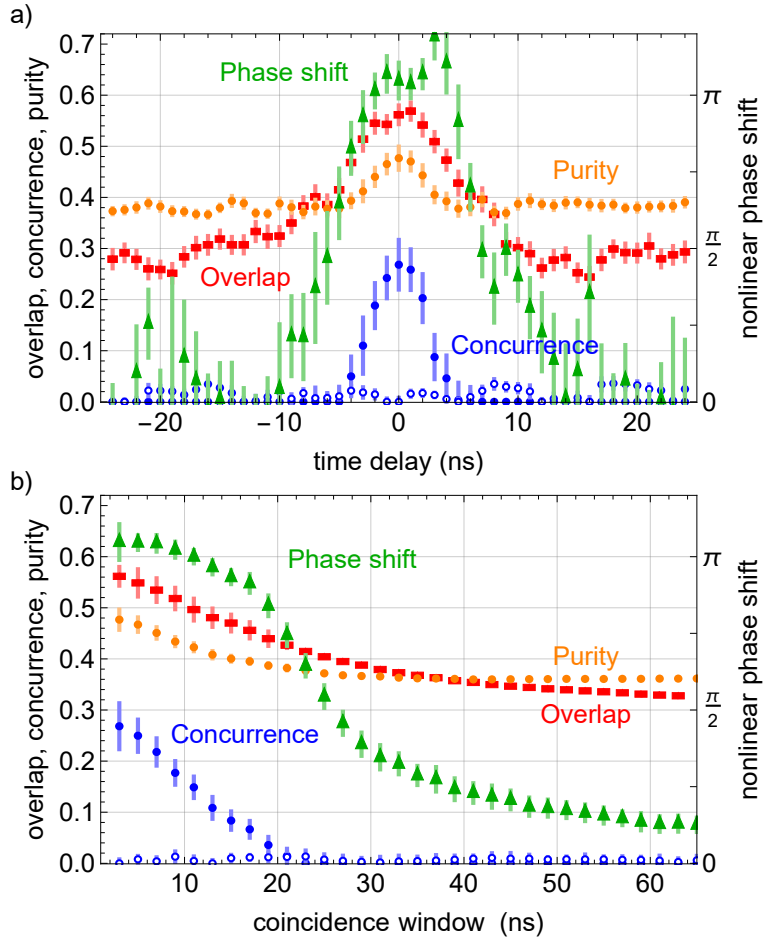


**Figure 6.10:** Overlap with the ideal state, nonlinear phase shift, purity and concurrence of the measured output state plotted for a) a fixed coincidence window of 3 ns as a function of the delay between two photon detections and b) for zero delay as a function of the coincidence window length. For comparison, the concurrence obtained without the atom is shown as well (open blue circles). The error bars were determined by adding Poissonian noise to the measured correlations, followed by a density matrix reconstruction and subsequent evaluation of the respective quantity. The plotted data corresponds to the values along the dashed lines in Fig. 6.9a.

### 6.4.2 Nonlinear phase shift and entanglement

We can use the reconstructed density matrix to further characterize the two-photon output state. In particular, the nonlinear phase shift can be determined directly from the density matrix according to

$$\phi_{\text{NL}} = \phi_2 - 2\phi_1 = \phi_{HH} - 2\phi_{HV} = \arg(\hat{\rho}_{HH,A}) - \arg(\hat{\rho}_{A,VV}) . \quad (6.11)$$

Other combinations of density matrix elements would also provide the nonlinear phase shift, but we choose these two density matrix elements because of their higher signal-to-noise ratio. Figure 6.9b shows the nonlinear phase shift as a function of the mean delay between the detections of two photons and of the width of the coincidence window. We find a maximum nonlinear phase shift of  $(1.05 \pm 0.04)\pi$ , which is close to the value of  $\pi$  expected under ideal conditions, for a 3 ns time window and zero mean delay between the two photons.

As is apparent from Eq. (6.8), the  $\pi$  nonlinear phase shift ideally generates a non-separable, maximally entangled state of light from the initially uncorrelated photons. In order to quantify the non-classical character of the experimentally prepared two-photon state, we calculate its concurrence [183] as described in App. A.8. The results are plotted in Fig. 6.9d. We find a maximum concurrence of  $0.27 \pm 0.04$  at zero mean detection time difference, thereby clearly demonstrating that  $\rho_{\text{meas}}$  corresponds to an entangled state. The concurrence and, thus, the entanglement vanishes when the time delay between the photons increases beyond the effective atomic lifetime  $\tau_{sp} = 8$  ns (see Fig. 6.9). This is expected because for larger delays the photons interact one-by-one with the atom-resonator system. For clarity, we also plot cuts along 3 ns window length for varying mean delay and zero mean delay as a function of the window length in Fig. 6.10.

## 6.5 Outlook: Implementing a photon–photon gate

In the experiment described in this chapter, we have demonstrated the maximal nonlinear phase shift for the smallest amount of light possible. Such maximum nonlinearities can readily be used for a variety of applications, such as the realization of deterministic Bell-state analyzers [184, 185]. Furthermore, deterministic photon–photon interactions also play a key role for quantum information processing. There, the ultimate goal is to realize a deterministic two-photon gate for optical qubits. In conjunction with single qubit rotations, such a gate forms a universal set of gates for quantum computation.

The demonstrated Kerr nonlinearity cannot directly be exploited for the realization of a high-fidelity photon–photon gate [161, 186, 187]. This can be seen from a simple bandwidth argument: For a typical gate operation the input fields should be photon Fock states, i.e. photons have to be in a well defined temporal mode. Their temporal pulse shape, which is characterized, e.g., by the pulse length  $\tau_p$ , has to be sufficiently short to guarantee that both photons interact at the same time with the Kerr nonlinearity, i.e.  $\tau_p \ll 1/\Gamma$ , where  $\Gamma$  is the bandwidth of the Kerr medium. At the same time, the pulse has a spectral width of  $\Delta_\nu \approx 1/\tau_p$ . For efficient interaction the Kerr medium and the photons have to be resonant, which requires  $\Delta_\nu \ll \Gamma$ , or  $\tau_p \gg 1/\Gamma$ . These two conditions cannot be fulfilled at the same time. According to Ref. [186–188] this inherently

limits the obtainable fidelity of a gate process to  $\sim 70\%$ .

However, this can be overcome and a deterministic controlled sign-flip gate for photons can be realized by using a two-step process. There, the state of the first photon is stored in the atom prior to the interaction with the second photon. For our experiment a universal gate, in particular a controlled phase gate (CPG), could be implemented in the following way. We assume that the mode of incident photons is defined by their temporal degree of freedom, i.e., the single-photon pulses have a relative delay which is much larger than their coherence time and their interaction time with the atom–resonator system. The atom is initially prepared in a state  $|g_c\rangle$  that couples to the resonator (e.g., the  $F = 3$  hyperfine ground state of  $^{85}\text{Rb}$ ). The fiber–resonator coupling is adjusted such that the resonator is under-coupled when the atom couples to the resonator and over-coupled if the atom does not couple. In the case where the two incident photons are  $D$ -polarized, the total state before the interaction with the resonator is given by

$$|\Psi\rangle_0 = |D_2\rangle|D_1\rangle|g_c\rangle = \frac{1}{2}(|H_2\rangle + |V_2\rangle)(|H_1\rangle + |V_1\rangle)|g_c\rangle. \quad (6.12)$$

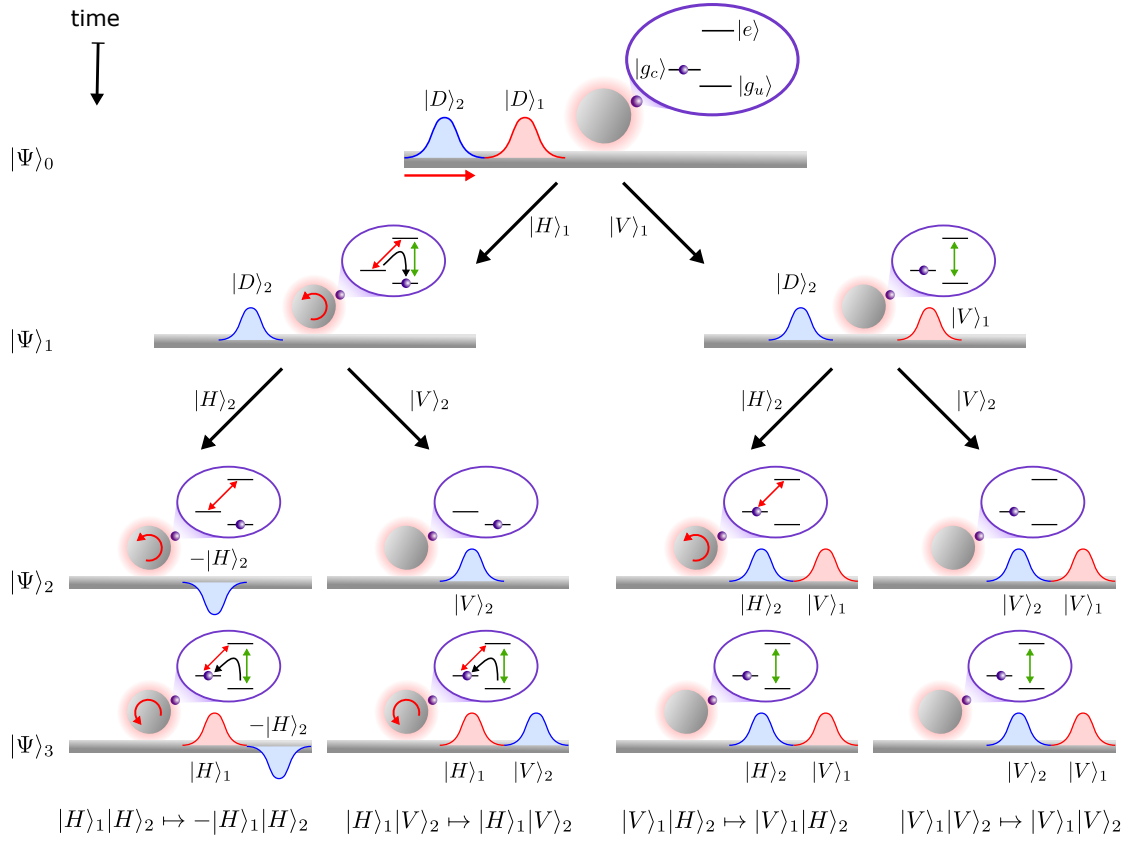


**Figure 6.11:** Implementation of a controlled phase gate (CPG) using a WGM resonator coupled to a three-level atom. The resonator mode couples to the  $|g_c\rangle \leftrightarrow |e\rangle$  transition and the external vSTIRAPs laser drives the  $|g_u\rangle \leftrightarrow |e\rangle$  transition.

The subscripts 1 and 2 indicate the two incident photons. When the first photon arrives at the resonator an additional control laser induces a vacuum-stimulated Raman adiabatic passage (vSTIRAP) [189] which transfers the atom from  $|g_c\rangle$  to  $|g_u\rangle$  if and only if the incident photon 1 is  $H$ -polarized and enters the resonator. Here,  $|g_u\rangle$  is a second ground state of the atom that does not couple to the resonator (e.g., the  $F = 2$  hyperfine ground state of  $^{85}\text{Rb}$ ) as shown in Fig. 6.11. As a consequence, the  $H$ -photon is stored in the atom and the state is now given by

$$|\Psi\rangle_1 = \frac{1}{2}(|H_2\rangle + |V_2\rangle)(|0\rangle|g_u\rangle + |V_1\rangle|g_c\rangle). \quad (6.13)$$

Thus, if the first photon is  $H$ -polarized, the atom is switched to a state that is off-resonant with respect to the resonator mode and the  $H$  component of the second photon will acquire a phase shift of  $\pi$ . Otherwise, the atom is resonant with the resonator mode and no phase shift occurs:

$$|\Psi\rangle_2 = \frac{1}{2}[(-|H_2\rangle + |V_2\rangle)|0\rangle|g_u\rangle + (|H_2\rangle + |V_2\rangle)|V_1\rangle|g_c\rangle]. \quad (6.14)$$

In the final step, the stored photon can be released using a second vSTIRAP process and we obtain the desired state

$$|\Psi\rangle_3 = \frac{1}{2}(-|H_2\rangle|H_1\rangle + |V_2\rangle|H_1\rangle + |H_2\rangle|V_1\rangle + |V_2\rangle|V_1\rangle)|g_c\rangle. \quad (6.15)$$

The described process introduces an undesired delay between  $|H_1\rangle$  and  $|V_1\rangle$ . However, this can be compensated by a polarization-dependent, actively controlled delay line. We note that other implementations of a controlled phase-flip gate which do not require the implementation of vSTIRAPs have been proposed [190, 191] and recently implemented [192].

The scheme described above would realize a photonic sign-flip gate or CPG, which is a universal two-qubit quantum gate that together with single qubit operations can be used to implement arbitrary quantum computational protocols. Thus, using single-qubit gates a CPG can be transformed into a controlled NOT (CNOT) gate which can directly be extended to become a Bell state analyzer or quantum non-demolition detector [193]. Thereby, such a gate would also provide an essential ingredient in quantum communication and optical quantum information processing [4].

## Quantum circulator

Optical data processing has the potential to largely outperform its electronic counterpart in terms of bandwidth and energy consumption [194]. For this purpose, integrated optical circuits are required in which light is guided via micro- or nanoscale waveguides. In such circuits, light is routed and controlled by integrated optical components. These components, on the one hand, should direct the signal to the desired destination. On the other hand, we also need devices which only allow unidirectional light flow. This is essential for noise suppression and to protect the source from spurious signals that might act back on it. In addition, directional light flow which can be achieved by nonreciprocal devices, is necessary for realizing quantum state transfer with high fidelity [195]. The most common examples of such nonreciprocal devices are optical isolators and circulators. Bulk optical implementations are readily available and rely mostly on nonreciprocal polarization rotation via the Faraday effect. The latter arises when light propagates through a magneto-optical material along the direction of an external magnetic field. However, this mechanism cannot straightforwardly be translated to integrated optics, since nano-optical waveguides are typically birefringent. Even though there has been significant progress in integrated optics, the realization of low-loss nonreciprocal devices that work at low optical powers is still an outstanding task. While most of the effort was put into employing magneto-optical materials, also several other approaches, including time-modulation of the waveguide properties via, e.g., electro-optical modulation [196, 197] or optomechanical effects [198–200], were investigated. However, none of these devices could simultaneously realize nonreciprocal transmission at the single-photon level and low insertion loss. The latter requirement is crucial when it comes to using such components for quantum applications, like quantum communication [4], quantum information processing [201], and quantum simulation [3]. There, information is encoded in individual photons. Since quantum signals can neither be amplified nor copied without introducing detrimental noise and decoherence, loss should be avoided as much as possible.

In the following, we demonstrate a new scheme of an optical circulator. It is based on a single atom that is chirally coupled to a whispering-gallery-mode microresonator that is interfaced by two tapered fiber couplers. We manage to realize a circulator that combines nonreciprocal transmission and low insertion loss ( $\sim 1.5$  dB) at the level of single photons, rendering it compatible

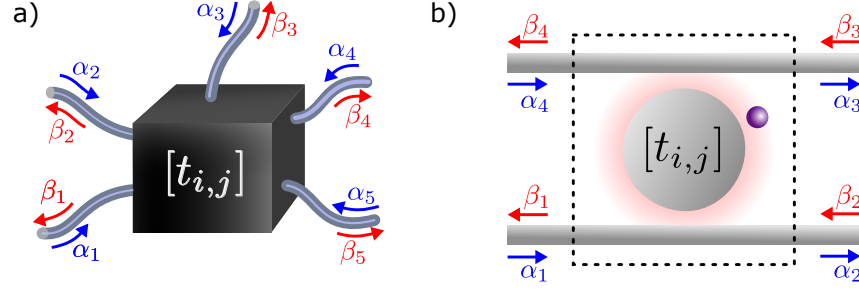


**Figure 7.1:** a) An  $N$ -port device can be characterized by an  $N \times N$  scattering matrix  $[t_{i,j}]$ . It relates the input and output fields  $\alpha_i$  and  $\beta_i$  via  $\beta_j = t_{i,j}\alpha_i$ . b) The BMR-based circulator is a 4-port device.

for quantum applications. In addition, for our circulator scheme it is possible to change the direction of operation by controlling the state of the atom. Thus, this device has the potential to make use of the atom's quantum nature to form a quantum circulator.

In this chapter, we first elaborate on the general properties of nonreciprocal devices and briefly discuss the connection between reciprocity and time-reversal symmetry. Then, we review the state-of-the-art of integrated nonreciprocal devices. Then, the working principle of our 4-port circulator is explained in detail, followed by the experimental modifications of the setup necessary to implement and characterize the circulator. Subsequently, the obtained experimental results are discussed and the potential of the scheme assessed. Parts of this chapter were published in Ref. [202].

## 7.1 Characteristics of a nonreciprocal device

### 7.1.1 The scattering matrix formalism

A general formalism to describe the operation of a device uses the so-called scattering matrix  $[t_{i,j}]$  [203]. It relates the input field amplitudes  $\alpha = (\alpha_1, \alpha_2, \dots, \alpha_N)^T$  and the output field amplitudes  $\beta = (\beta_1, \beta_2, \dots, \beta_N)^T$  of an  $N$ -port device via

$$\beta = [t_{i,j}] \alpha, \quad (7.1)$$

as schematically shown in Fig. 7.1a. The matrix entries  $t_{i,j}$  are the respective transmission coefficients for signals entering the device via port  $i$  and exiting through port  $j$ . In principle, the ports do not have to be independent single-mode waveguides as shown in Fig. 7.1a but can also represent e.g. certain spatial modes in a multi-mode waveguide, free space modes or frequency components. However, orthogonality of the ports requires that there is no coupling between the ports outside the device.

A lossless device is represented by a unitary scattering matrix [23]

$$[t_{i,j}]^\dagger [t_{i,j}] = 1 \quad \text{or} \quad \sum_{i,j} |t_{i,j}|^2 = N, \quad (7.2)$$

which follows from energy conservation. If Eq. 7.2 is not fulfilled we speak of a lossy device. We consider a device to be reciprocal if the output at port  $i$  for a given input signal from port  $j$  is the same as the output at port  $j$  if the same signal impinges on port  $i$ , i.e.  $t_{i,j} = t_{j,i}$  [204]. Thus, reciprocity imposes the scattering matrix to be symmetric

$$[t_{i,j}]^T = [t_{i,j}] . \quad (7.3)$$

If a device is described by an asymmetric scattering matrix it breaks Lorentz reciprocity [23], and the device is denoted to be nonreciprocal. Since the scattering matrix is not always accessible in the experiment we define the transmission matrix  $[T_{i,j}]$ , where  $T_{i,j} = |t_{i,j}|^2$ . Thus,  $T_{i,j}$  is the power transmission from input port  $i$  to output port  $j$ .

### 7.1.2 Reciprocity, losses and time-reversal symmetry

In past years, there has been some misconception concerning nonreciprocity and its relation to time-reversal symmetry and loss [204]. The main misapprehensions and misleading denotations should be addressed in the following.

#### Reciprocity and time-reversal symmetry

Nonreciprocal optical devices can be based on different physical effects, but all have to show an asymmetry between the forward and backward transmission, i.e. we obtain a different result when we send light onto our device from different directions. In the literature, it is common to state that such devices break time-reversal symmetry. This misleading denotation stems from several inaccuracies. Since time reversal changes the propagation direction of a traveling electromagnetic wave, nonreciprocity might be interpreted as an asymmetry between time running in forward and backward direction. However, the time-reversal operation  $\mathcal{T} : t \rightarrow -t$  implies [205]

$$\mathcal{T} : \quad \mathcal{E} \rightarrow \mathcal{E}^* \quad \text{and} \quad \mathbf{k} \rightarrow -\mathbf{k} , \quad (7.4)$$

where  $\mathcal{E}$  is the complex vector amplitude and  $\mathbf{k}$  the wavevector of the electric field. Thus, the reversal of the wavevector  $\mathbf{k}$ , i.e. the propagation direction of the electromagnetic wave, is always accompanied by the conjugation of the field vector. In addition, time-reversal has to be performed globally and not only on some subsystem, which is commonly omitted. If this is taken into account, time-reversal symmetry is preserved also for nonreciprocal devices. This should not be surprising since Maxwell's equations, which fully describe the propagation of electromagnetic waves, are invariant under time-reversal.

To further illustrate the difference between time-reversal and reciprocity, let us consider a simple example. A black box which acts as a lossless 3-port circulator as depicted in Fig. 7.2a. We are not interested in the internal effect on which the circulator is based, only in its operation that follows the protocol  $(1 \rightarrow 2 \rightarrow 3 \rightarrow 1)$ . This device is obviously nonreciprocal, since  $T_{i,i+1} \neq T_{i+1,i}$  for  $i \in \{1, 2, 3\}$ . So if we send light into port 1 we recover it at port 2. If we now reverse the propagation direction of the light wave such that it is impinging on port 2, we do not obtain the light in port 1, but recover it in port 3. However, reversing the propagation

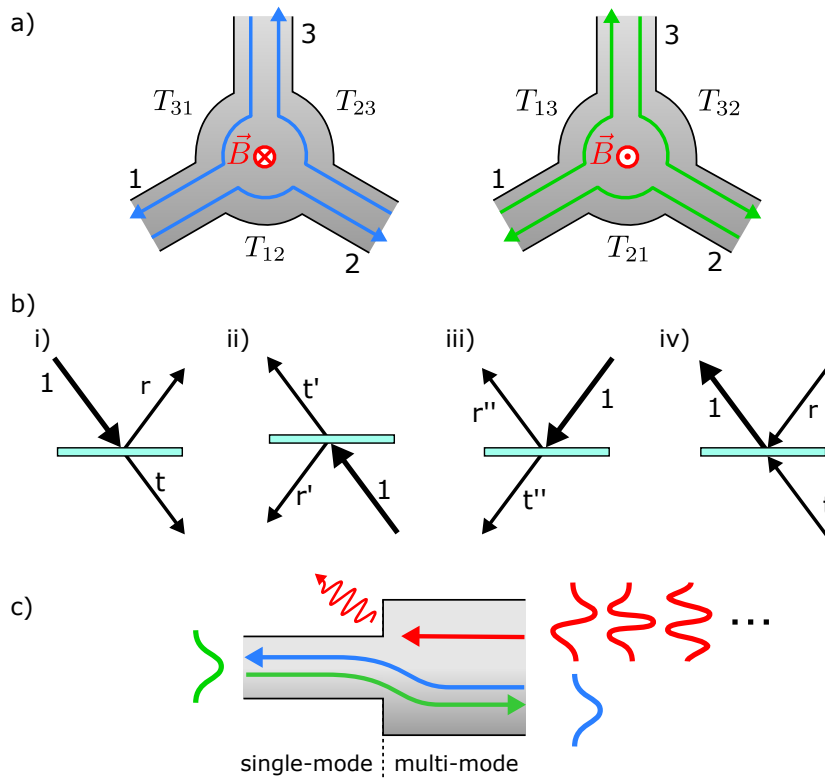


**Figure 7.2:** a) Circulators whose sense of operation is controlled by the direction of the magnetic bias field (red arrow), which breaks Lorentz reciprocity. When reversing time, not only does the propagation direction change, but also the magnetic field flips, thus obeying time-reversal symmetry. b) An electromagnetic wave impinging on a beam splitter. Some part of the wave will be reflected and some part will be transmitted. For the same angle of incidence, the respective coefficients of the reflected and transmitted amplitude are independent of the direction the wave is coming from, i.e.  $r = r' = r''$  and  $t = t' = t''$ . Time reversal of only one of the outgoing beams does not yield the initial amplitudes (e.g.  $t \cdot t' \neq 1$ ). However, if we manage to recombine the outgoing waves with the correct amplitude and phase relation, we will obtain the initial amplitude, i.e.  $|r|^2 + |t|^2 = 1$ . c) Junction between a single-mode and a multi-mode waveguide. While the single-mode section only supports the fundamental mode, the multi-mode section supports the fundamental and several higher order modes. When light impinges on the junction from the left it will be transmitted and guided in the fundamental mode of the multi-mode waveguide. When light is sent from the opposite direction, it is distributed between all modes of the multi-mode waveguide. However, only the fraction that is guided in the fundamental mode will be transferred to the single-mode waveguide and the rest scattered into free space.



direction of the light is only a local or partial time reversal transformation, which does not act on the circulator itself. Let us now assume that our circulator is based on the Faraday effect, which relies on a magneto-optic material and a strong magnetic bias field applied in propagation direction. When we reverse time, the sign of the magnetic bias field flips, and consequently its operation is inverted ( $1 \rightarrow 3 \rightarrow 2 \rightarrow 1$ ). Thus, light that impinges now on port 2 will be directed to port 1. Therefore, time-reversal symmetry is preserved, as long as we take into account the whole system including its environment. However, time-reversal symmetry might be broken locally which can be exploited to realize nonreciprocal devices.

### Losses and time-reversal symmetry

Another common misunderstanding is that losses are considered to break time-reversal symmetry. However, this only reflects the ignorance about certain input and output modes. To elaborate on this, let us first consider a simple example: An electromagnetic wave impinges on a beam splitter, as depicted in Fig. 7.2b. Part of the wave will be reflected and part will be transmitted, with the respective amplitudes  $r$  and  $t$ . When we now consider the fraction of the light which is reflected as loss and reverse the transmitted wave, we will not recover the initial amplitude of the incoming wave after passing the interface again. By disregarding certain modes, we could thus misleadingly claim to break time-reversal symmetry and argue that this could be employed to realize a nonreciprocal device. However, when reversing both the transmitted and the reflected wave, i.e. if we manage to recombine the outgoing waves with the correct amplitude and phase relation, we will recover the initial amplitude. Thus, also this system is symmetric under time reversal. Furthermore, reciprocity is preserved, since this only requires the equality of the forward and backward transmission coefficient, i.e.  $t = t'$  and  $r = r''$ .

While the first example was rather generic, let us now consider a more applied example: The junction between a single-mode and a multi-mode waveguide as depicted in Fig. 7.2c. The single-mode section only supports the fundamental mode while the multi-mode section supports a large number of modes. When light impinges from the single-mode section, the junction is designed such that the light is fully transferred into the fundamental mode of the multi-mode section. When sending light from the opposite direction it will be distributed between the numerous modes. However, only a small fraction of the light is guided in the fundamental mode which couples to the mode in the single-mode section. The rest of the light is guided in higher-order modes the will be scattered out of the waveguide at the junction. In this configuration, this gives rise to an imbalance between forward and backward transmission. However, if we manage to exclusively send light guided in the fundamental mode onto the junction it will be entirely transmitted. Thus, this junction preserves Lorentz reciprocity. When we take into account all modes, including the free space modes, we see that the junction also is symmetric under time-reversal. As a consequence, such a junction cannot be used for realizing an optical isolator [204]

### 7.1.3 Figures of merit for nonreciprocal devices

In this chapter, we will discuss the realization of an optical circulator. In order to characterize the performance of such a nonreciprocal device, we introduce several figures of merit. For the

sake of generality, the number of ports is kept as a variable  $N$  in the following definitions. Since we are mainly interested in characterizing the demonstrated circulator, some of the introduced quantities might not be straightforwardly applied to other devices, such as isolators.

The first requirement for our device is that it should introduce as little loss as possible. From both, the transmission and the scattering matrices, we can directly calculate the survival probability  $\eta$  of photons entering the device, averaged over all input ports

$$\eta = \sum_{i,j} T_{i,j}/N = \sum_{ij} |t_{i,j}|^2/N . \quad (7.5)$$

From Eq. (7.5) the average insertion loss, i.e. the loss of signal power resulting from the insertion of a device, can be calculated via

$$L = -10 \log(\eta) . \quad (7.6)$$

It should be mentioned that isolators are inherently dissipative devices with  $\eta \leq 0.5$ . Thus, for optical diodes the insertion loss is usually defined as  $L = -10 \log(\eta_{\text{FW}})$ , where  $\eta_{\text{FW}}$  is the photon survival probability in forward direction.

In the following, we introduce three figures of merit: The nonreciprocity  $\mathcal{N}$  evaluates the non-reciprocal behavior of the device, the fidelity  $\mathcal{F}$  compares the measured to the ideally expected output of the device, and the isolation  $I$  gives a measure of the imbalance between forward and backward transmission.

As already mentioned in the previous, a device is called Lorentz reciprocal if its scattering matrix satisfies the condition  $[t_{i,j}]^T = [t_{i,j}]$ , or  $t_{i,j} = t_{j,i}$ . However, for an isolator or circulator we are interested in the power transmission. Thus, we typically measure the transmission matrix  $[T_{i,j}]$ . We, thus, define its nonreciprocity as the difference between the transmission matrix and its transposed using

$$\mathcal{N} = \frac{1}{2N\eta} \sum_{i,j}^N (T_{i,j} - T_{j,i}) , \quad (7.7)$$

where we divide by the photon survival probability  $\eta$ , in order to separate the nonreciprocal behavior from photon loss. For an ideal circulator, this quantity reaches  $|\mathcal{N}| = 1$ , while for a reciprocal device,  $T_{i,j} = T_{j,i}$ , and consequently  $\mathcal{N} = 0$ . When reversing the operation direction of the circulator,  $\mathcal{N}$  also flips its sign. Since the definition of  $\mathcal{N}$  only includes the power transmission, it is insensitive to nonreciprocal phase shifts. However, for the performance of a circulator, this is not of relevance. In addition,  $\mathcal{N}$  by definition ignores asymmetric backscattering which might occur for the bare resonator, as this is a reciprocal effect [141, 142].

Another way to evaluate the performance of the device is to compare the renormalized transmission matrix  $[\tilde{T}] = [T_{i,j}/\eta_i]$  to the transmission matrix  $[T^{\text{id}}]$  expected for the ideal device, where  $\eta_i = \sum_k T_{i,k}$  is the survival probability of a photon entering port  $i$ . In order to quantify the overlap with the ideal device, we define the average operation fidelity by

$$\mathcal{F} = \frac{\text{Tr} \left[ [\tilde{T}] \cdot [T^{\text{id}}]^T \right]}{\text{Tr} \left[ [T^{\text{id}}] \cdot [T^{\text{id}}]^T \right]} = 1 - \frac{1}{2N} \sum_{i,j} |\tilde{T}_{i,j} - T_{i,j}^{\text{id}}| . \quad (7.8)$$

This quantity is also called inquisition [206] and gives the probability of a correct circulator operation averaged over its eigenstates. The minimum fidelity is  $\mathcal{F} = 0$ , while  $\mathcal{F} = 1$  is reached for ideal operation. For any reciprocal device ( $\tilde{T} = \tilde{T}^T$ ) the fidelity is bound by  $\mathcal{F} \leq 0.5$ . Moreover, the performance of an  $N$ -port circulator can be quantified by the performance of the  $N$  independent isolators, formed between adjacent ports (cf. Fig. 7.10a). Thus, the circulator performance can also be quantified by the isolation of its isolators, which is calculated using

$$I_{i,i+1} = 10 \log \left( \frac{T_{i,i+1}}{T_{i+1,i}} \right). \quad (7.9)$$

As the name already suggests, the isolation  $I$ , in conjunction with the insertion loss  $L$ , is the most commonly used figure of merit for optical isolators.

## 7.2 Review of integrated nonreciprocal devices

### Bulk optical implementations

Before discussing the developments and achievements in integrated optics, let us first consider the most commonly used nonreciprocal devices in bulk optics, i.e isolators and circulators which are based on the Faraday effect. The standard configuration of an optical isolator (or circulator) consists of two polarizers and a Faraday-rotator between them, as schematically shown in Fig. 7.3a. The Faraday-rotator consists of a magneto-optic material, such as yttrium iron garnet (YIG) or substituted iron garnets. This garnet is magnetized using an external magnetic field in propagation direction of the light (longitudinal biasing). The length of the Faraday rotator and the strength of the bias field are designed to impart a  $45^\circ$  polarization rotation on the incident light. When the polarizers have a relative polarization offset of  $45^\circ$ , light entering via the first polarizer exits through the second polarizer with little loss since its polarization coincides with the axis of the polarizer. When backward propagating light enters the isolator and passes through the Faraday rotator, its polarization is again rotated by  $45^\circ$ . The key feature of the isolator is the nonreciprocal nature of the Faraday effect, which imparts the same rotational sense to the polarization in both directions of propagation. As the light reaches the first polarizer in its backward progression, its polarization is rotated by  $90^\circ$  with respect to the axis of the first polarizer and is blocked. This realizes the unidirectional light propagation required for an optical isolator. For turning this isolator into a circulator, the polarizers have to be replaced by polarizing beam splitters, as shown in Fig. 7.3b. Commercial fiber-integrated circulators also often employ the beam walk-off that occurs when placing a Faraday-rotator between two birefringent beam displacers [209, 210].

### Integrated magneto-optics

For incorporating the standard Faraday rotation scheme used in bulk nonreciprocal devices into a photonic circuit one can directly employ magneto-optic waveguides, which are formed by YIG films. Those structures are then overlaid with a permanent magnet to bias the magneto-optic waveguide. This approach, however, faces dielectric birefringence which is also referred to as

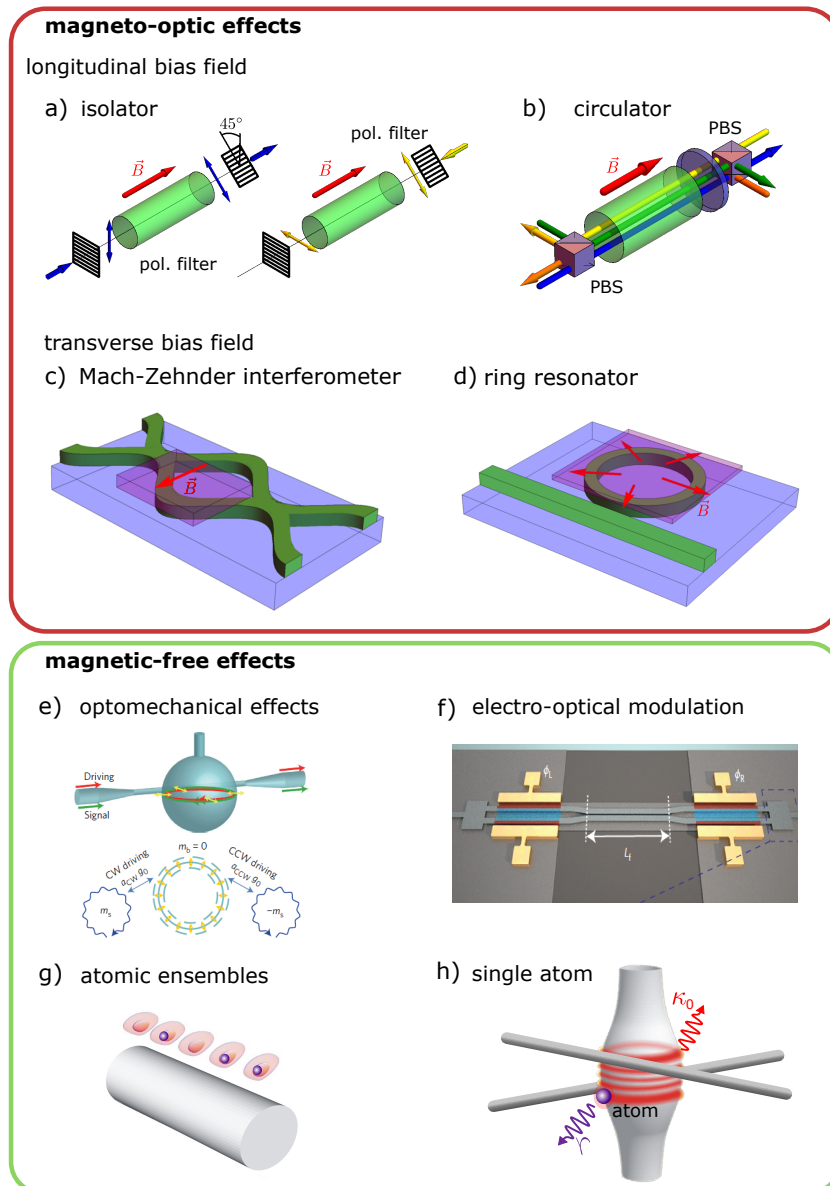


**Figure 7.3:** Different approaches for realizing nonreciprocal devices either use magneto-optic effects or magnetic-free effects. The former apply a strong magnetic bias field along the propagation direction of light or transverse to it. The longitudinal biasing is used for bulk realizations of a) isolators and b) circulators based on Faraday rotations. Using transverse biasing, it is possible to realize integrated nonreciprocal devices, for which the magneto-optic material can be placed in c) a Mach-Zehnder interferometer [207] or d) a ring resonator [208]. Magnetic-free approaches are either based on spatiotemporal modulation by means of e) optomechanics [200] and f) electro-optical modulation [197] or on coupling the light to g) atomic ensembles close to the waveguide or h) single atoms in high-Q resonators [125].

method	footprint	$I$	$L$	$\lambda$	bandwidth	Ref.
magneto-optic						
WG	3 mm	25 dB	3 dB	1550 nm	>70 nm	[211]
WG	3.5 mm	29 dB	7 dB	1550 nm	>70 nm	[212]
MZI	8 mm	19 dB	13.5 dB	1540 nm	>80 nm	[213]
NRA	0.7 mm	10 dB	5 dB	1550 nm	>30 nm	[214]
MZI	4 mm	20 dB	8 dB	1559 nm	10 nm	[215]
RR	290 $\mu\text{m}$	19.5 dB	19 dB	1550 nm	1.6 GHz	[208]
RR	n.a.	10 dB	50 dB	1550 nm	n.a.	[216]
magnetic-free						
EO	3 mm	2.4 dB	2.3 dB	1550 nm	100 nm	[217]
EO	10 mm	3 dB	20 dB	1558 nm	THz	[196]
EO	4 mm	3 dB	11 dB	1550 nm	n.a.	[218]
EO	8.35 mm	2.3 dB	n.a.	1570 nm	$\sim 2.5$ GHz	[197]
atomic ensemble	n.a.	7.8 dB	1.1 dB	852 nm	$\sim$ MHz	[125]
single atom	n.a.	13 dB	1.5 dB	780 nm	$\sim$ MHz	[125]
OM	n.a.	7 dB	11 dB	1542 nm	< MHz	[200]

**Table 7.1:** Experimental realizations of integrated optical isolators. We distinguish devices that employ magneto-optic effects from devices that work magnetic-free. For the former the magneto-optic material is either directly integrated into the waveguide (WG), a Mach-Zehnder interferometer (MZI), a ring resonator (RR) or they employ nonreciprocal mode attenuation (NRA). Magnetic-free devices used spatiotemporal modulation by electro-optic (EO) or optomechanical (OM) effects or employ chirally coupled atoms. The isolation  $I$ , the insertion loss  $L$  and the operation wavelength  $\lambda$  are given.

modal phase-mismatch [219]. This birefringence mainly originates from the asymmetry of the rectangular shape of the waveguide and from effects such as growth-induced anisotropy and film internal stress. The latter can arise from the lattice mismatch between the waveguide and magnetic material of different thermal expansion. Several solutions have been investigated to overcome the phase mismatch, with differing degree of success. The main problem still resides in the complexity of fabrication and the strict tolerance requirements [219]. Using relatively large ( $\sim$ cm) magneto-optic waveguides, isolations of up to 29 dB, with typically more than 3 dB insertion loss, have been demonstrated [211, 212].

Another approach is to use technologically advanced low-loss waveguide platforms, such as silicon or silica, and place the magneto-optic material, which is magnetized transverse to the propagation direction, on top of the waveguide. Such waveguides do not exhibit Faraday rotation, but a nonreciprocal phase retardation [220]. This effect is not present for bulk structures, since it relies on the formation of longitudinal field components which naturally occur for the strongly confined light in the waveguide structures as shown in Fig. 7.3d. Different schemes have been proposed to use this nonreciprocal phase shift to realize optical isolators or circulators. Some rely on interferometric structures. For example, the arm length of a Mach-Zehnder interferometer (MZI) can be designed such that a nonreciprocal phase shift of  $\pm 90^\circ$  is introduced, where the

sign depends on the propagation direction. This results in destructive or constructive interference at the output ports, yielding nonreciprocal transmission through the device. For MZI-based devices, isolation of 20 dB with 8 dB insertion loss has been realized [213,215]. Another approach is to incorporate the nonreciprocal phase shifter into a ring resonator. This causes a relative shift of the resonance frequencies for the two propagation directions of the resonator modes [221], which gives rise to asymmetric transmission properties (see Fig. 7.3c). Compared to other implementations, resonance effects limit the bandwidth of the device. Devices with up to 19 dB isolation but high insertion loss of  $> 19$  dB have been demonstrated [208,216].

Even though, significant reduction of the footprint has been achieved in magneto-optic nonreciprocal devices, the small Faraday rotation or phase shift per unit length requires relatively large interaction length on the order of several mm. This gave rise to another approach that employs photonic bandgap technology. The employed photonic crystals use periodic stacks or structures with defects, and can largely enhance the magneto-optical response. A variety of theoretical proposals exist [222,223] and an enhancement of Faraday-rotation has been shown [224]. However, no devices that show nonreciprocal transmission have yet been reported.

The average absorption of magneto-optical materials is typically on the order of several dB/mm. As a consequence, the insertion loss remains significant for such devices. In addition, despite the considerable advances in the fabrication of thin magnetic films in recent years [219], the miniaturization of the auxiliary magnets still significantly adds to the complexity of integrating magneto-optical nonreciprocal devices on photonic platforms. Thus, several ideas are pursued to obtain a magnetic-free nonreciprocity, which might allow one to realize devices with significantly smaller footprint.

### **Magnetic-free approaches**

According to the Lorentz reciprocity theorem, any linear system described by symmetric and time-independent permittivity and permeability tensors is necessarily reciprocal [204]. Therefore, to achieve nonreciprocity without magneto-optics, one has to rely upon either nonlinear or time-dependent effects. Nonreciprocity based on nonlinear effects has successfully been demonstrated in waveguides [225] and integrated resonator structures [67,226]. However, this requires large intensities and thus the corresponding devices cannot operate at the single-photon level. As a consequence, devices based on nonlinear effects are not suited for applications in quantum information processing. In addition, such devices are subject to small-amplitude noise in the backward direction [227]. An alternative approach makes use of strong optomechanical interaction in optical microresonators (see Fig. 7.3e). For example, whispering-gallery-mode (WGM) microresonators can be optically pumped in one direction. This can give rise to a strong optomechanical coupling which alters the transmission properties for signal co-propagating with the driving field, and thus causing a nonreciprocal response [228,229]. In other words, the phonons periodically modulate the resonator, thus breaking the symmetry of clockwise and counter-clockwise propagating resonator modes. Recent experimental realizations of nonreciprocal optomechanical devices that used WGM microresonators either employed Brillouin scattering induced transparency [198] or the less restrictive optomechanically induced transparency [199,200]. These first proof-of-principle experiments were able to demonstrate isolation

method	footprint	$I$	$L$	$\lambda$	Ref.
MZI NRPS	8.5 mm	3 dB	n.a.	1152 nm	[234]
MZI FR	22 mm	16 dB	3 dB	1550 nm	[235]
MZI NRPS	1.5 mm	(15.3,13.1,9.3,6.7)	>25 dB	1531 nm	[207]

**Table 7.2:** Experimental realizations of integrated optical circulators. These devices employ Faraday rotation (FR), nonreciprocal phase shift (NRPS) or Mach-Zehnder interferometer (MZI). The isolation  $I$ , the insertion loss  $L$  and the operation wavelength  $\lambda$  are given.

of 7 dB with 11 dB insertion loss. In addition to modulating the photonic modes by phonons, there are also several realizations of electrically modulated waveguides [196, 197, 217, 218]. However, these devices so far do not surpass isolations of 3 dB while still introducing significant insertion loss.

### Spin-controlled devices

Very recently, another alternative approach was put forward, in which the optical mode is coupled to single emitters (see Fig. 7.3g-h). The internal structure of the scatterer can cause an imbalance between the coupling to different polarization components of light. Such polarization-dependent scatterers can be, e.g. excitonic states in quantum dots [230, 231] or alkali atoms prepared in a spin-polarized state [122]. These scatterers can be coupled to nanophotonic optical waveguides or WGM microresonators. If those photonic structures supports modes that exhibit spin-momentum locking (SML), this gives rise to chiral, i.e. direction-dependent interaction. This can be used to realize nonreciprocal light transmission [232, 233]. In recent experiments two different approaches have been pursued to harness this effect for demonstrating an optical isolator [125]: In order to realize deterministic light-matter coupling we can either couple an ensemble of atoms to a nanophotonic waveguide, for which the interaction between the light and matter is collectively enhanced. Alternatively, a single atom is coupled to a WGM resonator, which enhances the coupling due to cavity quantum electrodynamics (CQED) effects. This method will also be employed in the following. The experimentally obtained isolation for the ensemble-based experiment was 7.8 dB and the insertion loss below 1.5 dB. The experiments for the single-atom realization, which was performed on this setup, achieved an isolation of 13 dB and comparable insertion loss. Although these experiments work with laser-cooled atoms and thus require large experimental overhead, the mechanism demonstrated is compatible with on-chip integration.

One should also note that this approach constitutes the quantum optical analog of microwave ferrite resonance isolators with transverse bias, performed at the ultimate limit of single or few spins which are resonantly coupled to the guided light.

Table 7.1 gives an overview of experimentally demonstrated isolators. While implementations of integrated optical circulators are rare (see Tab. 7.2 respectively), most of the schemes used for isolators can in principle be extended to circulators, however, bringing new challenges.

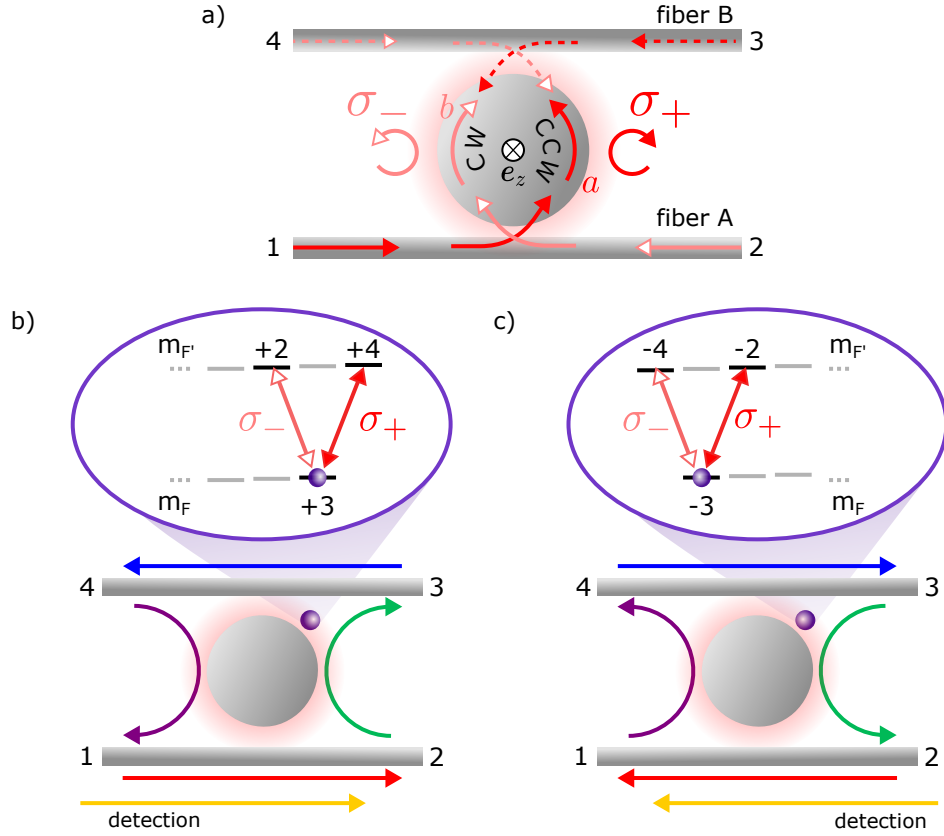


**Figure 7.4:** a) Schematic of a resonator interfaced with two coupling fibers, labeled *A* and *B*. When probing from port 1 or 3 light is coupled into the CCW propagating resonator mode *a*, for which the local polarization of the evanescent field is  $\sigma^+$ . From port 2 and 4 the CW propagating *b* mode is excited, which exhibits  $\sigma^-$  polarization. b) & c) Working principle of the programmable circulator. b) When the atom is prepared in the  $m_F = +3$  hyperfine ground state the circulator operation is defined as  $(1 \rightarrow 2 \rightarrow 3 \rightarrow 4 \rightarrow 1)$ . c) When the atom is prepared in the  $m_F = -3$  hyperfine ground state the circulator operation is reversed and now defined as  $(1 \rightarrow 4 \rightarrow 3 \rightarrow 2 \rightarrow 1)$ . The preparation of the atomic state is in our experiment achieved by sending the detection light field from the respective direction.

In the following, the working principle and implementation of an integrated optical circulator will be discussed that has been developed within this thesis.

### 7.3 Working principle of the single atom-controlled circulator

After this very general treatment we will now focus our discussion on the realization of a 4-port optical circulator which is controlled by a single atom. In the following, the general operation principle of the circulator and the underlying mechanism that gives rise to the nonreciprocal



transmission are described.

The key element of our experiment is a bottle microresonator (BMR) interfaced by two optical nanofibers. This realizes a 4-port device, for which we label the ports consecutively as shown in Fig. 7.1b. Let us first consider the case of an empty resonator. From the two coupling fibers, which are denoted  $A$  and  $B$ , light couples into and out of the resonator at a rate given by  $\kappa_A$  and  $\kappa_B$  respectively. For our BMR it is well justified to neglect direct mode–mode coupling between the two counter-propagating degenerate resonator modes (cf. Sec. 5.2.3). Thus, the transmission through fiber  $A$  is given by (cf. Sec. 4.5.2)

$$T_{12}^0 = T_{21}^0 = \left| \frac{\kappa_0 + \kappa_B - \kappa_A}{\kappa_0 + \kappa_A + \kappa_B} \right|^2, \quad (7.10)$$

and through fiber  $B$

$$T_{34}^0 = T_{43}^0 = \left| \frac{\kappa_0 + \kappa_A - \kappa_B}{\kappa_0 + \kappa_A + \kappa_B} \right|^2. \quad (7.11)$$

Here, the subscript indicates the involved ports. The transmission from one fiber into the other via the resonator is given by

$$T_{14}^0 = T_{23}^0 = T_{32}^0 = T_{41}^0 = \frac{4\kappa_A\kappa_B}{|\kappa_0 + \kappa_A + \kappa_B|^2}. \quad (7.12)$$

In this case, the transmission is the same for both fibers, even for the case  $\kappa_A \neq \kappa_B$ . From Eq. (7.10-7.12) we see that the empty resonator is reciprocal, since  $T_{i,j}^0 = T_{j,i}^0$ . In order to achieve efficient, low-loss photon routing, let us assume that the fiber–resonator coupling rates  $\kappa_A$  and  $\kappa_B$  are adjusted such that both fibers are almost critically coupled to the resonator, i.e.  $\kappa_A \approx \kappa_B \gg \kappa_0$  (cf. Sec. 4.5.2). In this setting, all the light sent from one fiber will be coupled into the resonator and transferred to the opposite fiber, as can easily be verified using Eq. (7.10) and (7.11).

In order to achieve nonreciprocal light transmission, we make use of the inherent link between propagation direction and polarization of the resonator fields and couple them to a polarization-dependent scatterer. Light that propagates in clockwise (CW) direction in the resonator is almost fully  $\sigma^-$ -polarized, while it is almost fully  $\sigma^+$ -polarized when it propagates in the counter-clockwise (CCW) direction. These two modes are driven via the respective probing directions through the coupling fibers, as illustrated in Fig.7.4a. A single  $^{85}\text{Rb}$  atom prepared in the outermost Zeeman sublevel  $m_F = +3$  of the  $5S_{1/2}^2$ ,  $F = 3$  hyperfine ground state is resonantly coupled to the resonator. The resonator fields then drive an effective V-system (see Fig.7.4b). The strength of the transition to the  $5P_{3/2}^2$ ,  $|F' = 4, m_{F'} = +4\rangle$  excited state is 28 times stronger than the one of the transition to the  $|F' = 4, m_{F'} = +2\rangle$  state (see App. A.1). Consequently, light that couples from one of the fibers into the CCW resonator mode couples strongly to the atom with the coupling constant  $g_{ccw}$ . In contrast, light coming from the opposite direction and thus coupling to the CW mode shows only negligible coupling  $g_{cw} \ll g_{ccw}$ . The presence of the atom modifies the power transmission, which in the approximation of perfectly circularly polarized

modes is given by (cf. Sec. 4.5.2)

$$T_{12(21)} = \left| \frac{\Gamma_{\text{ccw(cw)}} + \kappa_0 + \kappa_B - \kappa_A}{\Gamma_{\text{ccw(cw)}} + \kappa_0 + \kappa_A + \kappa_B} \right|^2, \quad (7.13)$$

$$T_{34(43)} = \left| \frac{\Gamma_{\text{ccw(cw)}} + \kappa_0 + \kappa_A - \kappa_B}{\Gamma_{\text{ccw(cw)}} + \kappa_0 + \kappa_B + \kappa_A} \right|^2, \quad (7.14)$$

$$T_{14(41)} = T_{32(23)} = \frac{4\kappa_A \kappa_B}{|\Gamma_{\text{ccw(cw)}} + \kappa_0 + \kappa_A + \kappa_B|^2}, \quad (7.15)$$

where

$$\Gamma_{\text{cw/ccw}} = g_{\text{cw/ccw}}^2 / \gamma, \quad (7.16)$$

is the additional loss rate for the resonator introduced by the atom and corresponds to the mean excited state population per intra-resonator photon  $g_{\text{cw/ccw}}^2 / \gamma^2$  multiplied by the excited state decay rate  $\gamma$ . This changes the total resonator loss rate from  $\kappa_{\text{tot}} = \kappa_0 + \kappa_A + \kappa_B$  to  $\kappa_{\text{tot}} + \Gamma_{\text{cw/ccw}}$ . For the case where the light couples to the CW resonator mode,  $g_{\text{cw}}$  and thus the atom-induced loss rate is small, i.e.  $\kappa_{\text{tot}} \gg \Gamma_{\text{cw}}$ , and the resonator transmission is not significantly modified by the atom. However, for the CCW direction,  $\Gamma_{\text{ccw}}$  can become comparable to or larger than  $\kappa_{\text{tot}}$ . In this case, the resonator–atom system is now in the under-coupled regime (see Sec. 4.5.1) and the incident light field remains in the initial fiber. The direction-dependent coupling thus breaks Lorentz reciprocity and realizes an optical circulator [232] that operates as shown in Fig. 7.4b). Interestingly, preparing the atom in the opposite Zeeman ground state  $|F=3, m_F=-3\rangle$  changes the role of the CW and CCW mode and yields a circulator with reversed operation direction as shown in Fig. 7.4c. This enables us to reconfigure the operation direction of the circulator using the internal spin-state of a single atom. For circulators based on magneto-optic material this would require to reconfigure the magnetic moments by reversing the external bias field.

## 7.4 Theoretical description of the circulator

The model introduced in the previous section uses a simplified treatment where the atom always exclusively couples to one of the two counter-propagating resonator modes. This allowed us to gain an intuitive understanding for the mechanism that enables us to realize a circulator. Unfortunately, in our experiment we do not fully encounter the situation described in the previous section. The polarization of our resonator modes is not perfectly circular. This enables the atoms to couple the two counter-propagating modes, even in the absence of mode–mode coupling. Thus, a fraction of the light might be scattered back into its initial port. In order to accurately describe the experimental data this has to be taken into account.

Our 4-port circulator is fully characterized by its  $4 \times 4$  scattering matrix  $[t_{i,j}]$ . We can employ the input output formalism described in Sec. 4.2, and apply it to both counter-propagating modes, which we now denote  $a$  and  $b$  for the CCW and CW respectively. When we probe all 4 ports, the scattering matrix can be expressed as

$$[t_{i,j}] = \frac{1}{s_{\text{in}}} \begin{pmatrix} \sqrt{2\kappa_A} \langle b_A^i \rangle & s_{\text{in}} - \sqrt{2\kappa_A} \langle a_A^d \rangle & \sqrt{2\kappa_B} \langle b_A^i \rangle & \sqrt{2\kappa_B} \langle a_A^d \rangle & 1 \\ s_{\text{in}} - \sqrt{2\kappa_A} \langle b_A^d \rangle & \sqrt{2\kappa_A} \langle a_A^i \rangle & \sqrt{2\kappa_B} \langle b_A^d \rangle & \sqrt{2\kappa_B} \langle a_A^i \rangle & 2 \\ \sqrt{2\kappa_A} \langle b_b^i \rangle & \sqrt{2\kappa_A} \langle a_B^d \rangle & \sqrt{2\kappa_B} \langle b_B^i \rangle & s_{\text{in}} - \sqrt{2\kappa_B} \langle a_B^d \rangle & 3 \\ \sqrt{2\kappa_A} \langle b_B^d \rangle & \sqrt{2\kappa_A} \langle a_B^i \rangle & s_{\text{in}} - \sqrt{2\kappa_B} \langle b_B^d \rangle & \sqrt{2\kappa_B} \langle a_B^i \rangle & 4 \end{pmatrix} \begin{matrix} \text{input} \\ \\ \\ \\ \end{matrix} \begin{matrix} 1 \\ 2 \\ 3 \\ 4 \end{matrix} \quad (7.17)$$

Here, we took into account that the light which exits port 1 or 3 stems from mode  $b$ , the light that exits port 2 and 4 is coupled out of mode  $a$ . In Eq. (7.17), the superscript of the respective mode operator determines whether the modes are driven directly or indirectly, indicated by (d) and (i) respectively. The subscript indicates the fiber from which the resonator is probed. In addition, we assumed that all inputs have the same amplitude and phase. In section 4.4.2, we have learned that the chiral coupling between the light in the resonator and a polarization-dependent scatterer can very well be approximated by a simple two-level atom with a circularly polarized optical transition that interacts with the resonator fields. Thus, to adequately describe the circulator, we can employ Eq. (4.31), but have to take into account the fact that we couple two fibers to the resonator and use different probing directions. This model then enables us to estimate the performance of such a circulator using state-of-the-art resonators (see Sec. 7.7.1).

## 7.5 Experimental procedure and modifications of the setup

To study the performance of the circulator it is necessary to consecutively send light into each of the four input ports while monitoring the power at all 4 output ports. Therefore, our fiber network is modified, as schematically depicted in Fig. 7.5. Each end of the coupling fibers was connected to a 99/1 beam splitter (BS), that enabled us to efficiently collect light coming from the resonator. The 1%-ports of these BSs are used to couple probe light into the coupling fibers. In order to guarantee a proper operation of the circulator we have to reliably prepare the atoms in the desired outermost  $m_F$ -ground state. In our experiment, this is achieved automatically by the interaction of the atoms with the detection light during the detection process. Due to SML of the resonator field, the circularity of the local polarization will depend on the detection direction. This enables us to prepare different states by choosing the direction from which we detect the atoms. When sending the detection through port 1(2) the atoms will be prepared in the  $m_F = +3(-3)$  ground state (cf. Sec. 5.4.8). For detecting atom coupling events, the single photon counting modules (SPCMs) in port 2(1) are connected to the atom trigger FPGA (cf. Sec. 5.4.7). Once an atom coupling event is recorded, the FPGA switches the MZ modulator of

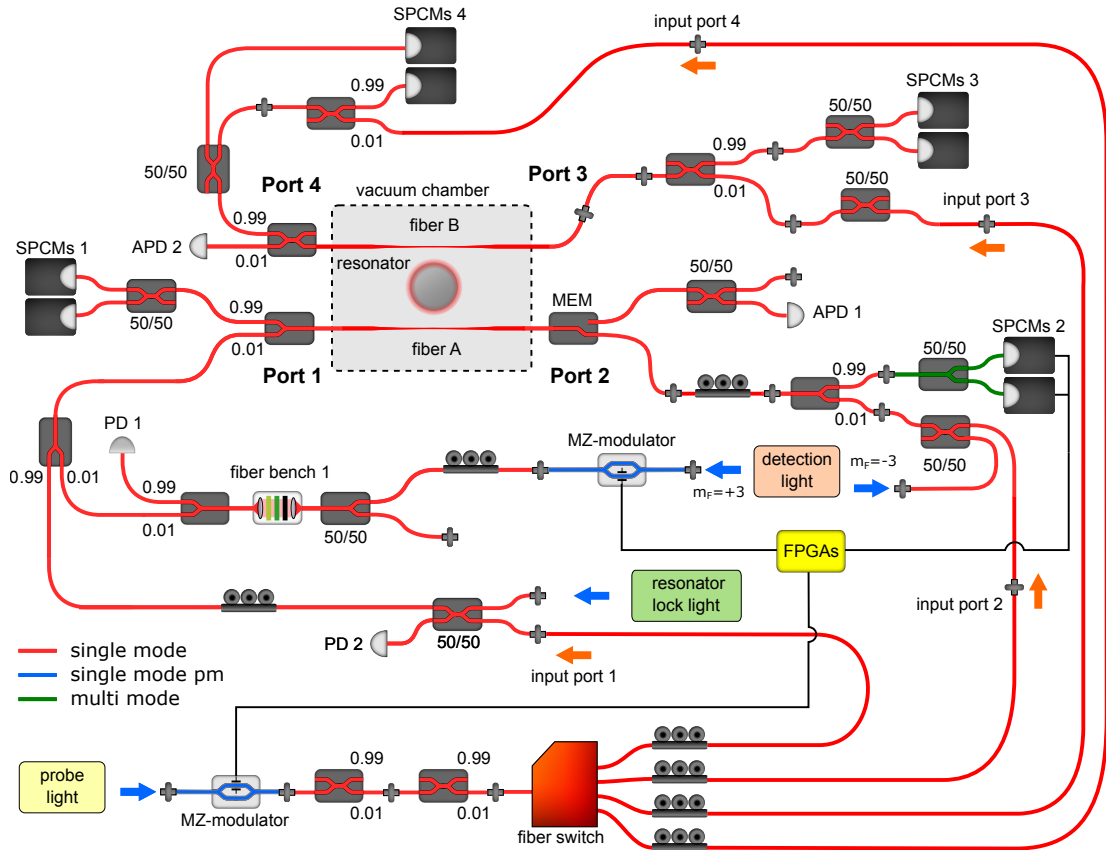


**Figure 7.5:** In order to be able to probe and monitor each of the four fiber ports, the fiber network introduced in Sec. 5.3.3 had to be vastly extended. For distributing the probe light between the 4 input ports, a single-mode fiber switch was inserted after the MZ modulator in the probing arm. This switch alternated the input port of the probe light every sequence run. While the length of the different probing arms look different in this schematic, in the experiment we tried to reduce the delay between the different arms as far as possible by using similar fiber lengths. To prepare the atoms in the opposite Zeeman ground state, the detection light was sent into port 2 instead of port 1, and the signal for the atom detection was recorded in output port 1 instead of port 2. Depending on the measurement setting, different output ports were equipped with one or two SPCMs. For an explanation of the symbols used see the legend in App. A.9.

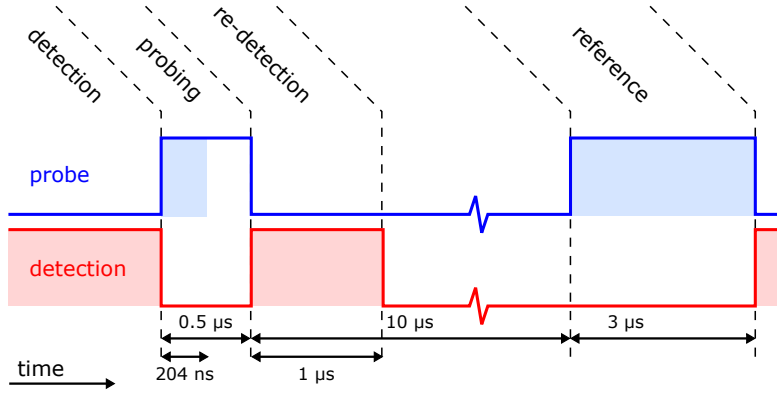


**Figure 7.6:** Schematic representation of the probing sequence used for the circulator measurement. After the detection of an atom coupling event, the detection light is switched off and the probe light is switched on for 500 ns, followed by a  $1 \mu\text{s}$  long re-detection. For the reference data without atom, the probe light is switched on again after  $10 \mu\text{s}$  which is well after the interaction time of the atom. Even though the probing window was 500 ns only the first 204 ns were analyzed to avoid contributions from atoms which were pumped out of the maximal  $m_F$ -state.

the detection light off and the MZ modulator of the probe light on. The probing window lasts for 500 ns of which only the first 204 ns were used in order to avoid repumping effects caused by the probe light. The probing window was followed by a re-detection for which the detection light was switched on again for  $\sim 1 \mu\text{s}$  (see Fig. 7.6). During the probing phase a small magnetic bias field of  $B = 1.5 \text{ G}$  is applied. In order to obtain the transmission without an atom present as reference,  $10 \mu\text{s}$  after the atom trigger a second probing pulse was applied. In order to probe the circulator consecutively from one of the 4 input ports, the probing light was sent onto a single-mode fiber switch (SM-Switch 2x4NIR850nm, Laser Components) after passing the MZ modulator. After each sequence run, the switch was reconfigured by the control program to send the light onto the next input port. This ensured that all probing directions are measured for the same experimental conditions. For each probing direction the light's polarization was aligned with the eigenpolarization of the resonator using paddle polarization controllers.

In order to be able to detect atoms while the resonator is interfaced by two fibers, the fiber used for detection, in our case fiber  $A$ , has to stay critically coupled, which implies that  $\kappa_A = \kappa_0 + \kappa_B$ . Thus, whenever setting a new measurement position of fiber  $B$ , fiber  $A$  has to be re-positioned accordingly. For the experiments described in the following the atoms were detected using a weak coherent laser with mean photon flux of  $13 \text{ photons}/\mu\text{s}$  and employing a first trigger criterion of  $N_{\text{trig}} = 6$  within  $1.2 \mu\text{s}$ . The recorded atom detection events were post-analyzed with a second trigger criterion  $N_{\text{trig}2} = 2$  within the  $1 \mu\text{s}$  long re-detection window (see Fig. 7.6). For probing the circulator, we send a weak coherent laser beam onto the resonator with a power corresponding to a mean photon flux of (8, 6, 11, 6) photons/ $\mu\text{s}$  for the respective input port.

When probing from port 3 the low on/off suppression ratio of the MZ modulator caused a high background in the detection port, which leads to an increased number of accidental atom detection events. In order to guarantee the reliable detection of atom coupling events, an additional

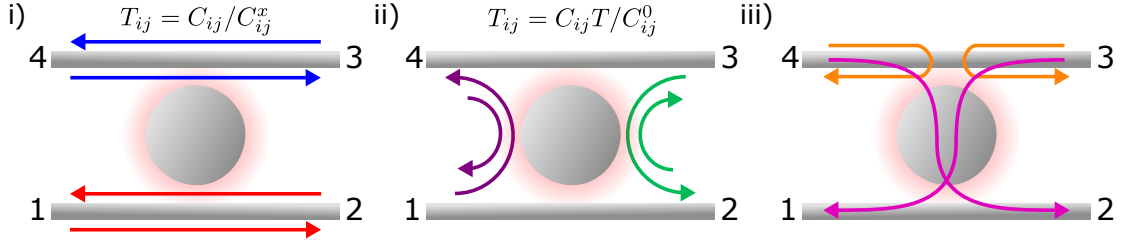


**Figure 7.7:** The three different groups of port-to-port transmission which we distinguish for normalizing the measured counts. The arrows indicate the respective beam paths considered in each case. In iii), not all paths are shown for clarity. See main text for further discussion.

fiber based electro-optical phase modulator (NIR-MX800, Photline) was inserted into the probe beam. The phase modulator was modulated with 2 GHz to shift the probe light out of resonance with the resonator while detecting atoms. During the probing window, the modulation was switched off again, such that the probe was resonant with atom and resonator.

For the experiment described in the following, resonator mode #2 was used, which has an intrinsic field decay rate  $\kappa_0 = 2\pi \times 5$  MHz (cf. Sec. 5.2.5). In order to determine  $\kappa_A$  and  $\kappa_B$  for each fiber setting, we employ the procedure described in Sec. 5.4.4.

### 7.5.1 Normalization of measured counts

For a correct estimation of the power transmissions  $T_{ij}$  of the circulator we have to take into account the a priori unknown input and output losses imposed by the auxiliary fiber network that is used to feed the probe light into and out of the tapered fiber couplers (see Fig.7.5), as well as, the unknown efficiencies of the photo-detectors. From the measurement we obtain count rates  $C_{ij}$ , which correspond to the average number of detected photons per probing interval and atom coupling event, when probing input port  $i$  and measuring at output port  $j$ . To obtain  $T_{ij}$  from  $C_{ij}$ , we devised the following measurement strategies which require two additional calibration measurements. For each setting of the coupling fibers, we determine the four transmission signals through the fibers while the resonator is far detuned from the probing frequency. Thus, the light is transmitted through the respective coupling fiber unaltered by the resonator, and is only subject to the losses along the fiber network, which we denote  $C_{ij}^x$ . In addition, we also record the output signal, when the resonator is resonant but no atoms are present,  $C_{ij}^0$ . To be able to employ the same analysis for these auxiliary measurements as is applied for the actual circulator measurements, we generate artificial triggers, which start the probing sequence. For the normalization, we distinguish three different groups of input–output combinations:

(i) The light is forward-transmitted through a given coupling fiber, as depicted in Fig. 7.7a ( $T_{12}$ ,  $T_{21}$ ,  $T_{34}$ ,  $T_{43}$ ): The corresponding output signal  $C_{ij}$  of the circulator obtained from the experiment, which includes the auxiliary fiber network, is normalized to the same output signal of the network  $C_{ij}^x$  when the BMR is far detuned from the probe light frequency. This directly yields the corresponding transmissions.

(ii) The light is transferred from a given input port to the adjacent output port of the other cou-

pling fiber, as depicted in Fig. 7.7b ( $T_{14}, T_{23}, T_{32}, T_{41}$ ): The measured output signal  $C'_{ij}$  of the circulator is normalized to the same output signal  $C_{ij}^0$  of the network when no atom is coupled to the BMR. We then multiply this normalized value by the predicted on-resonance transmission through the empty resonator, which is given by  $T = 1 - 2\kappa_0/\kappa_{\text{tot}}$  (cf. Eq. (7.15) for  $g=0$ ).

(iii) The light changes its propagation direction, as depicted in Fig. 7.7c ( $T_{i,i}$  and  $T_{i,i+2}$  with  $i \in \{1, 2, 3, 4\}$ ): From the design of the optical setup, we know that the output losses are approximately identical for ports 1 and 4. For these output ports the fiber network only consists of two spliced fiber beam splitters with known branching ratio. Taking advantage of this fact and using the normalization measurements carried out for points (i) and (ii) above, we can then derive the corresponding transmissions.

The most relevant characteristics of the circulator are included in (i) and (ii), for which a direct normalization is possible. For (iii) we need this additional assumption for normalization of the measured counts. However, their transmission values do not exceed a few percent, coming from small imperfections of the setup and thus carry little weight for the over-all performance of the circulator.

The three cases can be summarized in the normalization matrix as follows

$$[x_{i,j}] = \begin{pmatrix} T/C_{13}^0 & 1/C_{12}^x & C_{21}^x T^2 / C_{23}^0 C_{14}^0 & T/C_{14}^0 \\ 1/C_{21}^x & C_{14}^0 / C_{12}^x C_{14}^x T & T/C_{23}^0 & 1/C_{21}^x \\ 1/C_{34}^x & T/C_{32}^0 & C_{21}^x T / C_{34}^x C_{23}^0 & 1/C_{34}^x \\ T/C_{41}^0 & C_{12}^x T^2 / C_{41}^0 C_{14}^0 & 1/C_{13}^x & T/C_{41}^0 \end{pmatrix}, \quad (7.18)$$

from which the normalized transmissions can be calculated using  $T_{ij} = C_{ij} x_{ij}$ .

## 7.6 Experimental results

### 7.6.1 Optical circulator for single photons

Due to the imperfect circular polarization of the resonator modes, the ratio between  $\Gamma_{\text{ccw}}$  and  $\Gamma_{\text{cw}}$  in our experiment is finite. Concerning the performance of the circulator, there is, thus, a trade-off between efficient light transfer from one fiber to the other via the weakly coupled CW mode, which implies  $(\kappa_A, \kappa_B) \gg \kappa_0 + \Gamma_{\text{cw}}$ , and the condition that the presence of the atom should significantly influence the field decay rate,  $\Gamma_{\text{ccw}} \ll \kappa_{\text{tot}}$ . In order to find the optimum working point in our experiment, we measure the circulator performance as a function of the total resonator losses  $\kappa_{\text{tot}}$  by changing the distance between the fibers and the resonator, thus changing  $\kappa_A$  and  $\kappa_B$ . For each setting, we measure the output signal  $C_{ij}$  at all output ports  $j$  when sending a weak coherent probe field into the four different input ports  $i$  and normalize according to Sec. 7.5.1.

Figures 7.8 a and b show the relevant transmissions as a function of  $\kappa_{\text{tot}}$ . The solid lines are the theoretical prediction for our system, obtained from Eq. (7.17) for the case of a simple two-level atom exhibiting a circularly polarized transition coupled to the resonator modes (see

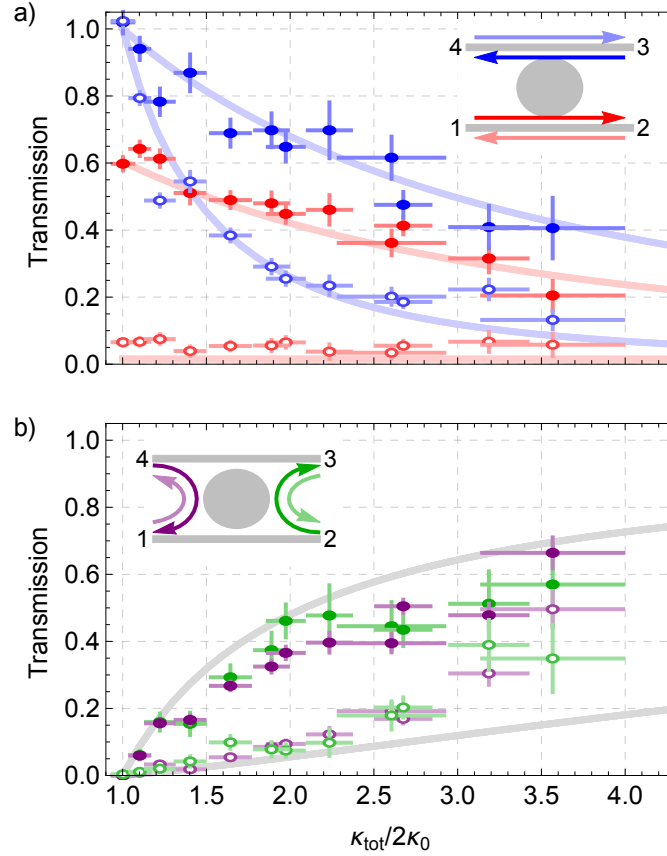


**Figure 7.8:** a) & b) Port to port transmissions as a function of the normalized field decay rate of the fiber-coupled resonator,  $\kappa_{\text{tot}}/2\kappa_0$ , in the presence of an atom prepared in the  $|F=3, m_F=+3\rangle$  Zeeman state. The insets show the color code used for the respective ports. For an optimal circulator performance the transmissions indicated by solid circles should be high while the transmissions shown as open circles should be low. The solid lines in both panels are the predictions of our theoretical model (see Sec. 4.4.2) with the atom–resonator coupling strength  $g_{\text{ccw}} = 2\pi \times 12$  MHz, the intrinsic field decay rate of the resonator  $\kappa_0 = 2\pi \times 5$  MHz and the polarization overlap  $|\alpha_{\sigma^+}|^2 = 0.97$ . The vertical error bars indicate the  $\pm 1\sigma$  statistical errors while the horizontal error bars represent an estimate of the variation of  $\kappa_{\text{tot}}$  due to drifts of the distances between the fiber couplers and the resonator during the corresponding measurement.



	$m_F = +3$	$m_F = -3$	no atom
$\mathcal{F}$	$0.72 \pm 0.03$	$0.70 \pm 0.02$	$0.48 \pm 0.04$
$\mathcal{N}$	$0.54 \pm 0.07$	$-0.49 \pm 0.04$	$0.02 \pm 0.07$
$\eta$	$0.73 \pm 0.04$	$0.70 \pm 0.02$	$0.67 \pm 0.03$
$I_{12}$	$10.9 \pm 2.5$ dB	$-8.3 \pm 0.8$ dB	$0.6 \pm 0.5$ dB
$I_{23}$	$6.8 \pm 1.3$ dB	$-4.9 \pm 0.7$ dB	$0.0 \pm 0.3$ dB
$I_{34}$	$4.7 \pm 0.7$ dB	$-3.7 \pm 0.4$ dB	$1.4 \pm 0.7$ dB
$I_{41}$	$5.4 \pm 1.1$ dB	$-5.6 \pm 0.5$ dB	$-0.2 \pm 0.4$ dB

**Table 7.3:** Summary of the circulator characterization.

Sec. 4.4.2). In the following we briefly discuss the evolution of the individual transmissions as fiber  $B$  approaches the resonator, i.e.  $\kappa_{\text{tot}}$  is changed.

Probing port 1 ( $T_{12}, T_{14}$ ): The strongly coupled atom ( $\Gamma_{\text{ccw}} > \kappa_{\text{tot}}$ ) suppresses the built up of a resonator field and the light is mainly transmitted to port 2. As  $\kappa_{\text{tot}}$  increases, the effect of the atom decreases ( $\kappa_{\text{tot}} \approx \Gamma_{\text{ccw}}$ ) and the resonator field starts to built up, leading to a slowly rising signal in port 4, while the signal in port 2 decreases.

Probing port 3 ( $T_{34}, T_{32}$ ): This probing direction again strongly interacts with the atom ( $\Gamma_{\text{ccw}} > \kappa_{\text{tot}}$ ). Thus, we expect a similar behavior as for probing port 1. However, for  $\kappa_{\text{tot}}/2\kappa_0 = 1$ , fiber  $B$  is not coupled to the resonator yielding unity transmission. As  $\kappa_{\text{tot}}$  increases, light slowly starts to couple into the resonator yielding a decreasing transmission to port 4 and a slowly increasing transmission through the resonator to port 2.

Probing port 2 ( $T_{23}, T_{21}$ ): Since the atom is only weakly coupled to this propagation direction ( $\Gamma_{\text{cw}} \ll \kappa_{\text{tot}}$ ) the resonator is nearly critically coupled to fiber  $A$ , causing the signal in port 2 to be almost zero. Since fiber  $A$  stays critically coupled for all measurements, the transmission stays close to zero when increasing  $\kappa_{\text{tot}}$ . However, the transmission to port 3 quickly rises as fiber  $B$  is coupled more and more efficiently.

Probing port 4 ( $T_{41}, T_{43}$ ): Again, for this probing direction the coupling to the atom is weak. However, since fiber  $B$  is initially not coupled to the resonator, most of the light is transmitted to port 3 and nothing transferred to port 1. When fiber  $B$  starts to couple to the resonator, the transmission to port 3 quickly decreases and the light is more and more efficiently coupled through the resonator to port 1.

From these measurements, we evaluate the performance of the circulator by calculating the figures of merit introduced in Sec. 7.1.3. In Fig. 7.9, we plot the nonreciprocity  $\mathcal{N}$ , the process fidelity  $\mathcal{F}$  and the survival probability  $\eta$  as a function of  $\kappa_{\text{tot}}$ . Both  $\mathcal{N}$  and  $\mathcal{F}$  show an optimum circulator performance for  $\kappa_{\text{tot}}/2\kappa_0 = 2.2$ , where  $\mathcal{F} = 0.72 \pm 0.03$ ,  $\mathcal{N} = 0.54 \pm 0.07$  and, at the same time,  $\eta = 0.73 \pm 0.04$ . Moreover, in Fig. 7.10b the isolations of the four independent isolators which form the circulator are plotted as a function of  $\kappa_{\text{tot}}$ . For the optimal working point, we obtain  $(I) = (10.9 \pm 2.5, 6.8 \pm 1.3, 4.7 \pm 0.7, 5.4 \pm 1.1)$  dB. The photon survival probability can be translated into an average insertion loss of  $L = -10 \log \eta = 1.4$  dB.

For the optimal working point,  $\kappa_{\text{tot}}/2\kappa_0 = 2.2$ , we also plot the measured transmission matrix of the circulator (Fig. 7.11c), which is in good quantitative agreement with the theoretical pre-

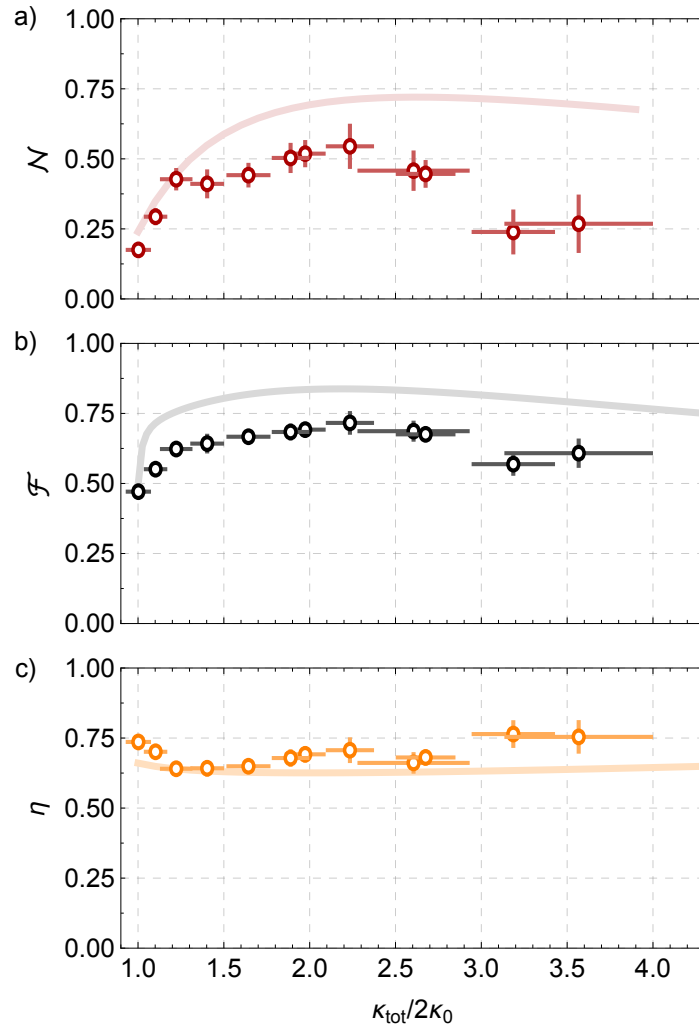


**Figure 7.9:** Performance of the circulator: a) Nonreciprocity  $\mathcal{N}$ , b) operation fidelity  $\mathcal{F}$  and c) photon survival probability  $\eta$  of the circulator, calculated from the full transmission matrices including the data shown in Fig. 7.8. The solid lines are the predictions from the same theoretical model used in Fig. 7.8. Both quantities  $\mathcal{N}$  and  $\mathcal{F}$  peak at  $\kappa_{\text{tot}}/2\kappa_0 = 2.2$ , giving the optimal fiber–resonator coupling for our experiment.

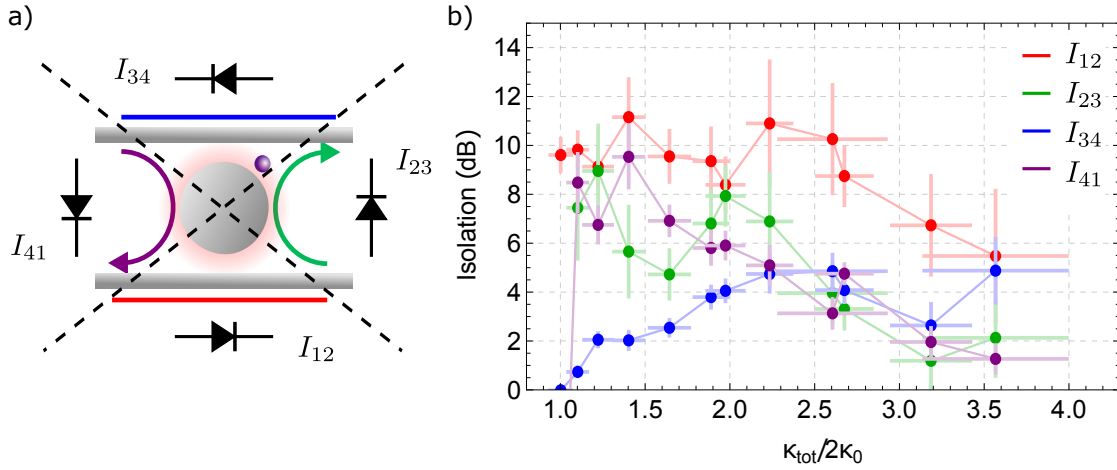


**Figure 7.10:** Isolation scan: a) The 4-port circulator can be decomposed into 4 isolators between two adjacent ports. b) For the data shown in Fig. 7.8 we can calculate the isolation of the respective isolators, using Eq. 7.9.  $I_{12}$ : For the ideal case of perfect circularly polarized modes, we expect zero transmission in backward direction since the light does not couple to the atom and the fibers are adjusted such that the empty resonator is critically coupled to fiber A. This would yield infinite isolation independent on the forward transmission. However, experimental imperfections, such as misaligned polarization, detector dark counts and the imperfect circular polarization of the modes, significantly reduce the obtained isolation.  $I_{34}$ : When fiber B is not efficiently coupled, the isolation is low and it monotonously increases with the coupling, as it approaches critical coupling for  $\kappa_B \gg 1$ .  $I_{23}$ ,  $I_{41}$ : These diodes require a strong effect by the atom to suppress the backward propagating light. Thus, as the total resonator loss increases the isolation decreases.

dictions (see Fig. 7.11b) and good qualitative agreement with the ideal transmission matrix (see Fig. 7.11a). From the transmission matrices, the nonreciprocal response is clearly visible as an asymmetry with respect to the diagonal.

In order to show that it is the atom that introduces the nonreciprocal behavior, we also analyze the behavior of our system for a time window in which the atom has already left the resonator mode. For  $\kappa_{\text{tot}}/2\kappa_0 = 2.2$  we obtain  $\mathcal{F} = 0.48 \pm 0.04$  and  $\mathcal{N} = 0.02 \pm 0.07$ , which indicates fully reciprocal transmission. But, we observe a comparable survival probability  $\eta = 0.67 \pm 0.03$ . The measured transmission matrix in the absence of an atom is plotted in Fig. 7.11c.

In order to prove that the circulator is indeed programmable and that we can reverse its operation direction, we have to prepare the atom in the opposite Zeeman ground state  $|F = 3, m_F = -3\rangle$ . For this configuration, we measure at the optimal coupling point  $\kappa_{\text{tot}}/2\kappa_0 = 2.2$  and obtain  $\mathcal{F} = 0.70 \pm 0.02$ ,  $\mathcal{N} = -0.49 \pm 0.04$  and  $\eta = 0.70 \pm 0.02$ . For the reversed operation direction the isolations become negative,  $(I) = -(8.3 \pm 0.8, 4.9 \pm 0.7, 3.7 \pm 0.4, 5.6 \pm 0.5)$  dB. The transmission matrix for this configuration is also shown in Fig. 7.11.

In Tab. 7.3 the obtained characteristics for both operation directions are summarized.

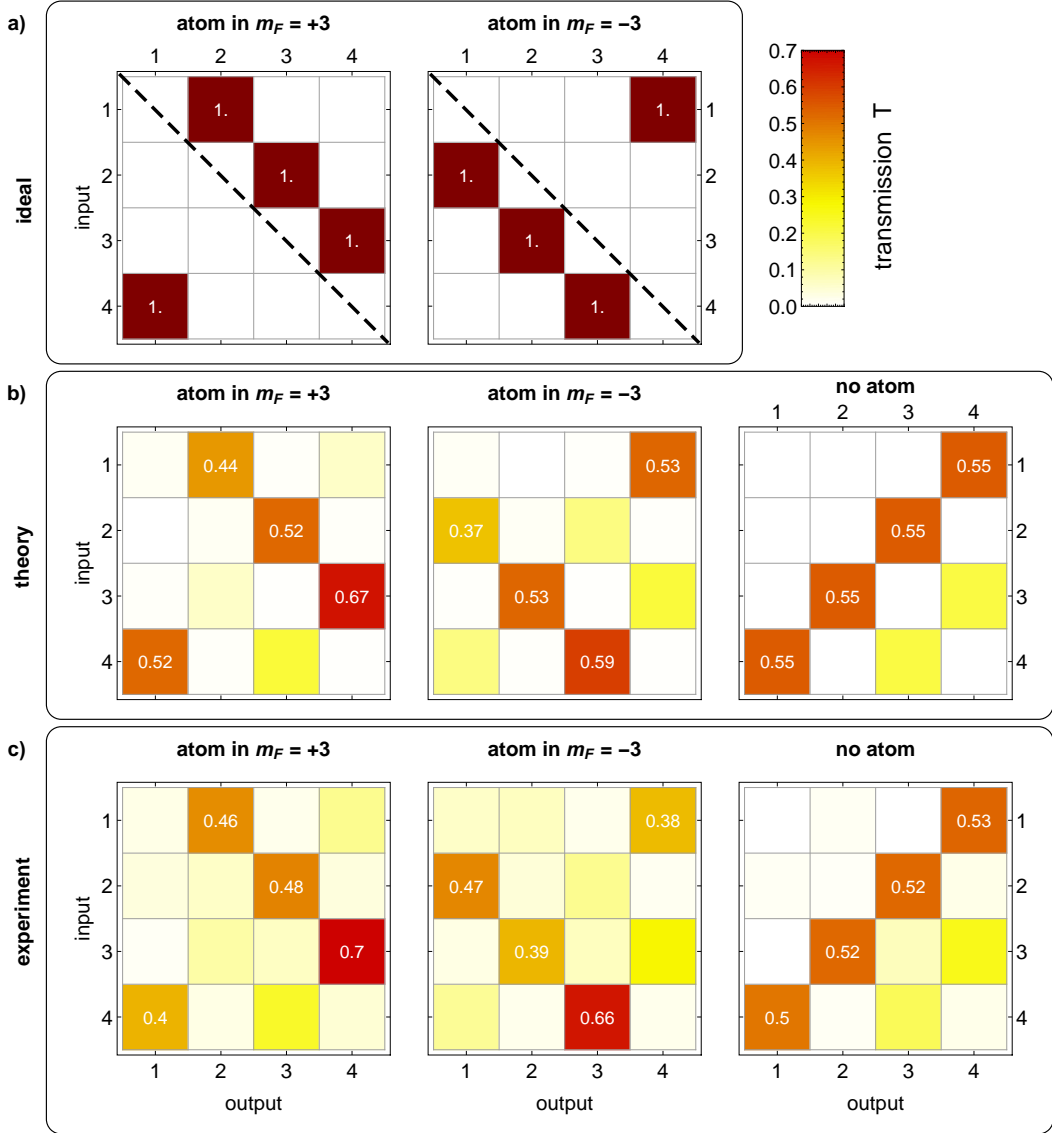


**Figure 7.11:** Transmission matrices  $[T_{i,j}]$ . The rows of each transmission matrix correspond to the input ports  $i$  and the columns to the output ports  $j$ . a) Transmission matrix for an ideal lossless circulator and its two operation directions. The broken symmetry with respect to the dashed line indicates the nonreciprocal character of the device. b) Transmission matrices calculated for our experimental parameters (see Fig. 7.8). For the case where the atom was prepared in  $m_F = -3$  we also consider a small atomic detuning of 4.2 MHz introduced by the small bias magnetic field of 1.5 G in our experiment. c) Measured transmission matrix. For b) and c), the fiber-resonator coupling was set to the optimal working point  $\kappa_{\text{tot}}/2\kappa_0 = 2.2$ . For comparison, the transmission matrix of the system measured without atom is also shown. Here, the symmetric matrix indicates reciprocal operation. In all panels, the four highest transmission values are displayed in the respective block. For the remaining values cf. App. A.4.1.

	$g^{(2)}(0)$	$\tau_{sp}$	$\gamma'$
1 $\rightarrow$ 2	0.44	9.3 $\pm$ 1.1 ns	8.6 $\pm$ 1.0 MHz
1 $\rightarrow$ 4	2.75	8.6 $\pm$ 0.8 ns	9.3 $\pm$ 0.7 MHz
3 $\rightarrow$ 4	0.84	7.2 $\pm$ 1.8 ns	11.1 $\pm$ 1.7 MHz
3 $\rightarrow$ 2	2.47	6.4 $\pm$ 1.1 ns	12.5 $\pm$ 1.0 MHz

**Table 7.4:** Fits to the bunching and anti-bunching features of the second-order correlation function.  $\tau_{sp}$  is the effective atomic lifetime, obtained from the HWHM of the Lorentzian fits, and  $\gamma'$  the corresponding Purcell-enhanced atomic emission rate.

## 7.6.2 Photon number-dependent routing

In the regime of strong coupling, a single atom suffices to significantly alter the state of the light, i.e. the critical atom number  $N_0 < 1$ . At the same time, a single photon already saturates the atom, i.e. the critical photon number  $n_0 < 1$ . Thus, similar to the observations in Ch. 6, we expect a strongly nonlinear optical response of the circulator down to the level of single photons. In particular, the atom-induced losses  $\Gamma$  and thus the transmission properties for the case of two photons simultaneously impinging on the circulator should strongly differ from the single-photon case. In order to demonstrate this quantum nonlinearity, we measure second-order intensity correlation functions (cf. App. A.5) for all input–output configurations when the atom is prepared in the  $|F=3, m_F=+3\rangle$  Zeeman ground state, at the optimal working point of the circulator. Therefore, each output port is equipped with a 50/50 BS and two SPCMs forming a Hanbury Brown–Twiss type setup [236] (see Fig. 7.5). From the arrival times of photons at the two detectors the time delay  $\tau$  between photon pairs can be calculated. Histogramming the time delay and normalizing such that  $g^{(2)}(\tau) = 1$  for  $\tau \gg 1/\kappa_{\text{tot}}$  yields the second-order correlation function,  $g^{(2)}(\tau)$ , as discussed in App. A.5.

In Fig. 7.12 the measured auto-correlation functions of the different output ports are shown as a function of the time delay  $\tau$ . As expected, nonlinear effects occur for the cases where the photons couple to the CCW resonator mode, which strongly couples to the atom. For (1  $\rightarrow$  2) and (3  $\rightarrow$  4), we observe photon anti-bunching which is more pronounced for the former case due to the unequal fiber couplings,  $\kappa_A > \kappa_B$ . In contrast, strong photon bunching is apparent for the settings 1  $\rightarrow$  4 and 3  $\rightarrow$  2. This agrees with the theoretical expectation because, here, both measurements amount to probing the photon statistics of the intra-resonator field. The bunching or anti-bunching vanishes when the time delay between the photons increases beyond the effective atomic lifetime  $\tau_{sp} = 1/2\gamma'$ , where we have introduced the Purcell-enhanced atomic emission rate  $\gamma' = g^2/\kappa_{\text{tot}} + \gamma$ . The measured widths are in good agreement with the theoretical predicted value of  $\tau_{sp} = 8.3$  ns corresponding to  $\gamma' = 2\pi \times 9.5$  MHz (see Tab.7.4). We note that,  $g^{(2)}(0) > 0$  for the settings 1  $\rightarrow$  2 and 3  $\rightarrow$  4 is not due to experimental imperfections but is theoretically expected as the light fields at output ports 2 and 4 are in a coherent superposition between the (bunched) resonator light field that couples back into the fiber and the coherent state of the probe laser field. For probing directions which couple to the cw mode (2  $\rightarrow$  1, 2  $\rightarrow$  3, 4  $\rightarrow$  3 and 4  $\rightarrow$  1), the light interacts only weakly with the atom and thus no nonlinear effects can be observed.

By measuring the second-order intensity correlations, we demonstrated the strong nonlinear response of the circulator. Thereby, we prove its capabilities of photon-number dependent sorting. While the measurements were performed for the optimal working point of the circulator operation, the nonlinear effect could be further optimized. However, as also discussed in Ch. 6, for optimum performance, this also requires a well-defined coupling between atom and resonator mode, which is not the case for the present experiment.

## 7.7 Discussion and outlook

In summary, we have realized a low-loss optical circulator which is not only fiber-integrated but, in addition, fully programmable. Thereby, our setup outperforms previous realizations in terms of insertion loss and gives comparable results in terms for isolation (cf. Sec. 7.2). In contrast to standard schemes, the operation direction is controlled by the internal state of the atom. This allows us to change the operation direction by flipping the internal atomic state. In magneto-optic devices this would require to flip the bias field, which is not straightforward for integrated devices.

However, for practical applications it is important for the atomic state not to change over time, e.g., due to optical depumping induced by the probing light. If the atom is prepared in the  $m_F = 3(-3)$  ground state, light that couples to the CCW (CW) mode, drives a closed cycling transition, thus no pumping occurs. However, light that couples to the opposite CW (CCW) mode, will progressively pump the atom into the opposite  $m_F$  state, as discussed in Sec. 5.4.8. As a consequence, the transmission properties change and the operation direction of the circulator is eventually reversed, when the atom has reached the opposite ground state. As discussed in Sec. 5.4.8, 12 photon can impinge onto the resonator before the population of the outermost  $m_F$ -state is reduced to  $1/e$ . Nevertheless, this unwanted optical pumping can be counteracted by using an additional light field that permanently pumps the emitter toward the desired internal state, thus enabling continuous operation of the circulator.

Another crucial parameter is the power range of the guided light field that allows proper performance. While other schemes require high powers, our circulator works for single photons. The upper power limit is set by the saturation intensity of the atoms and the atom–light coupling strength. For the demonstrated experimental realization, this yields an upper power limit on the order of 10 pW, which guarantees that there is never more than one photon present within the Purcell shortened atomic lifetime. By adding more atoms, this power limit can be increased at the cost of loosing the quantum functionalities of the circulator.

Within these specifications, our circulator concept is useful for the processing and routing of classical signals in integrated optical circuits and networks. In particular, the small insertion loss, makes it also applicable for quantum information processing.

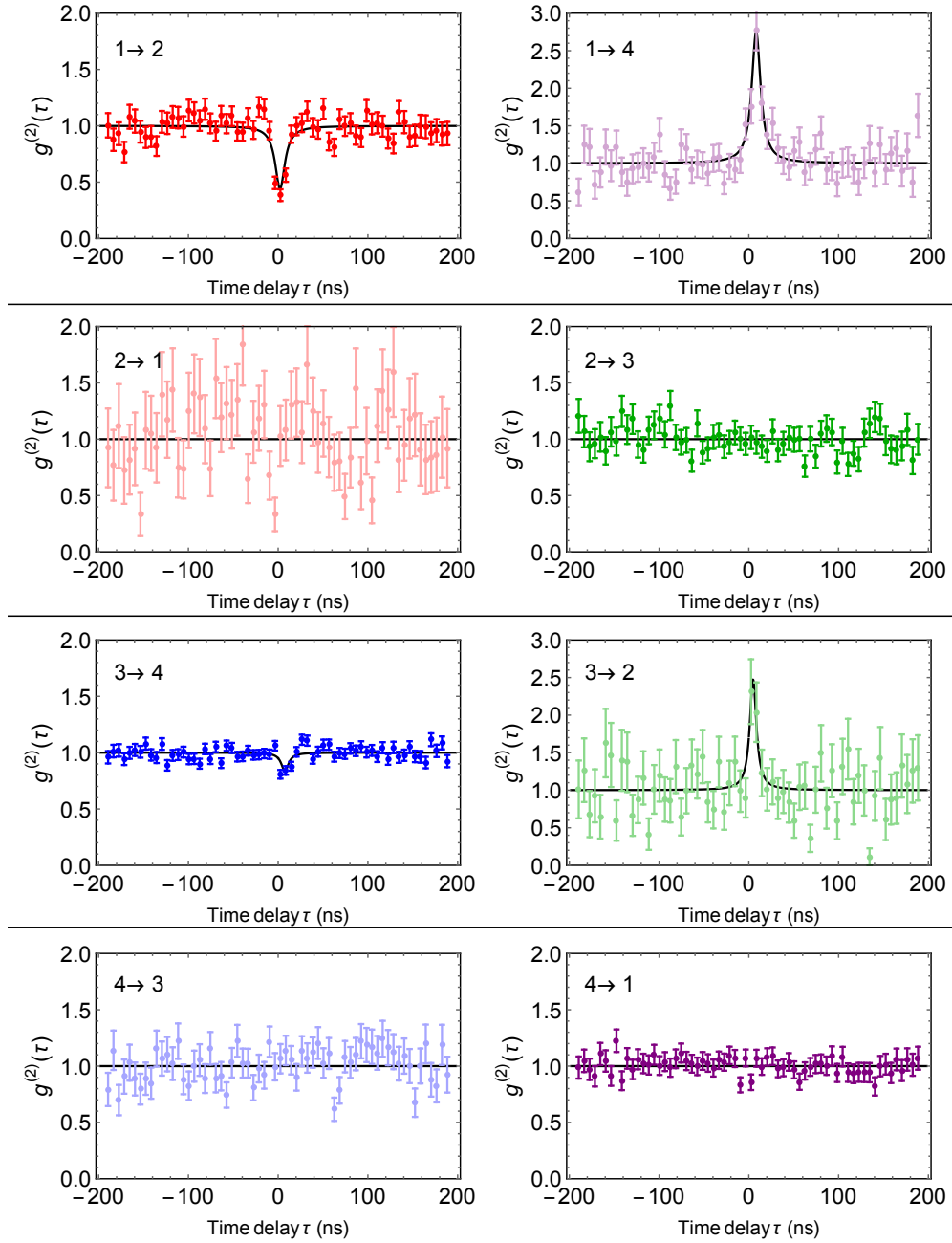


**Figure 7.12:** Quantum nonlinearity of the circulator. Second-order intensity correlation,  $g^{(2)}(\tau)$ , as a function of the detection time delay  $\tau$  between pairs of photons, normalized such that  $g^{(2)}(\tau) = 1$  for  $\tau \gg 1/\kappa_{\text{tot}}$  (cf. App. A.5). The labels  $i \rightarrow j$  indicate the input and output ports for the respective measurement. The solid lines are guides to the eyes, where the bunching and anti-bunching features are fitted with a Lorentzian. The error bars indicate the  $\pm 1\sigma$  statistical error. The measurement was performed for the optimal working point  $\kappa_{\text{tot}}/2\kappa_0 = 2.2$ .

### 7.7.1 Expected circulator performance

Even though the experiments performed in this chapter constitute only proof-of-principle demonstrations of a novel approach for realizing an optical circulator, it already yields comparable performance with respect to other integrated realizations. In particular, the unprecedented low insertion loss renders the circulator the first quantum-compatible nonreciprocal integrated device. However, our experiment has not yet exhausted the full potential of this new circulator scheme. On the one hand, the resonator mode we employ in our experiment has a  $Q$ -factor of  $4 \times 10^7$  which does not correspond to the state-of-the-art BMR mode [76]. On the other hand, the atom was not trapped which causes a variation of the coupling strength thereby reducing the performance. Using the analytical model described in App. A.4.2, we can estimate the performance of a circulator that can be achieved with our experimental scheme. Figure 7.13 compared  $\eta$  and  $\mathcal{F}$  as a function of the fiber-resonator coupling rate  $\kappa$  for two  $Q$ , one corresponding to the mode used in our experiment and the other corresponding to a state-of-the-art BMR mode. For the calculation, we assumed an atom-resonator coupling strength of  $g = 2\pi \times 30$  MHz, achievable by trapping the atom at a distance of about  $\sim 100$  nm from the resonator surface (cf. Fig. 5.3), and a silica BMR, for which the resonator field has an overlap with perfect circularly polarized light of  $\alpha = \sqrt{0.97}$ . For optimal fiber-resonator coupling at  $\kappa/\kappa_0 = 12.2(3.9)$  we obtain  $\eta = 0.93(0.8)$  and  $\mathcal{F} = 0.94(0.93)$  for a mode with  $Q_0 = 4 \times 10^8(4 \times 10^7)$ , which corresponds to  $\kappa_0 = 2\pi \times 0.5(5)$  MHz. Figure 7.13b shows the expected performance at the optimal coupling point as a function of the quality factor of  $Q_0$  ( $\kappa_0 \alpha^2 2\pi \times 0.5$  MHz). While the photon survival probability monotonously approaches unity with rising quality factor, the average operation fidelity is limited by the imperfect polarization overlap with  $\sigma^+$  polarization ( $\alpha^2 < 1$ ). This could be improved by using WGM resonators manufactured from materials with higher refractive index which would result in larger values of  $\alpha$ . Alternatively, a solid-state emitter could be placed inside the resonator structure, in a region of perfect circular polarization ( $\alpha^2 = 1$ ).

While for state-of-the-art BMRs coupled to a single trapped atom almost perfect circulator performances are feasible, it remains an open challenge to fabricate such a device on an integrated platform. Therefore, one requires solid-state emitters that can be directly placed on the chip with good coherence properties and well-controlled resonance frequencies. In addition, integrated WGM or ring resonators with adequate  $Q$ -values have to be fabricated.

### 7.7.2 Possible applications

Despite its importance for integrated light-based classical and quantum information processing the demonstrated circulator could also play an important part in quantum simulation. In principle, the atom can be prepared in a coherent superposition of two states, that cause different operation directions of the circulator. This realizes a circulator that is as well in a coherent superposition of its two operation direction. The interaction of an impinging photon with such a circulator would directly result in entanglement between the path degree of freedom of the photon and the state of the circulator. Thus, such a circulator would be capable of playing an active part in quantum information processing by entangling atoms with photons. In this context, our circulator is the first realization of a nonreciprocal quantum device.



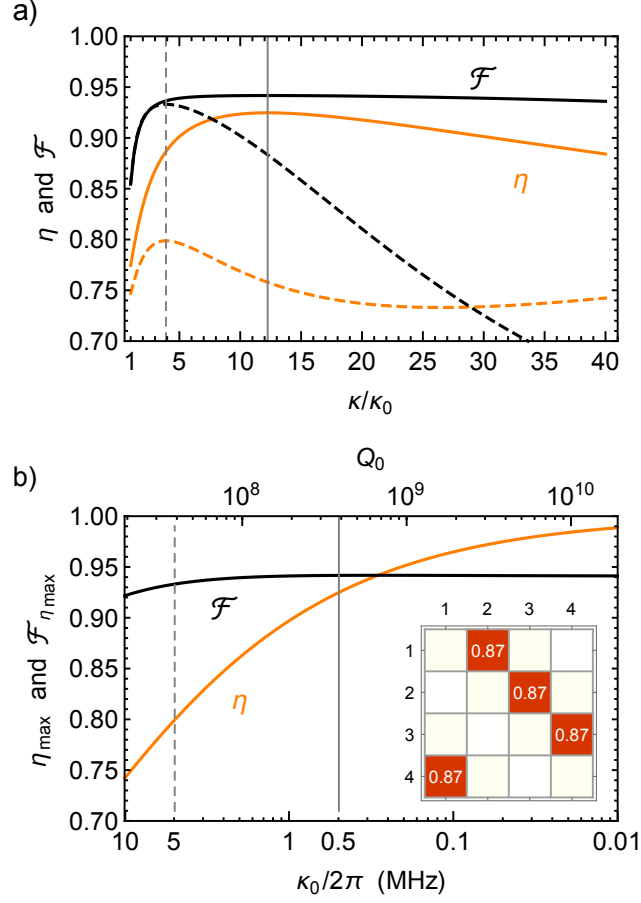


**Figure 7.13:** a) Operation fidelity  $\mathcal{F}$  and photon survival probability  $\eta$  as a function of the resonator–fiber coupling rate  $\kappa$ , for two different intrinsic resonator field decay rates  $\kappa_0/2\pi = 0.5$  MHz (solid lines) and  $\kappa_0/2\pi = 5$  MHz (dashed lines). Since the nonreciprocity  $\mathcal{N}$  gives very similar results as  $\mathcal{F}$  for the chosen parameters it is not plotted here. The vertical lines indicate the points of maximal survival probability  $\eta_{\max}$  at  $\kappa_{\eta_{\max}}$ , for the two settings. b) Maximum survival probability  $\eta_{\max}$  and corresponding fidelity  $\mathcal{F}_{\eta_{\max}} = \mathcal{F}(\kappa_{\eta_{\max}})$  as a function of the intrinsic field decay rate  $\kappa_0$  which can also be expressed via the intrinsic quality factor  $Q_0$ . The vertical lines indicate the exemplary values of  $\kappa_0$  used in a). The inset shows the transmission matrix obtained for a circulator with  $\kappa_0/2\pi = 0.5$  MHz ( $Q_0 = 4 \times 10^8$ ). For both figures and the inset, the following parameters were used:  $(g, \gamma) = 2\pi \times (30, 3)$  MHz and  $\alpha = \sqrt{0.97}$ .

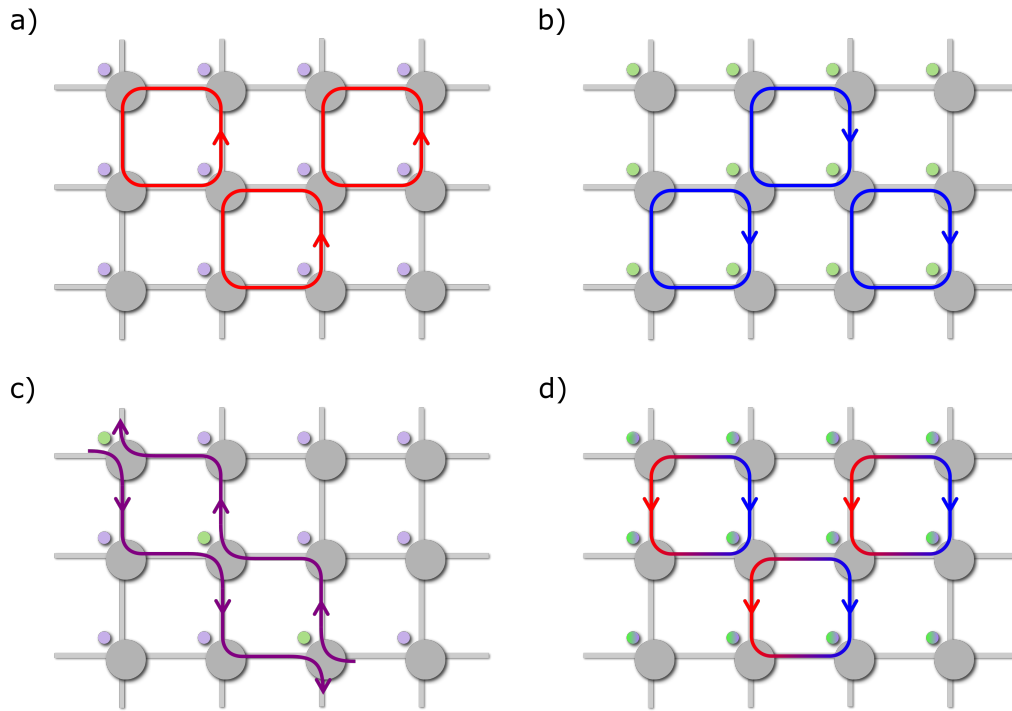


**Figure 7.14:** a) & b) A lattice formed by classical programmable circulators, where all have the same operation direction, i.e. all atoms are prepared in the same state. In this case, the light is trapped on circular trajectories. c) When introducing defects, i.e. circulators with opposite operation direction, light can flow along certain directions. d) When preparing the circulators in a coherent superposition of their operation directions, large entangled states can be created by sending photons through the network.

Since the circulator is a multi-port device, many such devices can be connected to form a network or lattice, where each node consists of a circulator. Arranging  $N$  circulators such that they form a linear array allows one to realize a  $(2N + 2)$ -port optical circulator. Moreover, such an array can be used as a programmable router, where, as long as all circulators are programmed to have the same operation sense, the light is trapped in a single placket of the array (see Fig. 7.14a). When introducing defects, by reprogramming some nodes to have the opposite sense of operation the photons can move in certain directions, as depicted in Fig. 7.14b. When making use of the quantum nature of our circulator by preparing all circulators of the lattice in a coherent superposition of both their operations directions, we would create massively entangled states, by sending photons through the network. In addition, such circulator arrays enable the implementation of artificial gauge fields for photons [228, 237, 238]. Here, with the nonlinearity at the level of single quanta allows the flux to become a dynamical degree of freedom that interacts with the particles themselves, opening the way for implementing non-classical artificial gauge fields [239].

## Summary and outlook

### Summary

In the framework of this thesis, two proof-of-principle demonstrations of nanophotonic devices have been performed. Both are based on a single rubidium atom which is chirally coupled to a BMR.

The first experiment realized an ultra-strong optical nonlinearity at the single-photon level. When probing the coupled atom–resonator system with a weak coherent beam, we observe a phase difference of  $\pi$  between single photons and coincident photons. In particular, this corresponds to the largest possible nonlinear phase shift for the smallest amount of light. Such a nonlinearity is the essential ingredient for implementing an efficient, error-proof Bell state analyzer [184, 185] and thereby provides a key element for quantum communication and optical quantum information processing. In addition, we have provided a scheme that could in principle be implemented in our experiment to realize a quantum-controlled phase-flip gate, which would then enable deterministic quantum computation protocols with photons.

The second experiment demonstrated a quantum optical circulator. This first realization of a low-loss fiber-integrated circulator has the advantage of being fully programmable. The demonstrated circulator is formed by a coupled atom–resonator system which is interfaced by two tapered fiber couplers. The chiral, i.e. direction-dependent, coupling between the atom and the resonator field gives rise to nonreciprocal transmission. Such a device is not only useful for the processing and routing of classical signals at ultra-low light levels in integrated optical circuits and networks. In contrast to dissipative nonreciprocal devices, a circulator that is controlled by a single quantum system also enables operation in coherent superposition states of routing light in one and the other direction, thereby providing a route toward its application in future photonic quantum protocols. Since the demonstrated operation principle is universal in the sense that it can straightforwardly be implemented with a large variety of different quantum emitters. Such a circulator could be fabricated on a chip using solid state emitters and high- $Q$  integrated resonator structures. These integrated quantum circulators could then be produced in large numbers and connected to form two- and three-dimensional networks. Such networks are potential candidates

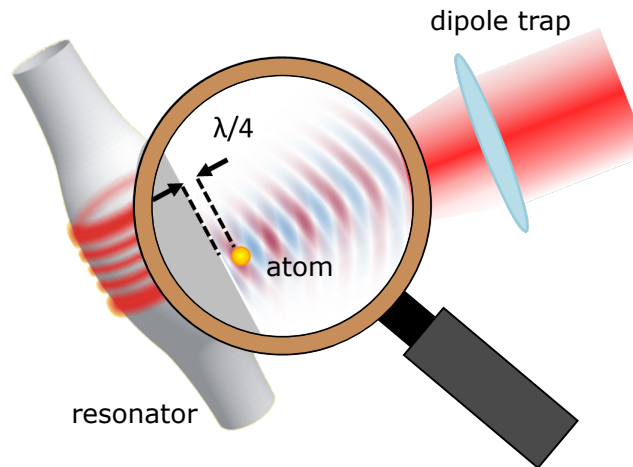


**Figure 8.1:** Sketch of a possible trapping scheme. The tightly focused trapping beam interferes with the partially reflected beam and forms a standing wave pattern with a dipole trap potential minimum at a distance of  $\lambda/4$  from the surface.

for implementing lattice-based quantum computation [240] and would enable the implementation of artificial gauge fields for photons [228, 237, 238]. In particular, utilizing the nonlinearity at the level of single quanta allows for the flux to become a dynamical degree of freedom that interacts with the particles themselves [239].

### Outlook: Trapping atoms close to a WGM resonator

The experiments described in this thesis were performed during the transit of free falling atoms through the resonator mode. As a result, the interaction time is limited to a few microseconds and the coupling events happen non-deterministically. In order to realize deterministic operation of devices which are based on the interaction between WGM resonators and single quantum emitters, the emitter has to be trapped in the resonator mode. Furthermore, trapping the atom in a small volume close to the resonator, would allow a stable coupling strength which is essential for many applications.

Even though the interaction between single atoms and WGMs has already been demonstrated several years ago using free falling atoms, to trap the atoms in the evanescent field of the resonator is still an open challenge. While there are proposals to employ the resonator fields themselves for trapping the atoms [241], we follow an approach similar to that demonstrated in Ref. [79]. This employs a red-detuned laser beam that is tightly focused onto the resonator. Interference between the incident beam and its reflection forms a partially modulated standing wave pattern. The light provides an optical dipole potential [242] which creates a trapping site at the first intensity maximum which is at a distance of  $\lambda/4$  from the surface, where  $\lambda$  is the wavelength of the trapping light. In order to load atoms into such a trap in the existing setup we

---

can employ the usual atom delivery via the atomic fountain and switch on the trap light upon an atom detection. If the atom is located at the position of the trap focus there is a certain probability to trap it. As the evanescent field of the resonator mode, and thus the atom–resonator coupling strength  $g$ , decrease exponentially with the distance to the surface (see Fig. 8.1b), it is crucial to minimize the atom–resonator distance. A standard far off resonant dipole trap (FORT) would use a trapping light field red-detuned from the  $5S_{1/2} \rightarrow 5P_{3/2}$  transition of  $^{85}\text{Rb}$  with a wavelength of  $\lambda_{\text{red}} \sim 781$  nm. This would form a stable trapping potential at a distance of about 195 nm from the resonator surface. At this position the coupling strength to the fundamental mode is  $g_{q=0} = 2\pi \times 13$  MHz, which would be comparable to the coupling strength observed in this thesis.

Since the atoms are not cooled during the loading process, also a cooling procedure has to be applied. With such a trapping scheme, it should be possible to increase the life time of the atom in the evanescent field by several orders of magnitude which would make a large range of applications experimentally feasible. For example, it would enable one to perform complex quantum protocols, such as the proposed controlled phase gate (CPG) introduced in Sec. 6.5. In addition, it would allow one to create Schrödinger cat states of light, by preparing our quantum circulator in a superposition of its operation direction.



# List of acronyms

<b>AOM</b> acousto-optic modulator	<b>MZ</b> Mach-Zehnder
<b>APD</b> avalanche photo diode	<b>MZI</b> Mach-Zehnder interferometer
<b>BMR</b> bottle microresonator	<b>PBS</b> polarizing beam splitter
<b>BS</b> beam splitter	<b>PD</b> photo diode
<b>CCW</b> counter-clockwise	<b>PDH</b> Pound–Drever–Hall
<b>CNOT</b> controlled NOT	<b>PGC</b> polarization gradient cooling
<b>CPG</b> controlled phase gate	<b>PM</b> polarization maintaining
<b>CQED</b> cavity quantum electrodynamics	<b>Rb</b> rubidium
<b>CW</b> clockwise	<b>SAM</b> spin angular momentum
<b>EIT</b> electromagnetically induced transparency	<b>SML</b> spin–momentum locking
<b>EOM</b> electro-optical modulator	<b>SPCM</b> single photon counting module
<b>FORT</b> far off resonant dipole trap	<b>TE</b> transverse electric
<b>FP</b> Fabry-Pérot	<b>TM</b> transverse magnetic
<b>FPGA</b> field programmable gate array	<b>UHV</b> ultra high vacuum
<b>FSR</b> free spectral range	<b>vSTIRAP</b> vacuum-stimulated Raman process
<b>HWHM</b> half width at half maximum	<b>WGM</b> whispering-gallery-mode
<b>MEM</b> microelectromechanical	<b>YIG</b> yttrium iron garnet
<b>MLE</b> maximum-likelihood estimation	
<b>MOT</b> magneto-optical trap	





# Appendices



## A.1 Transition strengths for the $D_2$ -line of $^{85}\text{Rb}$

The hyperfine structure occurs due to the coupling of the total electron angular momentum  $\mathbf{J} = \mathbf{S} + \mathbf{L}$  with the total nuclear angular momentum  $\mathbf{I}$ , where  $\mathbf{S}$  and  $\mathbf{L}$  are the spin and orbital angular momentum of the electron, respectively. The total atomic angular momentum is then given by  $\mathbf{F} = \mathbf{J} + \mathbf{I}$ . The matrix element that couples the two hyperfine state  $|F, m_F\rangle$  and  $|F', m_{F'}\rangle$  is given by [122]

$$\langle F, m_F | er_q | F', m_{F'} \rangle = \langle J || e\hat{r} || J' \rangle (-1)^{2F'+m_F+J+I} \mu_{m_F}^{m_{F'}}, \quad (\text{A.1})$$

using the transition matrix element  $\langle J || e\hat{r} || J' \rangle$  and

$$\mu_{m_F}^{m_{F'}} = \sqrt{(2F'+1)(2F+1)(2J+1)} \begin{pmatrix} F' & 1 & F \\ m_{F'} & q & -m_F \end{pmatrix} \begin{Bmatrix} J & J' & 1 \\ F' & F & I \end{Bmatrix}. \quad (\text{A.2})$$

Here, the last two terms are the 3-j and the 6-j symbols, respectively and  $q = \{1, 0, -1\}$  for  $\{\sigma^+, \pi, \sigma^-\}$  transitions.

In our experiment we use  $^{85}\text{Rb}$  which has  $I = 5/2$ . Its ground state ( $5^2S_{1/2}$ ),  $J = 1/2$  splits into the  $F = 2$  and  $F = 3$  hyperfine levels. For the excited state  $5^2P_{3/2}$  of the  $D_2$ -line,  $J = 3/2$ , and thus  $F$  can take any of the values 1, 2, 3 or 4. The transition strengths, i.e.  $(\mu_{m_F}^{m_{F'}})^2$ , for the  $|F=3\rangle \rightarrow |F'=4\rangle$  transition of the  $D_2$ -line are shown in Fig. A.1 for  $\sigma^+$ ,  $\pi$  and  $\sigma^+$  transition, respectively. When summing over all possible transitions coupling to a given excited state  $|F', m_{F'}\rangle$ , they add up to a factor which is independent from the chosen state [122]

$$\sum_{q,F} |\langle F, m_{F'} + q | er_q | F', m_{F'} \rangle|^2 = \frac{2J+1}{2J'+1} |\langle J || e\hat{r} || J' \rangle|^2, \quad (\text{A.3})$$

where the summation is performed over all possible ground states  $F$  and all polarizations  $q$ . The prefactor is called the degeneracy ratio is a direct consequence of the normalization convention [122] and is 1/2 for the  $D_2$  line of  $^{85}\text{Rb}$ .

The transition matrix element  $\langle J || e\hat{r} || J' \rangle$  is determined via [122]

$$\frac{1}{\tau} = 2\gamma = \frac{\omega^3}{3\pi\epsilon_0\hbar c^3} \frac{2J+1}{2J'+1} |\langle J || e\hat{r} || J' \rangle|^2. \quad (\text{A.4})$$

Here, we introduced the vacuum permittivity  $\epsilon_0$ , the light's angular frequency  $\omega$ , the speed of light  $c$  and the dipole decay rate  $\gamma$ . For the  $D_2$ -line of  $^{85}\text{Rb}$  the dipole matrix element, the excited state lifetime and the corresponding dipole decay rate are given in Tab. A.1.

	$D_2 (5^2S_{1/2} \rightarrow 5^2P_{3/2})$
$\langle J  e\hat{r}  J' \rangle$	$3.582 \times 10^{-29} \text{ Cm}$
$\tau$	26.24 ns
$\gamma$	$2\pi \times 3.033 \text{ MHz}$

**Table A.1:** Dipole matrix element  $\langle J||e\hat{r}||J' \rangle$ , the excited state lifetime  $\tau$  and the dipole decay rate  $\gamma$  for the  $D_2$ -line of  $^{85}\text{Rb}$  [122].

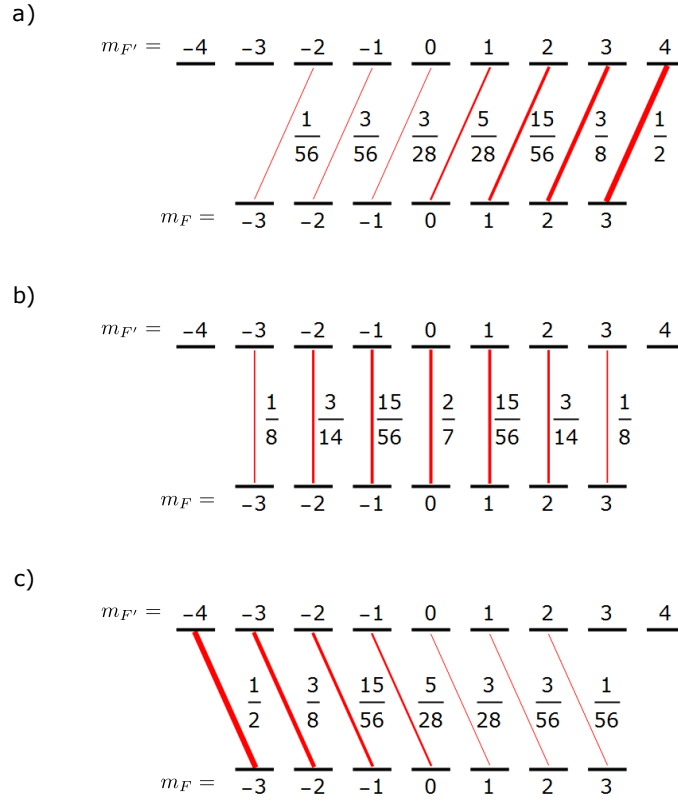


**Figure A.1:** Transition strengths for the  $|F=3\rangle \rightarrow |F'=4\rangle$  transition of  $^{85}\text{Rb}$   $D_2$ -line ( $5^2S_{1/2} \rightarrow 5^2P_{3/2}$ ), for a)  $\sigma^+$ , b)  $\pi$  and c)  $\sigma^-$  transitions [122].

## A.2 Numerical solution of the Master equation

Let us consider a linear differential equation of the form

$$\dot{\mathbf{x}} = \mathbf{A}\mathbf{x} . \quad (\text{A.5})$$

Every  $n \times n$  matrix  $\mathbf{A}$  can be transformed into a Jordan normal form using the invertible matrix  $\mathbf{P}$  such that

$$\mathbf{A} = \mathbf{P}\mathbf{J}\mathbf{P}^{-1} , \quad (\text{A.6})$$

where  $\mathbf{J}$  is the Jordan normal form of  $\mathbf{A}$ . Using the transformation  $\mathbf{x}(t) = \mathbf{P}\mathbf{y}(t)$ , Eq. (A.5) can be written as

$$\dot{\mathbf{x}} = \mathbf{P}\mathbf{J}\mathbf{P}^{-1}\mathbf{x} \rightarrow \dot{\mathbf{y}} = \mathbf{J}\mathbf{y} . \quad (\text{A.7})$$

If  $\mathbf{A}$  is diagonalizable, which is the case if the sum of the dimensions of its eigenspaces is equal to  $n$ ,  $\mathbf{J}$  is of diagonal form and the diagonal is formed by the eigenvalues of  $\mathbf{A}$  and the transition matrix  $\mathbf{P}$  is formed by the eigenvectors. Thus, the solution of Eq. (A.7) is formally given by [243]

$$\mathbf{y}(t) = \begin{pmatrix} e^{\lambda_1 t} & 0 & \dots & 0 \\ 0 & e^{\lambda_2 t} & & \vdots \\ \vdots & & \ddots & 0 \\ 0 & \dots & 0 & e^{\lambda_n t} \end{pmatrix} \mathbf{y}(0) = \hat{\mathbf{U}}(t)\mathbf{y}(0) . \quad (\text{A.8})$$

Here,  $\lambda_i$  are the eigenvalues of  $\mathbf{A}$  and  $\mathbf{y}(0)$  is the initial state at  $t=0$ . The matrix in Eq. (A.8) gives the time evolution operator  $\hat{\mathbf{U}}(t)$ . The solution of Eq. (A.5) in the original basis can be obtained via

$$\mathbf{x}(t) = \mathbf{P}\mathbf{y}(t) = \mathbf{P}\hat{\mathbf{U}}(t)\mathbf{y}(0) = \mathbf{P}\hat{\mathbf{U}}(t)\mathbf{P}^{-1}\mathbf{x}(0) . \quad (\text{A.9})$$

Solving the time evolution boils down to solving the eigenvalue problem. In the following, we will adapt this ansatz to solve the master equation.

The system of interest is described by the Hamiltonian  $\hat{H}$  and coupled to a bath. Under Markovian and Born approximation, the time evolution of the system, which is described by the  $n \times n$  density operator  $\rho$ , is given by the master equation (cf. Sec. 4.2)

$$\frac{\partial \hat{\rho}}{\partial t} = -i [\hat{H}, \hat{\rho}] + \hat{\mathcal{D}} , \quad (\text{A.10})$$

where  $\hat{\mathcal{D}}$  is the Lindblad operator (cf. Eq. (4.8)). Since Eq. A.10 is linear in  $\rho_{ij}$  the master equation can be written in Liouvillian form as

$$\frac{\partial \hat{\rho}}{\partial t} = \hat{\mathcal{L}}\hat{\rho} . \quad (\text{A.11})$$

using the Liouvillian super operator  $\hat{\mathcal{L}}$ . In order to apply the previously introduced ansatz, Eq. (A.11) has to be transferred into vector form such that

$$\frac{\partial \vec{\rho}}{\partial t} = \vec{\mathcal{L}}\vec{\rho} , \quad (\text{A.12})$$

where we have introduced the  $n^2 \times 1$ -dimensional column vector  $\vec{\rho} = (\rho_{11}, \rho_{12}, \dots, \rho_{nn})$  and the  $n^2 \times n^2$  expanded super operator. Equation (A.12) has now the form of Eq. (A.5). Thus, the time evolution of  $\vec{\rho}$ , and thus of  $\hat{\rho}$ , can be determined by calculating the eigenvalues and eigenvectors of  $\vec{L}$  via

$$\vec{\rho}(t) = \mathbf{P}\hat{U}(t)\mathbf{P}^{-1}\vec{\rho}(0). \quad (\text{A.13})$$

The transformation matrix  $\mathbf{P}$  and the time evolution operator  $\hat{U}(t)$  are now formed by the eigenvectors and eigenvalues of  $\vec{L}$  respectively. The eigenvalue problem can be solved numerically if the system is described in a finite dimensional state space using the eigenvalue solver of, e.g. *Mathematica*.

### A.3 Chirally coupled atom–resonator–waveguide system

In Sec. 4.5.2, we discussed the coupled atom–resonator system which is probed via a coupling fiber in the framework of chiral waveguides. Using the  $\beta$ -factors, which are given by Eqs. (4.49–4.52), we can write the forward (+) and backward (–) transmission and reflection amplitude as

$$t_+ = 1 - 2\beta_+ = 1 - \frac{2\kappa_{\text{ext}}}{\kappa_0 + \kappa_{\text{ext}}} \frac{C|\beta_{\sigma+}|^2 + 1}{C + 1}, \quad (\text{A.14})$$

$$t_- = 1 - 2\beta_- = 1 - \frac{2\kappa_{\text{ext}}}{\kappa_0 + \kappa_{\text{ext}}} \frac{C|\alpha_{\sigma+}|^2 + 1}{2(C + 1)}, \quad (\text{A.15})$$

$$r_{\pm} = -\sqrt{\beta_+^{\text{ccw}}\beta_-^{\text{ccw}}} - \sqrt{\beta_+^{\text{cw}}\beta_-^{\text{cw}}} = -\frac{\kappa_{\text{ext}}}{\kappa_0 + \kappa_{\text{ext}}} \frac{2C\alpha_{\sigma+}\beta_{\sigma+}}{(C + 1)}, \quad (\text{A.16})$$

where we have used the cooperativity  $C = g^2/\gamma(\kappa_0 + \kappa_{\text{ext}})$  and  $|\beta_{\sigma+}|^2 = 1 - |\alpha_{\sigma+}|^2$  for clarity. In addition, we can define the respective atom-modified resonator loss rates for the two counter-propagating modes

$$\gamma^{\text{ccw}} = \kappa_0 + C|\alpha_{\sigma+}|^2(\kappa_0 + \kappa_{\text{ext}}) \quad (\text{A.17})$$

$$\gamma^{\text{cw}} = \kappa_0 + C|\beta_{\sigma+}|^2(\kappa_0 + \kappa_{\text{ext}}). \quad (\text{A.18})$$

The corresponding waveguide-resonator coupling rates for the forward (+) and backward (–) probing direction coupling to either the CW or the CCW mode are

$$\Gamma_+^{\text{ccw}} = \frac{\kappa_{\text{ext}}(1 + C|\beta|^2 + \chi(|\beta|^2))(\kappa_0 + C|\alpha|^2(\kappa_0 + \kappa_{\text{ext}}))}{-2(1 + C)\kappa_0 + (-1 + C(2 - |\beta|^2) + \chi(|\beta|^2))}, \quad (\text{A.19})$$

$$\Gamma_+^{\text{cw}} = \frac{\kappa_{\text{ext}}(-1 + C|\beta|^2 + \chi(|\beta|^2))(\kappa_0 + C|\alpha|^2(\kappa_0 + \kappa_{\text{ext}}))}{-2(1 + C)\kappa_0 + (-1 - C(2 - |\beta|^2) - \chi(|\beta|^2))}, \quad (\text{A.20})$$

$$\Gamma_-^{\text{ccw}} = \frac{\kappa_{\text{ext}}(-1 + C|\alpha|^2 + \chi(|\alpha|^2))(\kappa_0 + C|\beta|^2(\kappa_0 + \kappa_{\text{ext}}))}{-2(1 + C)\kappa_0 + (-1 - C(2 - |\alpha|^2) - \chi(|\alpha|^2))}, \quad (\text{A.21})$$

$$\Gamma_-^{\text{cw}} = \frac{\kappa_{\text{ext}}(1 + C|\alpha|^2 + \chi(|\alpha|^2))(\kappa_0 + C|\beta|^2(\kappa_0 + \kappa_{\text{ext}}))}{-2(1 + C)\kappa_0 + (-1 - C(2 - |\alpha|^2) + \chi(|\alpha|^2))}, \quad (\text{A.22})$$

where we have introduced  $\chi(x) = \sqrt{C^2(2x^2 - x) + 2Cx^2 + 1}$ ,  $\alpha = \alpha_{\sigma+}$  and  $\beta = \beta_{\sigma+}$  for clarity. Interestingly, both, the internal loss rates and the coupling rates, are altered by the interaction with the atom.

## A.4 Supplement to the circulator

### A.4.1 Measured transmission matrices

The transmission matrix yields the power transmission from a certain input port and to a certain output port, where the row indicates the input port and the column gives the output port. For an ideal circulator the transmission matrices describing its two operation directions are given by

$$[T_{\odot}^{\text{id}}] = \begin{pmatrix} 0 & 1 & 0 & 0 \\ 0 & 0 & 1 & 0 \\ 0 & 0 & 0 & 1 \\ 1 & 0 & 0 & 0 \end{pmatrix}, \quad [T_{\ominus}^{\text{id}}] = \begin{pmatrix} 0 & 0 & 0 & 1 \\ 1 & 0 & 0 & 0 \\ 0 & 1 & 0 & 0 \\ 0 & 0 & 1 & 0 \end{pmatrix} \quad (\text{A.23})$$

In the following the measured transmission matrices at the optimal working point  $\kappa_{\text{tot}}/2\kappa_0 = 2.2$  are given.  $[T^{m_F=+3}]$  is the transmission matrix for the case where the atom is prepared in the  $|F=3, m_F=+3\rangle$  state,  $[T^{m_F=-3}]$  for the atom prepared in  $|F=3, m_F=-3\rangle$  and  $[T^{\text{no atom}}]$  for the case where no atom is present. The error bars indicate the  $\pm 1\sigma$  statistical error.

$$[T^{m_F=+3}] = \begin{pmatrix} 0.03 \pm 0.015 & 0.46 \pm 0.044 & 0.024 \pm 0.011 & 0.133 \pm 0.03 \\ 0.037 \pm 0.022 & 0.057 \pm 0.021 & 0.486 \pm 0.059 & 0.038 \pm 0.022 \\ 0.011 \pm 0.011 & 0.101 \pm 0.028 & 0.068 \pm 0.022 & 0.698 \pm 0.083 \\ 0.463 \pm 0.055 & 0.039 \pm 0.014 & 0.234 \pm 0.027 & 0.055 \pm 0.019 \end{pmatrix} \quad (\text{A.24})$$

$$[T^{m_F=-3}] = \begin{pmatrix} 0.063 \pm 0.01 & 0.072 \pm 0.013 & 0.021 \pm 0.007 & 0.394 \pm 0.025 \\ 0.487 \pm 0.028 & 0.045 \pm 0.01 & 0.122 \pm 0.017 & 0.016 \pm 0.005 \\ 0.029 \pm 0.007 & 0.379 \pm 0.029 & 0.066 \pm 0.012 & 0.274 \pm 0.021 \\ 0.108 \pm 0.011 & 0.005 \pm 0.001 & 0.647 \pm 0.029 & 0.02 \pm 0.005 \end{pmatrix} \quad (\text{A.25})$$

$$[T^{\text{no atom}}] = \begin{pmatrix} 0. \pm 0. & 0.014 \pm 0.008 & 0. \pm 0. & 0.572 \pm 0.061 \\ 0.012 \pm 0.012 & 0.008 \pm 0.008 & 0.533 \pm 0.062 & 0.025 \pm 0.018 \\ 0. \pm 0. & 0.539 \pm 0.063 & 0.075 \pm 0.023 & 0.252 \pm 0.052 \\ 0.583 \pm 0.06 & 0.016 \pm 0.009 & 0.183 \pm 0.025 & 0.027 \pm 0.014 \end{pmatrix} \quad (\text{A.26})$$

### A.4.2 Analytic solution for the circulator performance

In section 4.4.2 we showed that the polarization-dependent scattering of an  $^{85}\text{Rb}$  atom in its outermost Zeeman level  $|F=3, m_F=\pm 3\rangle$  which is coupled to a WGM resonator can be very well be approximated by a simple two level atom with a circularly polarized transition that interacts with two counter-propagating, elliptically polarized resonator modes. Based on this

model, we are able to derive an analytic expression for the transmission matrix of the circulator, for the case of symmetrically coupled fibers, i.e.  $\kappa_a = \kappa_b = \kappa$ ,

$$[T_{i,j}] = \begin{pmatrix} R & T_\alpha^{\text{trans}} & R & T_\alpha^{\text{cross}} \\ T_\beta^{\text{trans}} & R & T_\beta^{\text{cross}} & R \\ R & T_\alpha^{\text{cross}} & R & T_\alpha^{\text{trans}} \\ T_\beta^{\text{cross}} & R & T_\beta^{\text{trans}} & R \end{pmatrix} \begin{matrix} 1 \\ 2 \\ 3 \\ 4 \end{matrix} \text{ input} , \quad (\text{A.27})$$

output

where we have used

$$R = \frac{4g^4 \alpha^2 \beta^2 \kappa^2}{(2\kappa + \kappa_0)^2 (\gamma(2\kappa + \kappa_0) + g^2)^2} \quad (\text{A.28})$$

$$T_\chi^{\text{cross}} = \frac{4\kappa^2 (g^2(1 - \chi^2) + \gamma(2\kappa + \kappa_0))^2}{(2\kappa + \kappa_0)^2 (\gamma(2\kappa + \kappa_0) + g^2)^2} \quad (\text{A.29})$$

$$T_\chi^{\text{trans}} = \frac{(((2\kappa + \kappa_0)\chi^2 + \kappa_0(1 - (i)^2))g^2 + \gamma\kappa_0(2\kappa + \kappa_0))^2}{(2\kappa + \kappa_0)^2 (\gamma(2\kappa + \kappa_0) + g^2)^2} . \quad (\text{A.30})$$

For  $T^{\text{cross}}$  and  $T^{\text{trans}}$  we distinguished between probing the CCW or CW mode for which  $\chi$  becomes  $\alpha$  or  $\beta$  respectively. Here, we also used a simplified nomenclature for the polarization overlap  $\alpha \equiv \alpha_{\sigma+}$  and  $\beta \equiv \sqrt{1 - \alpha^2}$ . Using Eq. (A.27) we can straightforwardly calculate the survival probability  $\eta$  and the nonreciprocity  $\mathcal{N}$  from Eq. (7.5) and Eq. (7.7) respectively, which yield the simple analytic expressions

$$\eta = 1 - \kappa \frac{2\gamma^2(2\kappa + \kappa_0)^2 \kappa_0 + g^4 \kappa_0 + \gamma g^2(2\kappa + \kappa_0)((2\kappa + \kappa_0) + 2\kappa_0)}{(2\kappa + \kappa_0)^2 (\gamma(2\kappa + \kappa_0) + g^2)^2} , \quad (\text{A.31})$$

$$\mathcal{N} = \frac{\kappa g^2 (2\alpha^2 - 1)}{(2\kappa + \kappa_0)(\gamma(2\kappa + \kappa_0) + g^2)} \cdot \frac{1}{\eta} . \quad (\text{A.32})$$

For the process fidelity  $\mathcal{F}$ , a more lengthy expression can be derived

$$\mathcal{F} = \frac{1}{4} \left( \frac{8\kappa^2 (\gamma(2\kappa + \kappa_0) + \alpha^2 g^2)^2}{A} + \frac{2 (\gamma\kappa_0(2\kappa + \kappa_0) + g^2 (2\alpha^2 \kappa + \kappa_0))^2}{B} \right) , \quad (\text{A.33})$$

where we have introduced

$$\begin{aligned} A = & \gamma^2(2\kappa + \kappa_0)^2 (4\kappa^2 + \kappa_0^2) + g^4 (4\alpha^2 \kappa \kappa_0 + 4\kappa^2 + \kappa_0^2) \\ & - 2\gamma g^2(2\kappa + \kappa_0) (4(\alpha^2 - 1)\kappa^2 - 2\alpha^2 \kappa \kappa_0 - \kappa_0^2) \\ & + 4(2\alpha^2 - 1)g^2 \kappa (\gamma(\kappa_0^2 - 4\kappa^2) + g^2 \kappa_0) , \end{aligned} \quad (\text{A.34})$$



$$\begin{aligned}
B = & \gamma^2(2\kappa + \kappa_0)^2 (4\kappa^2 + \kappa_0^2) + g^4 (-4(\alpha^2 - 1)\kappa\kappa_0 + 4\kappa^2 + \kappa_0^2) \\
& + 2\gamma g^2(2\kappa + \kappa_0) (2\alpha^2\kappa(2\kappa - \kappa_0) + \kappa_0(2\kappa + \kappa_0)) .
\end{aligned} \tag{A.35}$$

Equations (A.31) and (A.33) are used to estimate the performance of a circulator based on a state-of-the-art BMR in Sec. 7.7.1.

## A.5 Second-order intensity correlation function

The normalized second-order intensity correlation function for a classical field of intensity  $I(t)$  is defined as [113]

$$g^{(2)}(\tau) = \frac{\langle I(t)I(t+\tau) \rangle}{\langle I(t) \rangle \langle I(t+\tau) \rangle} . \tag{A.36}$$

Here, we have introduced the time average which is indicated by the brackets. A field is said to be second-order coherent if  $g^{(2)} = 1$ , which requires that the numerator factorizes. In the framework of second quantization Eq. (A.36) can be expressed in terms of the photon creation and annihilation operators,  $\hat{c}^\dagger$  and  $\hat{c}$  [113]

$$g^{(2)}(\tau) = \frac{\langle \hat{c}^\dagger(t)\hat{c}^\dagger(t+\tau)\hat{c}(t+\tau)\hat{c}(t) \rangle}{\langle \hat{c}^\dagger(t)\hat{c}(t) \rangle \langle \hat{c}^\dagger(t+\tau)\hat{c}(t+\tau) \rangle} \tag{A.37}$$

This gives the joint probability of detecting one photon at time  $t$  and a second photon with time delay  $\tau$  at  $t + \tau$ , which is normalized by the probability of detecting two independent photons. A coherent state of light follows Poisson photon statistic for which photons are temporally uncorrelated and thus  $g^{(2)} = 1$  independent of  $\tau$ . If  $g^{(2)}(0) > 1$ , there is a positive correlation between the photon pairs and we say that the light is bunched. If  $g^{(2)}(0) < 1$  the photons are anti-correlated and we say that the light is anti-bunched. For classical states of light, the second-order intensity correlation function is bound by  $g^{(2)}(0) \geq 1$ . Quantum mechanics allows for  $g^{(2)}(0)$  to be greater than or less than 1. Hence, photon anti-bunching indicates correlations between pairs of photon which cannot be explained classically, and we speak of a non-classical state of light. For time delays much larger than the coherence times of the source  $g^{(2)}(\tau \rightarrow \infty) = 1$ . For simulating the second-order intensity correlation function for the light that is transmitted through our coupling fiber we have to insert the input–output relation, given by Eq. (4.25), into Eq. (A.37) and we obtain

$$g_t^{(2)}(\tau) = \frac{\langle (\hat{a}_{\text{in}}^\dagger - k\hat{a}^\dagger)(\hat{a}_{\text{in},\tau}^\dagger - k\hat{a}_\tau^\dagger)(\hat{a}_{\text{in},\tau} - k\hat{a}_\tau)(\hat{a}_{\text{in}} - k\hat{a}) \rangle}{\langle (\hat{a}_{\text{in},\tau} - k\hat{a}_\tau)(\hat{a}_{\text{in}} - k\hat{a}) \rangle \langle (\hat{a}_{\text{in},\tau}^\dagger - k\hat{a}_\tau^\dagger)(\hat{a}_{\text{in}}^\dagger - k\hat{a}^\dagger) \rangle} , \tag{A.38}$$

where we have used  $k = i\sqrt{2\kappa_{\text{ext}}}$  and dropped the time dependence for clarity using  $\hat{a} = \hat{a}(t)$  and  $\hat{a}_\tau = \hat{a}(t + \tau)$ . If the incoming pump field in the coupling fiber is a weak coherent state, which is usually the case in our experiment, one can replace the pump field operators  $\hat{a}_{\text{in}}$  and  $\hat{a}_{\text{in}}^\dagger$  in Eq. (A.38) with their expectation values  $\langle \hat{a}_{\text{in}} \rangle = \langle \hat{a}_{\text{in},\tau} \rangle = a_{\text{in}}$  and  $\langle \hat{a}_{\text{in}}^\dagger \rangle = \langle \hat{a}_{\text{in},\tau}^\dagger \rangle = a_{\text{in}}^*$  [121]. Thus, we only have to compute expectation values for different products of the resonator field operator.

For the reflected photons or photons that couple from the resonator into the second fiber, the expression for the second-order intensity correlation function is much simpler, since the additional pump term does not occur (cf. Eq. (4.27)). Thus, we directly obtain the second-order intensity correlation function for one of the two resonator fields, which is given by

$$g_r^{(2)}(\tau) = \frac{\langle \hat{a}^\dagger \hat{a}_\tau^\dagger \hat{a}_\tau \hat{a} \rangle}{\langle \hat{a}^\dagger \hat{a} \rangle \langle \hat{a}_\tau^\dagger \hat{a}_\tau \rangle} . \quad (\text{A.39})$$

For photons that exit the fiber at the same time, i.e.  $\tau = 0$ , the expectation values in Eq. (A.38) and Eq. (A.39) involve only operators at one point in time, which can be calculated according to the Master equation formalism introduced in Sec. 4.4.1, yielding, e.g.,  $\langle \hat{a} \rangle = \text{Tr}[\hat{a} \cdot \hat{\rho}]$  and  $\langle \hat{a} \hat{a} \rangle = \text{Tr}[\hat{a} \cdot \hat{a} \cdot \hat{\rho}]$ . When it comes to calculating expectation values of operator products at different times, we have to apply the quantum regression theorem [120], as discussed in Ref. [86]. The numerator of Eq. A.37 can be directly associated with raw, unnormalized photon correlations, i.e. two photon detections having a time delay  $\tau$ . If the correlation counts are acquired over an infinite amount of time, the denominator normalizes the raw coincidences by the total number of coincidences measured. In our experiment, we measure for a finite interval  $T_0$  which is restricted by the atomic lifetime in the resonator mode. Thus, coincidences only appear for  $\tau$  within the interval  $[-T_0/2, T_0/2]$ . For an otherwise constant correlation function, we obtain a triangular shape that is peaked at  $\tau = 0$  and zero at  $\tau = \pm T_0/2$ . A common strategy to compensate for the finite measurement time is to fit the asymptotic behavior of the raw correlation and multiply them by the factor  $\propto 1/(T_0 - |\tau|)$ . This gives the desired asymptotic behavior, although the fluctuation increase near  $|\tau| = T_0$ , where normalization factor diverges [244].

## A.6 Conditional single-atom phase shift

If the empty resonator is over-coupled, the additional losses introduced by a strongly coupled atom can put the resonator into the under-coupled regime. This imprints a linear phase shift of  $\pi$  onto the light transmitted through the coupling fiber compared to the light transmitted in the absence of the atom.

In our experiment, we choose a transverse magnetic (TM) mode. The polarization component of the light guided in the coupling fiber that couples to this modes is referred to as  $H$ -component. The orthogonal component which is unaffected by the resonator mode is denoted  $V$ -component. Let us consider the case, where we probe with light that is in a superposition of both polarizations. Thus, the incoming polarization state is  $|\psi\rangle_{\text{in}} = c_H |H\rangle + c_V |V\rangle$ , where  $c_H$  and  $c_V$  are two amplitudes, which we assume to be real. When passing the resonator, the  $H$ -component acquires an additional phase  $\phi$  and its amplitude is modified to be  $c'_H$ . The output state is given by  $|\psi\rangle_{\text{out}} = c'_H e^{i\phi} |H\rangle + c_V |V\rangle$ . Both, the phase and the transmitted amplitude of the transmitted light, now depend on whether the atom is coupled to the resonator or not. The respective powers transmitted to the  $H$ ,  $V$ ,  $D$  and  $\bar{D}$  port of the polarization analyzer are

$$P_H = |c'_H|^2, \quad P_D = \frac{1}{2} [ |c'_H|^2 + |c_V|^2 + 2c'_H c_V \cos(\phi) ] , \quad (\text{A.40})$$

$$P_V = |c_V|^2, \quad P_{\bar{D}} = \frac{1}{2} [ |c'_H|^2 + |c_V|^2 - 2c'_H c_V \cos(\phi) ] . \quad (\text{A.41})$$

From these equations, the relative phase shift introduced by the atom can then be obtained straight forwardly using

$$\Delta\phi = \phi_1 - \phi_0 \quad \text{and} \quad \phi_i = \arccos \left[ \frac{P_{\bar{D}}^i - P_D^i}{2\sqrt{P_H^i P_V^i}} \right], \quad (\text{A.42})$$

where the index  $i$  indicates whether the atom was present during the measurement or not.

## A.7 Density matrix reconstruction

### A.7.1 The density matrix

Systems that are subject to decoherence cannot be described by a pure state. Instead, their states have to be described by a density matrix

$$\hat{\rho} = \sum_i p_i |\psi_i\rangle \langle \psi_i|, \quad (\text{A.43})$$

where  $p_i$  is the probability of finding the system in a certain state  $|\psi_i\rangle$ , which has to fulfill  $\sum p_i = 1$ . If only one  $p_i$  is nonzero, that is when  $\hat{\rho}^2 = \hat{\rho}$ , the system is in a pure state. There are certain requirements the density matrix has to fulfill in order to describe a physically valid state:

- **Hermiticity** The density operator  $\rho$  is hermitian

$$\hat{\rho} = \hat{\rho}^\dagger \quad (\text{A.44})$$

- **Unity Trace** The trace of any density operator is 1, which corresponds to the normalization of the probability

$$\text{Tr}(\hat{\rho}) = 1 \quad (\text{A.45})$$

- **Positivity** The density operator has to be positive semidefinite

$$\langle \psi | \hat{\rho} | \psi \rangle \geq 0 \quad \forall | \psi \rangle, \quad (\text{A.46})$$

which implies that all eigenvalues of  $\hat{\rho}$  must lie in the interval  $[0,1]$ .

### A.7.2 Quantum state tomography of photonic qubits

In order to reconstruct the density matrix of a quantum state we have to perform tomographic measurements. If the qubit is encoded in the polarization state of single photons, we can count detected photons using single photon detectors which are placed behind a polarizer. This performs a projective measurement in which the state of the photon is projected onto the polarization

of the polarizer. In an ideal experiment, the number of detected photons  $n_\nu$  at the detector, is connected to the density matrix of the polarization state  $\hat{\rho}$  via

$$n_\nu = \mathcal{N} \langle \psi_\nu | \hat{\rho} | \psi_\nu \rangle = \mathcal{N} \text{Tr}[\hat{\rho} M_\nu];, \quad (\text{A.47})$$

where  $|\psi_\nu\rangle$  and  $M_\nu = |\psi_\nu\rangle \langle \psi_\nu|$  are the polarization state and projection matrix onto this state, respectively, and  $\mathcal{N}$  is a constant that depends on the photon flux and the detector efficiency. Thus, each measurement contains some information of the density matrix  $\hat{\rho}$ . To determine all entries of the density matrix via linear reconstruction, we have to perform a linearly independent set of measurements [182]. Different projective measurements can be realized by inserting a half- or quarter-wave plate in front of the polarizer. Using such a direct, linear reconstruction scheme, by construction, yields a density matrix which fulfill the requirements given by Eq. (A.44) and Eq. (A.45). However, when performing linear reconstruction for low-entropy states, the requirement stated by Eq. (A.46), is not always met, due to experimental inaccuracies and statistical fluctuations. Thus, a linear reconstruction in general does not yield a physically valid density matrix [182].

### A.7.3 Maximum-likelihood estimation

To avoid this problem, a maximum-likelihood estimation (MLE) can be employed [182]. The approach, is as follows: First we generate a physical  $m \times m$  density matrix  $\hat{\rho}_p$ , which by definition fulfills all three requirement. This can easily be achieved by making use of the so called Cholesky decomposition, which states that a matrix that can be written as  $A = T^\dagger T$  must be semidefinite. To ensure normalization we simply divide this matrix by its trace. Thus, a physical density matrix is given by [182]

$$\hat{\rho}_p(t_1, t_2, \dots, t_{m^2}) = \frac{T^\dagger T}{\text{Tr}[T^\dagger T]}, \quad (\text{A.48})$$

which is parametrized by  $m^2$  variables  $t_i$ . Under the assumption that our measurement suffers from Gaussian noise, the probability of finding a set of  $n$  measurement outcomes  $n_\nu$  for a given state is

$$P(n_1, n_2, \dots, n_n) = \frac{1}{N_{\text{norm}}} \prod_{\nu=1}^n \exp \left[ -\frac{(\bar{n}_\nu - n_\nu)^2}{2\sigma_\nu^2} \right], \quad (\text{A.49})$$

where we have introduced the normalization constant  $N_{\text{norm}}$ , the standard deviation of the  $\nu^{\text{th}}$  measurement  $\sigma_\nu = \sqrt{\bar{n}_\nu}$  and  $\bar{n}_\nu$  is the expected number of counts. When we assume  $\bar{n}_\nu = \mathcal{N} \langle \psi_\nu | \hat{\rho}_p(t_1, t_2, \dots, t_{m^2}) | \psi_\nu \rangle$ , which represents the expected number of counts for a given density matrix  $\hat{\rho}_p(t_1, t_2, \dots, t_{m^2})$ , Eq. (A.49) gives the probability that  $\rho_p$  reproduced the measured data set  $\{n_1, n_2, \dots, n_n\}$ . Here, we identified  $\mathcal{N}$  as the total number of detected photons in one basis,  $\mathcal{N} = \sum_{\nu \in \text{basis}} n_\nu$ . Instead of finding a maximum of Eq. (A.49), it is convenient to reduce the problem to finding the minimum by taking its logarithm. We thus define the likelihood function as

$$\mathcal{L}(t_1, t_2, \dots, t_{m^2}) = \sum_{\nu=1}^n \frac{(\mathcal{N} \langle \psi_\nu | \hat{\rho}_p(t_1, t_2, \dots, t_{m^2}) | \psi_\nu \rangle - n_\nu)^2}{2\mathcal{N} \langle \psi_\nu | \hat{\rho}_p(t_1, t_2, \dots, t_{m^2}) | \psi_\nu \rangle}. \quad (\text{A.50})$$

Now standard numerical optimization techniques can be employed to find an extremum of  $\mathcal{L}$ , thus giving a set of variables  $\{t_1^{(opt)}, t_2^{(opt)}, \dots, t_{m^2}^{(opt)}\}$  which give the best estimation for the density matrix  $\rho_p(t_1^{(opt)}, t_2^{(opt)}, \dots, t_{m^2}^{(opt)})$ . This is then the physical density matrix that most likely describes the measurement results.

#### A.7.4 Density matrix of two photons sharing a spatial mode

Let us now consider a two-qubit state, which is encoded in the polarization state of two photons. If the two photons are distinguishable by, e.g. their spatial mode, the density matrix is given by a  $4 \times 4$  matrix which usually is represented in the  $\{|HH\rangle, |HV\rangle, |VV\rangle, |VH\rangle\}$  basis as

$$\tilde{\rho} = \begin{pmatrix} \rho_{HH,HH} & \rho_{HH,HV} & \rho_{HH,VV} & \rho_{HH,VH} \\ \rho_{HV,HH} & \rho_{HV,HV} & \rho_{VV,VV} & \rho_{HV,VH} \\ \rho_{VV,HH} & \rho_{VV,HV} & \rho_{VV,VV} & \rho_{VV,VH} \\ \rho_{VH,HH} & \rho_{VH,HV} & \rho_{VH,VV} & \rho_{VH,VH} \end{pmatrix}. \quad (\text{A.51})$$

In the following, the tilde identifies density matrices that are represented in this basis. However, the experimental situation might not allow to discriminate the two photons by the measurements that are performed. That might be the case when both photons are guided by the same spatial mode, while the polarization state encodes the qubit, and thus carries the information. In this case, only three basis states remain,  $|HH\rangle$ ,  $|VV\rangle$  and the symmetric state  $|S\rangle = (|HV\rangle + |VH\rangle)/\sqrt{2}$ , and the system is described by a  $3 \times 3$  matrix. However, in an experimental setting, there might be an additional degree of freedom, such as e.g. frequency or arrival time, that is not of interest or not experimentally accessible for the measurement apparatus. Nevertheless, these inaccessible or hidden degrees of freedom can affect the outcome of the tomography performed on degrees of freedom which are accessible [180, 181].

#### Accessible density matrix

Boson statistics requires the state of photons to be fully symmetric, i.e. they have to be invariant under the exchange of particles. For a single degree of freedom  $\psi$ , e.g. polarization, the state is given by

$$|\Psi\rangle = |\psi_S\rangle, \quad (\text{A.52})$$

which is symmetric under particle exchange. However, when an additional degree of freedom is present, such as the spatial mode, we can also obtain an antisymmetric polarization state  $|\psi_A\rangle$  if the second degree of freedom also has an antisymmetric part  $\phi_A$ . The resulting total photon state has to obey boson statistics and therefore is given by

$$|\Psi'\rangle = \alpha |\psi_S\rangle |\phi_S\rangle + \beta |\psi_A\rangle |\phi_A\rangle, \quad (\text{A.53})$$

where  $\alpha$  and  $\beta$  are some constants. In Eq. (A.53), the symmetric (antisymmetric) part of the first degree of freedom acts on the symmetric (antisymmetric) part of the second degree of freedom. Thus, the existence of an antisymmetric contribution for the first degree of freedom is inevitably

linked to the existence of an additional degree of freedom which has to be correlated with the first.

It is instructive to represent the density matrix for the total polarization state in the symmetric and antisymmetric subspaces. For the two-photon case, the density matrix is divided into two submatrices, a  $3 \times 3$  matrix corresponding to the symmetric subspace, spanned by  $\{|HH\rangle, |S\rangle = (|HV\rangle + |VH\rangle)/\sqrt{2}, |VV\rangle\}$  and a  $1 \times 1$  forming the antisymmetric subspace, spanned by  $|A\rangle = (|HV\rangle - |VH\rangle)/\sqrt{2}$ :

$$\hat{\rho}_{\text{acc}} = \begin{pmatrix} \begin{pmatrix} \rho_{HH,HH} & \rho_{HH,S} & \rho_{HH,VV} \\ \rho_{S,HH} & \rho_{S,S} & \rho_{S,VV} \\ \rho_{VV,HH} & \rho_{VV,S} & \rho_{VV,VV} \end{pmatrix} & 0 \\ 0 & (\rho_{A,A}) \end{pmatrix}. \quad (\text{A.54})$$

The coherences between the symmetric and the antisymmetric subspaces are zero, which expresses the lack of information we obtain from our measurement which could be used to distinguish the photons. Under the assumption of indistinguishable photons all population is restricted to the symmetric subspace, i.e.  $\rho_{A,A} = 0$ .

### The effect of inaccessible degrees of freedom

The presence of an distinguishing degree of freedom can be inferred from the antisymmetric subspace which can be illustrated by using a simple example: Let us consider a two-photon state where the polarization degree of freedom ( $H, V$ ) might be correlated with the spatial degree of freedom ( $a, b$ ). The full bosonic state must be symmetric under the exchange of both spatial and polarization degrees of freedom. For the case where one photon is horizontally polarized and the other is vertically polarized the two-photon state is given by  $|\psi_1\rangle = (|HV\rangle |ab\rangle + |VH\rangle |ba\rangle)/\sqrt{2}$ . If we are only interested in the polarization of our photons, we can express our ignorance about the spatial modes by tracing over this degree of freedom. This leaves us with the density matrix  $\rho_{\text{acc}} = \text{Tr}_{ab}(\rho)$  that is accessible via our measurement. This reduced density matrix expressed in the basis  $\{|HH\rangle, |HV\rangle, |VV\rangle, |VH\rangle\}$  is

$$\tilde{\rho}_{\text{acc}}^{(1)} = \frac{1}{2}(|HV\rangle\langle HV| + |VH\rangle\langle VH|) = \frac{1}{2} \begin{pmatrix} 0 & 0 & 0 & 0 \\ 0 & 1 & 0 & 0 \\ 0 & 0 & 0 & 0 \\ 0 & 0 & 0 & 1 \end{pmatrix}, \quad (\text{A.55})$$

which is a mixed state. Contrary to this, if both photons would have occupied the same spatial mode, such that the state is given by  $|\psi_2\rangle = (|HV\rangle |aa\rangle + |VH\rangle |aa\rangle)/\sqrt{2}$ , the resulting accessible density matrix is describe by the pure state

$$\tilde{\rho}_{\text{acc}}^{(2)} = \frac{1}{2}(|HV\rangle + |VH\rangle)(\langle HV| + \langle VH|) = \frac{1}{2} \begin{pmatrix} 0 & 0 & 0 & 0 \\ 0 & 1 & 0 & 1 \\ 0 & 0 & 0 & 0 \\ 0 & 1 & 0 & 1 \end{pmatrix}. \quad (\text{A.56})$$

This already shows how the inaccessible degrees of freedom influence the outcome of the measurement of another. In order to clearly distinguish the two different cases, we have to change

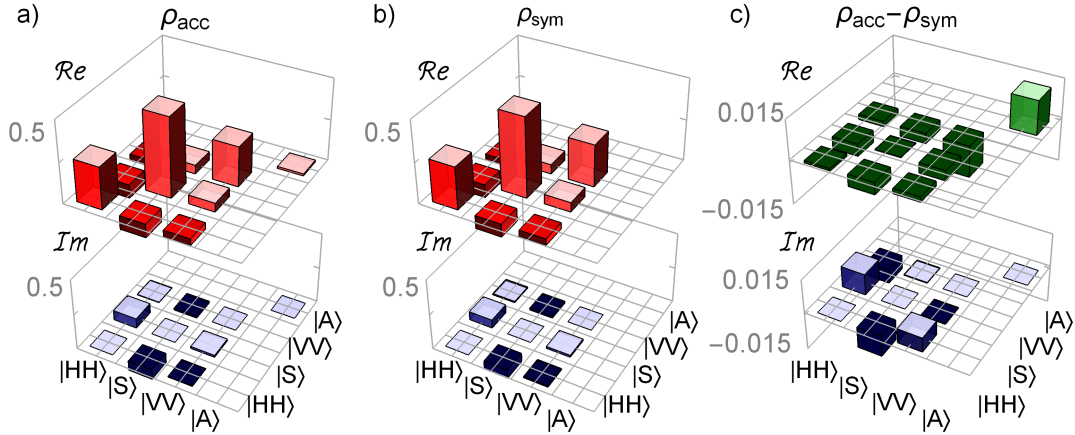


**Figure A.2:** a) Reconstructed full accessible density matrix  $\hat{\rho}_{\text{acc}}$  of the two-photon output state. b) Density matrix  $\hat{\rho}_{\text{sym}}$  obtained from restricting the reconstruction on the symmetric subspace. c) The difference  $\hat{\rho}_{\text{acc}} - \hat{\rho}_{\text{sym}}$ , which lies within the experimental errors. Note the different scale of the  $y$ -axis.

into the symmetric and antisymmetric basis  $\{|HH\rangle, |S\rangle, |VV\rangle, |A\rangle\}$ . In this basis, the density matrices for the two cases are given by

$$\hat{\rho}_{\text{acc}}^{(1)} = \frac{1}{2} \begin{pmatrix} \begin{pmatrix} 0 & 0 & 0 \\ 0 & 1 & 0 \\ 0 & 0 & 0 \end{pmatrix} & 0 \\ 0 & (1) \end{pmatrix}, \quad \hat{\rho}_{\text{acc}}^{(2)} = \begin{pmatrix} \begin{pmatrix} 0 & 0 & 0 \\ 0 & 1 & 0 \\ 0 & 0 & 0 \end{pmatrix} & 0 \\ 0 & 0 & 0 & (0) \end{pmatrix}. \quad (\text{A.57})$$

The population of the antisymmetric part is zero for  $\hat{\rho}_{\text{acc}}^{(2)}$ , where no additional degree of freedom is present, and one half for  $\hat{\rho}_{\text{acc}}^{(1)}$  for the case of an additional degree of freedom present. Thus, we can conclude that the indicator for the existence of one or more unobserved degrees of freedom is the population of the antisymmetric state  $|A\rangle$ , which is a measurable quantity even though the experimental apparatus cannot tell the two photons apart.

### A.7.5 Reconstruction of the transmitted two-photon state

In the experiments described in Ch. 6, we are interested in the two-photon polarization state transmitted through the coupling fiber after interacting with the atom–resonator system. Thus, both photons are guided in the same fiber mode. In order to perform state tomography of the two-photon polarization state, we perform correlation measurements between detectors in different arms of the polarization analyzer. The detectors can detect either a correlation between two photons in the same polarization  $A$ , thereby implementing the projector  $P_{AA} = |A_1, A_2\rangle\langle A_1, A_2|$ , or a correlation between different polarization modes, e.g. between polarization  $A$  and  $B$ ,

thereby implementing  $P_{BA} = |A_1, B_2\rangle\langle A_1, B_2| + |B_1, A_2\rangle\langle B_1, A_2|$ . Using the 10 detectors distributed as shown in Fig. 6.4 we obtain the following 19 projection matrices, represented in the basis  $\{|HH\rangle, |S\rangle, |VV\rangle, |A\rangle\}$ :

$$\begin{aligned}
M_{HH} &= \begin{pmatrix} 1 & 0 & 0 & 0 \\ 0 & 0 & 0 & 0 \\ 0 & 0 & 0 & 0 \\ 0 & 0 & 0 & 0 \end{pmatrix} & M_{HV} &= \begin{pmatrix} 0 & 0 & 0 & 0 \\ 0 & 1 & 0 & 0 \\ 0 & 0 & 0 & 0 \\ 0 & 0 & 0 & 1 \end{pmatrix} \\
M_{D\bar{D}} &= \begin{pmatrix} \frac{1}{2} & 0 & -\frac{1}{2} & 0 \\ 0 & 0 & 0 & 0 \\ -\frac{1}{2} & 0 & \frac{1}{2} & 0 \\ 0 & 0 & 0 & 1 \end{pmatrix} & M_{RL} &= \begin{pmatrix} \frac{1}{2} & 0 & \frac{1}{2} & 0 \\ 0 & 0 & 0 & 0 \\ \frac{1}{2} & 0 & \frac{1}{2} & 0 \\ 0 & 0 & 0 & 1 \end{pmatrix} \\
M_{RH} &= \begin{pmatrix} 1 & -\frac{i}{\sqrt{2}} & 0 & 0 \\ \frac{i}{\sqrt{2}} & \frac{1}{2} & 0 & 0 \\ 0 & 0 & 0 & 0 \\ 0 & 0 & 0 & \frac{1}{2} \end{pmatrix} & M_{DR} &= \begin{pmatrix} \frac{1}{2} & \frac{\frac{1}{2}-i}{\sqrt{2}} & -\frac{i}{2} & 0 \\ \frac{\frac{1}{2}+i}{\sqrt{2}} & \frac{1}{2} & \frac{\frac{1}{2}-i}{\sqrt{2}} & 0 \\ \frac{i}{2} & \frac{\frac{1}{2}+i}{\sqrt{2}} & \frac{1}{2} & 0 \\ 0 & 0 & 0 & \frac{1}{2} \end{pmatrix} \\
M_{RR} &= \begin{pmatrix} \frac{1}{4} & -\frac{i}{\sqrt{8}} & -\frac{1}{4} & 0 \\ \frac{i}{\sqrt{8}} & \frac{1}{2} & -\frac{i}{\sqrt{8}} & 0 \\ -\frac{1}{4} & \frac{i}{\sqrt{8}} & \frac{1}{4} & 0 \\ 0 & 0 & 0 & 0 \end{pmatrix} & M_{DH} &= \begin{pmatrix} 1 & \frac{1}{\sqrt{2}} & 0 & 0 \\ \frac{1}{\sqrt{2}} & \frac{1}{2} & 0 & 0 \\ 0 & 0 & 0 & 0 \\ 0 & 0 & 0 & \frac{1}{2} \end{pmatrix} \\
M_{DD} &= \begin{pmatrix} \frac{1}{4} & \frac{1}{\sqrt{8}} & \frac{1}{4} & 0 \\ \frac{1}{\sqrt{8}} & \frac{1}{2} & \frac{1}{\sqrt{8}} & 0 \\ \frac{1}{4} & \frac{1}{\sqrt{8}} & \frac{1}{4} & 0 \\ 0 & 0 & 0 & 0 \end{pmatrix} & M_{\bar{D}\bar{D}} &= \begin{pmatrix} \frac{1}{4} & -\frac{1}{2\sqrt{2}} & \frac{1}{4} & 0 \\ -\frac{1}{2\sqrt{2}} & \frac{1}{2} & -\frac{1}{2\sqrt{2}} & 0 \\ \frac{1}{4} & -\frac{1}{2\sqrt{2}} & \frac{1}{4} & 0 \\ 0 & 0 & 0 & 0 \end{pmatrix} \\
M_{H\bar{D}} &= \begin{pmatrix} 1 & -\frac{1}{\sqrt{2}} & 0 & 0 \\ -\frac{1}{\sqrt{2}} & \frac{1}{2} & 0 & 0 \\ 0 & 0 & 0 & 0 \\ 0 & 0 & 0 & \frac{1}{2} \end{pmatrix} & M_{HL} &= \begin{pmatrix} \frac{1}{2} & -\frac{1-i}{2\sqrt{2}} & -\frac{i}{2} & 0 \\ -\frac{1+i}{2\sqrt{2}} & \frac{1}{2} & -\frac{1-i}{2\sqrt{2}} & 0 \\ \frac{i}{2} & -\frac{1+i}{2\sqrt{2}} & \frac{1}{2} & 0 \\ 0 & 0 & 0 & \frac{1}{2} \end{pmatrix} \\
M_{VD} &= \begin{pmatrix} 0 & 0 & 0 & 0 \\ 0 & \frac{1}{2} & \frac{1}{\sqrt{2}} & 0 \\ 0 & \frac{1}{\sqrt{2}} & 1 & 0 \\ 0 & 0 & 0 & \frac{1}{2} \end{pmatrix} & M_{V\bar{D}} &= \begin{pmatrix} 0 & 0 & 0 & 0 \\ 0 & \frac{1}{2} & -\frac{1}{\sqrt{2}} & 0 \\ 0 & -\frac{1}{\sqrt{2}} & 1 & 0 \\ 0 & 0 & 0 & \frac{1}{2} \end{pmatrix} \\
M_{VR} &= \begin{pmatrix} 0 & 0 & 0 & 0 \\ 0 & \frac{1}{2} & -\frac{i}{\sqrt{2}} & 0 \\ 0 & \frac{i}{\sqrt{2}} & 1 & 0 \\ 0 & 0 & 0 & \frac{1}{2} \end{pmatrix} & M_{VL} &= \begin{pmatrix} 0 & 0 & 0 & 0 \\ 0 & \frac{1}{2} & \frac{i}{\sqrt{2}} & 0 \\ 0 & -\frac{i}{\sqrt{2}} & 1 & 0 \\ 0 & 0 & 0 & \frac{1}{2} \end{pmatrix}
\end{aligned}$$



$$\begin{aligned}
M_{DL} &= \begin{pmatrix} \frac{1}{2} & \frac{1+i}{2\sqrt{2}} & \frac{i}{2} & 0 \\ \frac{1-i}{2\sqrt{2}} & \frac{1}{2} & \frac{1+i}{2\sqrt{2}} & 0 \\ -\frac{i}{2} & \frac{1-i}{2\sqrt{2}} & \frac{1}{2} & 0 \\ 0 & 0 & 0 & \frac{1}{2} \end{pmatrix} & M_{\bar{D}R} &= \begin{pmatrix} \frac{1}{2} & -\frac{1+i}{2\sqrt{2}} & \frac{i}{2} & 0 \\ -\frac{1-i}{2\sqrt{2}} & \frac{1}{2} & -\frac{1+i}{2\sqrt{2}} & 0 \\ -\frac{i}{2} & -\frac{1-i}{2\sqrt{2}} & \frac{1}{2} & 0 \\ 0 & 0 & 0 & \frac{1}{2} \end{pmatrix} \\
M_{\bar{D}L} &= \begin{pmatrix} \frac{1}{2} & -\frac{1-i}{2\sqrt{2}} & -\frac{i}{2} & 0 \\ -\frac{1+i}{2\sqrt{2}} & \frac{1}{2} & -\frac{1-i}{2\sqrt{2}} & 0 \\ \frac{i}{2} & -\frac{1+i}{2\sqrt{2}} & \frac{1}{2} & 0 \\ 0 & 0 & 0 & \frac{1}{2} \end{pmatrix}.
\end{aligned}$$

Applying MLE for our measurement data, which is summarized in Tab. 6.2, yields the following accessible density matrix

$$\begin{aligned}
\hat{\rho}_{acc} &= \left( \begin{pmatrix} 0.258 & -0.084 + i0.07 & -0.041 + i0.003 \\ -0.084 - i0.07 & 0.484 & 0.054 - i0.014 \\ -0.041 - i0.003 & 0.054 + i0.014 & 0.245 \end{pmatrix} \quad 0 \right) \quad (\text{A.58}) \\
&\quad \left( \begin{matrix} 0 \\ 0 \end{matrix} \right) \quad (0.012) \\
&\pm \left( \begin{pmatrix} 0.016 & 0.011 + i0.014 & 0.012 + i0.012 \\ 0.011 + i0.014 & 0.022 & 0.011 + i0.015 \\ 0.012 + i0.012 & 0.011 + i0.015 & 0.018 \end{pmatrix} \quad 0 \right) \\
&\quad \left( \begin{matrix} 0 \\ 0 \end{matrix} \right) \quad (0.017)
\end{aligned}$$

The errors were determined by adding Poissonian noise to the measured uncorrected correlations, followed by a density matrix reconstruction. For each matrix this was repeated with a set of 100 random density matrices, from which the standard deviation was determined.

Within our experimental errors the population of the antisymmetric subspace is compatible with zero, which shows that there is no inaccessible degree of freedom which is ignored in our experiment. Thus, it is sufficient to restrict the reconstruction to the symmetric subspace. In this case, we reconstruct the  $3 \times 3$  density matrix using the 19 projection matrices given by

$$\begin{aligned}
M_{HH} &= \begin{pmatrix} 1 & 0 & 0 \\ 0 & 0 & 0 \\ 0 & 0 & 0 \end{pmatrix} & M_{HV} &= \begin{pmatrix} 0 & 0 & 0 \\ 0 & 1 & 0 \\ 0 & 0 & 0 \end{pmatrix} \\
M_{D\bar{D}} &= \begin{pmatrix} \frac{1}{2} & 0 & -\frac{1}{2} \\ 0 & 0 & 0 \\ -\frac{1}{2} & 0 & \frac{1}{2} \end{pmatrix} & M_{RL} &= \begin{pmatrix} \frac{1}{2} & 0 & \frac{1}{2} \\ 0 & 0 & 0 \\ \frac{1}{2} & 0 & \frac{1}{2} \end{pmatrix} \\
M_{RH} &= \begin{pmatrix} \frac{2}{3} & -\frac{i\sqrt{2}}{3} & 0 \\ \frac{i\sqrt{2}}{3} & \frac{1}{3} & 0 \\ 0 & 0 & 0 \end{pmatrix} & M_{DR} &= \begin{pmatrix} \frac{1}{3} & \frac{\frac{1}{3}-\frac{i}{3}}{\sqrt{2}} & -\frac{i}{3} \\ \frac{\frac{1}{3}+\frac{i}{3}}{\sqrt{2}} & \frac{1}{3} & \frac{\frac{1}{3}-\frac{i}{3}}{\sqrt{2}} \\ \frac{i}{3} & \frac{\frac{1}{3}+\frac{i}{3}}{\sqrt{2}} & \frac{1}{3} \end{pmatrix}
\end{aligned}$$

$$\begin{aligned}
M_{RR} &= \begin{pmatrix} \frac{1}{4} & -\frac{i}{2\sqrt{2}} & -\frac{1}{4} \\ \frac{i}{2\sqrt{2}} & \frac{1}{2} & -\frac{i}{2\sqrt{2}} \\ -\frac{1}{4} & \frac{i}{2\sqrt{2}} & \frac{1}{4} \end{pmatrix} & M_{DH} &= \begin{pmatrix} \frac{2}{3} & \frac{\sqrt{2}}{3} & 0 \\ \frac{\sqrt{2}}{3} & \frac{1}{3} & 0 \\ 0 & 0 & 0 \end{pmatrix} \\
M_{DD} &= \begin{pmatrix} \frac{1}{4} & \frac{1}{2\sqrt{2}} & \frac{1}{4} \\ \frac{1}{2\sqrt{2}} & \frac{1}{2} & \frac{1}{2\sqrt{2}} \\ \frac{1}{4} & \frac{1}{2\sqrt{2}} & \frac{1}{4} \end{pmatrix} & M_{\bar{D}\bar{D}} &= \begin{pmatrix} \frac{1}{4} & -\frac{1}{2\sqrt{2}} & \frac{1}{4} \\ -\frac{1}{2\sqrt{2}} & \frac{1}{2} & -\frac{1}{2\sqrt{2}} \\ \frac{1}{4} & -\frac{1}{2\sqrt{2}} & \frac{1}{4} \end{pmatrix} \\
M_{H\bar{D}} &= \begin{pmatrix} \frac{2}{3} & -\frac{\sqrt{2}}{3} & 0 \\ -\frac{\sqrt{2}}{3} & \frac{1}{3} & 0 \\ 0 & 0 & 0 \end{pmatrix} & M_{HL} &= \begin{pmatrix} \frac{2}{3} & \frac{i\sqrt{2}}{3} & 0 \\ -\frac{i\sqrt{2}}{3} & \frac{1}{3} & 0 \\ 0 & 0 & 0 \end{pmatrix} \\
M_{VD} &= \begin{pmatrix} 0 & 0 & 0 \\ 0 & \frac{1}{3} & \frac{\sqrt{2}}{3} \\ 0 & \frac{\sqrt{2}}{3} & \frac{2}{3} \end{pmatrix} & M_{V\bar{D}} &= \begin{pmatrix} 0 & 0 & 0 \\ 0 & \frac{1}{3} & -\frac{\sqrt{2}}{3} \\ 0 & -\frac{\sqrt{2}}{3} & \frac{2}{3} \end{pmatrix} \\
M_{VR} &= \begin{pmatrix} 0 & 0 & 0 \\ 0 & \frac{1}{3} & -\frac{i\sqrt{2}}{3} \\ 0 & \frac{i\sqrt{2}}{3} & \frac{2}{3} \end{pmatrix} & M_{VL} &= \begin{pmatrix} 0 & 0 & 0 \\ 0 & \frac{1}{3} & \frac{i\sqrt{2}}{3} \\ 0 & -\frac{i\sqrt{2}}{3} & \frac{2}{3} \end{pmatrix} \\
M_{DL} &= \begin{pmatrix} \frac{1}{3} & \frac{\frac{1}{3}+i}{\sqrt{2}} & \frac{i}{3} \\ \frac{\frac{1}{3}-i}{\sqrt{2}} & \frac{1}{3} & \frac{\frac{1}{3}+i}{\sqrt{2}} \\ -\frac{i}{3} & \frac{\frac{1}{3}-i}{\sqrt{2}} & \frac{1}{3} \end{pmatrix} & M_{\bar{D}R} &= \begin{pmatrix} \frac{1}{3} & -\frac{\frac{1}{3}+i}{\sqrt{2}} & \frac{i}{3} \\ -\frac{\frac{1}{3}-i}{\sqrt{2}} & \frac{1}{3} & -\frac{\frac{1}{3}+i}{\sqrt{2}} \\ -\frac{i}{3} & -\frac{\frac{1}{3}-i}{\sqrt{2}} & \frac{1}{3} \end{pmatrix} \\
M_{\bar{D}L} &= \begin{pmatrix} \frac{1}{3} & -\frac{\frac{1}{3}-i}{\sqrt{2}} & -\frac{i}{3} \\ -\frac{\frac{1}{3}+i}{\sqrt{2}} & \frac{1}{3} & -\frac{\frac{1}{3}-i}{\sqrt{2}} \\ \frac{i}{3} & -\frac{\frac{1}{3}+i}{\sqrt{2}} & \frac{1}{3} \end{pmatrix}.
\end{aligned}$$

Applying the reduced MLE, we obtain the following density matrix of the symmetric subspace

$$\begin{aligned}
\hat{\rho}_{sym} &= \begin{pmatrix} 0.259 & -0.08 + i0.061 & -0.039 + i0.009 \\ -0.08 - i0.061 & 0.484 & 0.058 - i0.015 \\ -0.039 - i0.009 & 0.058 + i0.015 & 0.257 \end{pmatrix} \quad (\text{A.59}) \\
&\pm \begin{pmatrix} 0.016 & 0.012 + i0.011 & 0.014 + i0.01 \\ 0.012 + i0.011 & 0.021 & 0.013 + i0.012 \\ 0.014 + i0.01 & 0.013 + i0.012 & 0.016 \end{pmatrix},
\end{aligned}$$

which agrees well with the  $3 \times 3$  symmetric submatrix in Eq. (A.58). In Fig. A.2 the full accessible density matrix, the density matrix obtained from the reduced reconstruction and their difference are plotted. The difference between the two methods lies well within the experimental errors.

## A.8 Concurrence

The concurrence is commonly used to quantify entanglement and for a two-qubit state, which is characterized by its density matrix  $\hat{\rho}$ , it is defined as [183, 245]

$$C(\hat{\rho}) = \max(0, \lambda_1 - \lambda_2 - \lambda_3 - \lambda_4) . \quad (\text{A.60})$$

Here,  $\lambda_i$  are the eigenvalues, which are labeled in decreasing order, of the Hermitian matrix

















$$R(\hat{\rho}) = \sqrt{\sqrt{\hat{\rho}} \tilde{\rho} \sqrt{\hat{\rho}}} , \quad (\text{A.61})$$

where

$$\tilde{\rho} = (\sigma_y \otimes \sigma_y) \hat{\rho}^* (\sigma_y \otimes \sigma_y) , \quad (\text{A.62})$$

are the spin-flip operators, with the Pauli matrix  $\sigma_y$ .

## A.9 Legend for fiber network

	single-mode fiber		4 port fiber beam splitter
	polarization maintaining single-mode fiber		3 port fiber beam splitter
	multi-mode fiber		MEM switch
	free space beam		single-mode switch
	fiber-fiber connector		MZ modulator
	fiber coupler		BMR
	photo diode		SPCM
	fiber polarization controller		fiber bench

**Figure A.3:** Symbols used for the setups described in Fig. 5.5 Fig. 6.4 and Fig. 7.5.



# Bibliography

- [1] V. Giovannetti, S. Lloyd, and L. Maccone. Advances in quantum metrology. *Nature Photonics*, 5(4):222–229, 2011.
- [2] C. Degen, F. Reinhard, and P. Cappellaro. Quantum sensing. *arXiv:1611.02427*, 2016.
- [3] Quantum Simulation. Insight issue. *Nature Physics*, 8(4):263–299, 2012.
- [4] N. Gisin and R. Thew. Quantum Communication. *Nature Photonics*, 1(3):165–171, 2007.
- [5] H. J. Kimble. The quantum internet. *Nature*, 453(7198):1023–1030, 2008.
- [6] T. Ladd, F. Jelezko, R. Laflamme, Y. Nakamura, C. Monroe, and J. O’Brien. Quantum computers. *Nature*, 464(7285):45–53, 2010.
- [7] A. Aspect, P. Grangier, and G. Roger. Experimental tests of realistic local theories via Bell’s theorem. *Physical Review Letters*, 47(7):460–463, 1981.
- [8] D. DiVincenzo. The physical implementation of quantum computation. *Fortschritte der Physik*, 48(9-11):771–783, 2000.
- [9] K. Hammerer, A. Sørensen, and E. Polzik. Quantum interface between light and atomic ensembles. *Reviews of Modern Physics*, 82(2):1041–1093, 2010.
- [10] A. Reiserer and G. Rempe. Cavity-based quantum networks with single atoms and optical photons. *Reviews of Modern Physics*, 87(4):1379–1418, 2015.
- [11] S. Haroche and D. Kleppner. Cavity Quantum Electrodynamics. *Physics Today*, 42(1):24–30, 1989.
- [12] H. Walther, B. Varcoe, B. Englert, and T. Becker. Cavity quantum electrodynamics. *Reports on Progress in Physics*, 69(5):1325–1382, 2006.
- [13] Royal Swedish Academy of Sciences. The nobel prize in physics 2012. *Press release*, 2012.
- [14] R. Thompson, G. Rempe, and H. J. Kimble. Observing of Normal-Mode Splitting for an Atom in an Optical Cavity. *Physical Review Letters*, 68(8):1132–1135, 1992.

- [15] J. Reithmaier, G. Sek, A. Löffler, C. Hofmann, S. Kuhn, S. Reitzenstein, L. Keldysh, V. Kulakovskii, T. Reinecke, and A. Forchel. Strong coupling in a single quantum dot-semiconductor microcavity system. *Nature*, 432:197–200, 2004.
- [16] T. Yoshie, A. Scherer, J. Hendrickson, G. Khitrova, H. Gibbs, G. Rupper, C. Ell, O. Shchekin, and D. Deppe. Vacuum Rabi splitting with a single quantum dot in a photonic crystal nanocavity. *Nature*, 432(November):9–12, 2004.
- [17] T. Aoki, B. Dayan, E. Wilcut, W. Bowen, A. Parkins, T. Kippenberg, K. Vahala, and H. J. Kimble. Observation of strong coupling between one atom and a monolithic microresonator. *Nature*, 443(7112):671–674, 2006.
- [18] K. Vahala. Optical microcavities. *Nature*, 424:839–846, 2003.
- [19] V. Ilchenko and A. Matsko. Optical Resonators With Whispering-Gallery Modes–Part II: Applications. *IEEE Journal of Selected Topics in Quantum Electronics*, 12(1):15 – 32, 2006.
- [20] D. Armani, T. Kippenberg, S. Spillane, and K. Vahala. Ultra-high-Q toroid microcavity on a chip. *Nature*, 421(6926):925–928, 2003.
- [21] A. Aiello, P. Banzer, M. Neugebauer, and G. Leuchs. Beyond beam optics – From transverse angular momentum to photonic wheels. *Nature Photonics*, 9:789–795, 2015.
- [22] P. Lodahl, S. Mahmoodian, S. Stobbe, A. Rauschenbeutel, P. Schneeweiss, J. Volz, H. Pichler, and P. Zoller. Chiral quantum optics. *Nature*, 541(7638):473–480, 2017.
- [23] D. Pozar. *Microwave Engineering*. John Wiley & Sons Inc., 1998.
- [24] B. Richards and E. Wolf. Electromagnetic diffraction in optical systems. ii. structure of the image field in an aplanatic system. *Proceedings of the Royal Society of London A: Mathematical, Physical and Engineering Sciences*, 253(1274):358–379, 1959.
- [25] Spin–orbit interactions. Focus issue. *Nature Photonics*, 9:771–808, 2015.
- [26] M. Berry. Optical currents. *Journal of Optics A*, 11(9):094001, 2009.
- [27] S. Barnett. Optical angular-momentum flux. *Journal of Optics B*, 4:S7, 2002.
- [28] R. Cameron, S. Barnett, and A. Yao. Optical helicity, optical spin and related quantities in electromagnetic theory. *New Journal of Physics*, 14:053050, 2012.
- [29] K. Bliokh, A. Bekshaev, and F. Nori. Extraordinary momentum and spin in evanescent waves. *Nature Communications*, 5:3300, 2014.
- [30] K. Bliokh, F. Rodríguez-Fortuño, F. Nori, and A. Zayats. Spin–orbit interactions of light. *Nature Photonics*, 9:799–808, 2015.

- 
- [31] A. Young, A. Thijssen, D. Beggs, P. Androvitsaneas, L. Kuipers, J. Rarity, S. Hughes, and R. Oulton. Polarization engineering in photonic crystal waveguides for spin–photon entanglers. *Physical Review Letters*, 115:153901, 2015.
- [32] L. Marrucci, C. Manzo, and D. Paparo. Optical spin-to-orbital angular momentum conversion in inhomogeneous anisotropic media. *Physical Review Letters*, 96:163905, 2006.
- [33] P. Banzer, M. Neugebauer, A. Aiello, C. Marquardt, N. Lindlein, T. Bauer, and G. Leuchs. The photonic wheel – demonstration of a state of light with purely transverse angular momentum. *Journal of the European Optical Society , Rapid Publ.*, 8:13032–13037, 2013.
- [34] T. Bauer, S. Orlov, U. Peschel, P. Banzer, and G. Leuchs. Nanointerferometric amplitude and phase reconstruction of tightly focused vector beams. *Nature Photonics*, 8:23–27, 2014.
- [35] T. Bauer, P. Banzer, E. Karimi, S. Orlov, a. Rubano, L. Marrucci, E. Santamato, R. W. Boyd, and G. Leuchs. Observation of optical polarization Mobius strips. *Science*, 347(6225):964–966, 2015.
- [36] J. Balthasar Mueller and Federico Capasso. Asymmetric surface plasmon polariton emission by a dipole emitter near a metal surface. *Physical Review B*, 88:121410, 2013.
- [37] Ji. Lin, J. Balthasar Mueller, Q. Wang, G. Yuan, N. Antoniou, X.-C. Yuan, and F. Capasso. Polarization-Controlled Tunable Directional Coupling of Surface Plasmon Polaritons. *Science*, 340(6130):331–334, 2013.
- [38] N. Shitrit, I. Yulevich, E. Maguid, D. Ozeri, D. Veksler, V. Kleiner, and E. Hasman. Spin-Optical Metamaterial Route to Spin-Controlled Photonics. *Science*, 340(6133):724–726, 2013.
- [39] D. O’Connor, P. Ginzburg, F. Rodriguez-Fortuno, G. Wurtz, and A. Zayats. Spin–orbit coupling in surface plasmon scattering by nanostructures: The role of transverse spin. *Nature Communications*, 5(5327), 2014.
- [40] M. Neugebauer, T. Bauer, P. Banzer, and G. Leuchs. Polarization tailored light driven directional optical nanobeacon. *Nano Letters*, 14(5):2546–2551, 2014.
- [41] J. Petersen, J. Volz, and A. Rauschenbeutel. Chiral nanophotonic waveguide interface based on spin-orbit interaction of light. *Science*, 346(6205):67–71, 2014.
- [42] R. Mitsch, C. Sayrin, B. Albrecht, P. Schneeweiss, and A. Rauschenbeutel. Quantum state-controlled directional spontaneous emission of photons into a nanophotonic waveguide. *Nature Communications*, 5:5713, 2014.
- [43] R. Coles, D. Price, J. Dixon, B. Royall, E. Clarke, P. Kok, M. Skolnick, A. Fox, and M. Makhonin. Chirality of nanophotonic waveguide with embedded quantum emitter for unidirectional spin transfer. *Nature Communications*, 7:11183, 2016.

- [44] I. Söllner, S. Mahmoodian, S. Hansen Lindskov, L. Midolo, A. Javadi, G. Kiršanske, T. Pregonlato, H. El-Ella, E. Lee, J. Song, S. Stobbe, and P. Lodahl. Deterministic photon–emitter coupling in chiral photonic circuits. *Nature Nanotechnology*, 10(9):775, 2015.
- [45] B. Le Feber, N. Rotenberg, and L. Kuipers. Nanophotonic control of circular dipole emission. *Nature Communications*, 6:6695, 2015.
- [46] C. Junge, D. O’Shea, J. Volz, and A. Rauschenbeutel. Strong Coupling between Single Atoms and Nontransversal Photons. *Physical Review Letters*, 110(21):213604, 2013.
- [47] J. Poynting. The wave motion of a revolving shaft, and a suggestion as to the angular momentum in a beam of circularly polarised light. *Proc. R. Soc. Lond. A*, 82:560–567, 1909.
- [48] L. Allen, M. Beijersbergen, R. Spreeuw, and J. Woerdman. Orbital angular momentum of light and the transformation of Laguerre-Gaussian laser modes. *Physical Review A*, 45(11):8185–8189, 1992.
- [49] A. Aiello, N. Lindlein, C. Marquardt, and G. Leuchs. Transverse angular momentum and geometric spin hall effect of light. *Physical Review Letters*, 103(10):100401, 2009.
- [50] K. Bliokh and F. Nori. Transverse and longitudinal angular momenta of light. *Physics Reports*, 592:1–38, 2015.
- [51] G. Pollack and D. Stump. *Electromagnetism*. Addison-Wesley, 2002.
- [52] F. Goos and H. Hänchen. Ein neuer und fundamentaler Versuch zur Totalreflexion. *Annalen der Physik*, 436(7):333–346, 1947.
- [53] F. Fedorov. To the theory of total reflection. *Journal of Optics*, 15(1):014002, 2013(1955).
- [54] S. Chu, B. Little, W. Pan, T. Kaneko, S. Sato, and Y. Kokubun. An eight-channel add-drop filter using vertically coupled microring resonators over a cross grid. *IEEE Photonics Technology Letters*, 11(6):691–693, 1999.
- [55] K. Volyanskiy, P. Salzenstein, H. Tavernier, M. Pogurmirskiy, Y. Chembo, and L. Larger. Compact optoelectronic microwave oscillators using ultra-high Q whispering-gallery-mode disk-resonators and phase modulation. *Optics Express*, 18(21):22358–22363, 2010.
- [56] B. Min, T. Kippenberg, and K. Vahala. Compact, fiber-compatible, cascaded raman laser. *Optics Letters*, 28(17):1507–1509, 2003.
- [57] D. Strelakov, C. Marquardt, A. Matsko, H. Schwefel, and G. Leuchs. Nonlinear and Quantum Optics with Whispering Gallery Resonators. *Journal of Optics*, 18:123002, 2016.
- [58] J. Fürst, D. Strelakov, D. Elser, M. Lassen, U. Andersen, C. Marquardt, and G. Leuchs. Naturally phase-matched second-harmonic generation in a whispering-gallery-mode resonator. *Physical Review Letters*, 104:153901, 2010.



- 
- [59] P. Del’Haye, A. Schliesser, O. Arcizet, T. Wilken, R. Holzwarth, and T. Kippenberg. Optical frequency comb generation from a monolithic microresonator. *Nature*, 450(7173):1214–1217, 12 2007.
- [60] M. Förtsch, J. Fürst, C. Wittmann, D. Strelakov, A. Aiello, M. Chekhova, C. Silberhorn, G. Leuchs, and C. Marquardt. A versatile source of single photons for quantum information processing. *Nature Communications*, 4:1818, 2013.
- [61] V. Almeida, C. Barrios, R. Panepucci, and M. Lipson. All-optical control of light on a silicon chip. *Nature*, 431:1081–1084, 2004.
- [62] D. O’Shea, C. Junge, M. Pöllinger, A. Vogler, and A. Rauschenbeutel. All-optical switching and strong coupling using tunable whispering-gallery-mode microresonators. *Applied Physics B*, 105:129–148, 2011.
- [63] M. Foreman, J. Swaim, and F. Vollmer. Whispering gallery mode sensors Matthew. *Advances in Optics and Photonics*, 7:168–240, 2015.
- [64] J. Nöckel and D. Stone. Ray and wave chaos in asymmetric resonant optical cavities. *Nature*, 385:45–47, 1997.
- [65] F. Monifi, J. Zhang, Ş. Özdemir, B. Peng, Y. Liu, F. Bo, F. Nori, and L. Yang. Optomechanically induced stochastic resonance and chaos transfer between optical fields. *Nature Photonics*, 10:399–405, 2016.
- [66] L. Chang, X. Jiang, S. Hua, C. Yang, J. Wen, L. Jiang, G. Li, G. Wang, and M. Xiao. Parity–time symmetry and variable optical isolation in active–passive-coupled microresonators. *Nature Photonics*, 8(7):524–529, 2014.
- [67] B. Peng, S. Ozdemir, F. Lei, F. Monifi, M. Gianfreda, G. Long, S. Fan, F. Nori, C. Bender, and L. Yang. Parity–time-symmetric whispering-gallery microcavities. *Nature Physics*, 10:394–398, 2014.
- [68] T. Kippenberg and K. Vahala. Cavity optomechanics: Back-action at the mesoscale. *Science*, 321(5893):1172–1176, 2008.
- [69] B. Dayan, S. Parkins, T. Aoki, E. Ostby, K. Vahala, and H. J. Kimble. A photon turnstile dynamically regulated by one atom. *Science*, 319(5866):1062–1065, 2008.
- [70] D. O’Shea, C. Junge, J. Volz, and A. Rauschenbeutel. Fiber-Optical Switch Controlled by a Single Atom. *Physical Review Letters*, 111(19):193601, 2013.
- [71] I. Shomroni, S. Rosenblum, Y. Lovsky, O. Bechler, G. Guendelman, and B. Dayan. All-optical routing of single photons by a one-atom switch controlled by a single photon. *Science*, 345(6199):903–906, 2014.
- [72] S. Rosenblum, O. Bechler, I. Shomroni, Y. Lovsky, G. Guendelman, and B. Dayan. Extraction of a single photon from an optical pulse. *Nature Photonics*, 10:19–22, 2016.

- [73] A. Savchenkov, A. Matsko, V. Ilchenko, and L. Maleki. Optical resonators with ten million finesse. *Optics Express*, 15(11):6768, 2007.
- [74] D. Hunger, T. Steinmetz, Y. Colombe, C. Deutsch, T. Hänsch, and J. Reichel. A fiber Fabry-Perot cavity with high finesse. *New Journal of Physics*, 12:065038, 2010.
- [75] C. Hood, H. J. Kimble, and J. Ye. Characterization of high-finesse mirrors: Loss, phase shifts, and mode structure in an optical cavity. *Physical Review A*, 64(3):033804, 2001.
- [76] M. Pöllinger, D. O’Shea, F. Warken, and A. Rauschenbeutel. Ultra-high-Q tunable whispering-gallery-mode microresonator. *Physical Review Letters*, 103:053901, 2009.
- [77] Y. Louyer, D. Meschede, and A. Rauschenbeutel. Tunable whispering-gallery-mode resonators for cavity quantum electrodynamics. *Physical Review A*, 72(3):031801, 2005.
- [78] Y. Akahane, T. Asano, B.-S. Song, and S. Noda. High-Q photonic nanocavity in a two-dimensional photonic crystal. *Nature*, 425:944–947, 2003.
- [79] J. Thompson, T. Tiecke, N. de Leon, J. Feist, A. Akimov, M. Gullans, A. Zibrov, V. Vuletić, and M. Lukin. Coupling a single trapped atom to a nanoscale optical cavity. *Science*, 340(6137):1202–1205, 2013.
- [80] E. Purcell. Spontaneous emission probabilities at radio frequencies. *Physical Review*, 69:681, 1946.
- [81] D. Steck. *Quantum and Atom Optics*, 2012.
- [82] H. J. Kimble. Strong Interactions of Single Atoms and Photons in Cavity QED. *Physica Scripta*, T76:127–137, 1998.
- [83] T. Kippenberg, S. Spillane, and K. Vahala. Demonstration of ultra-high-Q small mode volume toroid microcavities on a chip. *Applied Physics Letters*, 85(25):6113–6115, 2004.
- [84] J. Buck and H. J. Kimble. Optimal sizes of dielectric microspheres for cavity QED with strong coupling. *Physical Review A*, 67(3):033806, mar 2003.
- [85] M. Tomes, K. Vahala, and T. Carmon. Direct imaging of tunneling from a potential well. *Optics Express*, 17(21):19160–19165, 2009.
- [86] C. Junge. *Cavity Quantum Electrodynamics with Non-transversal Photons*. PhD thesis, Technische Universität Wien, 2013.
- [87] D. O’Shea. *Cavity QED experiments with a whispering-gallery-mode bottle resonator*. PhD thesis, Technische Universität Wien, 2013.
- [88] V. Braginsky, M. Gorodetsky, and V. Ilchenko. Quality-factor and nonlinear properties of optical whispering-gallery-modes. *Physics Letters A*, 137(7–8):393 – 397, 1989.

- 
- [89] Lord Rayleigh. The problem of the whispering gallery. *Philosophical Magazine Series 6*, 20(120):1001–1004, 1910.
- [90] F. Warken. *Ultradünne Glasfasern als Werkzeug zur Kopplung von Licht und Materie*. PhD thesis, Rheinische Friedrich-Wilhelms-Universität Bonn, 2007.
- [91] A. Oraevsky. Whispering-gallery waves. *Quantum Electronics*, 32(5):377–400, 2002.
- [92] M. Pöllinger. *Bottle microresonators for applications in quantum optics and all-optical signal processing*. PhD thesis, Johannes Gutenberg-Universität Mainz, 2010.
- [93] J. Dalibard and C. Cohen-Tannoudji. Laser cooling below the Doppler limit by polarization gradients: simple theoretical models. *Journal of the Optical Society of America B*, 6(11):2023, 1989.
- [94] P. Lett, W. Phillips, S. Rolston, C. Tanner, R. Watts, and C. Westbrook. Optical molasses. *Journal of the Optical Society of America B*, 6(11):2084, 1989.
- [95] E. Jaynes and F. Cummings. Comparison of Quantum and Semiclassical Radioation Theories with Application to the Beam Maser. *Proceedings of the IEEE*, 51:89–109, 1963.
- [96] D. Meschede, H. Walther, and G. Müller. One-Atom Maser. *Physical Review Letters*, 54:551 – 554, 1985.
- [97] M. Brune, F. Schmidt-Kaler, A. Maali, J. Dreyer, E. Hagley, J.-M. Raimond, and S. Haroche. Quantum Rabi Oscillation: A Direct Test of Field Quantization in a Cavity. *Physical Review Letters*, 76(11):1800–1803, 1996.
- [98] G. Nogues, A. Rauschenbeutel, S. Osnaghi, M. Brune, J.-M. Raimond, and S. Haroche. Seeing a single photon without destroying it. *Nature*, 400:239–242, 1999.
- [99] A. Rauschenbeutel, G. Nogues, S. Osnaghi, P. Bertet, M. Brune, J.-M. Raimond, and S. Haroche. Step-by-Step Engineered Multiparticle Entanglement. *Nature*, 288:2024–2028, 2000.
- [100] S. Deleglise, I. Dotsenko, C. Sayrin, J. Bernu, M. Brune, J.-M. Raimond, and S. Haroche. Reconstruction of non-classical cavity field states with snapshots of their decoherence. *Nature*, 455:510–514, 2008.
- [101] C. Sayrin, I. Dotsenko, X. Zhou, B. Peaudecerf, T. Rybarczyk, S. Gleyzes, P. Rouchon, M. Mirrahimi, H. Amini, M. Brune, J.-M. Raimond, and S. Haroche. Real-time quantum feedback prepares and stabilizes photon number states. *Nature*, 477(7362):73–77, 2011.
- [102] P. Maunz, T. Puppe, I. Schuster, N. Syassen, P. Pinkse, and G. Rempe. Cavity cooling of a single atom. *Nature*, 428(6978):50–52, 2004.
- [103] A. Reiserer, S. Ritter, and G. Rempe. Nondestructive Detection of an Optical Photon. *Science*, 342(6164):1349–1351, 2013.

- [104] A. Kuhn, M. Hennrich, and G. Rempe. Deterministic single-photon source for distributed quantum networking. *Physical Review Letters*, 90:249802, 2003.
- [105] J. McKeever, A. Boca, A. Boozer, R. Miller, J. Buck, A. Kuzmich, and H. J. Kimble. Deterministic generation of single photons from one atom trapped in a cavity. *Science*, 303(5666):1992–1994, 2004.
- [106] K. Birnbaum, A. Boca, R. Miller, T. Boozer, A. Northup, and H. J. Kimble. Photon blockade in an optical cavity with one trapped atom. *Nature*, 436(7047):87–90, 2005.
- [107] T. Wilk, S. Webster, A. Kuhn, and G. Rempe. Single-atom single-photon quantum interface. *Science*, 317(5837):488–490, 2007.
- [108] H. Specht, C. Nolleke, A. Reiserer, M. Uphoff, E. Figueroa, S. Ritter, and G. Rempe. A single-atom quantum memory. *Nature*, 473(7346):190–193, 2011.
- [109] S. Ritter, C. Nolleke, C. Hahn, A. Reiserer, A. Neuzner, M. Uphoff, M. Mücke, E. Figueroa, J. Bochmann, and G. Rempe. An elementary quantum network of single atoms in optical cavities. *Nature*, 484(7393):195–200, 2012.
- [110] K. Srinivasan, P. Barclay, O. Painter, J. Chen, A. Cho, and C. Gmachl. Experimental demonstration of a high quality factor photonic crystal microcavity. *Applied Physics Letters*, 83(10):1915–1917, 2003.
- [111] M. Cai, O. Painter, and K. Vahala. Observation of critical coupling in a fiber taper to a silica-microsphere whispering-gallery mode system. *Physical Review Letters*, 85:74–77, 2000.
- [112] T. Aoki, S. Parkins, D. Alton, C. Regal, B. Dayan, E. Ostby, K. Vahala, and H. J. Kimble. Efficient routing of single photons by one atom and a microtoroidal cavity. *Physical Review Letters*, 102(8):083601, 2009.
- [113] C. Gerry and P. Knight. *Introductory Quantum Optics*. Cambridge University Press, 2005.
- [114] H. Carmichael. *An Open Systems Approach to Quantum Optics*. Springer-Verlag, 1991.
- [115] P. Gardiner, C. Zoller. *Quantum Noise*. Springer, Berlin, 2005.
- [116] G. Ford, J. Lewis, and R. O’Connell. Quantum Langevin equation. *Physical Review A*, 37(11):4419, 1988.
- [117] R. Dum, P. Zoller, and H. Ritsch. Monte Carlo simulation of the atomic master equation for spontaneous emission. *Physical Review A*, 45(7):4879–4887, 1992.
- [118] K. Mølmer, Y. Castin, and J. Dalibard. Monte Carlo wave-function method in quantum optics. *Journal of the Optical Society of America B*, 10(3):524, 1993.

- 
- [119] C. Gardiner and M. Collett. Input and output in damped quantum systems: Quantum stochastic differential equations and the master equation. *Physical Review A*, 31(6):3761–3774, 1985.
- [120] H. Carmichael, editor. *Statistical Methods in Quantum Optics 1: Master Equations and Fokker-Planck Equations*, volume 1. Springer, 2002.
- [121] M. Collett and C. Gardiner. Squeezing of intracavity and traveling-wave light fields produced in parametric amplification. *Physical Review A*, 30(3):1386–1391, 1984.
- [122] D. Steck. *Rubidium 85 D Line Data*, 2001.
- [123] K. Birnbaum, S. Parkins, and H. J. Kimble. Cavity QED with multiple hyperfine levels. *Physical Review A*, 74(6):1–6, 2006.
- [124] V. Peano and M. Thorwart. Quasienergy description of the driven Jaynes–Cummings model. *Physical Review B*, 82:155129, 2010.
- [125] C. Sayrin, C. Junge, R. Mitsch, B. Albrecht, D. O’Shea, P. Schneeweiss, J. Volz, and A. Rauschenbeutel. Nanophotonic optical isolator controlled by the internal state of cold atoms. *Physical Review X*, 5:041036, 2015.
- [126] C. Hauswald. *Aufbau und Charakterisierung eines Atom-Springbrunnens für ein Resonator-QED-Experiment mit Flüstergaleriemoden-Mikroresonatoren*. Master’s thesis, Johannes Gutenberg Universität Mainz, 2010.
- [127] K. Friebe. *Strong Coupling of Single Atoms to a Whispering-Gallery-Mode Resonator of Ultrahigh Quality*. Master’s thesis, Johannes Gutenberg Universität, Mainz, 2011.
- [128] M. Scheucher. *Towards a Quantum Switch for Light*. Master’s thesis, Technische Universität Wien, 2013.
- [129] D. Vernooy, V. Ilchenko, H. Mabuchi, E. Streed, and H. J. Kimble. High-Q measurements of fused-silica microspheres in the near infrared. *Optics Letters*, 23(4):247–249, 1998.
- [130] M. Gorodetsky, A. Savchenkov, and V. Ilchenko. Ultimate q of optical microsphere resonators. *Optics Letters*, 21(7):453–455, 1996.
- [131] B. Gayral, J. M. Gérard, A. Lemaître, C. Dupuis, L. Manin, and J. Pelouard. High-q wet-etch gaas microdisks containing inas quantum boxes. *Applied Physics Letters*, 75, 1908:1908–1910, 1999.
- [132] T. Kippenberg, S. Spillane, D. Armani, and K. Vahala. Fabrication and coupling to planar high-Q silica disk microcavities. *Applied Physics Letters*, 83(4):797–799, 2003.
- [133] H. Lee, T. Chen, J. Li, K. Yang, S. Jeon, O. Painter, and K. Vahala. Chemically etched ultrahigh-Q wedge-resonator on a silicon chip. *Nature Photonics*, 6(6):369–373, 2012.

- [134] A. Matsko and V. Ilchenko. Optical Resonators With Whispering-Gallery Modes—Part I: Basics. *IEEE Journal of Selected Topics in Quantum Electronics*, 12(1):3 – 14, 2006.
- [135] J. Zhu, S. Özdemir, H. Yilmaz, B Peng, M. Dong, M. Tomes, T. Carmon, and L. Yang. Interfacing whispering-gallery microresonators and free space light with cavity enhanced Rayleigh scattering. *Scientific Reports*, 4:6396, 2014.
- [136] D. Rowland and J. Love. Evanescent wave coupling of whispering-gallery-modes of a dielectric cylinder. *IEE Proceedings J*, 140:177–188, 1993.
- [137] N. Dubreuil, J. Knight, D. Leventhal, V. Sandoghdar, J. Hare, and V. Lefèvre. Eroded monomode optical fiber for whispering-gallery mode excitation in fused-silica microspheres. *Optics Letters*, 20(8):813–815, 1995.
- [138] S. Spillane, T. Kippenberg, O. Painter, and K. Vahala. Ideality in a fiber-taper-coupled microresonator system for application to cavity quantum electrodynamics. *Physical Review Letters*, 91(4):043902, 2003.
- [139] J. Knight, G. Cheung, F. Jacques, and T. Birks. Phase-matched excitation of whispering-gallery-mode resonances by a fiber taper. *Optics Letters*, 22(15):1129–1131, 1997.
- [140] T. Kippenberg, S. Spillane, and K. Vahala. Modal coupling in traveling-wave resonators. *Optics Letters*, 27(19):1669–1671, 2002.
- [141] J. Wiersig. Structure of whispering-gallery modes in optical microdisks perturbed by nanoparticles. *Physical Review A*, 84:063828, 2011.
- [142] B. Peng, S. Özdemir, M. Liertz, W. Chen, J. Kramer, H. Yılmaz, J. Wiersig, S. Rotter, and L. Yang. Chiral modes and directional lasing at exceptional points. *Proceedings of the National Academy of Sciences*, 113(25):6845–6850, 2016.
- [143] A. Chiba, H. Fujiwara, J. Hotta, S. Takeuchi, and K. Sasaki. Resonant frequency control of a microspherical cavity by temperature adjustment. *Japanese Journal of Applied Physics*, 43(9 A):6138–6141, 2004.
- [144] D. Armani, B. Min, A. Martin, and K. Vahala. Electrical thermo-optic tuning of ultrahigh-Q microtoroid resonators. *Applied Physics Letters*, 85(22):5439–5441, 2004.
- [145] W. von Klitzing, R. Long, V. Ilchenko, J. Hare, and V. Lefèvre-Seguin. Frequency tuning of the whispering-gallery modes of silica microspheres for cavity quantum electrodynamics and spectroscopy. *Optics Letters*, 26(3):166–168, 2001.
- [146] D. O’Shea, A. Rettenmaier, and A. Rauschenbeutel. Active frequency stabilization of an ultra-high Q whispering-gallery-mode microresonator. *Applied Physics B*, 99(4):623–627, 2010.
- [147] M. Sumetsky, Y. Dulashko, and R. Windeler. Super free spectral range tunable optical microbubble resonator. *Optics Letters*, 35(11):1866–1868, 2010.

- 
- [148] E. Donley, T. Heavner, F. Levi, M. Tataw, and S. Jefferts. Double-pass acousto-optic modulator system. *Review of Scientific Instruments*, 76(6):063112, 2005.
- [149] E. Black. An introduction to Pound–Drever–Hall laser frequency stabilization. *American Journal of Physics*, 69(1):79–87, 2001.
- [150] C. Junge, S. Nickel, D. O’Shea, and A. Rauschenbeutel. Bottle microresonator with actively stabilized evanescent coupling. *Optics Letters*, 36(17):3488–3490, 2011.
- [151] M. Terraciano, R. Olson Knell, D. Norris, J. Jing, A. Fernández, and L. Orozco. Photon burst detection of single atoms in an optical cavity. *Nature Physics*, 5(7):480–484, 2009.
- [152] J. Yua and J. Zhanga. Recent progress on high-speed optical transmission. *Digital Communications and Networks*, 2(2):65–76, 2015.
- [153] E. Knill, R. Laflamme, and G. Milburn. A scheme for efficient quantum computation with linear optics. *Nature*, 409(6816):46–52, 2001.
- [154] J. W. Pan, Z. Chen, C. Lu, H. Weinfurter, A. Zeilinger, and M. Zukowski. Multiphoton entanglement and interferometry. *Reviews of Modern Physics*, 84(2), 2012.
- [155] R. Boyd. *Nonlinear Optics*. Elsevier, 2007.
- [156] P. Kok, H. Lee, and J. Dowling. Single-photon quantum-nondemolition detectors constructed with linear optics and projective measurements. *Physical Review A*, 66(6):063814, 2002.
- [157] M. Fleischhauer, A. Imamoglu, and J. Marangos. Electromagnetically induced transparency: Optics in coherent media. *Reviews of Modern Physics*, 77(2):633–673, 2005.
- [158] H. Kang and Y. Zhu. Observation of large Kerr nonlinearity at low light intensities. *Physical Review Letters*, 91(9):093601, 2003.
- [159] D. Petrosyan, J. Otterbach, and M. Fleischhauer. Electromagnetically induced transparency with Rydberg atoms. *Physical Review Letters*, 107:213601, 2011.
- [160] E. Urban, T. Johnson, T. Henage, L. Isenhower, D. Yavuz, T. Walker, and M. Saffman. Observation of Rydberg blockade between two atoms. *Nature Physics*, 5(2):110–114, 2009.
- [161] H. Hofmann, K. Kojima, S. Takeuchi, and K. Sasaki. Optimized phase switching using a single-atom nonlinearity. *Journal of Optics B*, 5:218, 2003.
- [162] A. Auffèves-Garnier, C. Simon, J.-M. Gérard, and J. Poizat. Giant optical nonlinearity induced by a single two-level system interacting with a cavity in the Purcell regime. *Physical Review A*, 75(5):1–16, 2007.
- [163] S. Baur, D. Tiarks, G. Rempe, and S. Dürr. Single-Photon Switch Based on Rydberg Blockade. *Physical Review Letters*, 112:073901, 2014.

- [164] W. Chen, K. Beck, R. Bücker, M. Gullans, M. Lukin, H. Tanji-Suzuki, and V. Vuletić. All-Optical Switch and Transistor Gated by One Stored Photon. *Science*, 341(6147):768–770, 2013.
- [165] H. Gorniaczyk, C. Tresp, J. Schmidt, H. Fedder, and S. Hofferberth. Single-photon transistor mediated by interstate Rydberg interactions. *Physical Review Letters*, 113:053601, 2014.
- [166] D. Tiarks, S. Baur, K. Schneider, S. Duerr, and G. Rempe. Single-photon transistor using a Forster resonance. *Physical Review Letters*, 113:053602, 2014.
- [167] A. Kubanek, A. Ourjoumtsev, I. Schuster, M. Koch, P. Pinkse, K. Murr, and G. Rempe. Two-photon gateway in one-atom cavity quantum electrodynamics. *Physical Review Letters*, 101:203602, 2008.
- [168] Q. Turchette, C. Hood, W. Lange, H. Mabuchi, and H. J. Kimble. Measurement of conditional phase shifts for quantum logic. *Physical Review Letters*, 75(25):4, 1995.
- [169] I. Fushman, D. Englund, A. Faraon, N. Stoltz, P. Petroff, and J. Vučković. Controlled Phase Shifts with a Single Quantum Dot. *Science*, 320(5877):769–772, 2008.
- [170] O. Firstenberg, T. Peyronel, Q.-Y. Liang, A. Gorshkov, M. Lukin, and V. Vuletić. Attractive photons in a quantum nonlinear medium. *Nature*, 502(7469):71–75, 2013.
- [171] D. Tiarks, S. Schmidt, G. Rempe, and S. Dürr. Optical  $\pi$  phase shift created with a single-photon pulse. *Science Advances*, 2(4):e1600036, 2016.
- [172] K. Beck, M. Hosseini, Y. Duan, and V. Vuletić. Large conditional single-photon cross-phase modulation. *Proceedings of the National Academy of Sciences*, 113(35):9740–9744, 2016.
- [173] J. Volz, M. Scheucher, C. Junge, and A. Rauschenbeutel. Nonlinear pi phase shift for single fiber-guided photons interacting with a single atom. *Nature Photonics*, 8:965–970, 2014.
- [174] T. Tiecke, J. Thompson, N. de Leon, L. Liu, V. Vuletić, and M. Lukin. Nanophotonic quantum phase switch with a single atom. *Nature*, 508:241–244, 2014.
- [175] A. Reiserer, N. Kalb, G. Rempe, and S. Ritter. A quantum gate between a flying optical photon and a single trapped atom. *Nature*, 508:237–240, 2014.
- [176] P. Androvitsaneas, A. Young, C. Schneider, S. Maier, M. Kamp, S. Höfling, S. Knauer, E. Harbord, C. Hu, J. Rarity, and R. Oulton. Charged quantum dot micropillar system for deterministic light–matter interactions. *Physical Review B*, 93:241409, 2016.
- [177] C. Sames, H. Chibani, C. Hamsen, P. Altin, T. Wilk, and G. Rempe. Antiresonance phase shift in strongly coupled cavity QED. *Physical Review Letters*, 112:043601, 2014.



- 
- [178] P. Androvitsaneas, A. Young, J. Lennon, C. Schneider, S. Maier, J. Hinchliff, G. Atkinson, M. Kamp, S. Höfling, J. Rarity, and R. Oulton. Efficient deterministic giant photon phase shift from a single charged quantum dot. *arXiv:1609.02851*, 2016.
- [179] H. Hofmann, K. Kojima, S. Takeuchi, and K. Sasaki. Entanglement and four-wave mixing effects in the dissipation-free nonlinear interaction of two photons at a single atom. *Physical Review A*, 68(4):043813, 2003.
- [180] R. Adamson, L. Shalm, M. Mitchell, and A. Steinberg. Multiparticle state tomography: Hidden differences. *Physical Review Letters*, 98(4):043601, 2007.
- [181] R. Adamson, P. Turner, M. Mitchell, and A. Steinberg. Detecting hidden differences via permutation symmetries. *Physical Review A*, 78(3):1–10, 2008.
- [182] D. James, P. Kwiat, W. Munro, and A. White. Measurement of qubits. *Physical Review A*, 64(5):052312, 2001.
- [183] S. Hill and W. Wootters. Entanglement of a pair of quantum bits. *Physical Review Letters*, 78:5022, 1997.
- [184] D. Witthaut, M. Lukin, and A. S. Sørensen. Photon sorters and QND detectors using single photon emitters. *Europhysics Letters*, 97:50007, 2012.
- [185] T. Ralph, I. Söllner, S. Mahmoodian, A. White, and P. Lodahl. Photon sorting, efficient bell measurements, and a deterministic controlled- Z gate using a passive two-level non-linearity. *Physical Review Letters*, 114:173603, 2015.
- [186] Jeffrey Shapiro. Single-photon Kerr nonlinearities do not help quantum computation. *Physical Review A*, 73:062305, 2006.
- [187] S. Rosenblum, S. Parkins, and B. Dayan. Photon routing in cavity QED: Beyond the fundamental limit of photon blockade. *Physical Review A*, 84:033854, 2011.
- [188] K. Koshino. Single-photon filtering by a cavity quantum electrodynamics system. *Physical Review A*, 77(2):1–6, 2008.
- [189] M. Hennrich, T. Legero, A. Kuhn, and G. Rempe. Vacuum-stimulated Raman scattering based on adiabatic passage in a high-finesse optical cavity. *Physical Review Letters*, 85(23):4872–4875, 2000.
- [190] L. M. Duan and H. J. Kimble. Scalable photonic quantum computation through cavity-assisted interactions. *Physical Review Letters*, 92(12):127902, 2004.
- [191] K. Koshino and Y. Ishizaka, S. and Nakamura. Deterministic photon-photon  $\sqrt{\text{swap}}$  gate using a  $\Lambda$  system. *Physical Review A*, 82:010301, 2010.
- [192] B. Hacker, S. Welte, G. Rempe, and S. Ritter. A photon–photon quantum gate based on a single atom in an optical resonator. *Nature*, 536:193–196, 2016.

- [193] D. Bruss, A. Ekert, S. Huelga, J. W. Pan, and A. Zeilinger. Quantum computing with controlled-NOT and few qubits. *Phil. Trans. R. Soc. Lond. A*, 355:2259226, 1997.
- [194] Silicon photonics. Focus issue. *Nature Photonics*, 4(8):491–578, 2010.
- [195] B. Vermersch, P.-O. Guimond, H. Pichler, and P. Zoller. Quantum State Transfer via Noisy Photonic and Phononic Waveguides. *Physical Review Letters*, 118:133601, 2017.
- [196] H. Lira, Z. Yu, S. Fan, and M. Lipson. Electrically driven nonreciprocity induced by interband photonic transition on a silicon chip. *Physical Review Letters*, 109:033901, 2012.
- [197] L. Tzuang, K. Fang, P. Nussenzveig, S. i Fan, and M. Lipson. Non-reciprocal phase shift induced by an effective magnetic flux for light. *Nature Photonics*, 8(9):701–705, 2014.
- [198] J. Kim, M. Kuzyk, K. Han, H. Wang, and G. Bahl. Non-reciprocal Brillouin scattering induced transparency. *Nature Physics*, 11(3):275–280, 2015.
- [199] Z. Shen, Y.-L. Zhang, Y. Chen, C.-L. Zou, Y. F. Xiao, X.-B. Zou, F. W. Sun, G.-C. Guo, and C. H. Dong. Experimental realization of optomechanically induced non-reciprocity. *Nature Photonics*, 10:657–661, 2016.
- [200] F. Ruesink, M.-A. Miri, A. Alù, and E. Verhagen. Nonreciprocity and magnetic-free isolation based on optomechanical interactions. *Nature Communications*, 7:13662, 2016.
- [201] M. Nielsen and I. Chuang. *Quantum Computation and Quantum Information*. Cambridge University Press, 2011.
- [202] M. Scheucher, A. Hilico, E. Will, J. Volz, and A. Rauschenbeutel. Quantum optical circulator controlled by a single chirally coupled atom. *Science*, 354(6319):1577–1580, 2016.
- [203] B. Lax and K. Button. *Microwave ferrites and ferrimagnetics*. McGraw-Hill Book Company, 1962.
- [204] D. Jalas, A. Petrov, M. Eich, W. Freude, S. Fan, Z. Yu, R. Baets, M. Popović, A. Melloni, J. Joannopoulos, M. Vanwolleghem, C. Doerr, and H. Renner. What is – and what is not – an optical isolator. *Nature Photonics*, 7(8):579–582, 2013.
- [205] R. Potton. Reciprocity in optics. *Reports on Progress in Physics*, 67(5):717–754, 2004.
- [206] A. White, A. Gilchrist, G. Pryde, J. O’Brien, M. Bremner, and N. Langford. Measuring two-qubit gates. *Journal of the Optical Society of America B*, 24(2):172, 2007.
- [207] K. Mitsuya, Y. Shoji, and T. Mizumoto. Demonstration of a silicon waveguide optical circulator. *IEEE Photonics Technology Letters*, 25(8):721–723, 2013.

- [208] L. Bi, J. Hu, P. Jiang, D. Hun Kim, G. Dionne, L. Kimerling, and C. Ross. On-chip optical isolation in monolithically integrated non-reciprocal optical resonators. *Nature Photonics*, 5(12):758–762, 2011.
- [209] K. Chang and W. Sorin. High-performance single-mode fiber polarization-independent isolators. *Optics Letters*, 15(8):449–451, 1990.
- [210] K. Shiraishi, T. Chuzenji, and S. Kawakami. Polarization-independent in-line optical isolator with lens-free configuration. *Journal of Lightwave Technology*, 10(12):1839–1842, 1992.
- [211] N. Sugimoto, H. Terui, A. Tate, Y. Katoh, Y. Yamada, A. Sugita, A. Shibukawa, and Y. Inoue. A hybrid integrated waveguide isolator on a silica-based planar lightwave circuit. *Journal of Lightwave Technology*, 14(11):2537–2546, 1996.
- [212] M. Levy, R. Osgood, H. Hegde, F. Cadieu, R. Wolfe, and V. Fratello. Integrated optical isolators with sputter-deposited thin-film magnets. *IEEE Photonics Technology Letters*, 8(7):903–905, 1996.
- [213] J. Fujita, M. Levy, R. Osgood, L. Wilkens, and H. Dötsch. Waveguide optical isolator based on Mach–Zehnder interferometer. *Applied Physics Letters*, 76(16):2158–2160, 2000.
- [214] H. Shimizu and Y. Nakano. Fabrication and characterization of an InGaAsP/InP active waveguide optical isolator with 14.7 dB/mm TE mode nonreciprocal attenuation. *Journal of Lightwave Technology*, 24(1):38–43, 2006.
- [215] Y. Shoji, T. Mizumoto, H. Yokoi, I. Hsieh, and R. Osgood. Magneto-optical isolator with silicon waveguides fabricated by direct bonding. *Applied Physics Letters*, 92(7):071117, 2008.
- [216] M.-C. Tien, T. Mizumoto, P. Pintus, H. Kromer, and J. Bowers. Silicon ring isolators with bonded nonreciprocal magneto-optic garnets. *Optics Express*, 19(12):11740–11745, 2011.
- [217] C. Doerr, N. Dupuis, and L. Zhang. Optical isolator using two tandem phase modulators. *Optics Letters*, 36(21):4293–5, 2011.
- [218] C. Doerr, L. Chen, and D. Vermeulen. Silicon photonics broadband modulation-based isolator. *Optics Express*, 22(4):4493–8, 2014.
- [219] M. Levy. The on-chip integration of magneto-optic waveguide isolators. *IEEE Journal of Selected Topics in Quantum Electronics*, 8(6):1300–1306, 2002.
- [220] R. Espinola, T. Izuhara, M.-C. Tsai, R. Osgood, and H. Dötsch. Magneto-optical nonreciprocal phase shift in garnet/silicon-on-insulator waveguides. *Optics Letters*, 29(9):941–943, 2004.

- [221] D. Jalas, A. Petrov, M. Krause, J. Hampe, and M. Eich. Resonance splitting in gyrotropic ring resonators. *Optics Letters*, 35(20):3438–3440, 2010.
- [222] M. Inoue, K. Arai, T. Fujii, and M. Abe. One-dimensional magnetophotonic crystals. *Journal of Applied Physics*, 85(8):5768–5770, 1999.
- [223] S. Fan and Z. Wang. An Ultra-Compact Circulator Using Two-Dimensional Magneto-Optical Photonic Crystals. *Journal of the Magnetics Society of Japan*, 30(6-2):641–645, 2006.
- [224] M. Steel, M. Levy, and R. Osgood. Photonic Band Gaps with Defects and the Enhancement of Faraday Rotation. *Journal of Lightwave Technology*, 18(9):1297–1308, 2000.
- [225] K. Gallo, G. Assanto, K. Parameswaran, and M. Fejer. All-optical diode in a periodically poled lithium niobate waveguide. *Applied Physics Letters*, 79(3):314–316, 2001.
- [226] L. Fan, J. Wang, L. Varghese, H. Shen, B. Niu, Y. Xuan, A. Weiner, and M. Qi. An all-silicon passive optical diode. *Science*, 335(6067):447–450, 2012.
- [227] Yu Shi, Z. Yu, and S. Fan. Limitations of nonlinear optical isolators due to dynamic reciprocity. *Nature Photonics*, 9(6):388–392, 2015.
- [228] M. Hafezi and P. Rabl. Optomechanically induced non-reciprocity in microring resonators Mohammad. *Optics Express*, 20(7):7672, 2012.
- [229] X. Xu and Y. Li. Optical nonreciprocity and optomechanical circulator in three-mode optomechanical systems. *Physical Review A*, 91(5):1–8, 2015.
- [230] A. Kuther, M. Bayer, A. Forchel, A. Gorbunov, V. B. Timofeev, F. Schäfer, and J. P. Reithmaier. Zeeman splitting of excitons and biexcitons in single InGaAs/GaAs self-assembled quantum dots. *Physical Review B*, 58(12):7508–7511, 1998.
- [231] J. Dreiser, M. Atatüre, C. Galland, T. Müller, A. Badolato, and A. Imamoglu. Optical investigations of quantum dot spin dynamics as a function of external electric and magnetic fields. *Physical Review B*, 77(7):1–15, 2008.
- [232] K. Xia, G. Lu, G. Lin, Y. Cheng, Y. Niu, S. Gong, and J. Twamley. Reversible nonmagnetic single-photon isolation using unbalanced quantum coupling. *Physical Review A*, 90:043802, 2014.
- [233] E. Lenferink, G. Wei, and N. Stern. Coherent optical non-reciprocity in axisymmetric resonators. *Optics Express*, 22:16099–16111, 2014.
- [234] T. Mizumoto, H. Chihara, N. Toku, and Y. Naito. Verification of waveguide-type optical circulator operation. *Electronics Letters*, 26(3):199–200, 1990.
- [235] N. Sugimoto, T. Shintaku, A. Tate, H. Terui, M. Shimokozono, E. Kubota, M. Ishii, and Y. Inoue. Waveguide Polarization-Independent Optical Circulator. *IEEE Photonics Technology Letters*, 11(3):355–357, 1999.

- 
- [236] R. Hambury Brown and R. Twiss. Correlation between photons in two coherent beams of light. *Nature*, 4497:27, 1956.
- [237] J. Koch, A. Houck, K. Hur, and S Girvin. Time-reversal-symmetry breaking in circuit-qed-based photon lattices. *Physical Review A*, 82:043811, 2010.
- [238] M. Schmidt, S. Kessler, V. Peano, O. Painter, and F. Marquardt. Optomechanical creation of magnetic fields for photons on a lattice. *Optica*, 2(7):635–641, 2015.
- [239] S. Walter and F. Marquardt. Classical dynamical gauge fields in optomechanics. *New Journal of Physics*, 18:113029, 2016.
- [240] R. Raussendorf and H. Briegel. A one-way quantum computer. *Physical Review Letters*, 86(22):5188–5191, 2001.
- [241] H. Mabuchi and H. J. Kimble. Atom galleries for whispering atoms: binding atoms in stable orbits around an optical resonator. *Optics Letters*, 19(10):749–751, 1994.
- [242] R. Grimm, M. Weidemüller, and Y. Ovchinnikov. Optical dipole traps for neutral atoms. *Advances in Atomic, Molecular and Optical Physics*, 42:95–170, 2000.
- [243] E. Nering. *Linear Algebra and Matrix Theory*. John Wiley & Sons Inc., 2nd edition, 1970.
- [244] A. Boca. *Experiments in Cavity QED: Exploring the Interaction of Quantized Light with a Single Trapped Atom*. PhD thesis, California Institute of Technology, 2005.
- [245] R. Horodecki, P. Horodecki, M. Horodecki, and K. Horodecki. Quantum entanglement. *Reviews of Modern Physics*, 81(2):865–942, 2009.



# Danksagung

Diese Arbeit wäre ohne die Unterstützung vieler großartiger Menschen in meinem Umfeld nicht zustande gekommen.

Allen voran bin ich meinem Betreuer Arno Rauschenbeutel zu großem Dank verpflichtet, der mir die Möglichkeit gegeben hat, meine Dissertation an diesem Experiment durchzuführen. Durch seine mitreißenden Vorlesungen konnte er mich für das Gebiet der Quantenoptik begeistern. Wie kaum ein anderer vermag er es, komplizierte Sachverhalte verständlich und anschaulich darzustellen. Seine Auffassungsgabe und sein physikalisches Verständnis waren auch während meiner Dissertation eine große Inspiration für mich. Es war mir eine große Freude, Teil seiner Arbeitsgruppe gewesen zu sein.

Besonderer Dank gilt auch Jürgen Volz, ohne dessen Hilfe meine Arbeit in dieser Form nicht zustande gekommen wäre. Er stand mir immer mit Rat und Tat zur Seite, unabhängig davon wie einfach oder kompliziert die Fragestellung war oder ob er gerade selbst viel zu tun hatte. Mit seiner intuitive Herangehensweise an physikalische Probleme konnte er mir viele Sachverhalte deutlich machen.

Außerdem möchte ich mich bei meinen KollegInnen am CQED-Experiment, Christian Junge, Elisa Will, Adèle Hilico und Luke Masters, für die großartige Zusammenarbeit bedanken. Ohne ihren Einsatz wäre die Durchführung der hier präsentierten Experimente nicht möglich gewesen. Danke auch an alle anderen Rauschis, von denen ich viele nicht nur als KollegInnen, sondern auch als FreundInnen schätzen gelernt habe. Das hervorragende Gruppenklima hat die vielen Stunden am ATI zu einer großartigen Zeit gemacht, an die ich gerne zurückdenken werde.

Mein Dank gilt auch dem Doktoratskolleg CoQuS, welches mir meinen Forschungsaufenthalt am Imperial College London ermöglicht hat.

Ganz besonders möchte ich mich auch bei meiner Familie und meinen FreundInnen bedanken. Meiner Cathi kann ich nicht genug für ihre immerwährende Unterstützung, ihr Verständnis und ihren Zuspruch während der letzten Jahre danken. Zu guter Letzt bedanke ich mich ganz herzlich bei meinen Eltern, die immer an mich geglaubt haben und mir durch ihre Unterstützung mein Studium ermöglicht haben.





## LEBENS LAUF

Michael Scheucher  
Trauttmansdorffgasse 22/1/10  
1130 Wien  
Österreich

### **Persönliche Daten**

Geburtsdatum: 14. Oktober 1987  
Geburtsort: Wien  
Staatsangehörigkeit: Österreich

### **Ausbildung**

seit 2013	Doktorand der technischen Wissenschaften, Technische Universität Wien
2011 - 2013	Master of Science in Technische Physik, Technische Universität Wien
2007 - 2011	Bachelor of Science in Technische Physik, Technische Universität Wien
1998 - 2006	Bundesrealgymnasium Wien IV
1994 - 1998	Volksschule, Wien